

**FIRST PRINCIPLES STUDY OF SELECTED METAL  
OXIDES: POLYMORPHS OF  $\text{LiAlO}_2$  AND  $\text{LiGaO}_2$   
AND CATALYTIC PROPERTIES OF  
Fe and Ni- DOPED  $\text{BaTiO}_3$**

**Wutthigrai Sailuam**

มหาวิทยาลัยเทคโนโลยีสุรนารี

**A Thesis Submitted in Partial Fulfillment of the Requirements for the  
Degree of Doctor of Philosophy in Physics  
Suranaree University of Technology  
Academic Year 2016**

การคำนวณแบบเฟิร์สพริ้นซิเปิลของโลหะออกไซด์บางชนิด :  
ภาวะพหุสัณฐานของ  $\text{LiAlO}_2$  และ  $\text{LiGaO}_2$  และคุณสมบัติ  
ตัวเร่งปฏิกิริยาของ  $\text{BaTiO}_3$ , เจือ Fe และ Ni

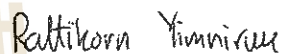


วิทยานิพนธ์นี้เป็นส่วนหนึ่งของการศึกษาตามหลักสูตรปริญญาวิทยาศาสตรดุษฎีบัณฑิต  
สาขาวิชาฟิสิกส์  
มหาวิทยาลัยเทคโนโลยีสุรนารี  
ปีการศึกษา 2559

**FIRST PRINCIPLES STUDY OF SELECTED METAL OXIDES:  
POLYMORPHS OF  $\text{LiAlO}_2$  AND  $\text{LiGaO}_2$  AND CATALYTIC  
PROPERTIES OF Fe AND Ni- DOPED  $\text{BaTiO}_3$**

Suranaree University of Technology has approved this thesis submitted in partial fulfillment of the requirements for the Degree of Doctor of Philosophy.

Thesis Examining Committee



(Assoc. Prof. Dr. Rattikorn Yimnirun)

Chairperson



(Prof. Dr. Sukit Limpijumng)

Member (Thesis Advisor)



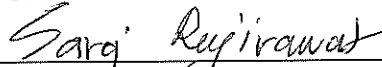
(Prof. Dr. Kriksana Sagarik)

Member



(Dr. Nongnuch Artrith)

Member



(Dr. Saroj Rujirawat)

Member



(Prof. Dr. Santi Maensiri)

  
(Prof. Dr. Sukit Limpijumng)

Vice Rector for Academic Affairs  
and Innovation

Dean of Institute of Science

วุฒิไกร ไสเหลือ้ม : การคำนวณแบบเพิร์สปรินซิเปิลของโลหะออกไซด์บางชนิด: ภาวะพหุสัณฐานของ  $\text{LiAlO}_2$  และ  $\text{LiGaO}_2$  และคุณสมบัติตัวเร่งปฏิกิริยาของ  $\text{BaTiO}_3$ , เจือ Fe และ Ni (FIRST PRINCIPLES STUDY OF SELECTED METAL OXIDES : POLYMORPHS OF  $\text{LiAlO}_2$  AND  $\text{LiGaO}_2$  AND CATALYTIC PROPERTIES OF Fe AND Ni- DOPED  $\text{BaTiO}_3$ ). อาจารย์ที่ปรึกษา : ศาสตราจารย์ ดร. ชูกิจ ลิ้มปิ๋จ้านงค์, 184 หน้า.

วิทยานิพนธ์นี้ได้ศึกษาคุณสมบัติของออกไซด์สามชนิดโดยวิธีการคำนวณแบบแอบ อินิชิโอ การเปลี่ยนแปลงโครงสร้างเฟสระหว่างโครงสร้างเฟสธรรมชาติและโครงสร้างเฟสภายใต้สภาวะความดันสูงของทั้ง  $\text{LiAlO}_2$  และ  $\text{LiGaO}_2$  ได้ถูกศึกษาและพฤติกรรมการเร่งปฏิกิริยาของการปรับปรุง  $\text{BaTiO}_3$  ยังถูกวิเคราะห์ด้วยเช่นกัน การเปลี่ยนแปลงเฟสระหว่าง  $\gamma$  -  $\text{LiAlO}_2$  และ  $\delta$  -  $\text{LiAlO}_2$  ถูกคำนวณใน 2 ระดับ คือ โดยใช้ Perdew – Burke – Ernzerhof (PRB) generalized – gradient approximation (GGA) ฟังก์ชันนอล และ Heyd Scuseria Ernzerhof (HSE) ฟังก์ชันนอล ผลการคำนวณได้ทำนายความดันสมดุลในการเปลี่ยนโครงสร้างซึ่งสอดคล้องเป็นอย่างดีกับผลการทดลอง แลပ်พลังงานและความหนาแน่นของสถานะพลังงานของ  $\gamma$  -  $\text{LiAlO}_2$  และ  $\delta$  -  $\text{LiAlO}_2$  ที่ความดันปรกติยังถูกนำเสนอด้วย การเปลี่ยนแปลงเฟสของโครงสร้างในธรรมชาติของ  $\beta$  -  $\text{LiGaO}_2$  ( $\text{Pna}2_1$ ) ที่ภายใต้สภาวะความดันแบบต่าง ๆ ได้ถูกทำการศึกษา พบว่าหลายโครงสร้างของ  $\text{LiGaO}_2$  เสถียรภายใต้ความเค้นเฉพาะแบบต่าง ๆ โดยบางโครงสร้างยังไม่มีรายงานมาก่อนในอดีต ( $\text{oP}16$ ,  $\text{I}41/\text{amd}$  และ  $\text{P}4_2/\text{2}$ ) การศึกษาพบว่าโครงสร้างแบบรอกซอลด์ของ  $\text{LiGaO}_2$  จะเสถียรภายใต้สภาวะความดันที่สูงมากพอ แต่ทว่าความเค้นแบบแกนเดียวก็สามารถทำให้โครงสร้างแบบเตตราโกนอลและออร์โธโรอมบิกเสถียรได้เช่นเดียวกัน โดยขึ้นกับทิศทางของความเค้นที่ให้เข้าไป กระบวนการเปลี่ยนโครงสร้างสามารถแสดงได้จากการคำนวณค่าเอนทัลปีพื้นผิวในฟังก์ชันของตัวแปร โครงสร้างผลึกและกำแพงพลังงานในการก้าวข้ามระหว่างตำแหน่งจุดต่ำสุดแต่ละบริเวณ ความเค้นและทิศทางการกดที่นำไปสู่เฟสใหม่ของ  $\text{LiGaO}_2$  ได้ถูกนำเสนอและอภิปรายด้วย ในส่วนสุดท้ายของวิทยานิพนธ์พฤติกรรมการเร่งปฏิกิริยาของ  $\text{BaTiO}_3$  สำหรับปฏิกิริยาการสังเคราะห์ออกซิเจนได้ถูกศึกษา พบว่าการเจือ Fe และ Ni สามารถทำให้สภาพการนำไฟฟ้าดีขึ้นและมีการลดค่าศักย์ไฟฟ้าส่วนเกินสำหรับปฏิกิริยาที่ใช้ในการสังเคราะห์ออกซิเจนบน  $\text{BaTiO}_3$  โดยขึ้นกับการคำนวณแผนภาพฟั๊วเบและค่าความเป็นกรดเบสและศักย์ไฟฟ้าที่ขึ้นกับแผนภาพพื้นผิว ซึ่งสนับสนุนว่า  $\text{BaTiO}_3$  มีความเสถียรอย่างมากภายใต้สภาวะซึ่งทำให้เกิดปฏิกิริยา แต่ไม่ไวต่อสารมัชยันตร์ในปฏิกิริยา และการดูดกลืนก๊าซไฮโดรเจน โดยข้อพิสูจน์นี้แสดงให้เห็นว่าการ

เปลี่ยนแปลงองค์ประกอบสารที่มีอยู่อย่างเล็กน้อยสามารถปรับปรุงพฤติกรรมการเร่งปฏิกิริยาของ  
สารให้ดีขึ้นเป็นอย่างดี



สาขาวิชาฟิสิกส์  
ปีการศึกษา 2559

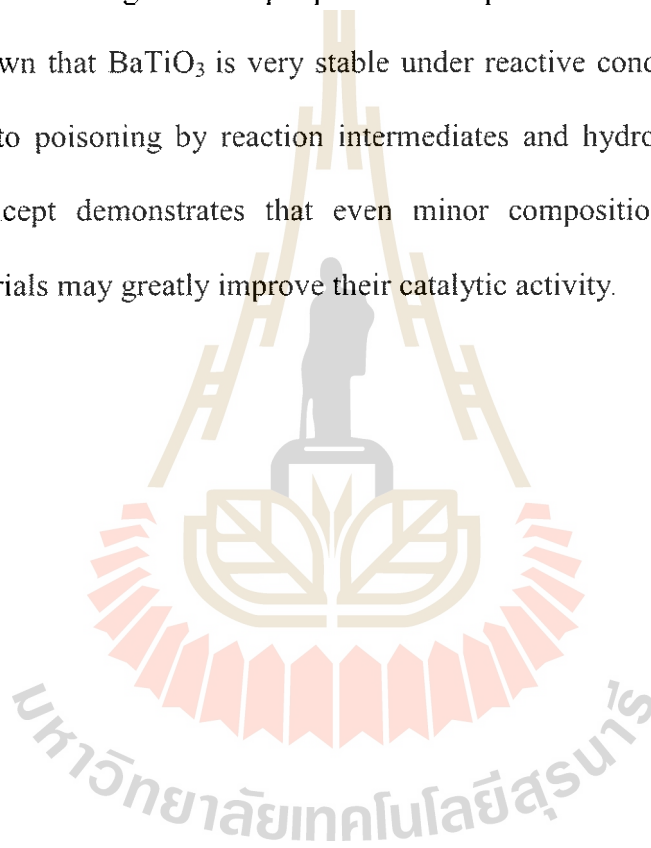
ลายมือชื่อนักศึกษา กมลวิภา โสภณสีทอง  
ลายมือชื่ออาจารย์ที่ปรึกษา ดร. อธิวัฒน์

WUTTHIGRAI SAILUAM : FIRST PRINCIPLES STUDY OF SELECTED  
METAL OXIDES: POLYMORPHS OF LiAlO<sub>2</sub> AND LiGaO<sub>2</sub> AND  
CATALYTIC PROPERTIES OF Fe AND Ni- DOPED BaTiO<sub>3</sub>. THESIS  
ADVISOR : PROF. SUKIT LIMPIJUMNONG, Ph.D. 184 PP.

PHASE TRANSFORMATION/ENTHALPY/CATALYZE ACTIVITY/*AB INITIO*

In this thesis, properties of three oxides have been investigated using *ab initio* calculations. The homogeneous structural phase transition between the natural and high-pressure forms of LiAlO<sub>2</sub> and LiGaO<sub>2</sub> have been determined, and the catalytic activity of modified BaTiO<sub>3</sub> was analyzed. The phase transition between  $\gamma$  - LiAlO<sub>2</sub> and  $\delta$  - LiAlO<sub>2</sub> was calculated on two levels of theory, using the Perdew - Burke - Ernzerhof (PBE) generalized-gradient approximation (GGA) functional and the Heyd - Scuseria - Ernzerhof (HSE) hybrid functional. Our calculations predict equilibrium phase pressures in reasonable agreement with experiment. Band structures and partial density of states of both  $\gamma$  - LiAlO<sub>2</sub> and  $\delta$  - LiAlO<sub>2</sub> at ambient pressure are reported. Phase transformations of the natural  $\beta$  - LiGaO<sub>2</sub> (Pna2<sub>1</sub>) structure under different pressure conditions were also studied. We found that various LiGaO<sub>2</sub> structures can be stabilized under specific stress conditions, some of which had not been previously reported (oP16, I41/amd, and P4<sub>1</sub>2<sub>1</sub>2). It is found that the rocksalt - like structures of LiGaO<sub>2</sub> can be stabilized under sufficiently high hydrostatic pressure, whereas uniaxial stress stabilizes either the tetragonal or the orthorhombic structure depending on the applied direction. The mechanisms of the phase transitions have been characterized by calculating the enthalpy surfaces in the crystal parameter space and

the barriers between each local minimum. Stresses and directions that lead to new phases of  $\text{LiGaO}_2$  are presented and discussed. In the final part of this thesis, the catalytic activity of  $\text{BaTiO}_3$  for the oxygen evolution reaction (OER) has been investigated. Fe and Ni doping is found to improve the electrical conductivity and reduce the overpotential required for water oxidation over  $\text{BaTiO}_3$ . Based on computed Pourbaix diagrams and pH/potential - dependent surface phase diagrams, it is further shown that  $\text{BaTiO}_3$  is very stable under reactive conditions but insensitive with respect to poisoning by reaction intermediates and hydrogen adsorption. This proof of concept demonstrates that even minor compositional modifications of existing materials may greatly improve their catalytic activity.



School of Physics

Academic Year 2016

Student's Signature กมลวิทย์ ใจบุญAdvisor's Signature ศาสตราจารย์ ดร. ธีรวิทย์ ใจบุญ

## ACKNOWLEDGEMENTS

I would first and foremost like to acknowledge my advisor Prof. Dr. Sukit Limpijumnong for his continuous support of my Ph.D. study and research, for his patience, motivation, and enthusiasm. Coming to SUT to do my graduate work with him is definitely one of the best decisions I have ever made. Without his thoughtful encouragement and careful supervision, this thesis would never have taken shape. I would like to express my appreciation to Dr. Nongnuch Artrith for her warm hospitality, her advice and her assistance during my visit at Department of Mechanical Engineering, Massachusetts Institute of Technology (MIT), Cambridge, Boston, USA. Many thanks to Dr. Kanoknan Sarasamuk for discussing phase transition under high pressure in my work. I would like to thank to Asst. Prof. Alexie M. Kolpak, Asst. Prof. Jiraroj T Thienprasert and Dr. Alex Urban for advice and help with some parts of my thesis. I would like to thank the Kolpak group members, especially from Xi Rong for introducing me the surface phase diagram and catalysis activity for perovskite materials. I would also like to thank the funding for this work by both the NANOTEC-SUT Center of Excellence on Advanced Functional Nanomaterials and Development and Promotion of Science and Technology Talents Project (DPST, Thailand). I would like to thank my friends in the condensed matters physics group. I also thank my parents for their love and support. I am today and also for giving me all the opportunities I needed to succeed.

Wutthigrai Sailuam



# CONTENTS

	<b>Page</b>
ABSTRACT IN THAI.....	I
ABSTRACT IN ENGLISH .....	III
ACKNOWLEDGMENTS .....	V
CONTENTS .....	VI
LIST OF TABLES .....	X
LIST OF FIGURES .....	XII
LIST OF ABBREVIATIONS.....	XXI
<b>CHAPTER</b>	
<b>I INTRODUCTION .....</b>	<b>1</b>
<b>II THEORETICAL BACKGROUND .....</b>	<b>9</b>
2.1 Density Functional Theory .....	9
2.1.1 The Schrödinger equation .....	9
2.1.2 Born-Oppenheimer approximation .....	11
2.1.3 The Hohnberg-Kohn theorem .....	12
2.2 The exchange-correlation energy .....	15
2.2.1 The Local Density Approximation (LDA).....	16
2.2.2 The Generalized Gradient Approximation (GGA).....	17
2.2.3 Revised Perdew-Burke-Ernzerhof function (RPBE).....	18
2.2.4 Hybrid functional .....	18

## CONTENTS (Continued)

	Page
2.3 Solving the Kohn-Sham equations .....	19
2.4 Pseudowavefunctions and Pseudopotentials .....	20
2.5 Projector augmented waves .....	23
2.6 Plane waves .....	24
2.7 Zeroth Order Regular Approximation .....	25
2.8 Van der Waals interactions .....	26
2.9 The Viena Ab initio Simulation Package (VASP) .....	27
2.10 The Fritz-Haber-Institut ab initio molecular simulations (FHI-aims).....	28
<b>III CALCULATION METHODS .....</b>	<b>31</b>
3.1 Phase transition in the solid state .....	31
3.1.1 Thermodynamic stability .....	32
3.2 Water adsorption and dissociation on BaTiO <sub>3</sub> surfaces .....	34
3.3 Water splitting on surface of perovskite .....	36
3.4 Pourbaix and Surface-phase diagrams .....	41
3.5 Experimental standard hydrogen electrode free energy .....	45
3.6 The oxygen evolution reduction (OER) activities on active sites .....	47
3.7 Reaction free energy profiles of the OER .....	49
<b>IV PHASE TRANSFORMATION OF ABO<sub>2</sub> METAL OXIDES BY FIRST PRINCIPLES CALCULATIONS .....</b>	<b>55</b>

## CONTENTS (Continued)

	Page
4.1 High pressure phase of $\text{LiAlO}_2$ : A first principles study .....	55
4.1.1 Introduction .....	55
4.1.2 Computational methods .....	56
4.1.3 Results and discussion .....	58
4.2 $\text{LiGaO}_2$ pressure-induced phase transformations from first principle .....	67
4.2.1 Introduction .....	71
4.2.2 Material and methods .....	72
4.2.3 Results and discussion .....	73
<b>V REDUCED OVERPOTENTIALS FOR ELECTROCATALYTIC</b>	
<b>WATER SPLITTING MODIFIED <math>\text{BaTiO}_3</math></b> .....	83
5.1 Introduction .....	83
5.2 Methods .....	86
5.2.1 Water adsorption and dissociation on $\text{BaTiO}_3$ surfaces .....	90
5.2.2 Pourbaix and surface phase diagrams .....	91
5.3 Results .....	95
5.3.1 Water molecule adsorption and dissociation on $\text{BaTiO}_3$ surfaces ..	95
5.3.2 Volcano of $\text{BaTiO}_3$ activity .....	98
5.3.3 Energetics and electronic structure of Fe- Ni- modified $\text{BaTiO}_3$	102
5.3.4 $\text{BaTiO}_3$ surface phases and solubility at catalytic conditions .....	108

**CONTENTS (Continued)**

	<b>Page</b>
5.3.5 Oxygen evolution reaction over pristine and Fe-/Ni-modified BaTiO <sub>3</sub> .....	113
5.4 Discussion .....	116
<b>VI CONCLUSIONS AND FUTURE RESEARCH</b> .....	<b>118</b>
REFERENCES .....	120
APPENDIX .....	144
CURRICULUM VITAE .....	185

## LIST OF TABLES

Table	Page
3.1 Values of the zero-point energy (ZPE) and the corrections for the vibrational entropy contributions (TS) for adsorbed and gas-phase molecules taken from reference (Valdeś et al., 2008) .....	45
4.1 Calculated lattice parameters ( $a$ , $b$ and $c$ ), equilibrium volume ( $V$ ) and energy gap ( $E_g$ ) for $\gamma$ -LAO and $\delta$ -LAO from HSE and GGA calculations. Note that the $E_d$ and $E_i$ in parentheses indicate that the band gaps are direct and indirect, respectively .....	63
4.2 Schematic illustrations of lattice parameters, percentage changes, Bulk modulus $B_0$ , average bond length and average bond angles for Pna2 <sub>1</sub> (WZ'), oP16 (HX'), R3m (RS'') and I41/amd (RS') structures under their equilibrium and loading conditions .....	76
4.3 Lattice parameters for the tetragonal P4 <sub>1</sub> 2 <sub>1</sub> 2 (BCT') LGO under tensile loading along [001] direction for $\sigma_c = 0, 2, 4.1$ and 6 GPa .....	82

## LIST OF TABLES (Continued)

Table	Page
5.1 Relative free energies of species occurring in the Ba and Ti Pourbaix diagrams at standard ambient conditions (25°C and 1bar).  The free energies relative to the standard hydrogen electrode (SHE), $\Delta G^0_{\text{SHE}}/\text{eV}$ , were taken from reference (Donald et al., 1982).  All activities $a_A$ were taken to be equal to $10^{-8}$ M .....	93
5.2 Summary of free energy path base on four electron paths representing the overpotentials ( $\eta^{\text{OER}}$ ) for the transition metal-doped $\text{TiO}_2$ -terminated surfaces and the free energies at the standard conditions ( $\text{pH} = 0$ , $T=298.15$ K) and $U=0$ V .....	99
5.3 Summary of free energy path base on four electron paths representing the overpotentials ( $\eta^{\text{OER}}$ ) for the metal-doped BaO-terminated surfaces and the free energies at the standard conditions ( $\text{pH} = 0$ , $T=298.15$ K) and $U=0$ V .....	100
5.4 Summary of adsorption energies of intermediate molecule ( $\text{H}^*$ , $\text{O}^*$ , $\text{OH}^*$ and $\text{OOH}^*$ ) on BaO and $\text{TiO}_2$ terminated. The coverage of $\frac{1}{4}\text{ML}$ , $\frac{1}{2}\text{ML}$ , $\frac{3}{4}\text{ML}$ and $1\text{ML}$ are considered .....	113

## LIST OF FIGURES

Figure	Page
2.1	Procedure of DFT calculations with constant lattice parameters.....20
2.2	Schematic illustrations of the pseudopotential, pseudowavefunction (solid curves) and the all electron wave function, core potential (dashed line). The cutoff radius $r_c$ represents a radius at which the all electron and pseudo quantities match .....22
2.3	The radial function $u_j(r)$ of the 3s orbital for a free silicon atom is plotted along radius $r$ . The free-atom like potential $v_j(r)$ and the steeply increasing confining potential $v_{cut}(r)$ are also shown. The dotted line indicates the confining radius $r_{cut}$ .....29
3.1	Side view and top view of the slab models of BaO- and TiO <sub>2</sub> terminated side. The green, light blue, red and gray spheres represent Ba, Ti, O and H atoms, respectively. The blue and violet spheres represent the doping site of metals and transition metal atom .....36
3.2	Schematic of alkaline electrolysis cell; left hand side is the hydrogen evolution reaction (HER) and right hand side is the oxygen evolution reaction (OER). The yellow circle is shown the catalyst surface react with water molecule to generate oxygen in oxygen evolution reaction (OER) .....38

## LIST OF FIGURES (Continued)

Figure	Page
3.3 Activity trends towards oxygen evolution plotted for perovskites. the negative theoretical overpotential ( $\eta$ ) was plotted against the standard free energy of the $\Delta G_{\text{O}^*}^0 - \Delta G_{\text{OH}^*}^0 / \text{eV}$ step .....	39
3.4 The top view of $\text{TiO}_2$ -terminated surface model shown the possibility of initial site/positions to adsorb the intermediate molecule. Number 1 represents the top site on center Ti or transition metal, number 2 represents the bridge center Ti or transition metal and O atom, number 3 represents the hollow site, number represents on the top of O atom and number 5 represents on top of Ti atom .....	41
3.5 Schematic of surface reconstruction via surface-solvent ion exchange.....	20
3.6 The reaction free energy diagram for the OER. The turquoise solid line indicates the reaction pathway without applied potential ( $U = 0 \text{ V}$ ). The applied equilibrium potential $U = 1.23 \text{ eV}$ ( $\text{pH} = 0$ and $T = 298.15 \text{ K}$ ), the ideal catalysis shown by black dash line with the over potential $\eta^{\text{OER}} = 0 \text{ V}$ . The red solid line indicates non-ideal catalyst case, $\eta^{\text{OER}} > 0 \text{ V}$ . The overpotential volume is shown by blue solid line. The red dash line indicates reaction free energy of the magnitude value ( $4.92 \text{ eV}$ ) at $U=0 \text{ V}$ (*represents the active site on surface catalyst) .....	20



## LIST OF FIGURES (Continued)

<b>Figure</b>		<b>Page</b>
4.1	<p>(Color online) (a) Schematic illustration of the natural and high-pressure phases of <math>\text{LiAlO}_2</math>, i.e., <math>\gamma</math>-LAO (left) and <math>\delta</math>-LAO (right) phases. Large spheres represent oxygen atoms, medium spheres: Al, and small spheres: Li. (b) The common unit cells of the two phases (<math>\gamma</math>-LAO and <math>\delta</math>-LAO), containing 16 atoms, used in the calculations. Red dashed squares A and B highlight the bond formation during the phase transformation (see text, for detail). (c) The side view of the crystal with the dashed black rectangles showing the unit cell</p>	59
4.2.	<p>(Color online) (a) The calculated HSE total energy as a function of volume for <math>\gamma</math>-LAO and <math>\delta</math>-LAO and the common tangent construction. (b) The enthalpy as a function of <math>c/a</math> ratio at various pressures. (The <math>c/a</math> ratio can be considered as the transformation coordinate of the homogeneous transformation from <math>\gamma</math>-LAO to <math>\delta</math>-LAO.) The black curve shows the enthalpy at the phase equilibrium pressure where both phases have the same enthalpy. The highest enthalpy point between the two phases defines the transformation barrier. (c) and (d) are the same as (a) and (b) but calculated using GGA functional</p>	60

## LIST OF FIGURES (Continued)

Figure		Page
4.3	Electronic band structures and partial density of states (PDOS) of (a) $\gamma$ -LAO and (b) $\delta$ -LAO obtained from HSE calculations.  The special k-points used for the band structures plot are according to the cubic Brillouin zone .....	65
4.4	Electronic band structures and partial density of states (PDOS) of (a) $\gamma$ -LAO and (b) $\delta$ -LAO obtained from GGA calculations .....	66
4.5	Schematic illustrations of the ambient and the high-pressure crystal structures of LGO: (a) Orthorhombic (Pna2 <sub>1</sub> ) - ambient condition structure, (b) Body-centered tetragonal (I41/amd) – hydrostatic compression ( $P_t$ ) structure, (c) the Rhombohedral (R3m) –another hydrostatic compression ( $P_t$ ) structure, (d) Orthorhombic (oP16) - [001] compressive stress ( $-\sigma_c$ ) structure, and (e) tetragonal (P4 <sub>1</sub> 2 <sub>1</sub> 2) - [001] tensile stress ( $\sigma_c$ ) structure.  In the structures, the green spheres represent Ga cations, blue spheres represent Li cations and red spheres represent O anions .....	70
4.6	Relationship between the crystal phases of the binary compound ZnO and the analogous ones of the ternary compound LGO .....	71
4.7	Total energy versus volume for five LGO structures: Green (RS''), Red (WZ'), black circles (HX'), black squares (RS') and blue squares (BCT') .....	75

## LIST OF FIGURES (Continued)

Figure	Page
<p>4.8 Enthalpy surface map (eV), and 2-D sections of the enthalpy surface maps for a Pna2<sub>1</sub> (WZ'), oP16 (HX') and I41/amd (RS') unit cell. Each point on the surface represents the minimum energy volume (<i>V</i>) is allowed to relax while <i>c/a</i> and <i>b/a</i> are kept constant: (a) Enthalpy surface map (eV) at <i>P<sub>t</sub></i> = 0 GPa, (b) Enthalpy surface map (eV) at <i>P<sub>t</sub></i> = 3.7 GPa, (c) 2-D sections of the enthalpy surface maps at <i>P<sub>t</sub></i> = 0 GPa and (d) 2-D sections of the enthalpy surface maps at <i>P<sub>t</sub></i> = 3.7 GPa. For <i>b/a</i> = 0.468 (red line) and <i>b/a</i> = 0.848 (blue line).....</p>	77
<p>4.9 (a) The enthalpy surface for the compression stress <math>\sigma_c = -3.5</math> GPa and (b) 2-D sections of the enthalpy surface maps with the compression stress <math>\sigma_c = -3.5</math> GPa for <i>b/a</i> = 0.468 (red line) and <i>b/a</i> = 0.848 (blue line) .....</p>	79
<p>4.10 (a) Schematic comparison of WZ' and BCT' LGO structures. Enthalpy (eV) as a function of <i>c/a</i> for <i>b/a</i> = 0.848 at different tensile stresses: (b) <math>\sigma_c = 0</math> GPa, (c) <math>\sigma_c = 2</math> GPa, (d) <math>\sigma_c = 4.1</math> GPa and (e) <math>\sigma_c = 6</math> GPa .....</p>	81
<p>5.1 Bulk structure models for (a) BaTiO<sub>3</sub> (b) BaTi<sub>0.75</sub>Ni<sub>0.25</sub>O<sub>3</sub> and (c) BaTi<sub>0.75</sub>Fe<sub>0.25</sub>O<sub>3</sub>. The structures of the Ni- and Fe-doped compositions were determined by enumeration as described in the text. (d) Example of a Fe-modified TiO<sub>2</sub>-terminated BaTiO<sub>3</sub> (001) surface slab model with adsorbed *OOH. The structure models were visualized using the VESTA software (Momma and Izumi, 2011).....</p>	89

## LIST OF FIGURES (Continued)

Figure	Page
5.2 Schematic illustration of the most favorable structure of 1/4– monolayer adsorption (1/4 ML) on the BaTiO <sub>3</sub> -surfaces: (a) initial system configuration, (b) the case with dissociated system and (c) the case with adsorbed WM without WM dissociation .....	96
5.3 Schematic illustrations of the most favorable structures of 1/4– monolayer adsorption (1/4ML) on the metal-doped BaO- terminated and transition metal doped TiO <sub>2</sub> -terminated surfaces. The adsorption energies ( $E_{ads}/\text{eV}$ ) are also shown .....	97
5.4 Calculated distances between the hydrogen atom of the water molecule and the oxygen atom on surface (OH <sub>s</sub> ) and the bondlength of the O-H <sub>w</sub> in WM for all of the most favorable structures (b) on the metal-doped BaO terminated on <i>A</i> -site and transition metal-doped TiO <sub>2</sub> -terminated on <i>B</i> -site, respectively .....	98
5.5 $-\eta^{\text{OER}}$ as a function of $\Delta G^{\text{O}^*} - \Delta G^{\text{HO}^*}/\text{eV}$ for the classes of the surfaces studied. This leads to a universal volcano relationship, metal-doped BaO terminated are shown by red circles and transition metal-doped TiO <sub>2</sub> terminated are shown by black squares .....	101

## LIST OF FIGURES (Continued)

Figure		Page
5.6	<p>Formation energies for <math>\text{BaTi}_{1-x}\text{B}_x\text{O}_3</math> with <math>B = \text{Fe}</math> (red) and <math>B = \text{Ni}</math> (blue) in the cubic and tetragonal perovskite structures obtained from enumeration of 826 distinct atomic configurations and spin orderings. The (high-temperature) cubic <math>\text{BaTiO}_3</math> structure was used as reference for the formation energy, so that negative formation energies mean that doping of <math>\text{BaTiO}_3</math> with species <math>B</math> is facile. The stable compositions are indicated by filled circles and connected by solid lines. 820 unstable and metastable structures are shown as red stars (Fe) and blue triangles (Ni).....</p>	103
5.7	<p>Electronic density of states for pristine and (a) Fe-modified and (b) Ni-modified <math>\text{BaTiO}_3</math> compositions. The most stable structures of Figure 5.6 were used. For each structure, the majority spin density is shown to the left and the minority spin density to the right. All plots have been aligned at the Fermi level <math>\epsilon_f</math>. The cubic structure refers to space group <math>\text{Pm}3\text{m}</math> (<math>=O_h</math>) and the hexagonal structure belongs to the space group <math>\text{P}6_3/\text{mmc}</math> .....</p>	106

## LIST OF FIGURES (Continued)

Figure		Page
5.8	Species-resolved electronic density of states (DOS) for pristine and (a) Fe-modified and (b) Ni-modified BaTiO <sub>3</sub> compositions. This data was obtained as the sum of the orbital-projected partial DOS (PDOS) for all atoms of each atomic species. Note that the intensities depend on the chosen atomic radii (we employed VASP defaults). The structures are the same as in Figure 5.7 .....	107
5.9	Computed Ba Pourbaix diagram with ionic concentrations of 10 <sup>-8</sup> M. The dashed orange lines indicate the potentials for water oxidation (2 H <sub>2</sub> O → O <sub>2</sub> + 4H <sup>+</sup> + 4e <sup>-</sup> , U = 1.23V at pH=0) and reduction (4H <sup>+</sup> + 4e <sup>-</sup> → 2H <sub>2</sub> , U = 0V at pH=0) .....	109
5.10	Computed Ti Pourbaix diagram with ionic concentrations of 10 <sup>-8</sup> M. The dashed orange lines indicate the potentials for water oxidation (2 H <sub>2</sub> O → O <sub>2</sub> + 4H <sup>+</sup> + 4e <sup>-</sup> , U = 1.23V at pH=0) and reduction (4H <sup>+</sup> + 4e <sup>-</sup> → 2H <sub>2</sub> , U = 0V at pH=0) .....	110
5.11	Stable BaTiO <sub>3</sub> (001) surface phase as function of the pH and the applied potential. The clean BaO and TiO <sub>2</sub> terminated surfaces were considered, as well as these surfaces with hydrogen coverages between 1/4 and 1 monolayer (ML). As in Figure 5.4 and Figure 5.5, dashed orange lines indicate the water oxidation and reduction potentials .....	112

## LIST OF FIGURES (Continued)

Figure	Page
<p>5.10 Reaction free-energy diagram for the oxygen evolution reaction over ideal (black) and Fe (red) and Ni (blue) doped BaTiO<sub>3</sub> following the elementary reaction steps of Eq. 5.1. The solid lines indicate the reaction pathway without applied potential (<math>U = 0</math> V) and the dashed lines are the reaction profiles at the required overpotentials for ideal Ti (<math>\eta = 1.22</math> V), Fe dopants (<math>\eta = 0.91</math> V), and Ni dopants (<math>\eta = 0.89</math> V) .....</p>	115

## LIST OF ABBREVIATIONS

DFT	= Density Functional Theory
LDA	= Local Density Approximation
GGA	= Generalized Gradient Approximation
PBE	= Perdew Burke and Ernzerhof
RPBE	= Revised Perdew Burke and Ernzerhof
HF	= Hartree-Fock
HSE	= Heyd-Scuseria-Ernzerhof
KS	= Kohn-Sham
ZORA	= Zeroth Order Regular Approximation
vdW	= Van Der Waals
VASP	= Vienna Ab initio-Simulation Package
FHI-aims	= Fritz-Haber-Institut ab Initio Molecular Simulations
WM	= Water Molecule
WMs	= Water Molecules
ML	= Monolayer
AEC	= Alkaline Electrolysis Cell
HER	= Hydrogen Evolution Reaction
OER	= Oxygen Evolution Reaction



**LIST OF ABBREVIATIONS (Continued)**

ZPE	= Zero Point Energy
SHE	= Standard Hydrogen Electrode
LAO	= $\text{LiAlO}_2$
LGO	= $\text{LiGaO}_2$
EOS	= Energy of State
PAW	= Projector Augmented Wave
DOS	= Density of State
ads	= Adsorption



## CHAPTER I

### INTRODUCTION

Applications of quantum mechanics and first principles calculations to study physical properties of materials can be done by solving the “Schrödinger equations” for the ground-state electron wave functions and the corresponding electron densities. First principle calculations are also known as “*ab initio*” calculations, which are generally based on density functional theory (DFT). DFT makes the study of atomic structures and electronic properties of materials possible. In many-body systems, sets of the full Schrödinger equations are too difficult to be solved. In these days, with the aid of DFT and high performance computers, the calculation of simplified Schrödinger equations is possible. The new development of more complicated exchange correlation functions, such as the so-called hybrid functional, makes high accuracy calculations of many atomic systems possible. In this thesis, first-principles calculations are used to study the microstructures, electronic properties and phase transformations of selected metal oxide compounds. Phase transformation has been computationally studied heavily in the past decades and is still an ongoing topic of interest. The phase transformations in this thesis is a transformation among different crystal structures of the same stoichiometry metal oxide compounds. The homogeneous transformation described by a consorted transformation of the whole crystal at once. Most of the time, a process with “symmetry-breaking” is taken place.

However, this homogeneous transformation is introduced to allow the feasibility of computation and might or might not taken place in real experiment. Computer simulation is, however, a very important component to aid understanding of how the phase transformation takes place. The symmetry-breaking process occurred during a phase transformation with different conditions such as under high pressure, under high temperature or doping condition. For instance, ZnO with a wurtzite structure at ambient pressure can transform to rocksalt structure under the transformation pressure of about 9.1 GPa (Miao and Lambrecht, 2003), the orthogonal  $\beta$ -LiAlO<sub>2</sub> can transform to the tetragonal  $\gamma$ -LiAlO<sub>2</sub> above 450°C (Vanfleet et al., 2008), and composition and microstructure characterizations indicated that Bi (~3 at. %) doping preserved Germanium telluride (GeTe) rhombohedral structure with slight X-ray diffraction peak shifts (Zhang et al., 2013).

There are two main parts in this thesis, the first part is about the phase transformation of ABO<sub>2</sub> metal oxide and the second part is about catalysts activity on BaTiO<sub>3</sub>. For the first part, phase transformations in ABO<sub>2</sub> oxide compounds, with A and B represents by Li and (Al,Ga), respectively, are studied. Lithium Dioxogallate (LiGaO<sub>2</sub>) and Lithium Aluminium Oxide (LiAlO<sub>2</sub>) systems have been experimentally and computationally studied for many years. There are two main reasons why these two systems are very attractive. First, the lattice parameters of LiAlO<sub>2</sub> and LiGaO<sub>2</sub> are nicely matched with that of GaN. Because GaN is an important material for blue, violet, UV and white LED, having a good substrate for growing GaN on is highly beneficial. Secondly, both materials are wide band gap semiconductors and could potentially serve as new wide band gap electronic materials. Both LiAlO<sub>2</sub> and LiGaO<sub>2</sub> have crystal structures in analogous to wurtzite ZnO with the substitutions of Zn

atoms alternately by Ga (or Al) atom and Li atom. Recent studies showed that wurtzite ZnO under ambient pressure with space group  $P6_3mc$  can transform to a rocksalt-type phase (R-3m) under high pressure (Desgreniers, 1998; Limpijumnong and Lambrecht, 2001).

Lithium aluminate,  $LiAlO_2$ , henceforth LAO, has potential applications in the energy industry as lithium battery cathodes and electrolyte tiles for molten carbonate fuel cells (MCFC) (Ceder et al., 1998). It has been reported that LAO has at least four different phases, the hexagonal  $\alpha$ -phase, the monoclinic  $\beta$ -phase (Marezio and Remeika, 1966; Zou et al., 2006), the tetragonal  $\gamma$ -phase (Marezio, 1965), and the tetragonal  $\delta$ -phase (Li et al., 2004). The  $\gamma$ -LAO (Marezio, 1965) has attracted much attention as a promising substrate for GaN-based laser diodes. This is because the lattice mismatch between  $\gamma$ -LAO and GaN is only -1.4% along  $[001]$  LAO and  $[11\bar{2}0]$  GaN and -0.1% along  $[010]$  LAO and  $[0001]$  GaN (Ke et al., 1998; Hellman and Harris, 1997). The  $\gamma$ - to  $\delta$ -phase transformation of LAO has been experimentally studied using several techniques and a wide range of the phase transformation pressure has been reported, i.e. from 2 GPa based on an anvil cell technique to 9 GPa based on a shock recovery technique (Li et al., 2004). However, to our knowledge, there is no report on the computation study of the transformation. Here, the  $\gamma$ - to  $\delta$ -phase transformation under hydrostatic pressure of LAO is investigated using first principles calculations within both Heyd-Scuseria-Ernzerhof (HSE) (Heyd et al., 2003) hybrid functional and generalized-gradient approximation (GGA). In addition, the electronic properties of both phases are also studied.

$\beta$ - $LiGaO_2$  ( $Pna2_1$ ) is the ambient-pressure structure of  $LiGaO_2$  (LGO) that can be obtained in a large single crystal form by a conventional Czochralski melt-pulling

method (Chen et al., 2014; Jungthawan and Limpijumnong, 2004). This material has a wurtzite derived structure with a good lattice match to GaN and ZnO. Both GaN and ZnO are technologically important materials for blue and purple optoelectronic devices (Chen et al., 2014). The crystal structure of  $\beta$ -LiGaO<sub>2</sub> (Pna2<sub>1</sub>) is an analogous of the wurtzite ZnO in which the group-II Zn is alternately substituted by group-III Ga and group-I Li. Due to the relaxation of the oxygen sub-lattice and symmetry-breaking cations, the structure of this ternary oxide slightly differs from the perfect wurtzite-type structure (P6<sub>3</sub>mc) (Jungthawan and Limpijumnong, 2004). This relaxation is mainly a result of the difference between LiO<sub>4</sub> and GaO<sub>4</sub> tetrahedra with LiO<sub>4</sub> being bigger than GaO<sub>4</sub>. The average bond lengths are 1.985 Å and 1.848 Å for Li–O and Ga–O, respectively. The difference between the average Li–O and Ga–O bond distances is less than 4%, allowing the formation of an orthorhombic structure (Pna2<sub>1</sub>) with the lattice parameters  $a = 5.402$  Å,  $b = 6.372$  Å,  $c = 5.007$  Å, and density = 4.187 g.cm<sup>-3</sup> (Marezio, 1965).  $\beta$ -LiGaO<sub>2</sub> is known to have a band gap of 5.6 eV; making it a good candidate for applications in bright UV optoelectronic applications (Omata et al., 2011; Omata et al., 2015).

Pressure induced phase transformations of wurtzite ZnO have been previously studied experimentally and theoretically (Sarasamak et al., 2008; Recio et al., 1998). It has been predicted that a 10 GPa tensile stress along the [0110] direction or 6 GPa compressive stress along [0001] direction (Kulkarni et al., 2006) could transform a wurtzite ZnO into an un-buckled phase (HX) (Kulkarni et al., 2006). A 7 GPa tensile stress along [0001] induces a formation of a body-centered-tetragonal phase (BCT-4) (Wang et al., 2007). A hydrostatic pressure of about 8.5 GPa leads to the well-known and experimentally-observed rocksalt cubic phase (Sarasamak et al., 2008). First

principles study on the stable phases and phase transformations of LGO is scarce. Due to the similar in the structural of  $\beta$ -LGO ( $Pna2_1$ ) to that of wurtzite ZnO, we propose to employ the theoretical investigations in a similar manner as those have been employed successfully for the case of ZnO (Sarasamak et al., 2008). These studies are very important to identify the transition mechanisms and to predict the undiscovered phases of LGO that can be reached by proper experimental conditions.

In this thesis, we used density functional theory (DFT) calculations to study phase transformations of LGO under hydrostatic and uniaxial pressures. We explored the LGO phase-space through the modeling of stress loads along different crystal directions. Three metastable phases of LGO, namely, oP16, I41/amd, and P4<sub>1</sub>2<sub>1</sub>2 are predicted based on the enthalpy surface diagrams for the transformations from ambient-pressure  $\beta$ -LGO ( $Pna2_1$ ). The compressive stress loading along the [001] direction produces a five-fold orthorhombic phase (oP16). The uniaxial tensile strain along [001] direction stabilizes a tetragonal structure (P4<sub>1</sub>2<sub>1</sub>2). The hydrostatic pressure leads to two structures that are energetically close to each other. One phase is the body center tetragonal (BCT, I41/amd) and another phase is trigonal (R3m) structure, previously found in experiments (Marezio, 1965). All structures are shown in Figure. 4.5 and the comparison with the analogous ones in the binary compound ZnO is shown in Figure. 4.6. For simplicity, henceforth the LGO phases are named after the analogous ones in ZnO, i.e., the orthorhombic ( $Pna2_1$ ) is named WZ', the body-center tetragonal (I41/amd) is named RS', the rhombohedral (R3m) is named RS'', the orthorhombic (oP16) is named HX', and the tetragonal (P4<sub>1</sub>2<sub>1</sub>2) is named BCT'.

Splitting of water ( $\text{H}_2\text{O}$ ) into oxygen and hydrogen gas is an attractive technology for the production of renewable alternative fuels (Kudo and Miseki, 2009), especially in combination with fuel cells (Suntivich et al., 2011). At standard conditions, the ideal voltage for the net water splitting reaction is 1.23 V, which is the potential difference between the anodic oxygen evolution reaction (OER; water oxidation) and the cathodic hydrogen evolution reaction (HER; water reduction). The OER half reaction that involves four elementary charge-transfer steps is, however, typically associated with large overpotentials and thus catalysts are required to increase the energy efficiency (McCrorry et al., 2013). While photocatalytic water splitting (i.e., driving the reaction by light-induced currents) is appealing, it requires catalysts with simultaneous activity for both OER and HER that at the same time also absorb light in the visible spectrum (Kudo and Miseki, 2009). Electrocatalytic water splitting (water electrolysis), on the other hand, allows the individual tuning of the cathode and anode material so that generally greater energy efficiency can be achieved. Unfortunately, the most efficient and stable known OER catalysts rely on rare and expensive Pt and noble metal based alloys (Cui et al., 2013; Gupta et al., 2009) rendering a global fuel economy based on water electrolysis nonviable. On the search for inexpensive, earth-abundant, and environmentally benign alternatives for Pt-group catalysts, perovskite oxides have emerged as a promising class of materials (Royer et al., 2014). Owing to their tunable electronic properties, perovskite-based materials are among the most efficient known photocatalysts for water splitting (Kudo and Miseki, 2009; Suntivich et al., 2011; Castelli et al., 2012; Luo et al., 2014). Recently, an improved understanding of the electronic-structure/reactivity relationship has further spurred the interest in perovskites as inexpensive catalysts for

water electrolysis (Mefford et al., 2016). Motivated by this new insight, we explored in the second part of this thesis to which extent the catalytic reactivity of barium titanate ( $\text{BaTiO}_3$ ) can be controlled by slightly altering its chemical composition.

$\text{BaTiO}_3$  is one of the most thoroughly investigated ferroelectric oxides and is used in diverse technical applications as piezoelectric material, dielectric ceramic, and as crystal in non-linear optics. As catalyst, Ni-supported  $\text{BaTiO}_3$  is active for  $\text{CO}_2$  reforming (Hayakawa et al., 1999), and also water electrolysis over  $\text{BaTiO}_3$  electrodes has been reported (Kennedy and Frese, 1976; Nasby, 1976). Interestingly, in some cases, small compositional modifications by introducing transition-metal dopants on the Ti site (the *B* site in the general  $\text{ABO}_3$  perovskite formula) have been found to increase the catalytic activity of  $\text{BaTiO}_3$  significantly. For example, Pd-modified  $\text{BaTiO}_3$  efficiently catalyzes  $\text{NO}_x$  reduction (Rodríguez et al., 2010), and Cr-modified  $\text{BaTiO}_3$  catalyzes the reduction of nitrobenzene and aniline (Srilakshmi et al., 2016). A strong impact of compositional modification on the catalytic activity has also been reported for other oxide, such as Ruddlesden-Popper oxides (Lee et al., 2014) and carbides (Wannakao et al., 2015), which opens up exciting opportunities for the design of improved catalysts based on well-known and abundant materials. Since  $\text{BaTiO}_3$  is both inexpensive and non-toxic,  $\text{BaTiO}_3$ -based catalysts for water electrolysis would be highly desirable. The oxides of  $d^0$  transition metals, especially Ti and Zr oxide, are known to catalyze the water splitting reaction (Kudo and Miseki, 2009). However, apart from having a small overpotential for water oxidation, a suitable anode material for water splitting must also be electrically conducting and has to be chemically stable with respect to dissolution/corrosion and surface poisoning at operation conditions. Pristine  $\text{BaTiO}_3$  is a wide band gap (3.2-3.4 eV)



(Wemple, 1970) semiconductor, and poor electrical conductivity was measured at conditions for catalytic methanol oxidation (Popescu et al., 2011). In view of the existing BaTiO<sub>3</sub>-based catalysts, our strategy for narrowing or closing the band gap is to introduce transition metals with non-empty *d*-bands on the B site. For this study, we consider Ni- and Fe-modified BaTiO<sub>3</sub>. We are interested in Ni doping because BaNiO<sub>3</sub> is known to be catalytically active for OER (Lee et al., 2016), but it forms in a hexagonal structure (Takeda, 1976), not in the tetragonal (P4mm) structure favored by BaTiO<sub>3</sub> at room temperature, so that Ni doping might thermodynamically undstable. On the other hand, BaFeO<sub>3</sub> forms in the cubic perovskite structure (Hayashi et al., 2011), which is the stable BaTiO<sub>3</sub> structure at temperatures above 120°C, i.e., at solid-state synthesis condition (Luspin et al., 1980). BaFeO<sub>3</sub> is also more likely to form a solid solution with BaTiO<sub>3</sub> because of the similar ionic radius of Fe<sup>4+</sup> and Ti<sup>4+</sup> (58.5 pm and 60.5pm, respectively (Shannon,1976)

## CHAPTER II

### THEORETICAL BACKGROUND

This chapter will focus on the theoretical background of studying in terms of solving the electron problems starting from the simplest example, solving hydrogen - atom system by Schrödinger equation, to more complicated problems – systems with many electrons and nuclei. Additionally, the density functional theory (DFT), basic DFT calculation methods and software used in this thesis will be introduced.

#### 2.1 Density Functional Theory

##### 2.1.1 The Schrödinger equation

Over the past few decades, density functional theory has been the most successful and widely used method in condensed-matter physics, computational physics and quantum chemistry. In principle, the properties of a system can be obtained by solving the quantum mechanical wave equation governing the system dynamics. The dynamics of a time-independent non-relativistic system are governed by the Schrödinger equation (Schrödinger, 1926). First, the simplest example in hydrogen - atom system can be written as following:

$$\left[ -\frac{\hbar^2}{2m} \nabla^2 - \frac{e^2}{4\pi\epsilon_0 r_1} \right] \Psi(r_i) = E\Psi(r_i), \quad (2.1)$$

where  $-\frac{\hbar^2}{2m} \nabla^2$  is the kinetic energy of the electron,  $-\frac{e^2}{4\pi\epsilon_0 r_1}$  is the potential due to the nucleus and  $\Psi(r_i)$  is the electron wave function (probability distribution of electron position), and  $E$  is the total energy of the electron. A single electron and a nucleus are separated by the distant  $r_i$ . The solutions of the Schrödinger equation for the hydrogen atom can be directly solved. There are multiple solutions, each defined by the set of quantum numbers: the principle quantum number ( $n$ ), the orbital angular momentum number ( $l$ ) and the magnetic quantum number ( $m_l$ ) in terms of wave function  $\psi_{nlm_l}(r, \theta, \phi)$ . The equation becomes more complicated when considering the Helium atom system. Helium has two electrons and one nucleus. We can separate the Hamiltonian to the first electron and the second electron, the Schrödinger equation becomes:

$$[H_1 + H_2 + W]\psi(r_1, r_2) = E\psi(r_1, r_2), \quad (2.2)$$

We have three distances to consider  $r_1$ ,  $r_2$ , and  $r_{12}$  (distance between the two electrons).  $W$  is the cross term between them and the operator can be spelled out as

$$\left[ -\frac{\hbar^2}{2m} \nabla_1^2 - \frac{e^2}{4\pi\epsilon_0 r_1} - \frac{\hbar^2}{2m} \nabla_2^2 - \frac{e^2}{4\pi\epsilon_0 r_2} + \frac{e^2}{4\pi\epsilon_0 r_{12}} \right] \psi(r_1, r_2) = E\psi(r_1, r_2), \quad (2.3)$$

where  $\frac{e^2}{4\pi\epsilon_0 r_{12}}$  is the problem that comes in. We have to consider the interaction between two electrons. In fact, we cannot simply solve this equation analytically. The full multi-electron and multi-nucleus Schrödinger equation for an  $N$ -atom and  $n$ -electron in a general form can be written as

$$H\psi(R_1, \dots, R_M; r_1, \dots, r_N) = E(R_1, \dots, R_M)\psi(R_1, \dots, R_M; r_1, \dots, r_N) \quad (2.4)$$

The wave function can be written in terms of  $R_1, \dots, R_M$  and  $r_1, \dots, r_N$ , which are the positions of nuclei and electrons, respectively. The Hamiltonian is given by

$$H = \left[ -\sum_{i=1}^N \frac{\hbar^2}{2M_i} \nabla_{R_i}^2 + \frac{1}{2} \sum_{i=1}^N \sum_{j<i}^N \frac{Z_i Z_j e^2}{|R_i - R_j|} - \frac{\hbar^2}{2m_e} \sum_{i=1}^N \nabla_{r_i}^2 + \sum_{i=1}^N \sum_{j=1}^N \frac{Z_i e^2}{|R_i - r_j|} + \frac{1}{2} \sum_{i=1}^N \sum_{j<i}^N \frac{e^2}{|r_i - r_j|} \right] \quad (2.5)$$

Here, the first term is the kinetic energy of the ions, the second term is the potential energy of the ions, the third term is the kinetic energy of the electrons, the fourth term is electron-ion interactions, and the last term is electron-electron interactions.

### 2.1.2 Born-Oppenheimer approximation

The Born-Oppenheimer approximation (Born and Oppenheimer, 1927) is based on the assumption that the electrons in a system move on a much faster time scale than the much heavier nuclei, and thus they adjust their positions “instantaneously” in response to such atomic motion. This simplifies the Schrödinger equation to a multi-electron equation in the presence of a potential due to fixed atomic nuclei  $R_i$ . The Hamiltonian of the system from Eq. 2.5 can be written as:

$$H = \left[ -\frac{\hbar^2}{2M_i} \sum_{i=1}^N \nabla_{r_i}^2 + \sum_{i=1}^N \sum_{j=1}^N \frac{Z_i e^2}{|R_i - r_j|} + \frac{1}{2} \sum_{i=1}^N \sum_{j<i}^N \frac{e^2}{|r_i - r_j|} \right] \quad (2.6)$$

However, according to Eq. 2.6, a  $3N$ -dimensional problem has to be solved, where  $N$  is the total number of electrons in the system. We still need to figure out a good way to account these interactions within the system. If we try to solve the many-body problems numerically, we still quickly run into trouble and burnout computational time. The Density functional theory (DFT) finally came along. It was formulated by Walter Kohn who won the Nobel Prize in 1998 (Hohenberg and Kohn,

1964) for the formulation of DFT. Basically, the density functional theory (DFT) mentions that working with the wave functions with  $3N$  variables is very complicated. Ideally, in the ground state, all aspects of the electronic structure of the interacting-electrons system in an “external” potential (due to the nuclei) are determined by electron density  $\rho(r)$  (Parr and Yang, 1989) which can be written as:

$$\rho(r) = \sum_i^N |\psi_i(r)|^2, \quad (2.7)$$

where  $N$  is the total number of electrons in the system.

### 2.1.3 The Hohenberg-Kohn theorem

The two basic theorems of the Hohenberg-Kohn theorem are:

- The first Hohenberg-Kohn (Hohenberg and Kohn, 1964) theorem establishes that for any external potential, there is a unique ground state electronic density.
- This implies that the ground state electronic density determines all of the properties of the system.

The first of Hohenberg-Kohn theorem (Hohenberg and Kohn, 1964) can be proven by supposing that there are two potentials, differing by more than a constant, that yield the same ground state density. The expectation value of the energy is defined as

$$E = \langle \psi | H | \psi \rangle = \int \psi^*(r) H \psi(r) dr \quad (2.8)$$

Assume that two external potentials (two Hamiltonians) with the same ground state

charge density  $\rho_0(r)$  are written as:

$$E_0 = \langle \psi | H | \psi \rangle \text{ and } E'_0 = \langle \psi' | H | \psi' \rangle \quad (2.9)$$

From the variational principle (Sakurai, 1994), if we compute the expectation value of the energy for a given Hamiltonian operating on the wave function which is not the ground state one we will always get an energy value greater than the ground state energy from Eq. 2.9. This can be denoted as:

$$E_0 < \langle \psi' | H | \psi' \rangle \text{ and } E'_0 < \langle \psi | H' | \psi \rangle \quad (2.10)$$

Then we can perform a very simple mathematical trick by rewriting the Hamiltonians  $H = H' + (H - H')$  and  $H' = H + (H' - H)$ . By substituting this back into Eq. 2.10 then we get

$$E_0 < E'_0 + \langle \psi' | H - H' | \psi' \rangle \text{ and } E'_0 < E_0 + \langle \psi | H' - H | \psi \rangle \quad (2.11)$$

It can be concluded that  $E_0 + E'_0 < E_0 + E'_0$ , which is obviously false. The second Hohenberg-Kohn theorem (Hohenberg and Kohn, 1964) can be proven by showing that this leads to a contradiction involving the expectation values of the energy. The DFT theorem implies that we can determine the ground state energy  $E_0$  of an interacting  $N$ -electron system in terms of the charge density,  $\rho(r)$ . The energy functional can be defined as:

$$E[\rho(r)] = T_s[\rho(r)] + \int V_{ext}(r)\rho(r)dr + \frac{e^2}{2} \int \frac{\rho(r)\rho(r')}{r-r'} drdr' + E_{xc}[\rho(r)], \quad (2.12)$$

where  $T_s[\rho(r)]$  is the kinetic energy of a homogeneous non-interacting electron gas,

$\int V_{ext}(r)\rho(r)dr$  is the energy due to the external potential,  $\frac{e^2}{2} \int \frac{\rho(r)\rho(r')}{r-r'} drdr'$  is the

Hartree energy, and  $E_{XC}[\rho(r)]$  is the exchange-correlation energy. The exchange-correlation energy basically includes all the stuff therefore it can be concluded that the interesting part of the kinetic energy, which is not included in the first term, is included in the exchange energy which is related to the Pauli exclusion principle (Pauli, 1925). Moreover, it also includes the correlation energy which is related to Coulomb repulsion (Coulomb, 1785) and overall spin and symmetry in the system. Finally it also includes the self-interaction correction. Therefore, the variational principle (Sakurai, 1994) has to be performed to find the wavefunctions that minimize this energy. To find the wavefunctions that minimize the energy, a functional derivative leads to the Kohn-Sham equations (Kohn and Sham, 1965) can be written as:

$$\left[ -\frac{\hbar^2}{2m} \nabla^2 + V_{ext}(r) + V_H(r) + V_{XC}(r) \right] \psi_i(r) = \varepsilon_i \psi_i(r), \quad (2.13)$$

where  $\psi_i(r)$  and  $\varepsilon_i$  are the single-electron Kohn-Sham orbitals and energies, respectively. We only have to solve  $N$  single-electron equations for non-interacting electrons in an effective potential due to the nuclei and the other  $N-1$  electrons.

## 2.2 The exchange-correlation energy

In principle, DFT is an exact formulation with no approximations. One can find exact solutions to the Schrödinger equation as long as one knows the form of the potential:

$$V = V_{ext}(r) + \frac{e^2}{2} \int \frac{\rho(r')}{|r-r'|} dr' + V_{xc}[\rho(r)] \quad (2.14)$$

Where  $V_{ext}(r)$  is the “external” potential generated by nuclei acting on the electron. Unfortunately, there is a remaining problem. is that we do not know the exact  $V_{xc}[\rho(r)]$  which can be defined as:

$$V_{xc}[\rho(r)] = \frac{\delta E_{xc}[\tilde{\rho}(r)]|_{\tilde{\rho}(r)=\rho(r)}}{\delta \tilde{\rho}(r)}. \quad (2.15)$$

The Kohn-Sham equations (Kohn and Sham, 1965) Eq. 2.13 can be written with the ground state energy  $E$  as:

$$E = \sum_{j=1}^N E_j + E_{xc}[\rho(r)] - \int V_{xc}(r) \rho(r) dr - \frac{1}{2} \frac{\rho(r)\rho(r')}{|r-r'|} dr dr'. \quad (2.16)$$

If  $E_{xc}[\rho(r)]$  and  $V_{xc}(r)$  are neglected, the KS equations are reduced to the self-consistent Hartree equations. Many-body effects are included in  $E_{xc}$  and  $V_{xc}$ . In practice, the main approximations for exchange correlation energy  $E_{xc}[\rho(r)]$  (Parr and Yang, 1989) are listed in following.



### 2.2.1 The Local Density Approximation (LDA)

The local density approximation (LDA) computes the exchange-correlation energy for a more simplified system than the actual one. It is a fairly good approximation as long as the charge density does not change very rapidly in the system. A few examples of LDA approximations are, for instance, LDA, LSDA (Karasiev et al., 2014), and X-alpha (Suele et al., 1999). The exchange-correlation energy can be written as:

$$E_{XC}^{LDA}[\rho(r)] = \int \rho(r) \epsilon_{XC}^{LDA}[\rho(r)] dr, \quad (2.17)$$

where  $\epsilon_{XC}^{LDA}[\rho(r)]$  is the exchange-correlation energy per particle of uniform electron gas of density  $\rho(r)$ . The exchange-correlation energy can be defined as:

$$\epsilon_{XC}^{LDA}(n) = \epsilon_X^{LDA}(n) + \epsilon_C^{LDA}(n), \quad (2.18)$$

where  $\epsilon_X^{LDA}(n)$  and  $\epsilon_C^{LDA}(n)$  are the exchange energy and correlation energy per particle, respectively. Dirac's expression (Dirac, 1930) can be used to define the exchange energy as:

$$\epsilon_x(n) = -\frac{3}{4} \left(\frac{3}{\pi}\right)^{\frac{1}{3}} n^{\frac{1}{3}} = -\frac{0.458}{r_s} a. u., \quad (2.19)$$

The correlation part was estimated by Wigner (Wigner, 1934) as

$$\epsilon_c(n) = -\frac{0.44}{r_s + 7.8} a. u., \quad (2.20)$$

where  $r_s$  is the mean interelectronic distance expressed in atomic unit, defined as  $r_s = \left[\left(\frac{3}{4\pi n}\right)\right]^{1/3}$ . Some of successes and failures to use LDA to approximate

$E_{xc}[\rho(r)]$  have been discussed by Jone and Gunnarsson (Jones and Gunnarsson, 1989).

### 2.2.2 The Generalized Gradient Approximation (GGA)

The generalized gradient approximation is used to improve the LDA. By expanding  $E_{xc}$  as a series in terms of the density and its gradient  $|\nabla\rho(r)|$  (Kohn, 1999), the inhomogeneity of density is also taken into account. This approach is known as gradient expansion. The exchange-correlation energy can be written in the following form:

$$E_{xc}[n] = \int \rho(r) \varepsilon_{xc}[\rho(r)] F_{xc}[\rho(r), \nabla\rho(r), \nabla^2\rho(r), \dots] dr, \quad (2.21)$$

where  $F_{xc}[\rho(r), \nabla\rho(r), \nabla^2\rho(r), \dots]$  is the function's factor for modifying LDA expressions according to the density variation at the considered point. The negativity of the exchange density can remarkably improve the quality of exchange energy. A modified gradient have been proposed, for instance, BLYP (Becke, 1988), PW91 (Perdew et al., 1992), and PBE (Perdew et al., 1996). Perdew, Burke, and Ernzerhof (PBE) (Perdew et al., 1996) presented a simplified construction, in which all parameters are fundamental constants.

$$F_X^{PBE}(s) = 1 + \kappa - \frac{\kappa}{1 + \frac{\mu s^2}{\kappa}} \quad (2.22)$$

where  $\mu = 0.21951$ ,  $\kappa = 0.804$ ,  $F_X^{PBE}(s)$  is the PBE exchange enhancement factor,  $s = |\nabla\rho(r)|/(2k_F\rho(r))$  is the exchange dimensionless reduced density gradient, and  $k_F = (3\pi^2\rho(r))^{1/3}$ .

### 2.2.3 Revised Perdew-Burke-Ernzerhof functional (RPBE)

Zhang and Yang (Zhang and Yang, 1998) introduced the Revised Perdew-Burke-Ernzerhof (RPBE) (Perdew et al., 1996) functional. Moreover, Hammar (Hammer *et al.*, 1999) improved the chemisorption energetics of atoms and molecules on transition-metal surface. Both PBE (Perdew et al., 1996) and RPBE give molecular bond energies and adsorption energies on metal surface that are more quantitatively accurate than LDA calculations, with the RPBE functional generally yielding the most accurate predictions. PBE and RPBE functions differ only in one parameter of the exchange term from  $\kappa = 0.804$  to  $\kappa = 1.245$ .

### 2.2.4 Hybrid functional

To improve and make accurate prediction of the electronic and band gap energy of ground state properties, the exact, nonlocal form for the many-electron Fock exchange energy is known from Hartree-Fock theory (Slater, 1951). However, it is a standard practice in density functional theory (DFT) to compute this energy by integrating a local energy density per electron which is specified by the local electron density and its derivatives. One of the most popular semilocal density approximations is the Perdew-Burke-Ernzerhof (PBE) (Perdew et al., 1996) model. Accuracy can be improved by mixing the PBE exchange energy with a fraction of the exact nonlocal Fock exchange energy. The certain mixture of the *HF* exchange and the PBE correlation are constructed into the  $E_{xc}$  of hybrid functional. It is generally known that the Fock exchange slowly decays with respect to distance. To avoid huge computational demands, it is possible to decouple the exchange interaction into short range ( $s_r$ ) and long-range ( $l_r$ ) parts. This concept was proposed by Heyd-Scuseria-

Ernzerhof, also known as HSE (Paier et al., 2006; Heyd et al., 2003). The  $E_{xc}$  of HSE functional can be written as:

$$E_{xc}^{HSE} = aE_x^{HF,SR}(\mu) + (1 - a)E_x^{PBE,SR}(\mu) + E_x^{PBE,LR}(\mu) + E_c^{PBE}, \quad (2.23)$$

where  $a$  indicates the mixing portion, the adjustable factor  $\mu$  defines the distance at which the short-range interactions become negligible. The typical values of  $a$  and  $\mu$  in HSE06 are 0.25 and  $0.3 \text{ \AA}^{-1}$ , respectively.

### 2.3 Solving the Kohn-Sham equations

The first step can be done by providing the atomic positions as inputs and the electron density  $\rho_{in}(r)$  can be generated by assuming from atomic orbitals on each atoms. Then, the effective potential of the system with  $\rho_{in}(r)$  is calculated and the new electron density  $\rho_{out}(r)$  can be obtained by solving the Kohn-Sham equation. The new electron density  $\rho_{out}(r)$  has to be checked if it is not equal to  $\rho_{in}(r)$ . Then, it is taken as an initial electron density  $\rho_{in}(r)$  and the procedure is performed repeatedly. If the new electron density  $\rho_{out}(r)$  equals to  $\rho_{in}(r)$  within the acceptable difference, the electronic charge density for the specific configuration system is obtained. After that, the first minimized atomic structure for the material is considered by computing the forces on the nuclei due to charge density. If the forces smaller than the tolerance, the loop will stop. Otherwise, the atoms will move in the direction according to the forces; it will be put back to the first step of the loop and the process will be done repeatedly. The procedure of DFT calculations is shown in the Figure 2.1.

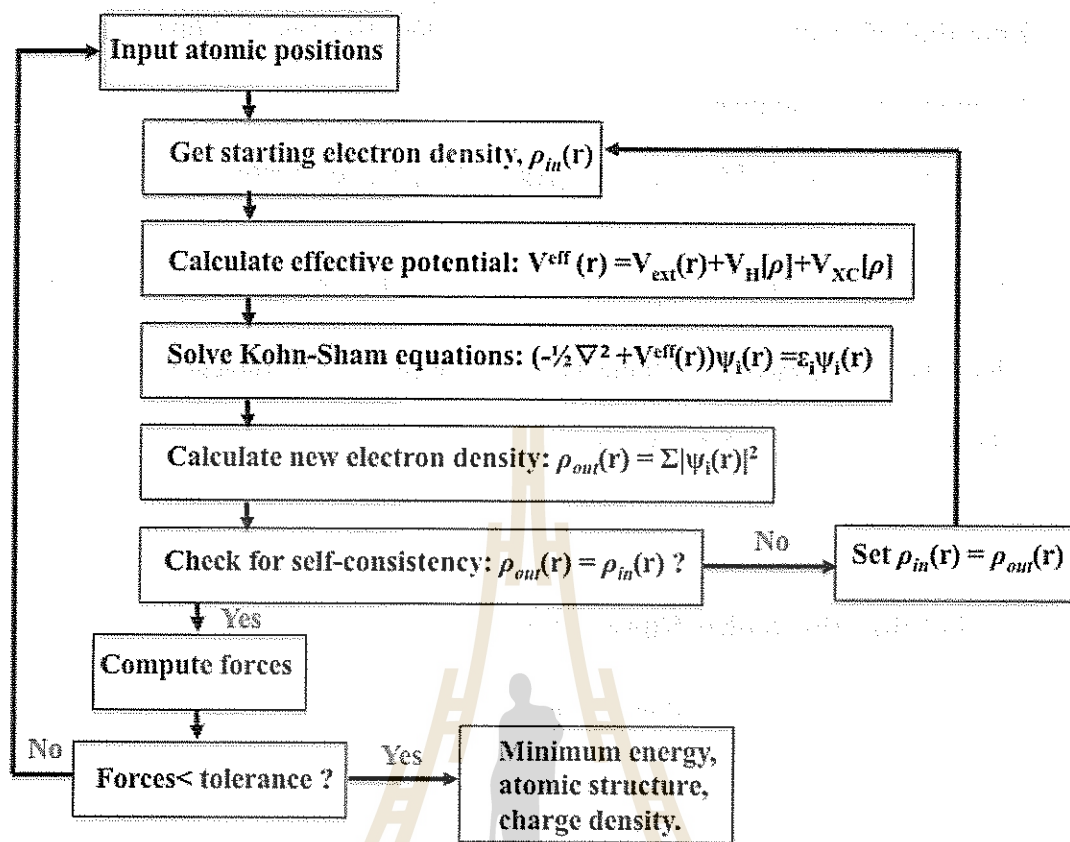
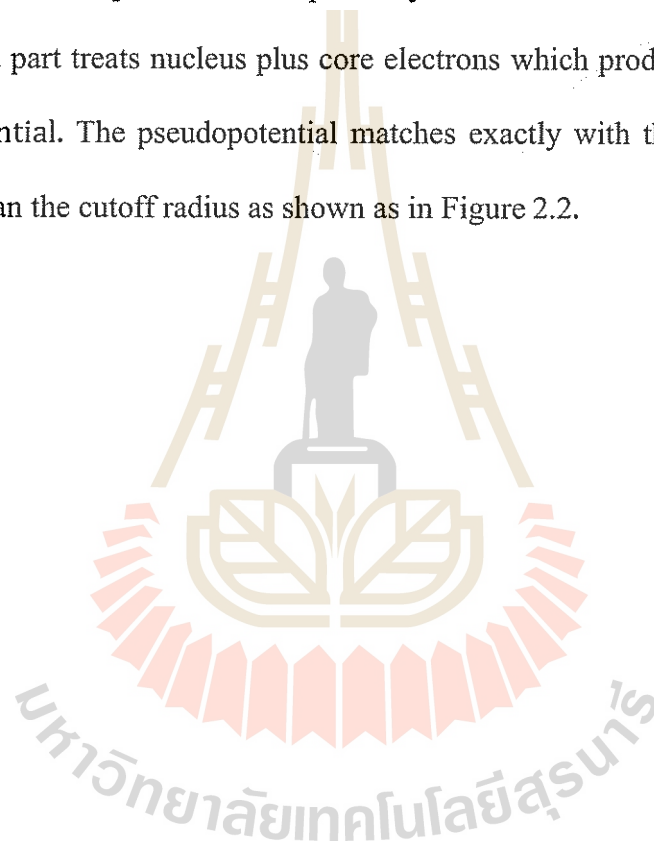


Figure 2.1 Procedure of DFT calculations with constant lattice parameters.

## 2.4 Pseudowavefunctions and Pseudopotentials

After providing the atomic positions as inputs, the first iteration begins by generating a starting electron density from a superposition at the atomic orbitals of system. The atomic orbitals are calculated by employing the single particle's the Kohn-Sham equations and the wave functions, then the energy for every electron orbitals of the atoms are obtained. This is called "all electron calculation". However, performing the all electron calculation for larger systems is very expensive. The wavefunctions for the lower energy states, e.g. 1s, are spatially localized closer to the nucleus while having larger amplitude away from the nucleus for the valance states. All of the wave functions also have sharper features closer to the nucleus. The sharper

feature in the wave functions requires many plane waves to represent. If the wavefunction is removed near the cutoff radius, ( $r_c$ ) from the nucleus, the wavefunction will have a very smooth behavior, which can represent by a few plane waves and the pseudowavefunction. This method yields a result that exactly matches with the all electron wave function (Heine, 1970). The pseudopotential approximation basically has two main parts. The first part only treats the valence electrons explicitly and the second part treats nucleus plus core electrons which produces an effective or "*pseudo*" potential. The pseudopotential matches exactly with the core potential in larger range than the cutoff radius as shown as in Figure 2.2.



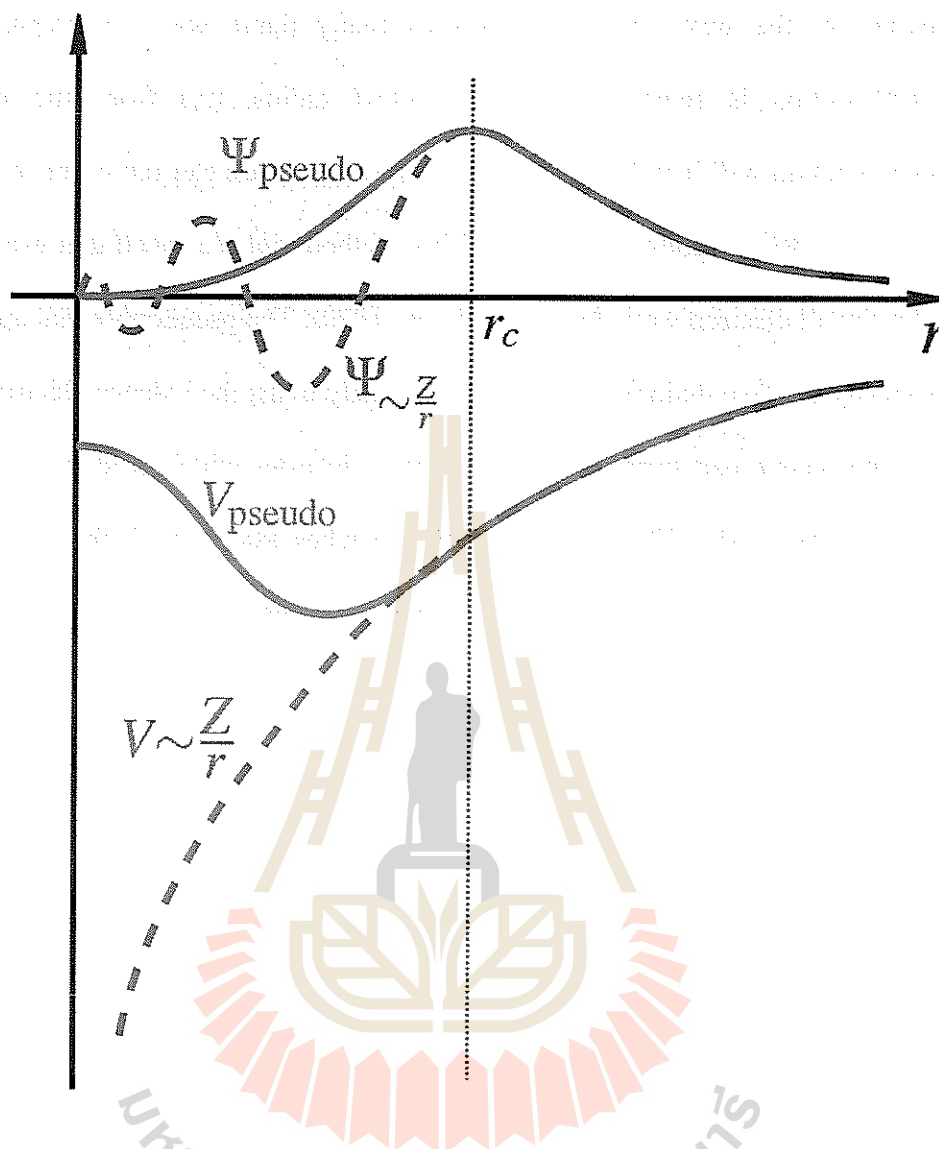


**Figure 2.2** Schematic illustrations of the pseudopotential, pseudowavefunction (solid curves) and the all electron wave function, core potential (dashed curves). The cutoff radius  $r_c$  represents a radius at which the all electron and pseudo quantities match Ref.(Wolfram Quester Source, www) (2006).

## 2.5 Projector augmented waves

A physicist, Blöchl (Blöchl, 1994), proposed the projector augmented waves (PAW) to create a smooth wavefunctions ( $\tilde{\Psi}$ ) by the transformation operator  $\tau$  which made a linear transformation relating between all electron wave function ( $\Psi$ ) to the smooth wave function defined as:

$$|\Psi\rangle = \tau|\tilde{\Psi}\rangle \quad (2.24)$$

The all electron wavefunction ( $\Psi$ ) can be written as:

$$|\Psi\rangle = |\tilde{\Psi}\rangle + \sum_m (|\Psi_m\rangle - |\tilde{\Psi}_m\rangle)\langle\tilde{p}_m|\tilde{\Psi}\rangle, \quad (2.25)$$

where  $\Psi_m$  is a localized all electron partial wave for state  $m$ ,  $\tilde{\Psi}_m$  is a localized smooth partial wave for state  $m$ , and  $\langle\tilde{p}_m|$  is the localized projection operator. The transformation operator  $\tau$  can be written as:

$$\tau = 1 + \sum_m (|\Psi_m\rangle - |\tilde{\Psi}_m\rangle)\langle\tilde{p}_m|. \quad (2.26)$$

The transformation operator  $\tau$  can be used to add back the core potential of all electron wave functions to the smoothed wavefunctions. Additionally, the equation can be applied equally well to core and valence states so that applying this equation to all electron state can derive all electron results (Martin, 2004).



## 2.6 Plane waves

The Blochl's theorem (Blochl, 1994) presented the plane waves (PWs) or the Blochl wave functions for the solutions of the Kohn-Sham equation. The plane waves (PWs) are given by

$$\Psi_{nk}(r) = e^{ik \cdot r} U_{nk}(r), \quad (2.27)$$

The wave functions in terms of  $e^{ik \cdot r}$ , times a function of periodic function,  $U_{nk}(r)$  (Kittel, 1982). The periodic part of the wave function can be expanded in terms of a special set of plane waves (Kittel, 1982):

$$U_{nk}(r) = \sum_G c_G e^{iG \cdot r}, \quad (2.28)$$

where  $e^{iG \cdot r}$  is the plane wave basis set, the summation is over the reciprocal lattice vectors (Give by  $G = m_1 b_1 + m_2 b_2 + m_3 b_3$  for all integers  $m_i$ ). This means that solving for  $\Psi_{nk}(r)$  at each point in  $k$ -space requires the summation over an infinite number of  $G$  vectors. Combining these two equations gives.

$$\Psi_{nk}(r) = \sum_G c_{k+G} e^{i(k+G) \cdot r}, \quad (2.29)$$

The function  $e^{i(k+G) \cdot r}$  are solutions of the Schrödinger equation and the lower energy solutions are more physically relevant than very high energy solutions. Therefore, the reciprocal lattice vectors are included only that lead to solutions with kinetic energy less than some cutoff energy which defines in Eq. 2.30 (Martin, 2004):

$$\frac{\hbar^2}{2m} |k + G|^2 < E_{cutoff}. \quad (2.30)$$

## 2.7 Zeroth Order Regular Approximation

The Zeroth order regular approximation (ZORA) (Lenthe et al., 1993; Chang et al., 1986) reduces the Dirac equation to one component equation where a potential dependent operator replaces the kinetic energy operator

$$\frac{p^2}{2m} \Rightarrow p \cdot \frac{1}{2c^2 - V} \cdot p, \quad (2.31)$$

where  $V$  is the coulomb potential due to electrons and nuclei. The relativistic effects may be important to explain the reaction dynamics when heavy element, of the special interest in catalysis, are involved, even at Hartree-Fock (Slater, 1951) or DFT level. Matrix elements of the kinetic energy operator thus become

$$(T^{ZORA})_{\mu\nu} = \left\langle \varphi_\mu \left| p \cdot \frac{1}{2c^2 - V} \cdot p \right| \varphi_\nu \right\rangle, \quad (2.32)$$

where  $(T^{ZORA})_{\mu\nu}$  is kinetic energy operator,  $\varphi_\mu$  and  $\varphi_\nu$  are wavefunctions of state  $\mu$  and  $\nu$ , respectively. For highly accurate quantum chemical calculations, the effect of relativity can be ignored.

## 2.8 Van der Waals interactions

The problem for the local and semi-local functional of DFT is that it takes into consideration only the electronic density at point  $\sim r$  (and its immediate vicinities). The density and its gradient expansion of variations arise more than 3-4 Å away from the point being evaluated. That is where attractive vdW interactions arise (McNaught and Wilkinson, 1997). In fact, it can be shown that with standard LDA and GGA functionals, the asymptotic tail of the energy, for a large separation  $R$  between atoms, approaches zero exponentially, while a proper theory that takes vdW interactions into account should have the characteristic  $1/R^6$  tail. In terms of the so-called Casimir-Polder integral (Casimir, 1948; Power and Thirunamachandran, 1993), the leading  $1/R^6$  term for the dispersion at long ranges can be written with respect to the (imaginary) frequency dependent polarizability  $\alpha(i\omega)$  of two atoms  $A$  and  $B$  defined as:

$$E_{disp} = -\frac{1}{R_{AB}^6} \frac{3}{\pi} \int \alpha_A(i\omega) \alpha_B(i\omega) d\omega = -\frac{1}{R_{AB}^6} C_6^{AB}, \quad (2.33)$$

which gives an expression for the heteronuclear  $C_6^{AB}$  coefficient. Tang and Toennies (Tang and Toennies, 1977) derived an expression for the heteronuclear coefficient in terms of the homonuclear coefficients  $C_6^{AA}$  and  $C_6^{BB}$  and their static polarizabilities  $(\alpha_0^A, \alpha_0^B)$ ,

$$C_6^{AB} = \frac{2C_6^{AA}C_6^{BB}}{\frac{\alpha_0^B}{\alpha_0^A}C_6^{AA} + \frac{\alpha_0^A}{\alpha_0^B}C_6^{BB}}. \quad (2.34)$$

The general form of this type of correction to the DFT energy is

$$E_{DFT+vdW} = E_{DFT} - \sum_A \sum_{B>A} f_{damp}(R_{AB}) \frac{C_6^{AB}}{R_{AB}^6}, \quad (2.35)$$

where  $f_{damp}$  is the damping function, which is arbitrary (to a certain extent), so that it remains an intrinsic “*empiricity*” for all these methods.

## 2.9 The Vienna Ab initio Simulation Package (VASP)

The phase-transformation calculations are performed with the Vienna *Ab initio* Simulation Package (VASP), developed by Kresse, Hafner, and Furthmüller (Kresse and Furthmüller, 1996(a); Kresse and Hafner, 1994). VASP uses plane waves (PWs) as a basis set to describe electron wavefunctions. The PAW (Blöchl, 1994) potentials needed for the calculations are included in the package. In this work, the k-point samplings are based on the Monkhorst-Pack approach (Monkhorst and Pack, 1976). The main computational part for solving the KS-equation self-consistency is obtained by using an iterative matrix-diagonalization scheme, such as a conjugate gradient scheme (Teter et al., 1989; Bylander et al., 1990) and block Davidson scheme (Davidson, 1983). There are two main loops in VASP calculations. The charge density is optimized in the outer loop. In the inner loop, the wave functions are optimized by solving KS equation in a self-consistent algorithm (Kresse and Furthmüller, 1996(a); Kresse and Furthmüller, 1996(b)).

## 2.10 The Fritz-Haber-Institut *ab initio* molecular simulations

### (FHI-aims)

The surface phase diagrams, Pourbaix diagrams and reaction free energy profiles for BaTiO<sub>3</sub> as OER catalyst were performed with the Fritz-Haber-Institut *ab initio* molecular simulations (FHI-aims) package (Blum et al., 2009; Havu et al., 2009) which based on all-electron full-potential DFT-code, the implementation of FHI-aims was used all-electron full-potential for all ground-state calculations. FHI-aims is an efficient computer program package to calculate physical and chemical properties of condensed matter and materials such as molecules, clusters, solids, and liquids. The principle is based on numerically tabulated atom-centered orbitals (NAOs) to capture a wide range of molecular and material properties from quantum-mechanical first principles, which is described as following form:

$$\phi_i(r) = \frac{u_i(r)}{r} Y_{lm}(\Theta, \Phi), \quad (2.36)$$

where  $Y_{lm}(\Theta, \Phi)$  are spherical harmonics,  $u_i(r)$  is a radial part function. The choice of  $u_i(r)$  is flexible and is obtained by solving a radial Schrödinger equation defined by

$$\left[ -\frac{1}{2} \frac{d^2}{dr^2} + \frac{l(l+1)}{r^2} + v_j(r) + v_{cut}(r) \right] u_j(r) = \varepsilon_i u_j(r), \quad (2.37)$$

where the potential  $v_j(r)$  defines the main behavior of  $u_j(r)$  commonly choices a self-consistent free-atom (or ion) radial potential or a hydrogen-like potential.  $v_{cut}(r)$  is a confining radius. It ensures that the radial function is strictly zero beyond the confining radius  $r_{cut}$  and decays smoothly. For example, the silicon 3s basis function

that obtained from Eq. 2.37 with two potential  $v_j(r)$  and  $v_{cut}(r)$  as shown in Figure 2.3.

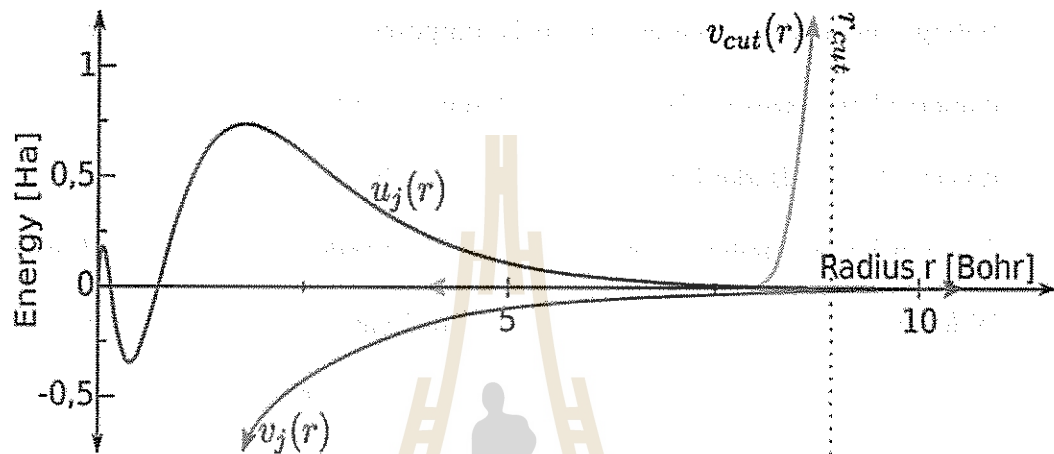
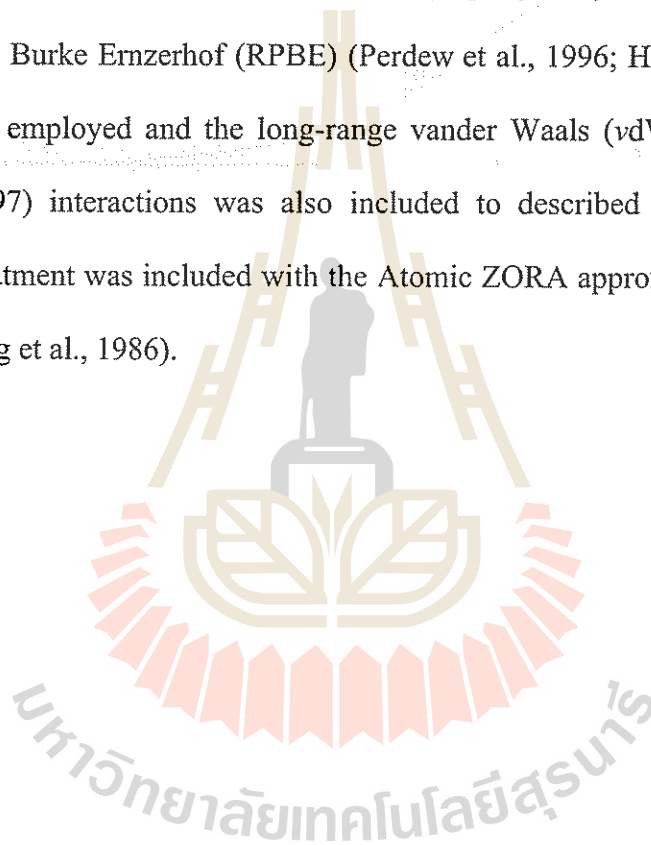


**Figure 2.3.** The radial function  $u_j(r)$  of the 3s orbital for a free silicon atom is plotted along radius  $r$ . The free-atom like potential  $v_j(r)$  and the steeply increasing confining potential  $v_{cut}(r)$  are also shown. The dotted line indicates the confining radius  $r_{cut}$  (Grades, 2015).

As a systematic improvement of the basis set allows the number of plane waves to be increased, NAOs cannot systematically be improved by a single parameter. To allow a systematic convergence of the calculation with respect of the basis size, FHI-aims (Blum et al., 2009; Havu et al., 2009) provides a library of predefined settings for all species, which governs the key parameters regarding the numerical accuracy. The library contains three different levels of accuracy, *light*, *tight*, and *really tight*. These three levels specify the accuracy of the real space grids, Hartree potential, and the basis set size. The basis sets are organized in *Tiers*, ordered

by increasing accuracy. Each *Tier* contains several basis functions of different angular momenta. We used *light* settings to gain a first insight into a system's properties or for structural to find a good first guess of the equilibrium atomic positions. The next level, the *tight* species defaults are rather safe for a variety of systems. The *really tight* settings are over-converged for most purposes. The convergence with respect to numerical and basis settings used for a specific property or system was ensured. The revised Perdew Burke Ernzerhof (RPBE) (Perdew et al., 1996; Hammer et al., 1999) functional was employed and the long-range vander Waals (vdW) (McNaught and Wilkinson, 1997) interactions was also included to described correlation effects. Relativistic treatment was included with the Atomic ZORA approximation (Lenthe et al., 1993; Chang et al., 1986).



## CHAPTER III

### CALCULATION METHODS

In this chapter, the methodologies required for investigating phase transformation in  $ABO_2$  oxide compounds are described. First principles calculations enable us to investigate their behaviors, properties, and phase-transition process to predict and investigate the new metastable phases. Additionally, method of analysis for water molecule adsorption and dissociation, surface phase diagrams, reaction free energy profiles on oxygen evolution reduction (OER) and pourbaix diagrams of  $BaTiO_3$ , are introduced.

#### 3.1 Phase transition in solid state

A phase transition in solid state is an alteration of crystallographic data for crystalline solids, i.e., space group, lattice parameters, occupied positions and atomic coordinates. The structural phase transitions can be induced by pressure, temperature, doping and others. The transitions are always supplemented by structural changes which are sometimes very small.



Properties including volume, density, elasticity, electric, magnetic, optical, or chemical properties can abruptly changed during the phase transition. Phase transitions are grouped to three types (Muller, 2013):

- Reconstructive phase transitions: the chemical bonds in solid are broken and reassembled; the reconstruction involves considerable atomic motions. Such conversions are always first-order transitions.
- Displacive phase transitions: small shifts of atomic positions.
- Order–disorder transitions: different kinds of atoms that statistically occupy the same crystallographic point orbit in a crystal become ordered in different orbits or vice versa. Or molecules that statistically take several orientations become ordered in one orientation.

### 3.1.1 Thermodynamic stability

A thermodynamically stable phase can become unstable relative to another phase by a change of the external conditions (temperature, pressure, electric field, magnetic field, mechanical forces) or doping. This work focuses on a pressure-induced transformation. According to the laws of thermodynamics, (negative) entropy, and volume are the first derivatives of the Gibbs free energy (Martin, 2004) which are characterized by temperature and pressure as the following:

$$G = H - TS = E + pV - TS, \quad (3.1)$$

where  $G$  = Gibbs free energy (in the unit of eV),  $H$  = enthalpy (in the unit of eV),  $E$  = internal energy (in the unit of eV),  $S$  = entropy (in the unit of eV/K), and  $V$  = volume (in the unit of  $\text{\AA}^3$ ). In the case of high pressure with low temperature ( $T = 0$  K), the Gibbs free energy becomes a simple enthalpy  $H$  which is given by

$$H = E + PV. \quad (3.2)$$

Under applied pressure, the lowest enthalpy is the thermodynamically stable phase. Although, the zero-temperature theory often results in good agreement with experiments, the effects of finite temperature in some cases are substantial. For example, phase transition becomes easier to defeat the energetic barriers of the transformation when the temperature is increased, so that the hysteresis is reduced (Mujica et al., 2003). The calculations can reveal the relationships between fundamental quantities of materials, for instance, energy ( $E$ , in the unit of eV), pressure ( $P$ , in the unit of GPa), and bulk modulus ( $B$ , in the unit of GPa) (Martin, 2004). The subsequent steps are performed to determine the equilibrium volume  $V_0$ , (for  $P = 0$  and  $T = 0$ ), and bulk modulus  $B$  of discriminative material with known crystal structure. First, the energy ( $E$ ) for several values of the volume ( $V$ ) are calculated to get the energy-volume relation ( $E = E(V)$ ), in other words, the equation of state (EOS), and it is fitted to an analytic form such as Murnaghan's equation of state (Murnaghan, 1944). For adequately small range of volume, the  $E$ - $V$  curve can be fitted by a simple 3<sup>rd</sup> degree polynomial. The minimum point gives the predicted volume  $V_0$  and its total energy. The second derivative at that point (the equilibrium volume) is the bulk modulus ( $B = -V \frac{dP}{dV} = V \frac{d^2E}{dV^2}$ ).

### 3.2 Water adsorption and dissociation on BaTiO<sub>3</sub> surfaces

BaTiO<sub>3</sub> based on the WM adsorption behavior can be designed and manufactured for the humidity sensors and prototypes of capacitive sensing devices because the water molecules (WMs) are easily adsorbed on surface of BaTiO<sub>3</sub> (Hwang and Choi, 1993; Yeh and Tseng, 1988). However, the effect of water molecules could change the electrical resistivity and dielectric constant which may damage these devices made of BaTiO<sub>3</sub> (Beltran et al., 1991). The WM absorption on BaTiO<sub>3</sub> surfaces has attracted intensive research attentions. In this thesis, BaTiO<sub>3</sub> (010) surfaces are modeled by layer slab with (2x2) in-plane super cell. The bottom three layers were fixed at the bulk ferroelectric positions  $a = 4.005 \text{ \AA}$  and  $c = 4.217 \text{ \AA}$ , with the polarization that was localized in plane along [010] of slab shown in Figure 3.1. The top two layers of solid and adsorbed molecules were relaxed and considered converged when the force on the atomic nuclei is less than  $0.5 \text{ meV/\AA}$ . The BaTiO<sub>3</sub> ideal surfaces were modeled using symmetric (with respect to the mirror plane) geometry. BaO consists of a supercell containing 48 atoms while the TiO<sub>2</sub> plane consists of a supercell containing 52 atoms. In both cases, the vacuum layer is set at  $\sim 19 \text{ \AA}$ . The ideal slabs are nonstoichiometric, with unit cell formulas Ba<sub>12</sub>Ti<sub>8</sub>O<sub>28</sub> for BaO surface and Ba<sub>8</sub>Ti<sub>12</sub>O<sub>32</sub> for TiO<sub>2</sub> surface. For slabs with a defect surface, substituted Ba atom by a metal on top of the layer for the BaO surface (the metal  $A = \text{Be, Bi, Ge, Mg, Na, and Sr}$ ) the formula becomes  $ABa_{11}Ti_8O_{28}$ . This results in the atomic percentage of the impurity of 2.08 %. Oxygen vacancy was also considered in the TiO<sub>2</sub> termination. Additionally, one Ti atom on the top layer at the center of the TiO<sub>2</sub> surface was substituted by a transition metal atom ( $B = \text{Co, Cu, Fe, Mn and Ni}$ ) resulting in the formula  $BBa_7Ti_{12}O_{32}$ . The atomic percentage of the impurity in this

case is equal to 1.92 %. To study the absorption of WM, a WM was placed on top of a two-unit-cell surface in scanned different initial configurations positions for all surfaces following Figure 3.4 and the most favorable absorption is reported. The absorption energy (Li et al., 2014) was calculated from following equation.

$$E_{\text{ads}}(\text{H}_2\text{O}) = E_{\text{tot}}(\text{free slab}, n) + E_{\text{tot}}(\text{H}_2\text{O}) - E_{\text{tot}}(\text{slab} + \text{water}, n), \quad (3.6)$$

where  $E_{\text{tot}}(\text{free slab}, n)$  is the total energy of the optimized ferroelectric  $n$ -layer bare slab (e.g. without water),  $E_{\text{tot}}(\text{H}_2\text{O})$  the total energy of the free water molecule and  $E_{\text{tot}}(\text{slab} + \text{water}, n)$ , the total energy of the optimized  $n$ -layer slab with one  $\text{H}_2\text{O}$  water adsorbed (1/4ML).

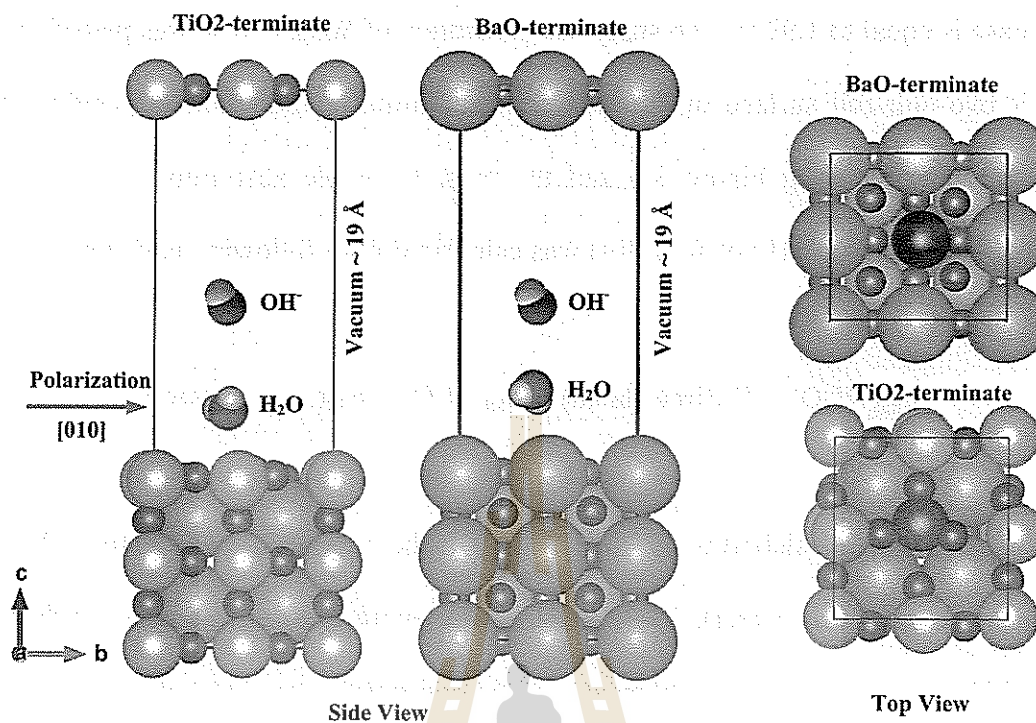
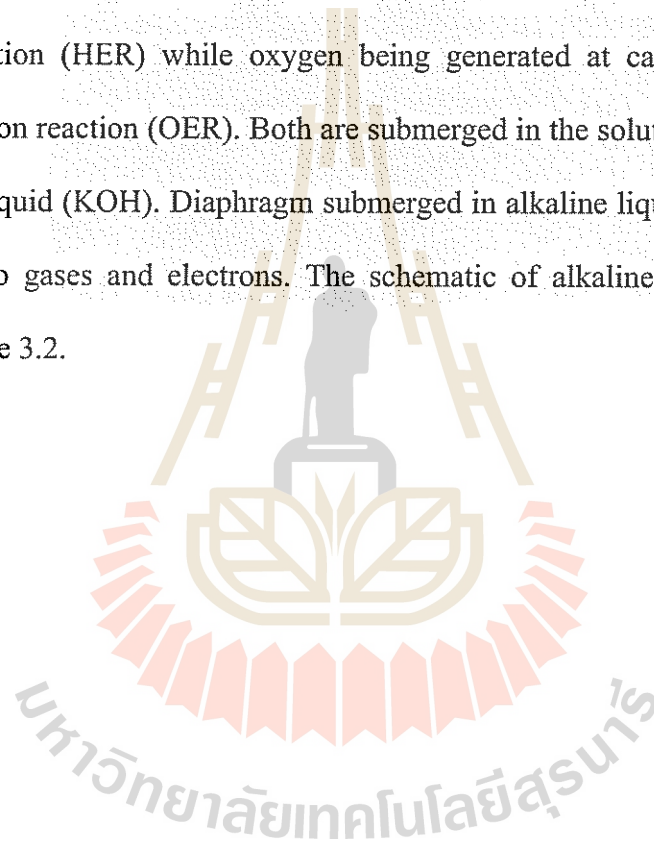


**Figure 3.1** Side view and top view of the slab models of BaO- and TiO<sub>2</sub> terminated side. The green, light blue, red and gray spheres represent Ba, Ti, O and H atoms, respectively. The blue and violet spheres represent the doping site of metal and transition metal atoms.

### 3.3 Water splitting on surface of perovskite material

Water is abundant in nature and water molecule consists of two hydrogen atoms and one oxygen atom. Therefore, direct splitting of water is a choice of interest to produce the hydrogen and oxygen gases. The hydrogen production from water splitting is clean, efficient and of high-quality with by-product of oxygen gas (Carmo et al., 2013; Holladay et al., 2009). Based on thermodynamics, the water can be spitted at 25°C and  $pH=7$  with 1.23 eV per electron or photon transfer. In real experiment, the electricity higher than 1.23 eV is required to overcome any kind of

energy loss and reaction barriers. It is called the over potential ( $\eta$ ). The alkaline electrolysis cell (AEC) (Carmo et al., 2013) operates around room temperature and is available commercially. The main advantages of this cell is that it uses a simple structure comparing with the other cells (Zeng and Zhang, 2010; Badwal et al., 2006). The AEC cell consists of two electrodes connected by electrolyte. Driven by electricity, the anode generate hydrogen, in which the reaction is called the hydrogen evolution reaction (HER) while oxygen being generated at cathode is called the oxygen evolution reaction (OER). Both are submerged in the solution. The electrolyte uses alkaline liquid (KOH). Diaphragm submerged in alkaline liquid  $\text{OH}^-$  while being impermeable to gases and electrons. The schematic of alkaline electrolysis cell is shown in Figure 3.2.



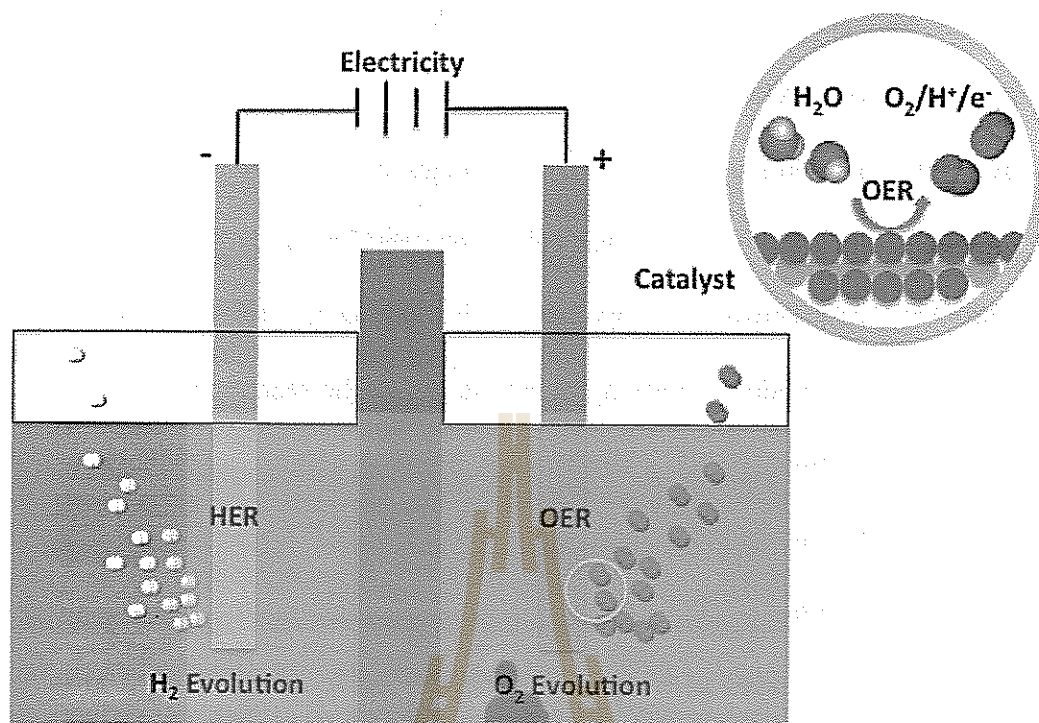


**Figure 3.2** Schematic of alkaline electrolysis cell; left hand side is the hydrogen evolution reaction (HER) and right hand side is the oxygen evolution reaction (OER). The yellow circle is shown the catalyst surface react with water molecule to generate oxygen in oxygen evolution reaction (OER).

A good catalyst can efficiently accelerate the rate of OER by decreasing reaction energy. Platinum (Pt) is one of the best choices due to its very high catalytic activity (Lim et al., 2009). However, it is very expensive. Pt has been studied extensively, for example, the optimization of size and shape of the platinum particles to maximize the amount of reactive sites for OER or alloying platinum with other metals (Zhang et al., 2010; Stamenkovic et al., 2007). Recently, Norskov's group found a descriptor to govern catalytic activity of difference materials. This activity

can be described by binding energies of OER intermediates (binding energies of  $-O$ ,  $-OH$ ,  $-OOH$  on catalyst surface) (Man et al., 2011). They shown the volcano plot to describe the reaction intermediate which can neither bind too strong nor too weak on a catalyst surface. Due to the cost-effective of perovskite-base oxide, the catalyst activities of them were shown in the volcano plot as shown in Figure 3.3. The materials close to the top of volcano exhibit high catalytic activities. Interestingly, the study on catalyst activity on  $BaTiO_3$ , which is the most widely known perovskite-base oxide with cost efficacy, and earth abundant, as OER catalyst is still lacking.

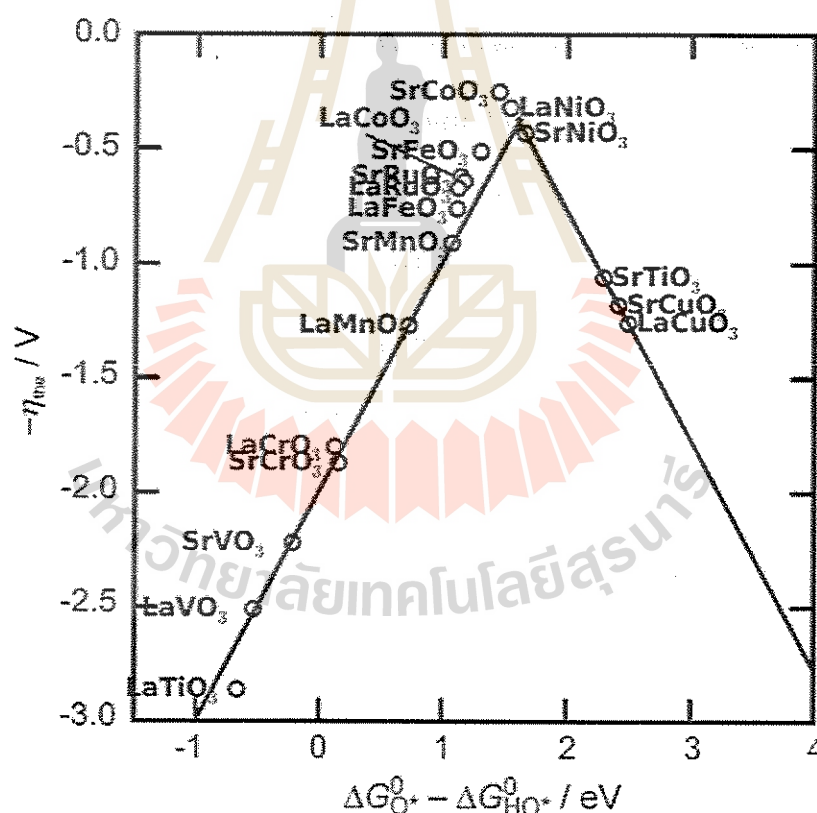


**Figure 3.3** Activity trends towards oxygen evolution plotted for perovskites. the negative theoretical overpotential ( $\eta$ ) was plotted against the standard free energy of the  $\Delta G_{O^*}^0 - \Delta G_{HO^*}^0 / eV$  step (Man et al., 2011).



We propose theoretical investigations of activity trends toward oxygen evolution in BaTiO<sub>3</sub>. These studies are very important to identify oxygen evolution mechanisms and to predict the over potential and active site of BaTiO<sub>3</sub> in range of experimental conditions. Additionally, the unit cell formulas Ba<sub>12</sub>Ti<sub>8</sub>O<sub>28</sub> for BaO surface and Ba<sub>8</sub>Ti<sub>12</sub>O<sub>32</sub> for TiO<sub>2</sub> surface are also studied. Slabs with defect surfaces, substituted transition metals on one Ba atom on top of the layer for BaO surfaces ( $A = \text{Be, Bi, Ge, Mg, Na and Sr}$ ) the formula became  $ABa_{11}Ti_8O_{28}$ . The atomic percentage of the impurity was 2.08 % and the TiO<sub>2</sub> terminated, one Ti atom on top layer at center of TiO<sub>2</sub> surface was substituted by transition metal atom ( $B = \text{Co, Cu, Fe, Mn and Ni}$ ) formulas  $BBa_7Ti_{12}O_{32}$ , the atomic percentage of the impurity was 1.92 % are considered. To find the global structure/global minimum energy, we made sure to have the lowest energy structure by setting up the possibility of initial site/positions as shown in Figure 3.4. To adsorb the intermediate molecule (O\*, H\*, OH\*, OOH\*, O<sub>2</sub> and H<sub>2</sub>O) and then compare the energies of different structures. Finally, only the lowest energy of each intermediate will be used for analysis.

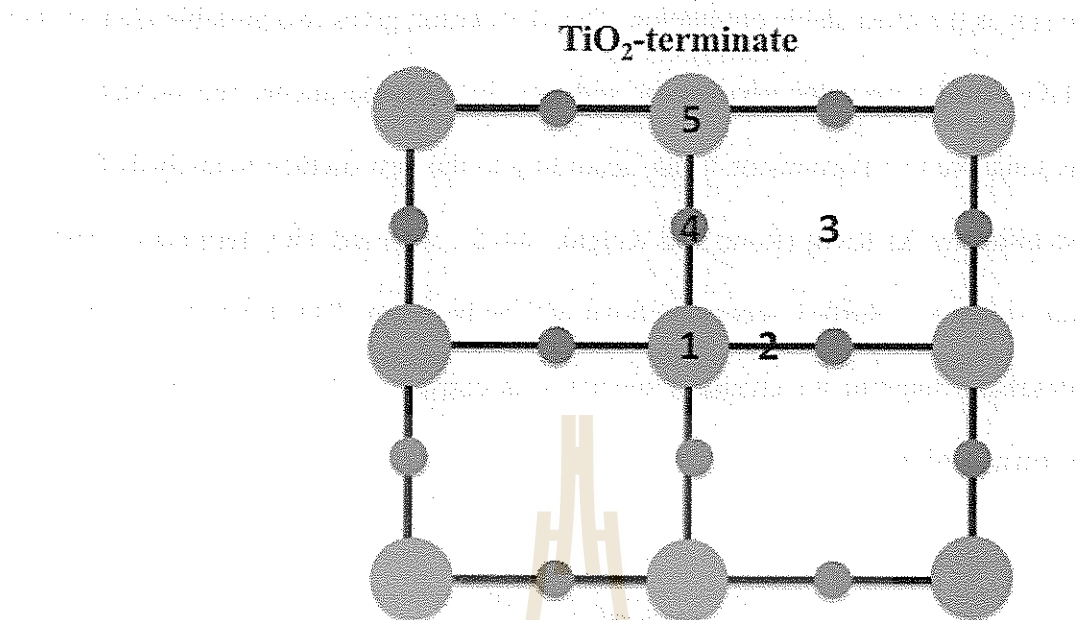


**Figure 3.4** The top view of TiO<sub>2</sub>-terminated surface model shown the possibility of initial site/positions to adsorb the intermediate molecule. Number 1 represents the top site on center Ti or transition metal, number 2 represents the bridge center Ti or transition metal and O atom, number 3 represents the hollow site, number 4 represents on the top of O atom and number 5 represents on top of Ti atom. The blue and red circles are Ti and O atoms, respectively.

### 3.4 Pourbaix and Surface-phase diagrams

Pourbaix diagrams map the preferred states of an electrochemical system in equilibrium as a function of electrochemical potential and *pH* value and, thus, allow in the context of this thesis to predict whether an oxide is stable or if dissolution is thermodynamically favorable. To estimate the stability of the catalyst under operation conditions, we considered non-polar (001) oriented surface because it is generally

taken as the most stable orientation. This orientation gives two possible ideal surfaces:  $\text{TiO}_2$ -BaO terminated asymmetric surfaces. In the experiments, the surface structure is sensitive to environment. Thus, according to the new method to analysis for surface stability by Xi Rong (Rong and Kolpak, 2015), we used  $\text{TiO}_2$  terminated surface as our reference. Surface reconstructions will be based on  $\text{TiO}_2$  terminated surface. The Pourbaix diagram for chemical species  $A$  is constructed by considering two steps as shown in Figure 3.5.

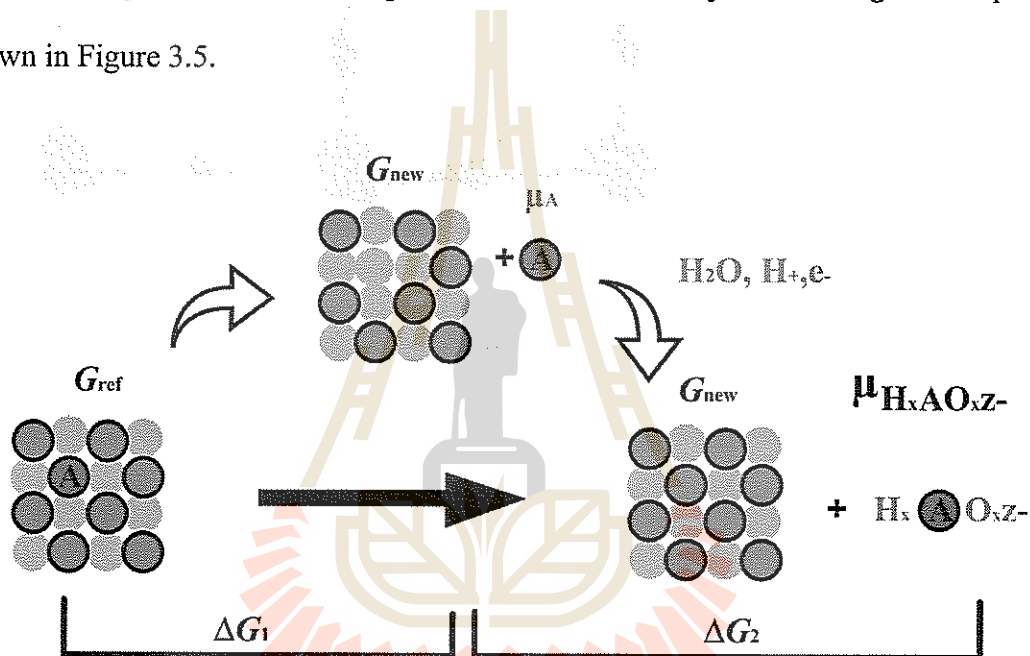


**Figure 3.5** Schematic of surface reconstruction via surface–solvent ion exchange (Rong and Kolpak, 2015).

On the first step, the dismissal of a neutral atom of  $A$  from the surface reaches to a change in free energy first step ( $\Delta G_1$ ) as shown following:

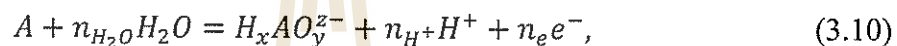
$$\Delta G_1 = G_{new} + \mu_A - G_{ref}, \quad (3.9)$$

where  $G_{ref}$  and  $G_{new}$  are the free energies of the reference and reconstructed surfaces

respectively, and  $\mu_A$  is the chemical potential of species  $A$ .

$\Delta G_1$  is computed directly from DFT with respect to the standard state of  $A$  by approximating the free energy of solids by the DFT total energy.

On the second step,  $A$  reacts with water molecules, and/or protons, electrons to form a solvated ion ( $H_xAO_y^{z-}$ ), the identity of which depends on the environmental condition, as discussed below.



where  $n_{H_2O}$  is number of  $H_2O$  molecule and  $n_{H^+}, n_e$  are number of activity of protons and electrons respectively. Thus the free energy of the second step ( $\Delta G_2$ ) is:

$$\Delta G_2 = \mu_{H_xAO_y^{z-}} - \mu_A - \sum n_i \mu_i, \quad (3.11)$$

where  $\mu_{H_xAO_y^{z-}}$  is the chemical potential of  $H_xAO_y^{z-}$  and  $\mu_A$  are the number and chemical potential of species  $i$  ( $i = H_2O, H^+,$  and  $e^-$ ). The total free energy of formation for the surface reconstruction is therefore:

$$\Delta G = \Delta G_1 + \Delta G_2 \quad (3.12)$$

It can be seen that  $A$  is the intermediate product from the reference surface to the reconstructed surface along with the solvated ion,  $H_xAO_y^{z-}$ . Therefore,  $\Delta G$  is independent of  $\mu_A$ . This empowers us to determine  $\Delta G_1$  and  $\Delta G_2$  relative to  $\mu_A$  at standard temperature and pressure without touching the value of  $\Delta G$ . The standard state of the metal atom is the particular bulk metal at 25°C, while oxygen atoms are referred to  $O_2(g)$  at 25°C and 1 atm. Due to the over binding of  $O_2(g)$  within DFT

(Wang et al., 2006), in practice we expressed the latter such that the chemical potential of oxygen is the difference between the chemical potential of  $\text{H}_2\text{O}(l)$  and  $\text{H}_2(g)$  at  $25^\circ\text{C}$  and 1 atm (Man et al., 2011). Under the above setup, corrections for the zero-point energy and vibrational entropy for gas phase species and surface adsorbates were computed. Our DFT calculations shown that the corrections of the same adsorbate on different surfaces were closed to each other; thus, we used the values on the ideal  $\text{TiO}_2$  termination for all the considered surfaces in this thesis. As commonly practiced,  $\text{H}_2\text{O}(l)$  at  $25^\circ\text{C}$  and 1atm was considered to be in equilibrium with  $\text{H}_2\text{O}(g)$  at  $25^\circ\text{C}$  and 0.03 atm (Man et al., 2011).

$$\mu_{\text{H}_2\text{O}(l)} = E_{DFT}^{\text{H}_2\text{O}(g)} + \text{ZPE} - TS^0(0.03\text{atm}) \quad (3.13)$$

Thus, the standard chemical potential of  $\text{H}_2\text{O}(l)$  is equivalent to the DFT total energy of  $\text{H}_2\text{O}(g)$  together with corrections for the zero-point energy (ZPE) and entropy at  $25^\circ\text{C}$  and 0.03 atm (Assael et al., 1996). All corrections relative to the DFT total energy were summarized in Table 3.1.

**Table 3.1** Values of the zero-point energy (ZPE) and the corrections for the vibrational entropy contributions (TS) for adsorbed and gas-phase molecules taken from reference (Valdes et al., 2008).

	TS/eV	ZPE/eV	(ZPE-TS)/eV
H <sub>2</sub> O	0.67 (at 0.0035)	0.56	-0.11
*OH	0	0.35	0.35
*O	0	0.05	0.05
*OOH	0	0.41	0.41
H <sub>2</sub>	0.41	0.27	-0.14

### 3.5 Experimental standard hydrogen electrode free energy

Standard hydrogen electrode (SHE) free energies were obtained from experimentals. Due to limited data of SHE potentials from literatures, we used standard formation energies based on oxygen gas  $\Delta G^0$  and correct them to SHE free energies  $\Delta G_{SHE}^0$  (Pourbaix, 1974). Such correction was the change of free energy reference from oxygen gas to liquid water and hydrogen gas at standard condition. For the reaction of  $\text{H}_2\text{O}(l) = \text{H}_2(g) + \frac{1}{2} \text{O}_2(g)$ , the Gibbs free energy change per electron transfer was 1.23eV at the standard condition. Therefore, the correction can be generalized as

$$\Delta G_{SHE}^0 = \frac{\Delta G^0 + 2.46n_0 eV}{n_i} \quad (3.14)$$

where  $n_0$  is the number of oxygen atoms in the formula of ion species. For example,

$n_0$  of  $\text{Ba}(\text{OH})^+$  is 1 and  $\text{TiO}_2(\text{s})$  is 2.  $n_i$  is the number of metal atoms in the formula of ion species. For example,  $n_i$  of  $\text{Ba}(\text{OH})^+$  is 1.  $n_i$  was presented in the correction because  $\Delta G^0$  is the formation energy per ion species formula while  $\Delta G_{SHE}^0$  (Pourbaix, 1974) is the free energy per metal atom. Note that standard hydrogen electrode potentials derived from  $\Delta G_{SHE}^0$  are in consistent with those from experiments. The following table shows  $\Delta G^0$ ,  $\Delta G_{SHE}^0$ , and  $\Delta G_{U,pH}$  for all ions considered in this work. Thus, the free energy of the second step (Rong and Kolpak, 2015) is

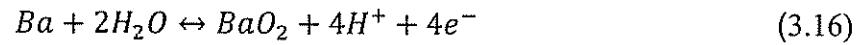
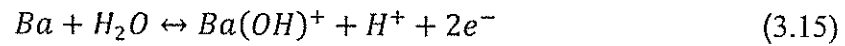
$$\Delta G_2 = \Delta G_{SHE}^0 - n_e(eU_{SHE}) - 2.3n_H + kT \ln a_{H_xAO_y^{z-}} \quad (3.15)$$

A series of process involving loss and adsorption of atoms from a reference surface to form a new surface, since the change of Gibbs free energy is independent of mechanism. The general equation for the reconstruction formation is therefore given by the formation energy with respect to the standard state of the exchanged atom and the electrochemical reaction free energy with respect to SHE. The formation energy of surface reconstruction in general form is written as.

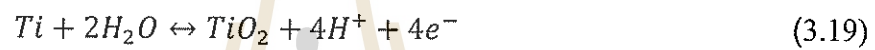
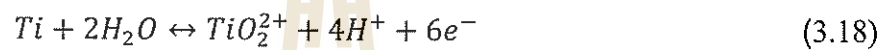
$$\Delta G = (G_{new} - G_{ref} + \sum n_A \mu_A^0) + \sum n_A [\Delta G_2]_A \quad (3.16)$$

where  $n_A$ , the number of exchanged atoms, is positive for vacancy formation and negative for adsorption (Rong and Kolpak, 2015). Based on Eq. 3.16, Table 3.1 lists expression of  $\Delta G_2$  for  $\text{BaTiO}_3$  component-related ion species at room temperature.

In the case of  $\text{BaTiO}_3$ , the second step of Ba and Ti react with water molecules, and/or protons, electrons to form a solvated ion ( $H_xAO_y^{z-}$ ), the chemical equations when Ba atom left from the surface are shown as follows:



For the case of Ti atom left from the surface:

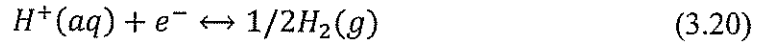


According to Eq. 3.14 to Eq. 3.19, the free energy of the second step of BaTiO<sub>3</sub> component-related ion species at T = 25°C were listed as Table 5.1.

### 3.6 The oxygen evolution reduction (OER) activities on active sites

The OER activities on active sites of BaO and TiO<sub>2</sub> terminations were studied in details by Norskov's group, following four electron reaction paths (Man et al., 2011). The free energies for all steps will be derived further on, for the temperature T=298.15 K (25°C). The relation between the reference electrodes in our case is the Standard Hydrogen Electrode (SHE) and the chemical potential of protons and electrons as seen from another papers of Norskov (Norskov et al., 2004). We assumed the hydrogen to be in equilibrium, e.g. the solvated protons and electrons were in equilibrium with the hydrogen in the gas phase (Rossmeisl et al., 2007)





The expression of the chemical potential the equilibrium was shown as follows:

$$\mu_{H^+} + \mu_{e^-} = 1/2\mu_{H_2(g)} \quad (3.21)$$

The chemical potential of protons, electrons and electrons and hydrogen could be derived further as follows:

$$\mu_{H^+} = \mu_{H^+}^0 + k_B T \ln a_{H^+} \quad (3.22)$$

$$\mu_{e^-} = \mu_{e^-}^0 - eU \quad (3.23)$$

$$\mu_{H_2(g)} = \mu_{H_2}^0 + k_B T \ln p_{H_2} \quad (3.24)$$

where  $a_{H^+}$  represents the activity of protons,  $eU$  represents the shift in electron energy when a bias is applied and  $p_{H_2}$  is the partial pressure of hydrogen.  $\mu_{H^+}^0$ ,  $\mu_{H_2}^0$  and  $\mu_{e^-}^0$  represent the chemical potential of proton, hydrogen and electrons at standard conditions ( $p_{H_2} = 1\text{bar}$ ,  $a_{H^+} = 1$ ,  $T = 298.15\text{K}$ ). Therefore, at these conditions, the relation can be written as:

$$\mu_{H^+}^0 + \mu_{e^-}^0 = 1/2\mu_{H_2(g)}^0 \quad (3.25)$$

We can define the standard potential of hydrogen gas on DFT scale as:

$$\mu_{H_2(g)}^0 = E_{DFT}^{H_2(g)} + ZPE_{H_2(g)} - TS_{H_2(g)}^0 \quad (3.26)$$

where  $S^0$  is the standard entropy of hydrogen and is taken from thermodynamic tables for gas-phase molecules (Atkins and Paula, 2006). Another approximation is that the

chemical potential of water in liquid phase equals to the chemical potential of water in gas phase at T=298.15 K and pressure 0.035 bars. The potential of water in gas phase is described in terms of DFT scale as

$$\mu_{H_2O(g)} = E_{DFT}^{H_2O(g)} + ZPE - TS^0(0.035bars) \quad (3.27)$$

The last approximation is the use for the experimental value of 2.46 eV for standard free energy change of reaction in the DFT energy of the oxygen in the gas phase:  $H_2O(l) \leftrightarrow \frac{1}{2}O_2(g) + H_2(g)$ . Thereby, we have derived the following relation:

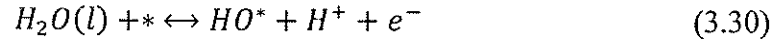
$$G_{H_2O(l)}^0 - \frac{1}{2}G_{O_2(g)}^0 - G_{H_2(g)}^0 = 2.46eV \quad (3.28)$$

Thus, we can approximate the free energy of an oxygen molecule in terms of the  $H_2O(g)$ ,  $H_2(g)$  energetic as follows:

$$E_{DFT}^{O^*} + \Delta ZPE_{O_2(g)} - TS_{O_2(g)}^0 = 4.92 + 2 \left( E_{DFT}^{H_2O(g)} + \Delta ZPE_{H_2O(g)} - TS_{H_2O(g)}^0 \right) \\ 2 \left( E_{DFT}^{H_2(g)} + \Delta ZPE_{H_2(g)} - TS_{H_2(g)}^0 \right) \quad (3.29)$$

### 3.7 Reaction free energy profiles of the OER

The free energy diagram path way for oxygen evolution reaction (OER) follows the four elementary reaction steps each involving the transfer of a single electron-proton pair at T =298.15 K (Man et al., 2011). The first step is water splitting on the active site with releases of a photon and an electron (\* represents the catalyst adsorption site).

**Step I:**

The reaction free energy is:

$$\Delta G_1 = G_{HO^*} + \mu_{H^+} + \mu_{e^-} - G_* - \mu_{H_2O(l)} \quad (3.31)$$

where  $G_{HO^*}$  and  $G_*$  are the free energies of the surface with and without  $HO^*$  respectively and could be written in terms of DFT energies:

$$\begin{aligned} \Delta G_1 = & E_{DFT}^{HO^*} - E_{DFT}^* - \left( E_{DFT}^{H_2O(g)} - \frac{1}{2} E_{DFT}^{H_2(g)} \right) + (\Delta ZPE - T\Delta S^0) \\ & + k_B T \ln a_{H^+} - eU \end{aligned} \quad (3.32)$$

The second step of the reaction is the oxidation of  $HO^*$  species to  $O^*$  with a release of a photon and an electron.

**Step II:**

The change in free energy for the forward reaction is:

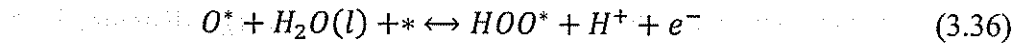
$$\Delta G_2 = G_{O^*} - G_{HO^*} + \mu_{H^+} + \mu_{e^-} \quad (3.34)$$

where  $G_{O^*}$  and  $G_{HO^*}$  represent the free energies of the surface with  $O^*$  and  $HO^*$  species. Replacing again the same equations as in the case for the first step in Eq. 3.32, the reaction free energy could be expressed as follows:

$$\Delta G_2 = E_{DFT}^{O^*} - E_{DFT}^{HO^*} + \frac{1}{2} E_{DFT}^{H_2(g)} + (\Delta ZPE - T\Delta S^0) + k_B T \ln a_{H^+} - eU \quad (3.35)$$

The water splitting on top of oxygen with the corresponding change in free energy represents the third step:

**Step III:**



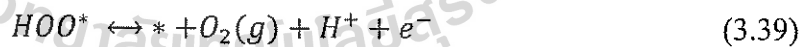
$$\Delta G_3 = G_{HOO^*} - G_{O^*} + \mu_{H^+} + \mu_{e^-} - \mu_{H_2O(l)} \quad (3.37)$$

The same equations as for step one and two are replaced gradually in the Eq. 3.37. The relation for  $G_{O^*}$ , in terms of DFT energies, is similar to the relation for  $G_{HO^*}$ . In the end we get:

$$\begin{aligned} \Delta G_3 = & E_{DFT}^{HOO^*} - E_{DFT}^{O^*} - \left( E_{DFT}^{H_2O(g)} - \frac{1}{2} E_{DFT}^{H_2(g)} \right) + (\Delta ZPE - T\Delta S^0) \\ & + k_B T \ln a_{H^+} - eU \end{aligned} \quad (3.38)$$

The last step is the evolution of oxygen:

**Step IV:**



$$\Delta G_4 = G_* + G_{O_2(g)} + \mu_{H^+} + \mu_{e^-} - G_{HOO^*} \quad (3.40)$$

With Eq. 3.40, we proceed again as in the previous steps, the expression in terms of DFT energies:

$$\begin{aligned} \Delta G_4 = & E_{DFT}^* - E_{DFT}^{HOO^*} - \left( 2E_{DFT}^{H_2O(g)} - \frac{1}{2} E_{DFT}^{H_2(g)} \right) + 4.92 + (\Delta ZPE - T\Delta S^0) \\ & + k_B T \ln a_{H^+} - eU \end{aligned} \quad (3.41)$$

In Table 3.1, for the adsorbed species the ZPE and TS for all the relevant species are listed at T=298.15 K.

In the process of determining the overpotentials ( $\eta^{\text{OER}}$ ): A very important parameter, which can be deduced from the free energy diagram, is the size of the potential-determining step. The catalytic performance was estimated by the magnitude of the potential-determining step for the OER ( $G^{\text{OER}}$ ). This was the last step to become downhill in free energy as the potential increased (blue solid line in Figure 3.6), that is, the specific reaction step in the four-step mechanism with the largest  $\Delta G$  (Man et al., 2011).

$$G^{\text{OER}} = \max\{\Delta G_1, \Delta G_2, \Delta G_3, \Delta G_4\} \quad (3.42)$$

The theoretical overpotential ( $\eta^{\text{OER}}$ ), which is independent of pH, at standard conditions is then given by

$$\eta^{\text{OER}} = (G^{\text{OER}}/e) - 1.23 \quad (3.43)$$

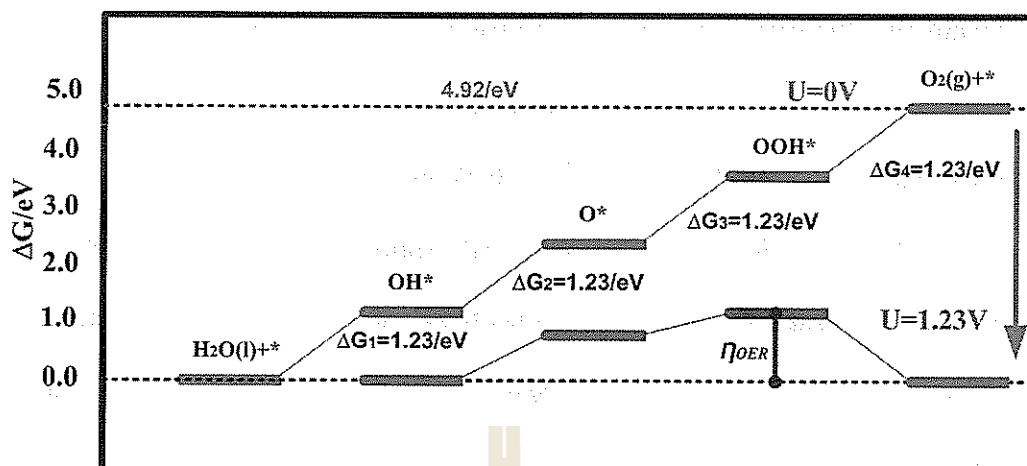


**Figure 3.6** The reaction free-energy diagram for the OER. The turquoise solid line indicates the reaction pathway without applied potential ( $U=0V$ ). The applied equilibrium potential  $U = 1.23 V$  ( $pH=0$  and  $T = 298.15 K$ ), the ideal catalyst is shown by black dash line with the over potential  $\eta^{OER} = 0 V$ . The red solid line indicates non-ideal catalyst case,  $\eta^{OER} > 0 V$ . The overpotential volume  $\eta^{OER}$  is shown by the blue solid line. The red dash line indicates reaction free energies of the magnitude value ( $4.92 eV$ ) at  $U=0 V$  (\* represents the active site on surface catalyst).

An ideal catalyst should be able to facilitate water oxidation just above the equilibrium potential, but requires all the four charge transfer steps to have reaction free energies of the same magnitude at zero potential (i.e.,  $4.92 eV/4 = 1.23 eV$ ) as shown in the red dash line in Figure 3.6. This is equivalent to all the reaction free energies being zero at the equilibrium potential,  $1.23 V$ . Standard free energy diagram for the OER at zero potential ( $U = 0 V$ ), equilibrium potential for oxygen evolution ( $U = 1.23 V$ ) the ideal catalyst at the potential for which all steps become downward at  $pH = 0$  and  $T = 298.15 K$ . The ideal catalyst was shown in black dash line which

means that the over potential  $\eta^{\text{OER}}$  equals to 0 eV. However, in the case of the non-ideal catalyst, when we apply equilibrium potential for oxygen evolution ( $U = 1.23 \text{ V}$ ) the overpotential is still not flat  $\eta^{\text{OER}} > 0 \text{ eV}$  as shown in Figure 3.6.

To investigate the surface adsorption properties and their coverage dependences (normalized as per adsorbate), we extracted the surface adsorption energies,  $\Delta\bar{E} = (X = \text{HO}^*, \text{O}^*, \text{HOO}^*, \text{and H}^*)$  on one side of the slab and the adsorbate coverage was varied from 1/4 to 1 monolayer (ML), where 1 ML corresponds to one adsorbate per (1x1) surface.  $\text{H}^*$  is adsorbed at surface terminated oxygen and the other  $\text{OH}^*/\text{O}^*/\text{OOH}^*$  species are coverage at the metal or the transition metal site of surfaces, the adsorption energies are calculated as follows (Lee et al., 2015):

$$\Delta\bar{E}(X^*) = \frac{E_{\text{DFT}}^{X^*}(N) - E_{\text{DFT}}^*}{N} - \left[ a_{X^*} \cdot E_{\text{DFT}}^{\text{H}_2\text{O}} - \frac{b_{X^*}}{2} E_{\text{DFT}}^{\text{H}_2} \right], \quad (3.44)$$

Where  $X^*$  is the intermediate molecules ( $X = \text{HO}^*, \text{O}^*, \text{HOO}^*, \text{and H}^*$ ),  $E_{\text{DFT}}^{X^*}$  and  $E_{\text{DFT}}^*$  is the DFT total energy of slab with and without intermediate molecules.  $N$  is the number of  $X^*$  adsorbed on the simulated.  $a_{X^*}$  is the number of  $\text{H}_2\text{O}$  and  $b_{X^*}$  is the number of  $\text{H}_2$  divided by 2 to be used as the reference energies for the adsorbed species.

## CHAPTER IV

### PHASE TRANSFORMATION OF $ABO_2$ METAL OXIDES BY FIRST PRINCIPLES CALCULATIONS

In this chapter, the phase transformation under pressure of ternary alloys in the form of  $ABO_2$ , namely  $LiAlO_2$  and  $LiGaO_2$  alloys, are reported. These works have been publicized in the publication forms through two manuscripts (Sailuam et al., 2014; Sailuam et al., 2017) and the work are reproduced here in two sections for the completeness of the thesis. Section 4.1 and 4.2 covers the work on  $LiAlO_2$  (Sailuam et al., 2014) and  $LiGaO_2$  (Sailuam et al., 2017), respectively.

#### 4.1 High pressure phase of $LiAlO_2$ : A first principles study

##### 4.1.1 Introduction

Lithium aluminate,  $LiAlO_2$ , henceforth LAO, has potential applications in the energy industry as lithium battery cathodes and electrolyte tiles for molten carbonate fuel cells (MCFC) (Ceder et al., 1998). It has been reported that LAO has at least four different phases, the hexagonal  $\alpha$ -phase the monoclinic  $\beta$ -phase (Marezio and Remeika, 1966; Zou et al., 2006), the tetragonal  $\gamma$ -phase (Marezio, 1965), and the tetragonal  $\delta$ -phase (Li et al., 2004). The  $\gamma$ -LAO (Marezio, 1965) has attracted much attention as a promising substrate



for GaN-based laser diodes. This is because the lattice mismatch between  $\gamma$ -LAO and GaN is only -1.4% along [001] LAO and [11  $\bar{2}$  0] GaN and -0.1% along [010] LAO and [0001] GaN (Ke et al., 1998; Hellman and Harris, 1997). The  $\gamma$ - to  $\delta$ -phase transformation of LAO has been experimentally studied using several techniques and a wide range of the phase transformation pressure has been reported, i.e. from 2 GPa based on an anvil cell technique to 9 GPa based on a shock recovery technique (Li et al., 2004). However, to our knowledge, there is no computation study on the transformation published. Here, the  $\gamma$ - to  $\delta$ - phase transformation under hydrostatic pressure of LAO is investigated using first principles calculations within both Heyd-Scuseria-Ernzerhof (HSE) (Heyd et al., 2003) hybrid functional and generalized-gradient approximation (GGA). In addition, the electronic properties of both phases are also studied.

#### 4.1.2 Computational methods

First principles calculations were carried out to study LAO in the  $\gamma$ - phase and the high-pressure phase,  $\delta$ -phase. The calculations were based on the density functional theory (DFT) and the projector-augmented wave method (PAW) (Blöchl, 1994) as implemented in the VASP code (Kresse and Furthmüller, 1996(a); Kresse and Hafner, 1994). All calculations were carried out using a high performance computer system at the Synchrotron Light Research Institute (SLRI), Thailand. For an exchange-correlation functional, both generalized gradient approximation (GGA) and Heyd-Scuseria-Ernzerhof (HSE) hybrid functional (Heyd et al., 2003) calculation were used. A cutoff energy for the plane wave basis set was set at 500 eV and 520 eV for GGA and HSE calculations, respectively. A  $k$ -point sampling mesh of  $10 \times 10 \times 8$

according to the Monkhorst-Pack scheme (Monkhorst and Pack, 1976) was used for the GGA calculations. For the HSE calculations, which required a higher computational demand, reduced  $k$ -point sampling mesh of  $2 \times 2 \times 2$  was used. In the HSE calculations, a consistent screening parameter of  $\mu = 0.2 \text{ \AA}^{-1}$  was used for the screened nonlocal exchange as suggested for the HSE06 functional (Heyd et al., 2003). The  $\gamma$ -LAO and  $\delta$ -LAO structures are described by the lattice parameters  $a$ ,  $b$ , and  $c$  as shown in Figure 4.1(a). To study a homogeneous phase transformation between the two phases, a common unit cell size containing 16 atoms (4 Li atoms, 4 Al atoms, and 8 O atoms) was used (see Figure 4.1(b)). The stability of each phase can be determined by analyzing the enthalpy as a function of cell shape defined using  $c/a$  and  $b/a$ , as described in detail in Ref. (Jungthawan and Limpijumnong, 2004). The enthalpy under hydrostatic pressure is defined as

$$H = E + pV, \quad (4.1)$$

where  $E$  is the energy per unit cell,  $p$  is the pressure, and  $V$  is the unit cell volume. For each  $c/a$  and  $b/a$  pair, the unit cell volume,  $V$ , is allowed to relax to minimize  $H$ . In principle, for a given pressure,  $p$ , the  $c/a$  and  $b/a$  that give the lowest enthalpy define the most stable cell shape. In practice, because  $b/a$  is the same for both  $\gamma$ -LAO and  $\delta$ -LAO phases, the  $b/a$  value is fixed at 1 and only the  $c/a$  ratio is varied in the range from 1.20 – 2.15.

### 4.1.3 Results and discussion

The  $\gamma$ -LAO to  $\delta$ -LAO phase transformation occurs through the formations of additional O-Li bonds and O-Al bonds labeled by the dashed squares A and B in Figure 4.1(b) and 1(c). The Li, Al and O atoms at the corner of A and B squares move toward the square center to form new bonds; making each of them 6-fold coordinated (see Figure 4.1(b) and 4.1(c)). While we only selectively labeled the dashed squares to highlight the bond formations, actual bond formations on the planes between A and B squares are also taken place. These bond formations lead to the elongation of the cell shape along the  $c$ -axis. The calculated lattice parameters of the  $\gamma$ -LAO and  $\delta$ -LAO for both HSE and GGA calculations in comparison with the literatures are tabulated in Table 4.1. Similar to the trend generally observed in other materials, the GGA calculations give larger lattice parameters and cell volumes in comparison with the corresponding HSE calculations. Nevertheless, the two sets of calculations give the lattice parameters in agreement to within 1 % and the cell volumes to within 3%. Our calculated results are also in good agreement with other computational results. The agreement is even better when we compare the results from the calculations that used the same exchange-correlation functional. The calculated total energies, as a function of volume for both  $\gamma$ -LAO and  $\delta$ -LAO, are shown in Figure 4.2(a). The minimum energy point of  $\gamma$ -LAO is lower than  $\delta$ -LAO, indicating that  $\gamma$ -LAO is the stable phase at ambient pressure. These energy curves are called the energy of states (EOS). The phase equilibrium pressure is defined by the slope of the common tangent between the EOS curves of the two phases shown using the dashed line in Figure 4.2(a). From the slopes, we obtained the phase equilibrium pressures of 2.3 GPa and 3.1 GPa for the HSE and GGA calculations,

respectively. The calculated equilibrium pressure is in a reasonable agreement with the transformation pressure of 2 GPa obtained by an anvil cell technique (Li et al., 2004).

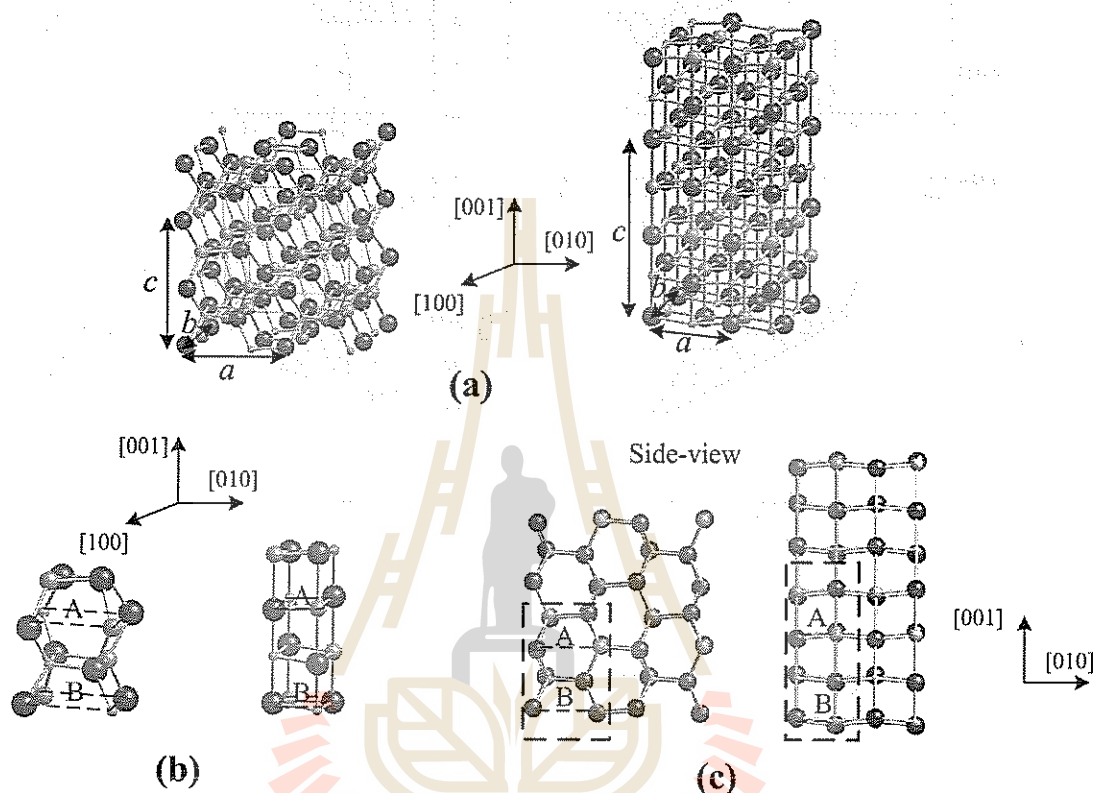


**Figure 4.1** (Color online) (a) Schematic illustration of the natural and high-pressure phases of  $\text{LiAlO}_2$ , i.e.,  $\gamma$ -LAO (left) and  $\delta$ -LAO (right) phases. Large spheres represent oxygen atoms, medium spheres: Al, and small spheres: Li. (b) The common unit cells of the two phases ( $\gamma$ -LAO and  $\delta$ -LAO), containing 16 atoms, used in the calculations. Red dashed squares A and B highlight the bond formation during the phase transformation (see text, for detail). (c) The side view of the crystal with the dashed black rectangles showing the unit cell.

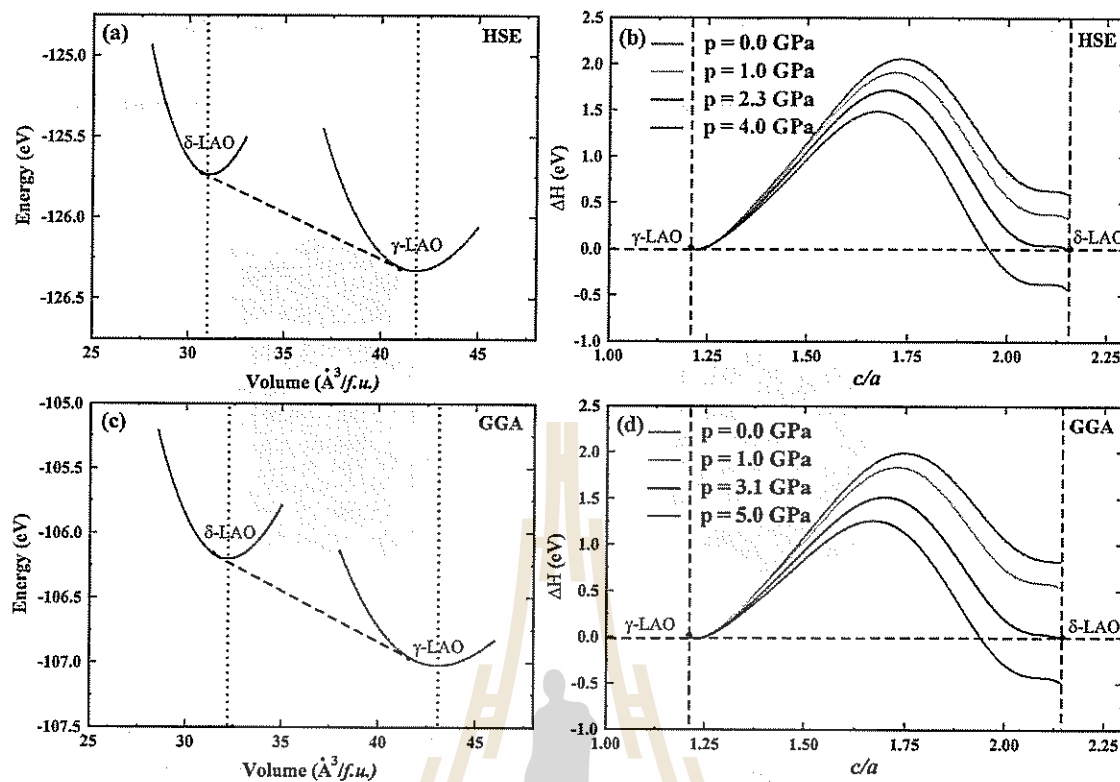


**Figure 4.2** (Color online) (a) The calculated HSE total energy as a function of volume for  $\gamma$ -LAO and  $\delta$ -LAO and the common tangent construction. (b) The enthalpy as a function of  $c/a$  ratio at various pressures. (The  $c/a$  ratio can be considered as the transformation coordinate of the homogeneous transformation from  $\gamma$ -LAO to  $\delta$ -LAO.) The black curve shows the enthalpy at the phase equilibrium pressure where both phases have the same enthalpy. The highest enthalpy point between the two phases defines the transformation barrier. (c) and (d) are the same as (a) and (b) but calculated using GGA functional.

Note, however, that the value obtained by a shock recovery technique is much higher at 9 GPa (Li et al., 2004). The strong dependency on the measuring technique of the transformation pressure could be attributed to a transformation barrier between the two phases. To overcome the barrier, a higher pressure than the equilibrium value is needed. Different techniques might have different difficulty in overcoming this barrier.

While the actual transformation process is too complicated to simulate with the DFT calculations, the calculations of homogeneous phase transformation were proven to be useful and possible to be performed with DFT level (Sarasamak et al., 2008). Here, we studied the homogeneous transformation between  $\gamma$ -LAO and  $\delta$ -LAO. This was done by calculating the enthalpy,  $\Delta H = \Delta E + p\Delta V$ , along the path  $b/a = 1.00$  at different pressures, where,  $E$  and  $V$  were taken at the volume for which the enthalpy was minimized. The  $\Delta$  sign means the difference from  $\delta$ -LAO. The enthalpy curves for different pressures are shown in Figure 4.2(b). At an ambient pressure,  $\gamma$ -LAO has lower enthalpy than  $\delta$ -LAO by  $\sim 0.6$  eV and  $\sim 0.8$  eV for the HSE and GGA calculations, respectively. At higher pressures, the enthalpy differences between the two phases decrease. The enthalpies of both phases ( $\gamma$ -LAO and  $\delta$ -LAO) are equal at  $p = 2.3$  GPa and 3.1 GPa for the HSE and GGA calculations, respectively. At this pressure, the two phases are in equilibrium. This is equivalent to the phase equilibrium pressure calculated from the common tangent between the EOS curves of the two phases. Above the phase equilibrium pressure,  $\delta$ -LAO turn to be more stable (has lower enthalpy). At the equilibrium pressure, it can be seen that the transformation barriers between the two phases are  $\sim 1.7$  eV and  $\sim 1.5$  eV for the HSE and GGA calculations, respectively. These transformation barriers

are quite high and would certainly raise the transition pressure in real experiment beyond than the phase equilibrium pressure. In order for the transition to take place, not only the enthalpy of the targeted phase has to be equal or lower than the initial phase, but the enthalpy barrier between the two phases also has to be sufficiently low (Jungthawan and Limpijumnong, 2004). To lower the barrier, often the pressure has to be increased passed the equilibrium pressure. Therefore, it is not surprising that the transition pressure can go up as high as 9 GPa in the shock recovery technique (Li et al., 2004). Next, we look at the electronic properties of  $\gamma$ -LAO and  $\delta$ -LAO. The band structures of both phases at the ambient pressure calculated using HSE and GGA are shown in Figure 4.3 and Figure 4.4, respectively. From the band structures we can see that  $\gamma$ -LAO has a direct band gap with the band gap values of 6.56 eV and 4.64 eV for HSE and GGA calculations, respectively. Unlike  $\gamma$ -LAO,  $\delta$ -LAO has an indirect band gap with the band gap values of 8.11 eV and 5.74 eV for HSE and GGA calculations, respectively. These large band gaps indicate that both phases of LAO are an insulator. The band gap values are shown in Table 4.1 in comparison with the known experimental value for  $\gamma$ -LAO. For  $\delta$ -LAO, to our knowledge, no experimental band gap value has been reported.

**Table 4.1** Calculated lattice parameters ( $a$ ,  $b$  and  $c$ ), equilibrium volume ( $V$ ) and energy gap ( $E_g$ ) for  $\gamma$ -LAO and  $\delta$ -LAO from HSE and GGA calculations. Note that the  $E_d$  and  $E_i$  in parentheses indicate that the band gaps are direct and indirect, respectively.

Parameters	$\gamma$ -LAO			$\delta$ -LAO		
	Present		Others	Present		Others
	HSE	GGA		HSE	GGA	
$a$ (Å)	5.172	5.221	5.223 <sup>a</sup> 5.168 <sup>b</sup> 5.18 <sup>c</sup>	3.866	3.923	3.886 <sup>d</sup>
$b$ (Å)	Same as $a$ , due to symmetry			Same as $a$ , due to symmetry		
$c$ (Å)	6.250	6.308	6.309 <sup>a</sup> 6.268 <sup>b</sup> 6.29 <sup>c</sup>	8.328	8.397	8.300 <sup>d</sup>
$V$ (Å <sup>3</sup> )	41.79	43.04	43.03 <sup>a</sup> 42.19 <sup>b</sup> 41.86 <sup>c</sup>	31.34	32.19	
$E_g$ (eV)	6.56( $E_d$ )	4.64( $E_d$ )	6.2 <sup>f</sup>	8.11( $E_i$ )	5.74( $E_i$ )	

<sup>a</sup> DFT-GGA calculations by Wu et al. (Wu et al., 2009).

<sup>b</sup> XRD measurement by Marezio (Marezio, 1965).

<sup>c</sup> Li nuclear magnetic resonance measurements by Indris and Heitjans (Indris and Heitjans, 2006)

<sup>d</sup> shock recovery technique by Li et al. (Li et al., 2004)

<sup>f</sup> measured from a single crystal growth by Czochralski method by Hao Teng et al. (Teng et al., 2010)



We can see that the band gap value of  $\gamma$ -LAO obtained by GGA calculation is underestimated compared to the experimental value due to well-known DFT problems, as expected. On the other hand, HSE calculations (Teng et al., 2010) give the band gap in a good agreement with the experiment with the error of only  $\sim 5\%$ . Similar accuracy of the calculated band gap can be expected for the high-pressure phase where there is no experimental value to compare. To investigate the source of the electron states near the band edges, the partial density of states (PDOS) are calculated (Figure 4.3 and Figure 4.4). Both HSE and GGA calculations give similar PDOS. Note that, because of a limited  $k$ -point sampling used, the PDOS of HSE calculations appears to be discontinuous especially near the conduction band minimum. If more  $k$ -points were used, the PDOS would be continuous similar to what obtained by GGA calculations. For  $\gamma$ -LAO, the valence band maximum is dominated by O  $2p$  states with some contributions from Li  $p$ . The conduction band minimum is dominated by Li  $s$ . For  $\delta$ -LAO, the valence band maximum is dominated by O  $2p$  states with some contributions from of Al  $p$  and Li  $p$  states. The conduction band minimum is dominated by Al  $s$ .

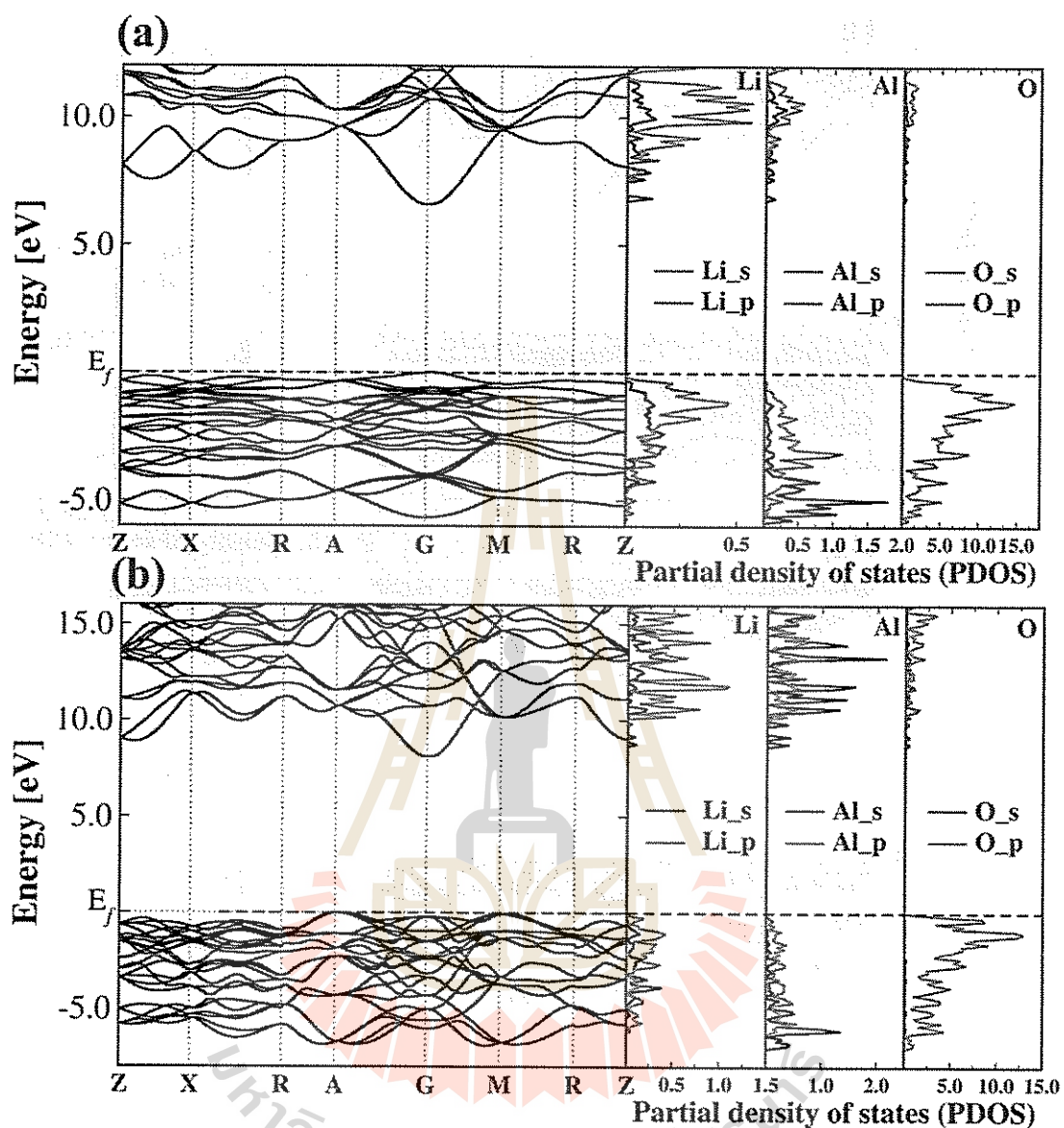


**Figure 4.3** Electronic band structures and partial density of states (PDOS) of (a)  $\gamma$ -LAO and (b)  $\delta$ -LAO obtained from HSE calculations. The special k-points used for the band structures plot are according to the cubic Brillouin zone defined in Ref. (Limpijumnong and Lambrecht, 2001)

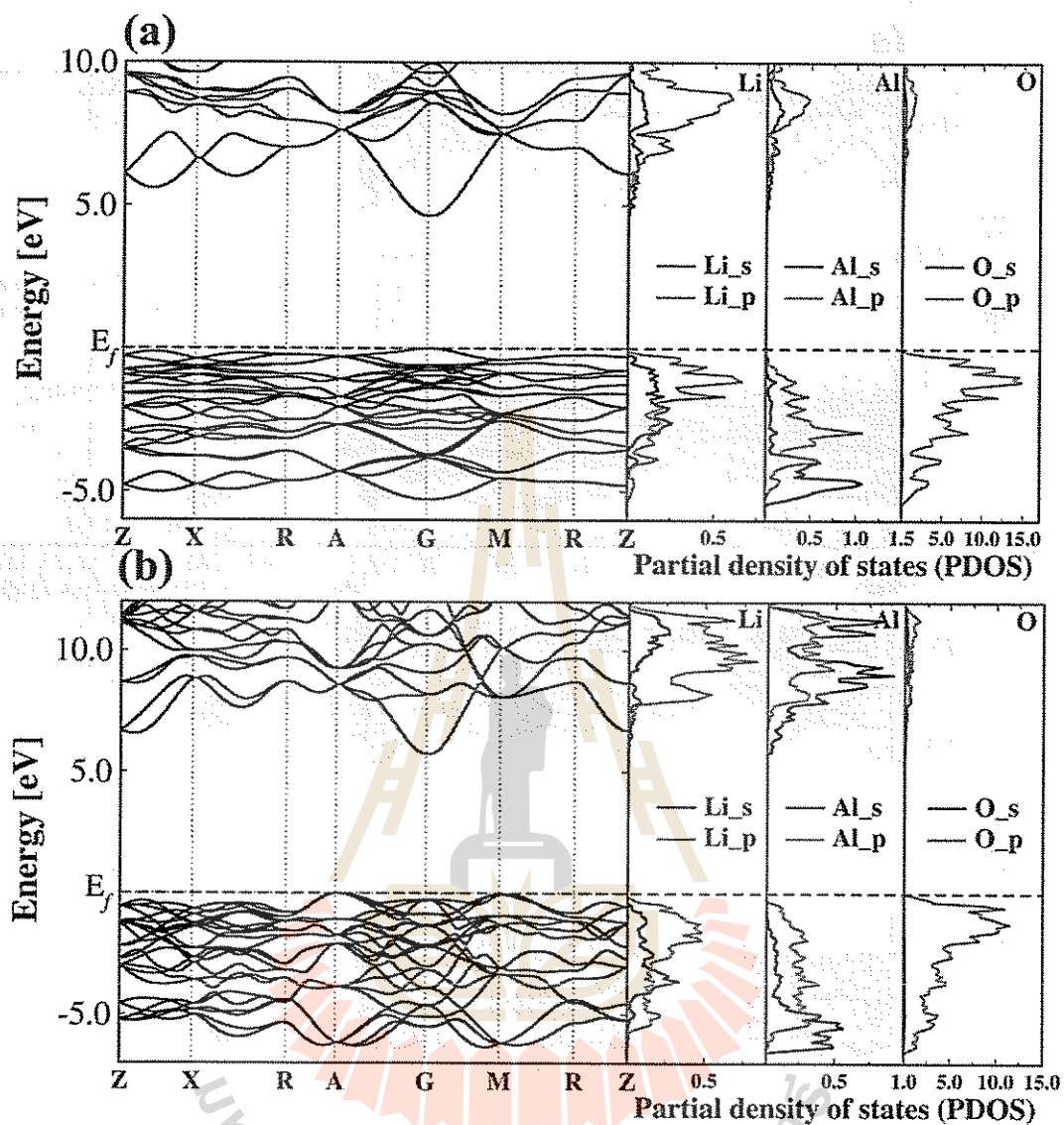


Figure 4.4 Electronic band structures and partial density of states (PDOS) of (a)  $\gamma$ -LAO and (b)  $\delta$ -LAO obtained from GGA calculations.

## 4.2 Pressure-induced phase transformations of LiGaO<sub>2</sub> :first principles study

### 4.2.1 Introduction

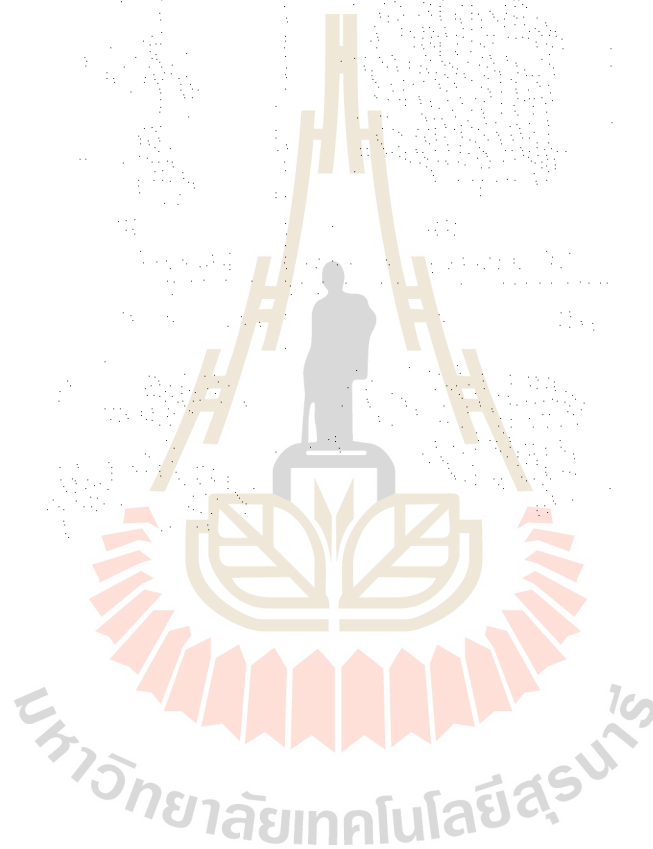
$\beta$ -LiGaO<sub>2</sub> (Pna2<sub>1</sub>) is the ambient-pressure structure of LiGaO<sub>2</sub> (LGO) that can be obtained in a large single crystal form by a conventional Czochralski melt-pulling method (Chen et al., 2014; Jungthawan and Limpijumnong, 2004). This material has a wurtzite derived structure with a good lattice match to epitaxially grown GaN and ZnO thin-films. Both GaN and ZnO are technologically important materials for blue and purple optoelectronic devices (Chen et al., 2014). The crystal structure of  $\beta$ -LiGaO<sub>2</sub> (Pna2<sub>1</sub>) is an analogous of the wurtzite ZnO in which the group-II Zn is alternately substituted by group-III Ga and group-I Li. Due to the relaxation of the oxygen sub-lattice and symmetry-breaking cations, the structure of this ternary oxide slightly differs from the perfect wurtzite-type structure (P6<sub>3</sub>mc) (Jungthawan and Limpijumnong, 2004). This relaxation is mainly a result of the difference between LiO<sub>4</sub> and GaO<sub>4</sub> tetrahedra with LiO<sub>4</sub> being bigger than GaO<sub>4</sub>. The average bond lengths are 1.985 Å and 1.848 Å for Li–O and Ga–O, respectively. The difference between the average Li–O and Ga–O bond distances is less than 4%, allowing the formation of an orthorhombic structure (Pna2<sub>1</sub>) with the lattice parameters  $a = 5.402$  Å,  $b = 6.372$  Å,  $c = 5.007$  Å, and density = 4.187 g.cm<sup>-3</sup> (Marezio, 1965).  $\beta$ -LiGaO<sub>2</sub> is known to have a band gap of 5.6 eV; making it a good candidate for applications in bright UV optoelectronic applications (Omata et al., 2011; Omata et al., 2015).

Pressure induced phase transformations of wurtzite ZnO have been previously studied experimentally and theoretically (Sarasamak et al., 2008; Recio et al., 1998).

It has been predicted that a 10 GPa tensile stress along the [0110] direction or 6 GPa compressive stress along [0001] direction (Kulkarni et al., 2006) could transform a wurtzite ZnO into an un-buckled phase (HX) (Kulkarni et al., 2006), A 7 GPa tensile stress along [0001] induces a formation of a body-centered-tetragonal phase (BCT-4) (Wang et al., 2007), A hydrostatic pressure of about 8.5 GPa leads to the well-known and experimentally-observed rocksalt cubic phase (Sarasamak et al., 2008). First principles study on the stable phases and phase transformations of LGO is scarce. Due to the similar in the structural of  $\beta$ -LGO (Pna2<sub>1</sub>) to that of wurtzite ZnO, we propose to employ the theoretical investigations in a similar manner as those have been employed successfully for the case of ZnO (Sarasamak et al., 2008) These studies are very important to identify transition mechanisms and to predict the undiscovered phases of LGO that can be reached by proper experimental conditions.

In this thesis, we used density functional theory (DFT) calculations to study phase transformations of LGO under hydrostatic and uniaxial pressures. We explored the LGO phase-space through the modeling of stress loads along different crystal directions. Three metastable phases of LGO, namely, oP16, I41/amd, and P4<sub>1</sub>2<sub>1</sub>2 are predicted based on the enthalpy surface diagrams for the transformations from ambient-pressure  $\beta$ -LGO (Pna2<sub>1</sub>). The compressive stress loading along the [001] direction produces the five-fold orthorhombic phase (oP16). The uniaxial tensile strain along [001] direction stabilizes a tetragonal structure (P4<sub>1</sub>2<sub>1</sub>2). The hydrostatic pressure leads to two structures that are energetically close to each other. One phase is the body center tetragonal (BCT, I41/amd) and another phase is trigonal (R3m) structure, previously found in experiments (Marezio, 1965). All structures are shown in Figure 4.5 and the comparison with the analogous ones in the binary compound

ZnO is shown in Figure 4.6. For simplicity, henceforth the LGO phases are named after the analogous ones in ZnO, i.e., the orthorhombic (Pna21) is named WZ', the body-center tetragonal (I41/amd) is named RS', the rhombohedral (R3m) is named RS'', the orthorhombic (oP16) is named HX', and the tetragonal (P4<sub>1</sub>2<sub>1</sub>2) is named BCT'.



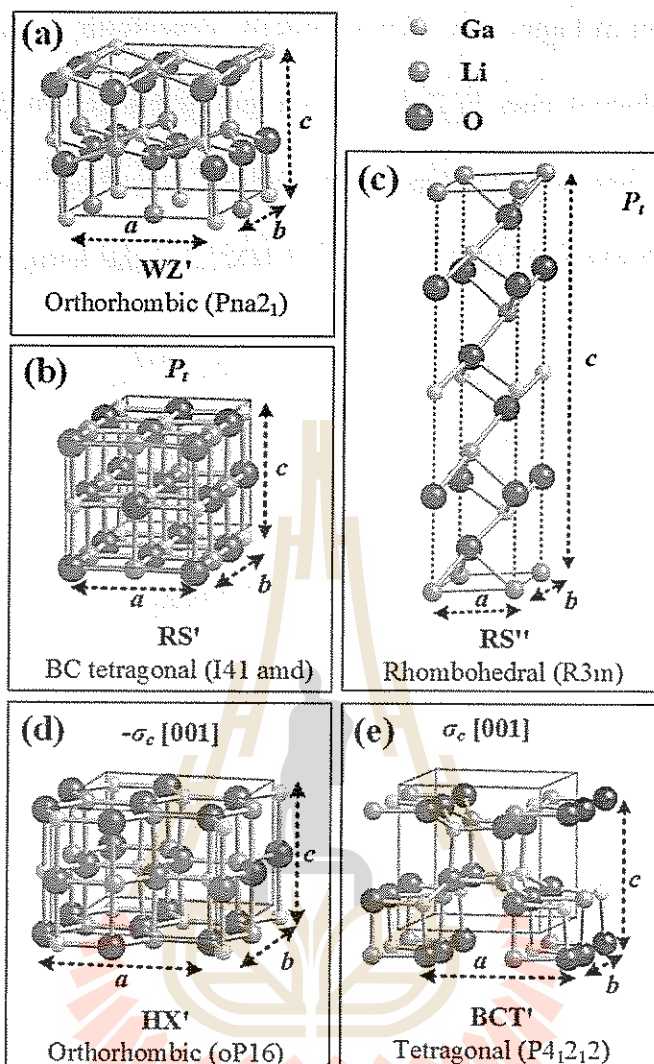


**Figure 4.5** Schematic illustrations of the ambient and the high-pressure crystal structures of LGO: (a) Orthorhombic ( $Pna2_1$ ) - ambient condition structure, (b) Body-centered tetragonal ( $I41/amd$ ) - hydrostatic compression ( $P_t$ ) structure, (c) the Rhombohedral ( $R3m$ ) - another hydrostatic compression ( $P_t$ ) structure, (d) Orthorhombic ( $oP16$ ) -  $[001]$  compressive stress ( $-\sigma_c$ ) structure, and (e) tetragonal ( $P4_12_12$ ) -  $[001]$  tensile stress ( $\sigma_c$ ) structure. In the structures, the green spheres represent Ga cations, blue spheres represent Li cations and red spheres represent O anions.

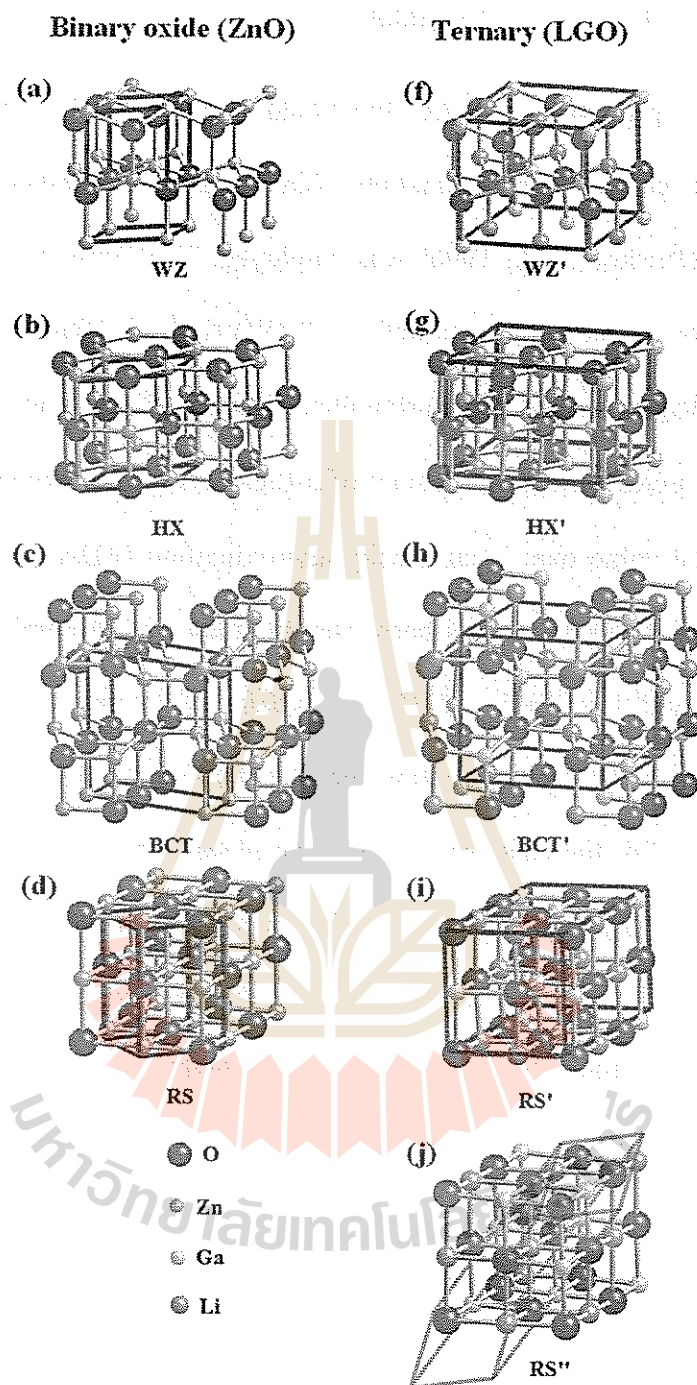


**Figure 4.6** Relationship between the crystal phases of the binary compound ZnO and the analogous ones of the ternary compound LGO.



#### 4.2.2 Material and methods

First principles density functional theory (DFT) calculations with the generalized gradient approximations (GGA) as the exchange correlation (XC) functional (Perdew et al., 1996) was employed. The ultrasoft pseudopotentials with the projector augmented wave method (PAW) (Blöchl, 1994) as implemented in the VASP package (Kresse and Furthmüller, 1996(a); Kresse and Hafner, 1994) were used. GGA gives the lattice constant of  $\beta$ -LiGaO<sub>2</sub> in better agreement with the known experimental value than local density approximation (LDA) XC functional (Perdew and Zunger, 1981) which has been used to study ZnO (Limpijumnong et al., 1996; Boonchun and Lambrecht, 2010). A typical LGO unit cell for the study of a homogeneous phase transformation consists of 16 atoms (4 Li atoms, 4 Ga atoms, and 8 O atoms). For the basis set we used the plane wave expansions set up to 520 eV and for the k-point sampling of the Brillouin zone for the energy integrations, we used at least  $7 \times 7 \times 7$  Monkhorst-Pack scheme (Monkhorst and Pack, 1976) For the structural relaxations, the calculations are considered converged when the acting forces on each atom is less than 0.1 meV/Å; corresponding to the total energies convergence of  $\sim 0.1$  meV/atom. The stability of each phase can be determined by analyzing the enthalpy as a function of cell shape defined using the ratios  $c/a$  and  $b/a$ , as described in detail by Jungthawan and Limpijumnong (Limpijumnong and Jungthawan, 2004) . For different loading conditions, we used distinct equations of state from which we obtain the minimum enthalpy for each combination of  $c/a$ - $b/a$  pairs and loading conditions. When two phases share the same minimum enthalpy, those two phases are equally favored. The enthalpy ( $H$ ) under hydrostatic pressure is defined as Eq. 4.1

where  $E$  is the energy per unit cell,  $p = -(\partial E/\partial V)$  is the pressure, and  $V$  is the unit cell volume. For each  $c/a$  and  $b/a$  pairs,  $V$  is allowed to relax to minimize  $H$ . In principle, for a given  $p$ , the  $c/a$  and  $b/a$  ratios that give the lowest enthalpy define the most stable cell shape. In practice, we calculated the enthalpy surface as a function of two independent strain parameters, i.e.,  $c/a$  and  $b/a$  in the range from 0.787 to 0.468 and 0.848 to 0.468, respectively. A total of 36 strained configurations, corresponding to the increments of 0.05 in  $c/a$  and 0.05 in  $b/a$  in the  $c/a$ - $b/a$  space are investigated.

For uniaxial loading, the stability of each crystal and compound can be determined by

$$H\left(\frac{c}{a}, \frac{b}{a}\right) = E(c, b, a) \mp A_{jk} \times \sigma_i q_i, \quad (4.2)$$

where  $E$  is the energy per unit cell,  $\sigma_i$  is the stress along the  $i$  direction,  $q_i$  is the lattice parameter in the  $i$  direction,  $A_{jk}$  is the cross section area of the unit cell perpendicular to the stress direction, and  $A_{jk} \times \sigma_i q_i$  is external work. For the stresses along the  $c$  axis,  $i = c$ ,  $A_{ab} = ab$  and  $q_c = c$ , with  $-\sigma_c$  being a compressive stress and  $+\sigma_c$  being a tensile stress. For each strained configuration (each  $c/a$ - $b/a$  pair), the energies associated with at least five different unit cells are calculated. An equation of state (energy-volume relation) is obtained by a third-degree polynomial fit.

### 4.2.3 Results and discussion

In addition to the natural phase of LGO (WZ'), there are other phases that are metastable and have rather low energies (within 25 meV/atom). They are orthorhombic oP16 (HX'), and tetragonal P4<sub>1</sub>2<sub>1</sub>2 (BCT'). Figure 4.7 shows the total

energies of five different phases of LGO as a function of the unit-cell volume. They are orthorhombic  $Pna2_1$  (WZ'), orthorhombic  $oP16$  (HX'), body center tetragonal  $I41/amd$  (RS'), rhombohedral  $R3m$  (RS'') and tetragonal  $P4_12_12$  (BCT'). The minimum point of each curve gives the equilibrium cohesive energy of the corresponding phase of LGO and the stable volume. As expected, the WZ' structure which is the natural phase of LGO (Marezio, 1965) is the computationally most stable one. Interestingly, we also found other metastable phases close in energy to the ground state WZ'. The HX' and BCT' have energies only 0.021 eV/atom and 0.017 eV/atom, respectively, higher than that of WZ'. The RS' has the highest relative energy among structures studied at 0.037 eV/atom above WZ'. The relative energies of the five phases follow the order of  $RS' > HX' > RS'' > BCT' > WZ'$ . By using the common tangent approach (Yu et al., 2007), two WZ-RS phase transitions under hydrostatic pressure:  $WZ' \rightarrow RS''$  and  $WZ' \rightarrow RS'$  are predicted to take place at the equilibrium hydrostatic pressures of 1.4 GPa and 3.7 GPa, respectively. Table 4.2 shows the calculated equilibrium lattice parameters, bulk modulus ( $B_0$ ), transformation pressures ( $P_t$ ), stresses, and volumes for all the different phases studied under pressure conditions. The lattice parameters of these structures are in good agreement with previous theoretical and experimental data.

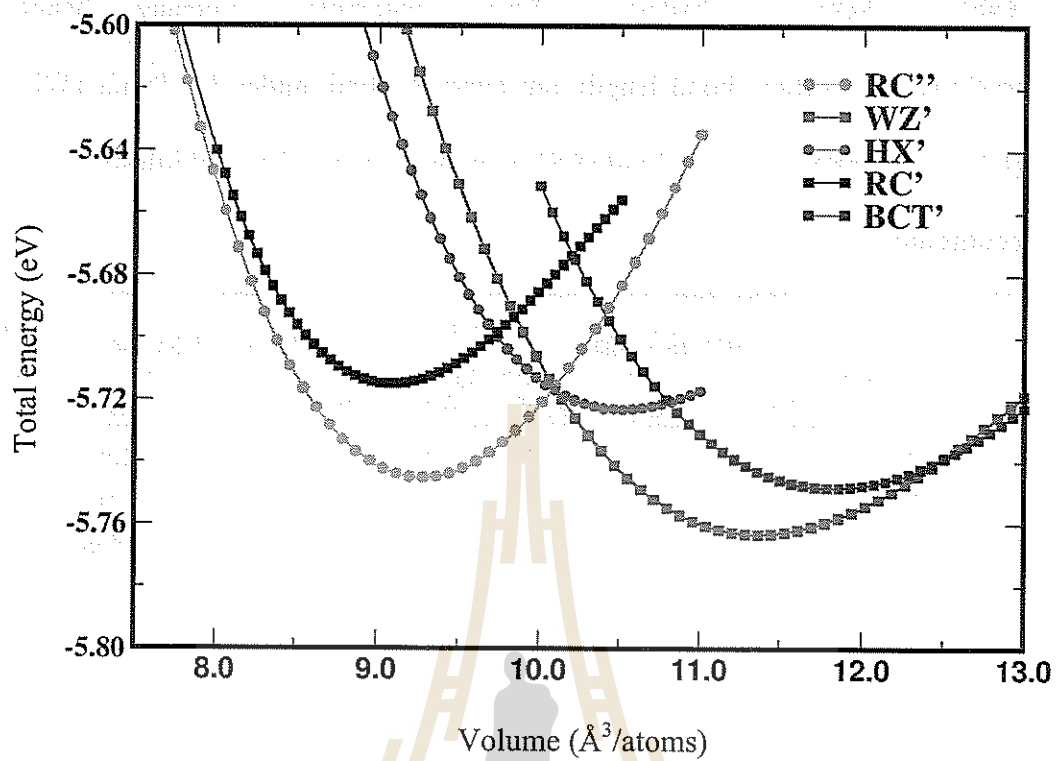


**Figure 4.7** Total energy versus volume per atoms for five LGO structures: Green (RS''), Red (WZ'), Indigo circles (HX'), black squares (RS') and blue squares (BCT').

**Table 4.2** Schematic illustrations of lattice parameters, percentage changes, Bulk modulus  $B_0$ , average bond length and average bond angles for Pna2<sub>1</sub> (WZ'), oP16 (HX'), R3m (RS'') and I41/amd (RS') structures under their equilibrium and loading conditions.

Parameters	WZ' ( $p=0$ GPa)			HX'	RS'' ( $p_f=1.5$ GPa)			RS'
	Present	LDA <sup>a,b</sup>	Exp <sup>d</sup>	$\sigma_\epsilon=-3.5$ GPa	Present	Exp <sup>c</sup>	LDA <sup>b</sup>	$p_f=3.7$ GPa
$a$ (Å)	6.457	6.255 <sup>a</sup>	6.372	6.891	2.997	2.911	2.903	8.728
$b$ (Å)	5.479	5.361 <sup>a</sup>	5.402	5.781	2.997	2.911	2.903	4.082
$c$ (Å)	5.080	4.953 <sup>a</sup>	5.007	4.223	14.693	14.47	14.401	4.082
$b/a$	0.848			0.839	1.000			0.468
$c/a$	0.787			0.613	4.903			0.468
$V$ (Å <sup>3</sup> /f.u.)	44.93	41.53 <sup>a</sup>	43.09	33.65	22.55			29.09
$\Delta V$ (%)	-			-7.45	-49.36			-19.99
$\Delta b$ (%)	-			5.51	-45.31			-25.50
$\Delta c$ (%)	-			-16.87	65.42			-19.65
$B_0$ (GPa)	80.93	95.69 <sup>b</sup>		102.58	189.2		142.29	164.79
Average bond lengths (Å <sup>3</sup> )								
Ga-O	1.896	1.858 <sup>b</sup>	1.848	1.984	2.021	2.00		2.029
Li-O	1.988	1.923 <sup>b</sup>	1.985	2.061	2.208	2.14		2.161
Average bond angles (Å <sup>3</sup> )								
O-Ga-O	110.21	112.3 <sup>b</sup>	109.2	90.54	92.87	93.4		92.21
O-Li-O	108.68	107.5 <sup>b</sup>	103.3	89.60	86.39	85.9		90.36

<sup>a</sup> VASP code DFT- LDA calculation by A. Boonchun et al.(Boonchun and Lambrecht, 2010)

<sup>b</sup> CASTEP code DFT-LDA calculation by Li Lei et al.(Lei et al., 2013)

<sup>c</sup> Piston and cylinder device by M.Mareziro. (Mareziro and Remeika, 1965)

<sup>d</sup>General Electric XRD by M.Mareziro. (Mareziro, 1965)

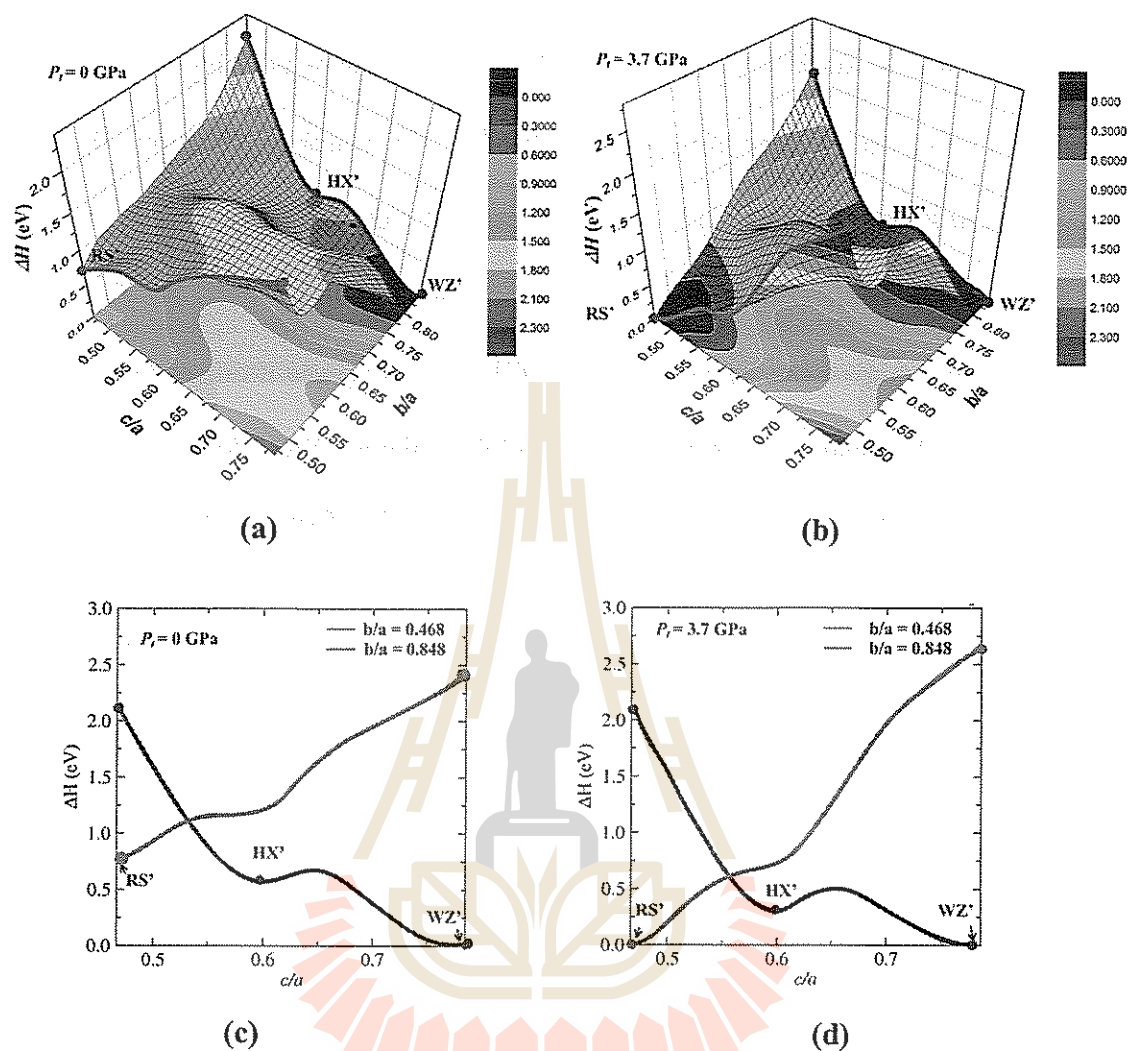
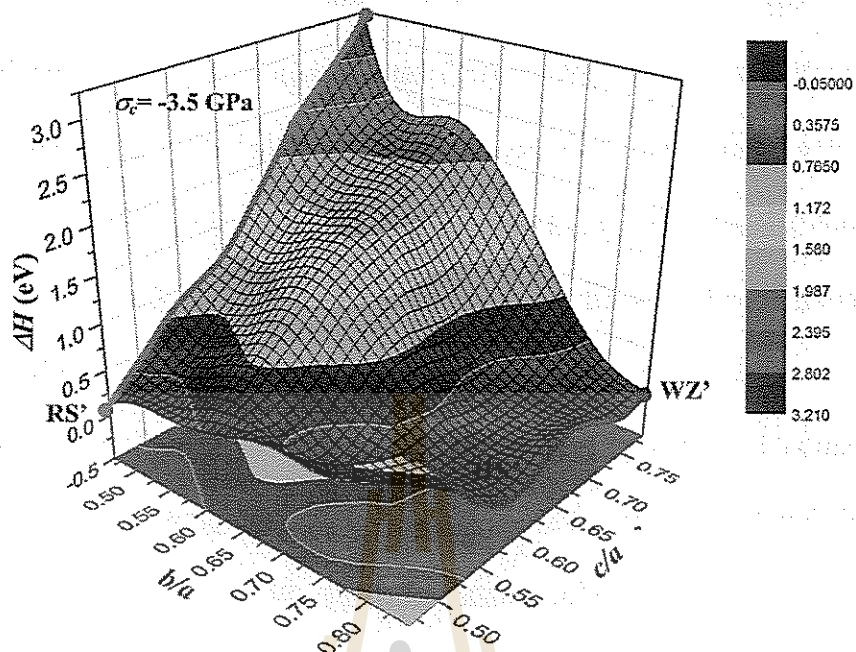
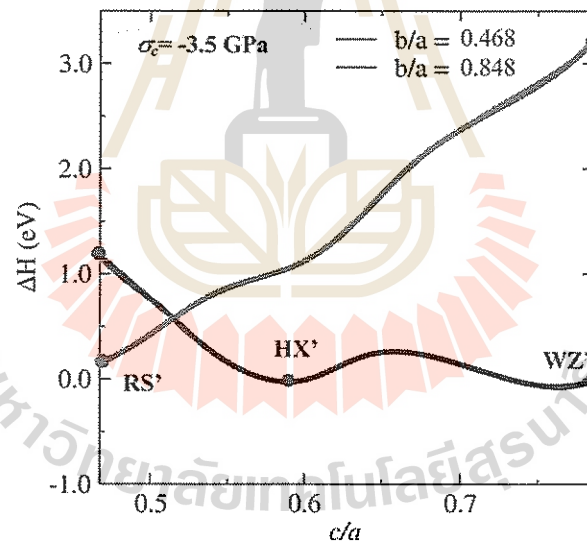


**Figure 4.8** Enthalpy surface map (eV), and 2-D sections of the enthalpy surface maps for  $Pna2_1$  ( $WZ'$ ),  $oP16$  ( $HX'$ ) and  $I41/amd$  ( $RS'$ ) unit cell. Each point on the surface represents the minimum energy volume ( $V$ ) is allowed to relax while  $c/a$  and  $b/a$  are kept constant: (a) Enthalpy surface map (eV) at  $P_t = 0$  GPa, (b) Enthalpy surface map (eV) at  $P_t = 3.7$  GPa, (c) 2-D sections of the enthalpy surface maps at  $P_t = 0$  GPa and (d) 2-D sections of the enthalpy surface maps at  $P_t = 3.7$  GPa. For  $b/a = 0.468$  (red line) and  $b/a = 0.848$  (blue line).

Because the calculated transition pressure under hydrostatic pressure of  $WZ' \rightarrow RS''$  is much lower than that of  $WZ' \rightarrow RS'$  as shown in Figure 4.8, in principle, the former will be more likely to take place and  $RS'$  is unlikely to form. Based on this formation energy plot, other phases of LGO cannot be achieved by applying hydrostatic compression. We will show next that the  $WZ' \rightarrow HX'$  can be achieved by applying uniaxial pressure and  $WZ' \rightarrow BCT'$  can take place if one can apply sufficient negative hydrostatic pressure (i.e., expand the volume). We calculated the enthalpy as a function of two crystal parameters ( $c/a$  and  $b/a$ ); forming the enthalpy surfaces under different pressure conditions. Compression along the  $[001]$  direction transforms  $WZ' \rightarrow HX'$  by means of the reduction in the  $c$  lattice parameter, and consequently decreasing the unit cell volume ( $c$ -axis of  $HX'$  is 16.87% shorter than that of  $WZ'$  with a smaller volume of 17.45%). Figure 4.9(a) and Table 4.2 show the lattice parameters change during this phase transformation. The stability of the  $HX'$  phase can be better analyzed through the enthalpy difference  $\Delta H = H^{HX} - H^{WZ}$  as a function of the compressive stress along the  $c$  direction. For this, we obtained the enthalpy surface and energy cross-section corresponding to an applied compressive stress along the  $c$ -axis,  $-\sigma_c$  (negative sign indicates compression) as shown in Figure 4.9(a) and 4(b) for compressive stress at 0 GPa and 3.5 GPa, respectively. We found the equilibrium stress for the  $WZ' \rightarrow HX'$  transformation is  $\sigma_c = 3.5$  GPa. At this stress, the enthalpy of  $WZ'$  phase (four-fold) and  $HX'$  (five-fold) phase are equal and both phases can co-existed.



(a)



(b)

**Figure 4.9** (a) The enthalpy surface for the compression stress  $\sigma_c = -3.5$  GPa and (b) 2-D sections of the enthalpy surface maps with the compression stress  $\sigma_c = -3.5$  GPa for  $b/a = 0.468$  (red line) and  $b/a = 0.848$  (blue line).



The calculated homogeneous transformation enthalpy barrier is only 12.5 meV/atom for this  $WZ' \rightarrow HX'$  transformation. The BCT' can be stabilized by applying uniaxial tensile stress along [001] on the WZ'. This transformation occurs through a combination of: 1) The breaking of every other Li-O bond along the [001] direction (bonds labeled B in Figure 4.10(a)), and 2) The formation of an equal number of Li-O bonds (labeled A in Figure 4.10(a)). This bond breaking and bond formation is repeated between Ga-O bond and Li-O on alternate planes along the [010] direction. Table 4.3 shows the calculated lattice parameters for the tetragonal phase at different values of tensile stress. For WZ',  $c/a$  and  $b/a$  ratios are 0.787 and 0.848, respectively.

Through the transformation,  $b/a$  remains constant (0.848), while  $c/a$  increases with stress as shown in Figure 4.10. Increasing tensile stress the relative stability of BCT' with respect to that of the WZ', while the unit cell volume increases by 5.3%, 5.7%, 6.8%, and 7.9% for  $\sigma_c = 0, 2, 4.1, 6$  GPa, respectively. Because both WZ' and BCT' share the same  $b/a$  ratio at 0.848, it is not necessary to vary this parameter when studying the relative phase stability. Figure 4.10 shows cross-sections of enthalpy surfaces at  $b/a = 0.848$  at different values of tensile strain. At 0 GPa, WZ' is the most stable crystal structure and its enthalpy is lower than that of BCT' by 0.26 eV/atom, see Figure 4.10(b). As the stress is increased to 2 GPa (Figure 4.10(c)), the enthalpy difference decreases, and at the stress of 4.1 GPa (Figure 4.10(d)) the two minima,  $H^{WZ'}$  and  $H^{BCT'}$ , become equal. This means the two phases are equally favored and 4.1 GPa is the equilibrium tensile stress. Above this equilibrium stress BCT' becomes more stable. At 6 GPa (Figure 4.10(e)), BCT' is more stable than WZ' by 0.13

meV/atom. The enthalpy barrier at the equilibrium pressure 4.1 GPa is estimated by measuring the  $\Delta H$  between the minima of the plots and their intersection point ( $c/a = 0.85$ ). This gives the barrier of only 3.36 meV.

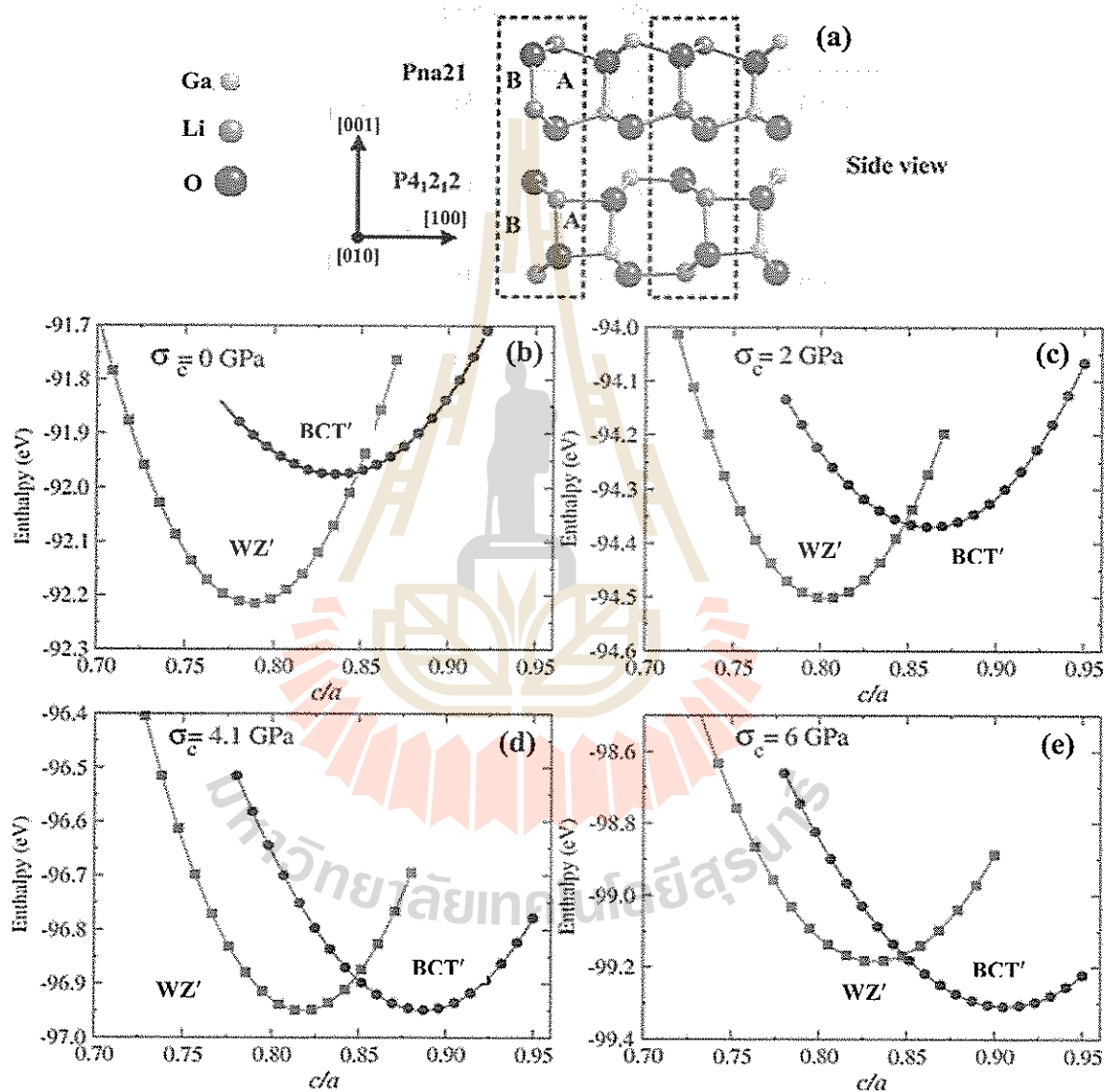


**Figure 4.10** (a) Schematic comparison of WZ' and BCT' LGO structures. Enthalpy (eV) as a function of  $c/a$  for  $b/a = 0.848$  at different tensile stresses: (b)  $\sigma_c = 0$  GPa, (c)  $\sigma_c = 2$  GPa, (d)  $\sigma_c = 4.1$  GPa and (e)  $\sigma_c = 6$  GPa.

**Table 4.3** Lattice parameters for the tetragonal P4<sub>1</sub>2<sub>1</sub>2 (BCT') LGO under tensile loading along [001] direction for  $\sigma_c = 0, 2, 4.1$  and 6 GPa.

Parameters	BCT'			
	$\sigma_c=0$ GPa	$\sigma_c=2$ GPa	$\sigma_c=4.1$ GPa	$\sigma_c=6$ GPa
$a$ (Å)	6.476	6.442	6.382	6.364
$b$ (Å)	5.406	5.377	5.327	5.313
$c$ (Å)	5.406	5.485	5.647	5.738
$V$ (Å <sup>3</sup> /f.u.)	47.32	47.50	47.97	48.50
$c/a$	0.835	0.852	0.885	0.902

# **CHAPTER V**

## **REDUCED OVERPOTENTIALS FOR**

### **ELECTROCATALYTIC WATER SPLITTING OVER**

#### **MODIFIED BaTiO<sub>3</sub>**

This chapter covers the computation work on BaTiO<sub>3</sub> as a catalyst for electrocatalytic water splitting after modified by Fe and Ni doping. The work has been publicized in the publication form (Artrith et al., 2016) and is reproduced here for the completeness of the thesis.

#### **5.1 Introduction**

Water splitting into oxygen and hydrogen gas is an attractive technology for the production of renewable alternative fuels (Kudo and Miseki, 2009), especially in combination with fuel cells (Suntivich et al., 2011). At standard conditions, the ideal voltage for the net water splitting reaction is 1.23 V, which is the potential difference between the anodic oxygen evolution reaction (OER; water oxidation) and the cathodic hydrogen evolution reaction (HER; water reduction). The OER half reaction that involves four elementary charge-transfer steps is, however, typically associated with large overpotentials and thus catalysts are required to increase the energy efficiency (McCrary et al., 2013). While photocatalytic water splitting

(i.e., driving the reaction by light-induced currents) is appealing, it requires catalysts with simultaneous activity for both OER and HER that at the same time also absorb light in the visible spectrum (Kudo and Miseki, 2009). Electrocatalytic water splitting (water electrolysis), on the other hand, allows the individual tuning of the cathode and anode material so that generally greater energy efficiency can be achieved. Unfortunately, the most efficient and stable known OER catalysts rely on rare and expensive Pt and noble metal based alloys (Cui et al., 2013; Gupta et al., 2009) rendering a global fuel economy based on water electrolysis nonviable.

On the search for inexpensive, earth-abundant, and environmentally benign alternatives for Pt-group catalysts, perovskite oxides have emerged as a promising class of materials (Royer et al., 2014). Owing to their tunable electronic properties, perovskite-based materials are among the most efficient known photocatalysts for water splitting (Kudo and Miseki, 2009; Suntivich et al., 2011; Castelli et al., 2012; Luo et al., 2014). Recently, an improved understanding of the electronic-structure/reactivity relationship has further spurred the interest in perovskites as inexpensive catalysts for water electrolysis (Mefford et al., 2016). Motivated by this new insight, we explore in the present article to which extent the catalytic reactivity of barium titanate ( $\text{BaTiO}_3$ ) can be controlled by slightly altering its chemical composition.

$\text{BaTiO}_3$  is one of the most thoroughly investigated ferroelectric oxides and is used in diverse technical applications as piezoelectric material, dielectric ceramic, and as crystal in non-linear optics. As catalyst, Ni-supported  $\text{BaTiO}_3$  is active for  $\text{CO}_2$  reforming (Hayakawa et al., 1999), and also water electrolysis over  $\text{BaTiO}_3$  electrodes

has been reported (Kennedy and Frese, 1976; Nasby, 1976). Interestingly, in some cases small compositional modifications by introducing transition-metal dopants on the Ti site (the *B* site in the general  $ABO_3$  perovskite formula) have been found to increase the catalytic activity of  $BaTiO_3$  significantly. For example, Pd-modified  $BaTiO_3$  efficiently catalyzes  $NO_x$  reduction (Rodríguez et al., 2010), and Cr-modified  $BaTiO_3$  catalyzes the reduction of nitrobenzene and aniline (Srilakshmi et al., 2016). A strong impact of compositional modification on the catalytic activity has also been reported for other oxide, such as Ruddlesden-Popper oxides (Lee et al., 2014) and carbides (Wannakao et al., 2015), which opens up exciting opportunities for the design of improved catalysts based on well-known and abundant materials. Since  $BaTiO_3$  is both inexpensive and non-toxic,  $BaTiO_3$ -based catalysts for water electrolysis would be highly desirable. The oxides of  $d^0$  transition metals, especially Ti and Zr oxide, are known to catalyze the water splitting reaction (Kudo and Miseki, 2009). However, apart from having a small overpotential for water oxidation, a suitable anode material for water splitting must also be electrically conducting and has to be chemically stable with respect to dissolution/corrosion and surface poisoning at operation conditions.

Pristine  $BaTiO_3$  is a wide band gap (3.2-3.4 eV) (Wemple, 1970) semiconductor, and poor electrical conductivity was measured at conditions for catalytic methanol oxidation (Popescu et al., 2011). In view of the existing  $BaTiO_3$ -based catalysts, our strategy for narrowing or closing the band gap is to introduce transition metals with non-empty *d*-bands on the *B* site. For this study, we consider Ni- and Fe-modified  $BaTiO_3$ . We are interested in Ni doping because  $BaNiO_3$  is known to be catalytically active for OER (Lee et al., 2016), but it forms in a

hexagonal structure (Takeda, 1976), not in tetragonal ( $P4mm$ ) structure favored by  $BaTiO_3$  at room temperature, so that Ni doping might thermodynamically not be feasible. On the other hand,  $BaFeO_3$  forms in the cubic perovskite structure (Hayashi et al., 2011), which is the stable  $BaTiO_3$  structure at temperatures above  $120^\circ\text{C}$ , i.e., at solid-state synthesis condition (Luspin et al., 1980).  $BaFeO_3$  is additionally more likely to form a solid solution with  $BaTiO_3$  because of the similar ionic radius of  $Fe^{4+}$  and  $Ti^{4+}$  (58.5 pm and 60.5 pm, respectively (Shannon, 1976)).

In the case of lanthanum-based perovskite, the catalytic activity was found to vary strongly with the surface coverage (Lee et al., 2015). Thus, to determine the  $pH$  and potential dependent surface phases and to estimate the stability of  $BaTiO_3$  at the conditions required for water electrolysis, we further determine computational Pourbaix diagrams and surface phase diagrams.

In the following methods section, we will provide a brief overview of the computational setup and the techniques used. In the results section, we first establish the energetics of Fe and Ni doping and their effect on the electronic structure and the band gap of  $BaTiO_3$ . Next, the most stable  $BaTiO_3$  surface phases at catalytic conditions are determined before evaluating the reaction free energies for water oxidation over pristine and Fe/Ni-modified  $BaTiO_3$  surfaces. Finally, the computational results are critically examined in the discussion section.

## 5.2 Methods

Density-functional theory (DFT) calculations were used to obtain first-principles predictions of phase stability, adsorption energies, and electronic structure properties. To obtain reasonable band-gaps, electronic density of states (DOS)

calculations of Fe and Ni-doped BaTiO<sub>3</sub> bulk structures were carried out using Hubbard-U corrected DFT (DFT+U) calculations in the rotationally invariant approximation (Liechtenstein et al., 1995; Anisimov et al., 1997). The U parameters for Fe and Ni *d* electrons were 4.0 eV and 6.0 eV, respectively, following the parametrization by Jain et al. (Jain et al., 2011). All DOS calculations employed the Perdew-Burke-Ernzerhof (PBE) exchange-correlation functional (Jain et al., 2011) and projector-augmented wave (PAW) (Blöchl, 1994) pseudopotentials as implemented in the Vienna Ab Initio Simulation Package (VASP) (Kresse and Furthmüller, 1996(a); Kresse and Furthmüller, 1996(b)), and the cutoff for plane wave expansions was 520 eV. Energies and forces were converged to 0.05 meV per atom and 50 meVÅ<sup>-1</sup>, respectively. For geometry and cell optimizations of bulk structures, k-point meshes with a density of 1000 divided by the number of atoms were employed, which corresponds to a 6 × 6 × 6 mesh for the primitive BaTiO<sub>3</sub> unit cell. Three times finer k-point meshes were used to converge the DOS. Structure enumerations were done based on the method by Hart and coworkers (Hart et al., 2012; Hart and Forcade, 2009) using the Python Materials Genomics (pymatgen) tool (Ong et al., 2013). Examples of bulk structures for pristine and modified BaTiO<sub>3</sub> are shown in Figure 5.1. Pourbaix diagrams, surface phase diagrams, and reaction free energy profiles were calculated with the DFT implementation in the FHI-aims software (Blum et al., 2009). FHI-aims uses local basis sets of numeric atomic orbitals for the representation of wavefunctions, which is more efficient than plane waves for surface models. To obtain accurate adsorption energies, these calculations employed the revised PBE functional (RPBE) by Nørskov et al. (Hammer et al., 1999) which has been widely used in the area of computational catalysis and



improves the accuracy of adsorbant binding energies compared to PBE (Wannakao et al., 2015; Hammer et al., 1999). In addition, the method by Tkatchenko and Scheffler (Tkatchenko and Scheffler, 2009) was used to correct for the missing van der Waals interaction on this level of DFT. All FHI-aims calculations further included relativistic corrections on the level of the Atomic ZORA approximation (van Lenthe et al., 1994).

For optimal computational efficiency, geometry optimizations with FHI-aims employed the predefined light basis set (4<sup>th</sup> order expansion of the Hartree potential, radial integration grids with 302 points in the outer shell, and a tier 1 basis set). Structural energies were subsequently refined with the tight basis set (6<sup>th</sup> order expansion, 434 grid points, and a tier 2 basis). All of these calculations employed k-point meshes corresponding to  $8 \times 8 \times 8$  for the BaTiO<sub>3</sub> bulk structure.

At room temperature BaTiO<sub>3</sub> crystallizes in a tetragonal structure (space group *P4mm*) in which the atoms are slightly displaced from their sites in the ideal symmetric cubic (*Pm3m*) perovskite structure (Harada et al., 1970). This atomic displacement results in ferroelectric polarization parallel to the (001) plane. In this work we consider the non-polar (001) surface (Padilla and Vanderbilt, 1997).

Symmetric surface slab models with a surface area of  $2 \times 2$  surface unit cells and a thickness of 6 atomic layers were used to model adsorption of OER reaction intermediates and hydrogen on BaTiO<sub>3</sub> surfaces. The lower 4 layers of the slabs were kept fixed at the bulk atomic positions, and the topmost 2 layers were fully relaxed. Examples of surface slab models are shown in Figure 5.1(d).

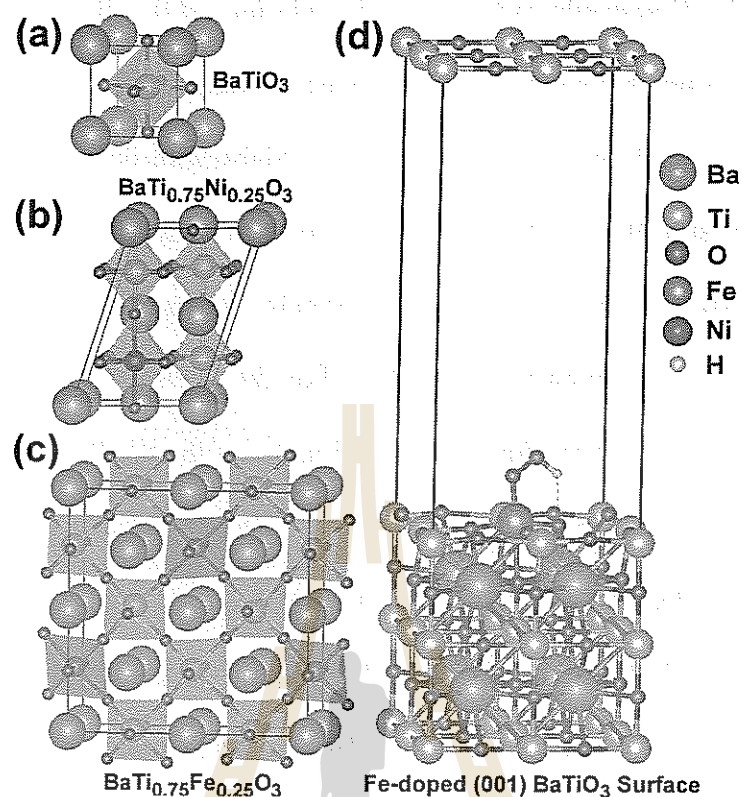


**Figure 5.1** Bulk structure models for (a)  $\text{BaTiO}_3$  (b)  $\text{BaTi}_{0.75}\text{Ni}_{0.25}\text{O}_3$ , and (c)  $\text{BaTi}_{0.75}\text{Fe}_{0.25}\text{O}_3$ . The structures of the Ni- and Fe-doped compositions were determined by enumeration as described in the text. (d) Example of a Fe-modified  $\text{TiO}_2$ -terminated  $\text{BaTiO}_3$  (001) surface slab model with adsorbed  $\text{*OOH}$ . The structure models were visualized using the VESTA software (Momma and Izumi 2011).

At  $120^\circ\text{C}$ ,  $\text{BaTiO}_3$  undergoes a phase transition to the cubic ( $Pm3m$ ) perovskite structure, which is thus the relevant structure at synthesis conditions. To estimate the feasibility of Ni and Fe incorporation, we therefore considered the formation energy of mixed compositions in the cubic structure.

### 5.2.1 Water adsorption and dissociation on BaTiO<sub>3</sub> surfaces

To study the surface, we employed the unit cell formulas Ba<sub>12</sub>Ti<sub>8</sub>O<sub>28</sub> for BaO surface and Ba<sub>8</sub>Ti<sub>12</sub>O<sub>32</sub> for TiO<sub>2</sub> surface. Slabs with defect surfaces, i.e., for BaO surface we substituted a Ba atom on the top layer with a transition metal *A* (*A* = Be, Bi, Ge, Mg, Na and Sr) and the formula becomes *ABa*<sub>11</sub>Ti<sub>8</sub>O<sub>28</sub>. The atomic percentage of the impurity is 2.08%. For the TiO<sub>2</sub> terminate surface, an oxygen vacancy as well as a substitution of a Ti atom on the top layer (at the center of TiO<sub>2</sub> surface) by a transition metal *B* (*B*= Co, Cu, Fe, Mn and Ni) where formula becomes *BBa*<sub>7</sub>Ti<sub>12</sub>O<sub>32</sub> are studied. The atomic percentage of the impurity is 1.92%.

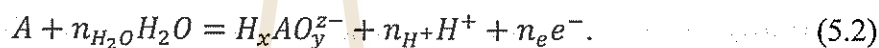
To study the absorption of WM, a WM was placed on top of a two-unit-cell surface in scanned different initial configurations positions for all surfaces following Figure 3.4 and the most favorable absorption is reported. The absorption energy (Li et al., 2014) was calculated from following equation.

$$E_{\text{ads}}(\text{H}_2\text{O}) = E_{\text{tot}}(\text{free slab}, n) + E_{\text{tot}}(\text{H}_2\text{O}) - E_{\text{tot}}(\text{slab} + \text{water}, n), \quad (5.1)$$

where  $E_{\text{tot}}(\text{free slab}, n)$  is the total energy of the optimized ferroelectric *n*-layer bare slab (e.g. without water),  $E_{\text{tot}}(\text{H}_2\text{O})$  the total energy of the free water molecule and  $E_{\text{tot}}(\text{slab} + \text{water}, n)$ , the total energy of the optimized *n*-layer slab with one H<sub>2</sub>O water adsorbed (1/4ML).

## 5.2.2 Pourbaix and surface-phase diagrams

Pourbaix diagrams map the preferred states of an electrochemical system in equilibrium as function of the electrochemical potential and the  $pH$  value and, thus, allow in the context of this work to predict whether an oxide is stable or if dissolution is thermodynamically favorable. To estimate the stability of the catalyst at operation conditions, we computed Pourbaix and  $pH$ /potential-dependent surface phase diagrams. The Pourbaix diagram for a chemical species  $A$  is constructed by considering all relevant electrochemical equilibria of  $A$  in aqueous solution



Following the Nernst equation, the free energy of the aqueous species, ( $H_xAO_y^{z-}$ ), relative to a free atom of species  $A$  can then be estimated as

$$\Delta G = \Delta G_{SHE}^0 - n_e(eU_{SHE}) - 2.3n_H kT pH + kT \ln a_{H_xAO_y^{z-}}, \quad (5.3)$$

where  $\Delta G_{SHE}^0$  is the free energy relative to the standard hydrogen electrode (SHE) at standard ambient conditions,  $eU_{SHE}$  is the energy due to the electrochemical potential  $U_{SHE}$  relative to the SHE,  $a_{H_xAO_y^{z-}}$  is the activity,  $k_B$  is Boltzmann's constant, and  $T$  is the temperature (for a derivation see reference (Rong and Kolpak, 2015)). Note that the factor of 2.3 in front of the  $pH$  arises from the approximate conversion of the natural to the common logarithm.

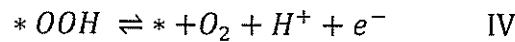
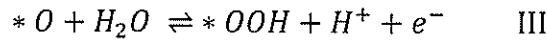
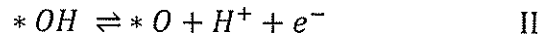
The relevant electrochemical equilibria for Ba and Ti are shown in Table 5.1. Since uncorrected DFT energies are not sufficiently accurate to predict reliable Pourbaix diagrams (Persson et al., 2012), measured values of the relative free energies at standard conditions,  $\Delta G^\circ$ , were obtained from thermochemical tables (Wagman et al., 2011). However, DFT surface-slab calculations were employed to evaluate the

adsorption energy of reaction intermediates on the BaTiO<sub>3</sub> surface and the defect formation energies for the creation of surface Ba, Ti, or O vacancies

$$\Delta G_{reference} \approx E_{recon.}^{DFT} - E_{idel.}^{DFT} + \Delta G_{ads.} \quad (5.3)$$

where  $E_{idel.}^{DFT}$  and  $E_{recon.}^{DFT}$  are the energies of the ideal and the reconstructed surfaces, and  $\Delta G_{ads.}$  is the free energy change of the adsorbants. Combining these DFT energies with the solvation free energies from Table 3.1, the stable surface phases at different pH values and electrochemical potentials were determined. A detailed description of the approach can be found in the work by Rong and Kolpak (Rong and Kolpak, 2015). As is commonly done (Norskov et al., 2004), the binding energy of O<sub>2</sub> was referenced to the energy of a water molecule in the gas phase,  $\frac{1}{2}E^{O_2} = E^{H_2O} - E^{H_2}$  because of the large DFT error for molecular oxygen.

To estimate the stability of the catalyst at operation conditions, we computed Pourbaix and pH/potential- dependent surface phase diagrams. We consider the catalytic oxygen evolution reaction (OER) by water oxidation in four elementary reaction steps each involving the transfer of a single electron-proton pair (Norskov et al., 2004):



The reaction free energies of these charge transfer steps at the ideal equilibrium potential ( $U = 1.23\text{V}$ ) determine the overpotential  $\eta$  that is required to drive the overall reaction.

**Table 5.1** Relative free energies of species occurring in the Ba and Ti Pourbaix diagrams at standard ambient conditions ( $25\text{C}^\circ$  and 1bar). The free energies relative to the standard hydrogen electrode (SHE),  $\Delta G^0_{\text{SHE}}/\text{eV}$ , were taken from reference (Donald et al., 1982). All activities  $a_A$  were taken to be equal to  $10^{-8}$  M.

A	Aqueous species	$\Delta G^0_{\text{SHE}}/\text{eV}$	$\Delta G_2/\text{eV}$
	$\text{Ba}^{2+}$	-5.81	$-2eU_{\text{SHE}} + 0.026\ln a_{\text{Ba}^{2+}} - 5.81$
Ba	$\text{Ba}(\text{OH})^+$	-5.11	$-2eU_{\text{SHE}} - 0.059\text{pH} + 0.026\ln a_{\text{Ba}(\text{OH})^+} - 5.11$
	$\text{BaO}_2(\text{s})$	-1.08	$-4eU_{\text{SHE}} - 0.236\text{pH} - 1.08$
	$\text{TiO}_2(\text{s})$	-3.91	$-4eU_{\text{SHE}} - 0.239\text{pH} - 3.91$
Ti	$\text{TiO}_2^{2+}$	0.59	$-6eU_{\text{SHE}} - 0.239\text{pH} + 0.026\ln a_{\text{TiO}_2^{2+}} + 0.59$
	$\text{Ti}^{2+}$	-3.63	$-2eU_{\text{SHE}} + 0.026\ln a_{\text{Ti}^{2+}} - 3.63$
	$\text{H}_2\text{O}$	0	$2eU_{\text{SHE}} + 0.118\text{pH}$ [ $\text{H}_2\text{O}(\text{l})/\text{H}_2(\text{g})$ as reference]
O	$\text{H}_2\text{O}$	-2.46	$2eU_{\text{SHE}} + 0.118\text{pH} - 2.46$ [ $\text{O}_2(\text{g})$ as reference]

Using the computational standard hydrogen electrode (CSHE) (Ke et al.1998) approach, the reaction free energy  $\Delta G$  of the charge transfer reaction  $AH \rightleftharpoons A + H^+ + e^-$  at standard conditions ( $U = 0$  V,  $pH = 0$ ,  $p = 1$  bar,  $T = 298.15$  K) can be related to the reaction  $AH \rightleftharpoons A + \frac{1}{2}H_2$ . The reaction free energies of the individual charge transfer steps,  $\Delta G_I$ ,  $\Delta G_{II}$ ,  $\Delta G_{III}$ , and  $\Delta G_{IV}$ , were approximated as

$$\Delta G_i = \Delta E_i + \Delta ZPE_i - T\Delta S_i - eU, \quad (5.5)$$

where  $\Delta E_i$  was obtained as difference of DFT energies, and the zero-point energy (ZPE) difference,  $\Delta ZPE_i$ , and the vibrational entropy contributions,  $T\Delta S_i$ , were taken from Valdeś et al. (Valdeś et al., 2008) (see Table 3.1). The final term in Eq. 5.5 accounts for the electrode potential  $U$  ( $e$  is the elementary charge). For a given catalyst, the overpotential is thus given by the smallest potential  $\eta$  such that for  $U = 1.23$  V +  $\eta$  all reaction steps are exothermic, i.e.,  $\Delta G_i \leq 0$ . As in the case of surface Pourbaix diagrams, the binding energy of molecular  $O_2$  was referenced to the energy of water.

## 5.3 Results

### 5.3.1 Water molecule adsorption and dissociation on BaTiO<sub>3</sub> surfaces

The most favorable structures of 1/4-monolayer adsorption (1/4ML) on the BaO-terminated surface which is doped by a metal (Sr, Be, Mg, Bi, Na and Ge) and on the TiO<sub>2</sub>-terminated surface which is doped by a transition metal (Ni, Cu, Co, Mn and Fe) were calculated and used to study how water molecule (WM) adsorb in a low vapor pressure conditions. The calculated results are shown in Figure 5.3. In the metal-doped BaO-terminated surface, the adsorbed WM is strongly distorted after geometry optimizations. The calculated adsorption energies are varied between 1.22 and 2.03 eV. The distance between the hydrogen of the water molecule and the surface oxygen (OH<sub>s</sub>) are in the range of 1.01-1.03 Å. The length of the hydrogen bonding with the oxygen in water molecule (OH<sub>w</sub>) are extended to around 1.50-1.59 Å. The summaries of bond distance are shown in Figure 5.4(b), indicating that one of the H atom in the water molecule moves to the surface oxygen, forming an OH hydroxyl. The alignment of the OH<sub>s</sub> is parallel to the direction of the polarization of BaTiO<sub>3</sub>. This phenomena is called the water dissociation, the model is shown in Figure 5.2(b). Interestingly, in the case of Mg and Be-doped BaO-terminated surface, the adsorption energies are increased from the BaO-terminated ( $E_{\text{ads}}/\text{eV}= 1.41$ ) to  $E_{\text{ads}}/\text{eV}= 2.03$  and 1.45, respectively. WM adsorptions on transition metal-doped TiO<sub>2</sub>-terminated surfaces were also studied. The most favorable structures are shown in Figure 5.3. The calculated adsorption energies are varied between 0.68 – 1.31 eV. Unlike the adsorption on the metal-doped BaO terminated surfaces, here, the WM maintains its initial configuration with the molecular plane aligned parallel to the surface plane, i.e., sitting on top of the Ti atom and the transition metals. The bond



length of the  $\text{OH}_s$  are in the range of 1.50 -2.10 Å and that of the  $\text{OH}_w$  are 0.98- 1.06 Å as shown in Figure 5.4(c). The WM maintains its molecular state. This phenomena is called the water adsorption, the model is shown in Figure 5.2(c). For all the surfaces with doped transition metals the adsorption energies of WM are higher than that of the bare  $\text{TiO}_2$ -terminated surface ( $E_{\text{ads}}/\text{eV}= 0.68$ ). Especially, in the case of Ni-doped surface, the calculated adsorption energy of WM is 1.31 eV which is 48% higher than that of the bare surface. The calculated molecular adsorption energies of WM ( $E_{\text{ads}}$ ) are shown in Figure 5.3.

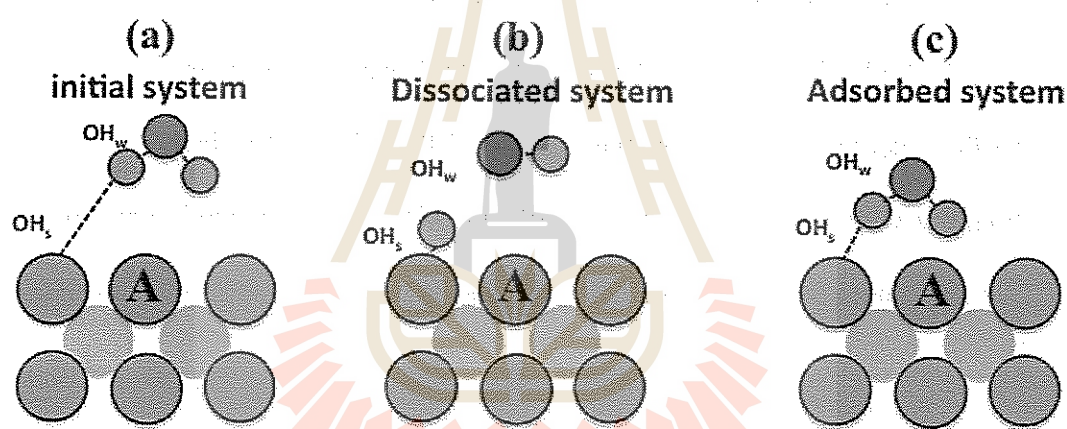


**Figure 5.2** Schematic illustration of the most favorable structure of 1/4-monolayer adsorption (1/4 ML) on the  $\text{BaTiO}_3$ -surfaces: (a) initial configuration, (b) the case with dissociated WM and (c) the case with adsorbed WM without WM dissociation.

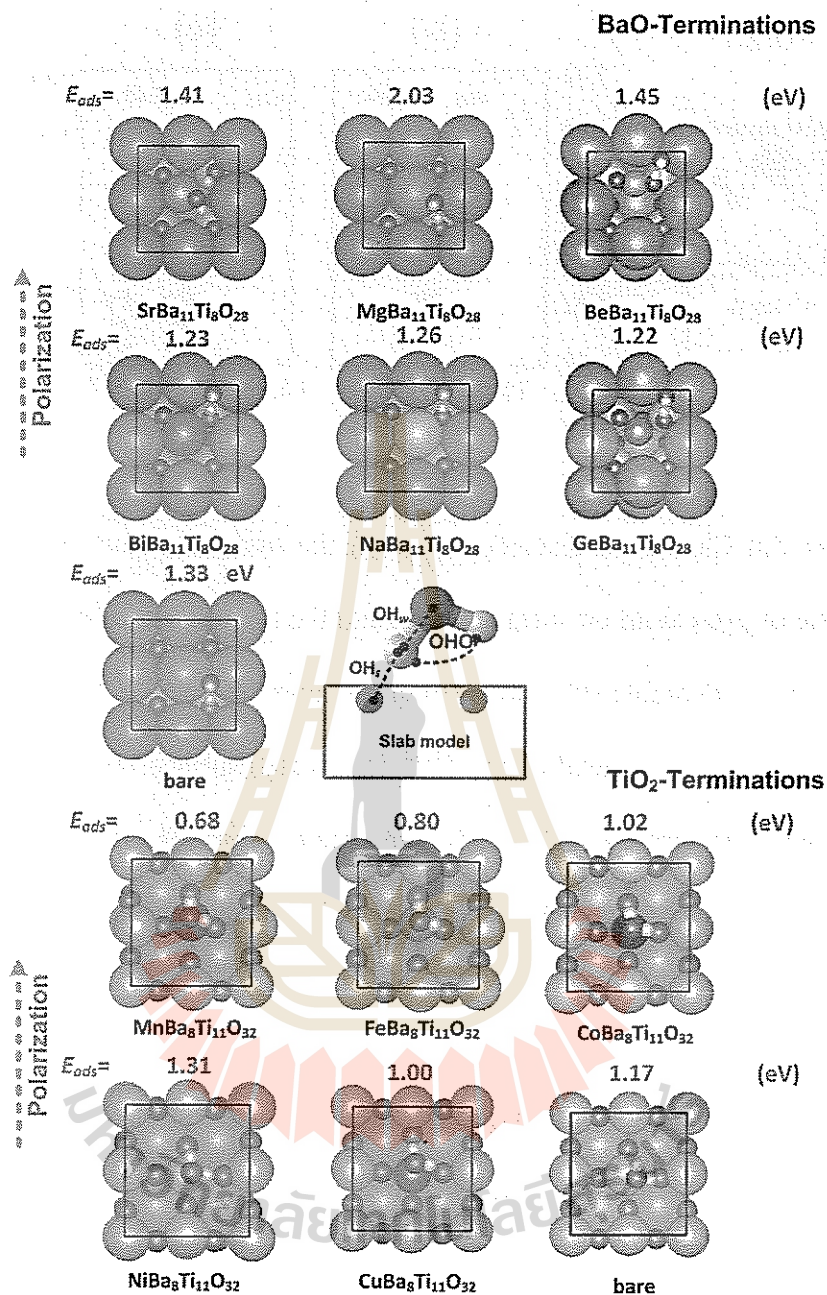


**Figure 5.3** Schematic illustrations of the most favorable structures of 1/4-monolayer adsorption (1/4ML) on the metal-doped BaO-terminated and transition metal-doped TiO<sub>2</sub>-terminated surfaces. The adsorption energies ( $E_{ads}/\text{eV}$ ) are also shown.

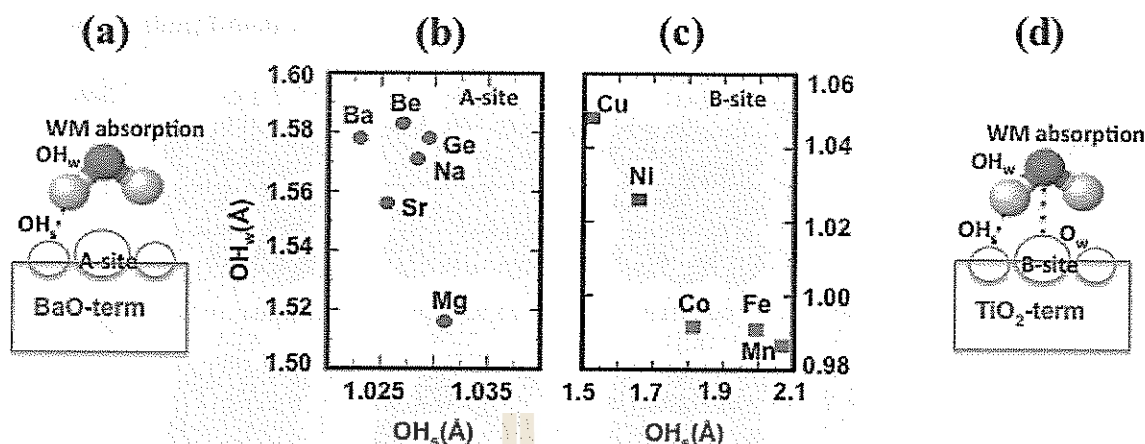


**Figure 5.4** Calculated distances between the hydrogen atom of the water molecule and the oxygen atom on surface ( $\text{OH}_s$ ) and the bondlength of the  $\text{O-H}_w$  in WM for all of the most favorable structures, (b) on the metal-doped BaO terminated surface, and (c) on the transition metal-doped  $\text{TiO}_2$ -terminated surface. (a) and (d) Models of 1/4-monolayer adsorption (1/4 ML) on the metal-doped BaO-terminated on *A*-site and transition metal-doped  $\text{TiO}_2$ -terminated on *B*-site, respectively.

### 5.3.2 Volcano of $\text{BaTiO}_3$ activity

In this section, the framework of the thermodynamic over potential methods (described in detailed in Section 3.3.4) is utilized to construct the OER volcanoes and predict the OER activities on (001) BaO and  $\text{TiO}_2$  surfaces of perovskite  $\text{BaTiO}_3$ . Figure 5.5 shows  $-\eta^{\text{OER}}$  as a function of  $\Delta G_{\text{O}^*}^0 - \Delta G_{\text{HO}^*}^0 / \text{eV}$  for the classes of the systems studied here. This leads to a universal volcano relationship for the unit cell formulas  $\text{Ba}_{12}\text{Ti}_8\text{O}_{28}$  for BaO surface and  $\text{Ba}_8\text{Ti}_{12}\text{O}_{32}$  for  $\text{TiO}_2$  surface. In the case of BaO-terminated surfaces, the relative overpotentials ( $\eta^{\text{OER}}/V$ ) of bare and all metal-doped surfaces follow the order of bare (0.57 V) < Sr (0.68 V) < Be (0.69 V) < Mg

(0.83 V) < Na (0.86 V) < Bi (1.47 V) < Ge (1.78 V); indicating that bare BaO surface has the lowest overpotential. Similarly, for the case of TiO<sub>2</sub>-terminated surfaces, the relative overpotential ( $\eta^{\text{OER}}/V$ ) of bare and transition metal-doped surfaces follow the order of Ni (0.89 V) < Fe (0.91 V) < Co (1.19 V) < Cu(1.19 V) < bare (1.22 V); indicating that Ni- and Fe-modified TiO<sub>2</sub>-terminated can increase the efficiency of BaTiO<sub>3</sub> catalysis activity on OER by decreasing the overpotential of BaTiO<sub>3</sub>. The summary of free energy path, based on four electron paths, represents the overpotentials ( $\eta^{\text{OER}}$ ) for the transition metal-doped TiO<sub>2</sub>-terminated and the metal-doped BaO-terminated and the free energies at the standard conditions ( $pH = 0$ ,  $T=298.15$  K) and  $U= 0$  V are shown in Table 5.2 and 5.3.

**Table 5.2** Summary of free energy path based on four electron paths representing the overpotentials ( $\eta^{\text{OER}}$ ) for the transition metal-doped TiO<sub>2</sub>-terminated surfaces and the free energies at the standard conditions ( $pH = 0$ ,  $T=298.15$  K) and  $U= 0$  V.

Terminated	$\Delta G^{\theta}_{\text{OH}^*}/\text{eV}$	$\Delta G^{\theta}_{\text{O}^*}/\text{eV}$	$\Delta G^{\theta}_{\text{OOH}^*}/\text{eV}$	$\Delta G^{\theta}_4/\text{eV}$	$\eta^{\text{OER}}/V$
Ideal	1.23	2.46	3.69	4.92	0
TiO <sub>2</sub> -clean	1.53	3.98	4.78	4.92	1.22
Co	0.50	2.93	2.96	4.92	1.19
Cu	2.02	4.45	3.14	4.92	1.19
Fe	0.25	2.38	3.86	4.92	0.91
Mn	-0.44	0.23	1.20	4.92	2.49
Ni	1.48	2.97	2.85	4.92	0.89

**Table 5.3** Summary of free energy path based on four electron paths representing the overpotentials ( $\eta^{\text{OER}}$ ) for the metal-doped BaO-terminated surfaces and the free energies at the standard conditions ( $p\text{H} = 0$ ,  $T=298.15$  K) and  $U= 0$  V.

Terminated	$\Delta G^{\circ}_{\text{OH}^*}/\text{eV}$	$\Delta G^{\circ}_{\text{O}^*}/\text{eV}$	$\Delta G^{\circ}_{\text{OOH}^*}/\text{eV}$	$\Delta G^{\circ}_4/\text{eV}$	$\eta^{\text{OER}}/\text{V}$
Ideal	1.23	2.46	3.69	4.92	0
BaO-clean	1.80	2.50	3.88	4.92	0.57
Mg	1.58	3.63	3.59	4.92	0.83
Sr	1.90	2.39	3.72	4.92	0.67
Be	1.61	2.28	4.21	4.92	0.69
Bi	-1.16	0.96	2.21	4.92	1.47
Ge	1.05	0.18	1.91	4.92	1.78
Na	2.09	2.27	4.08	4.92	0.86

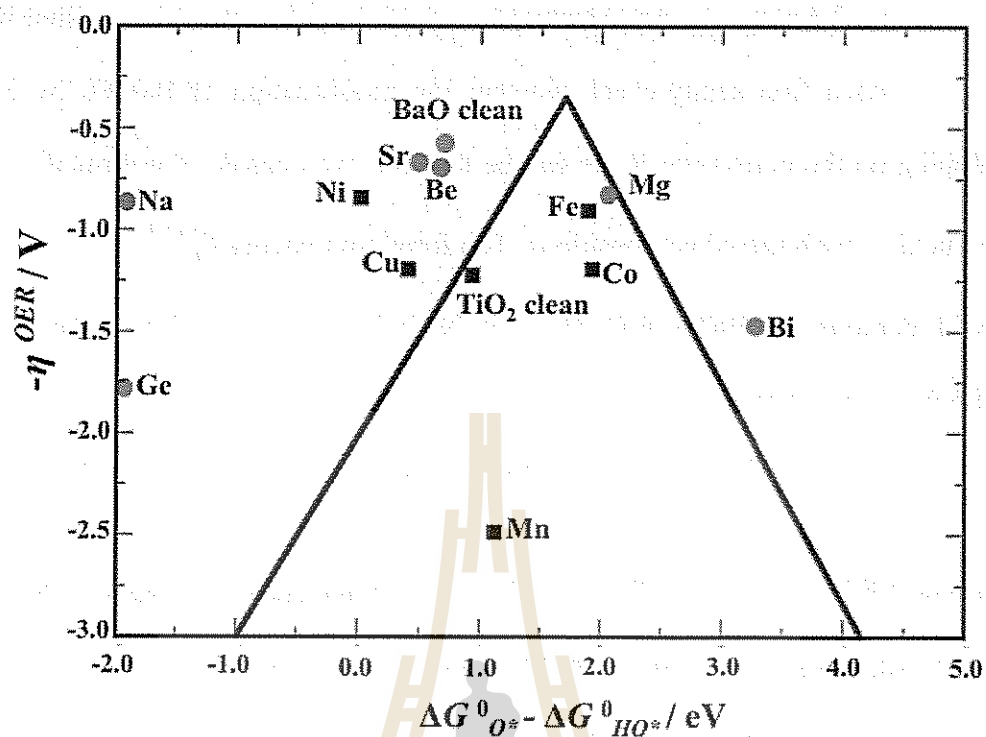


Figure 5.5  $-\eta^{\text{OER}}$  as a function of  $\Delta G^0_{\text{O}^*} - \Delta G^0_{\text{HO}^*}/\text{eV}$  for the classes of the surfaces studied. This leads to a universal volcano relationship, metal-doped BaO-terminated are shown by red circles and transition metal-doped  $\text{TiO}_2$ -terminated are shown by black squares.

### 5.3.3 Energetics and electronic structure of Fe- and Ni-modified BaTiO<sub>3</sub>

As a first sanity-check whether the modification of BaTiO<sub>3</sub> by Fe and Ni doping on the perovskite *B* site can be feasible, we consider the formation energy of structures with mixed compositions. The formation energy  $E_f^{\text{BaTi}_{1-x}\text{B}_x\text{O}_3}$  of a structure with composition BaTi<sub>1-x</sub>B<sub>x</sub>O<sub>3</sub> (B = Fe, Ni) relative to the end members BaTiO<sub>3</sub> and BaBO<sub>3</sub> is given by

$$E_f^{\text{BaTi}_{1-x}\text{B}_x\text{O}_3} = E^{\text{BaTi}_{1-x}\text{B}_x\text{O}_3} - (1-x)E^{\text{BaTiO}_3} - xE^{\text{BaBO}_3}, \quad (5.6)$$

where  $E^{\text{BaTi}_{1-x}\text{B}_x\text{O}_3}$ ,  $E^{\text{BaTiO}_3}$ , and  $E^{\text{BaBO}_3}$  are total energies obtained from (VASP) DFT calculations. With this definition, negative formation energies mean that doping with species *B* is facile. The thermodynamically stable compositions lie on the lower convex hull of all negative formation energies (Urban et al., 2016).

Figure 5.6 shows the formation energies of compositions with 25%, 50%, and 75% Ti replaced by species *B*. These compositions were chosen as a proxy for the general mixing energetics, as they can be realized with relatively small numbers of atoms. To ensure convergence to the correct configurational and electronic ground state, we enumerated all symmetrically distinct Ti/*B* arrangements in structures with unit cells containing up to 8 ABO<sub>3</sub> formula units (i.e., 40 atoms) using a technique developed by Hart and coworkers (Hart et al., 2012; Hart and Forcade, 2009).

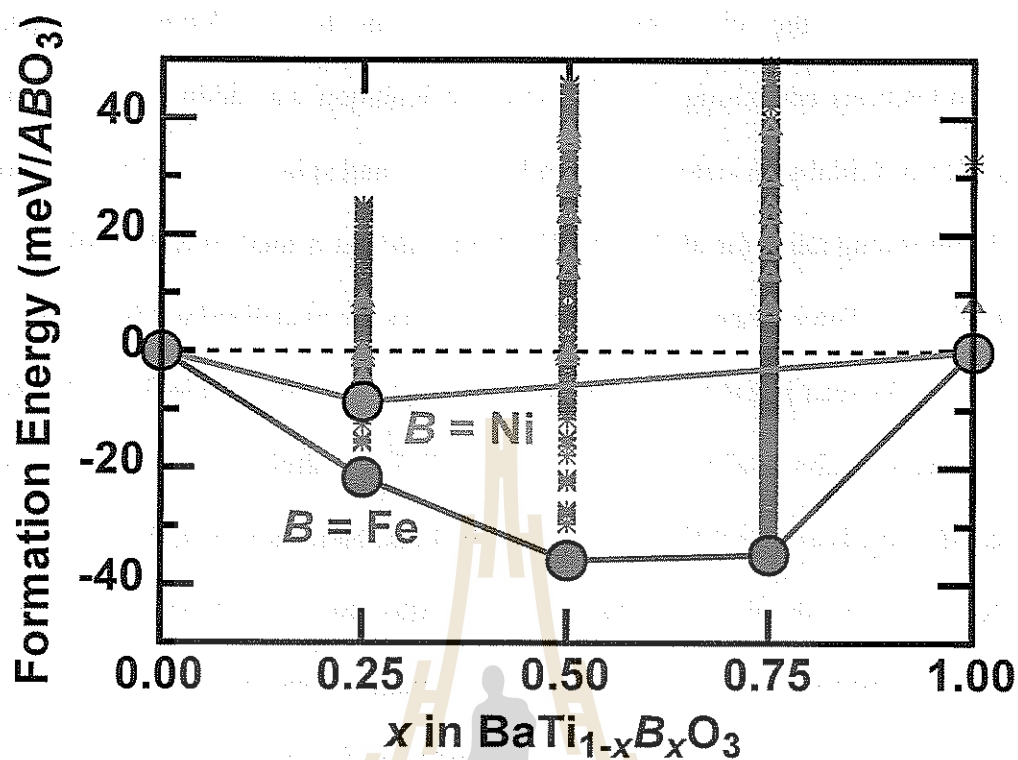


**Figure 5.6** Formation energies for  $\text{BaTi}_{1-x}\text{B}_x\text{O}_3$  with  $B = \text{Fe}$  (red) and  $B = \text{Ni}$  (blue) in the cubic and tetragonal perovskite structures obtained from enumeration of 826 distinct atomic configurations and spin orderings. The (high-temperature) cubic  $\text{BaTiO}_3$  structure was used as reference for the formation energy, so that negative formation energies mean that doping of  $\text{BaTiO}_3$  with species  $B$  is facile. The stable compositions are indicated by filled circles and connected by solid lines. 820 unstable and metastable structures are shown as red stars (Fe) and blue triangles (Ni).



Since the electronic convergence can be problematic (especially for compositions containing  $d^f$   $\text{Fe}^{4+}$ ), every calculation was additionally repeated with different initial spin states (low spin/high spin) and spin orderings (ferromagnetic and antiferromagnetic) for all Fe and Ni atoms, so that a total of 826 configurations are evaluated. The energies of all of these structures are visualized in Figure 5.6.

As seen in Figure 5.6, the negative formation energies indicate that Ni and Fe doping of cubic  $\text{BaTiO}_3$ , i.e., the stable  $\text{BaTiO}_3$  structure at solid-state synthesis conditions, is energetically favorable in the bulk. Note, however, that the reference for Ni doping in the figure is the (hypothetical) cubic  $\text{BaNiO}_3$  structure, whereas the thermodynamic ground state structure is actually hexagonal. The cubic reference is chosen as it allows to estimate the tendency for phase separation in the same structural framework, which is the relevant quantity when only small amounts of Ni are doped into  $\text{BaTiO}_3$ . The formation energies relative to the hexagonal  $\text{BaNiO}_3$  structure (not shown in the figure) are generally greater than  $0.2 \text{ eV}/\text{ABO}_3$ , which means that compositions with comparable Ti and Ni concentrations are thermodynamically unstable against phase separation into the parent perovskites. For Fe there is no such ambiguity regarding the reference structure, as  $\text{BaFeO}_3$  forms in the cubic perovskite structure. Hence, our calculations predict with reasonable certainty that mixed compositions containing Fe and Ti on the  $B$  site can be synthesized

The electronic density of states (DOS) was computed for the most stable structure at each composition to gain insight into the effect of compositional modification on the electronic structure and conductivity. The results are visualized in Figure 5.7. Note that the band gap of  $\text{BaTiO}_3$  predicted by our GGA calculations ( $1.7$

eV) is significantly smaller than the band gap observed in optical absorption and electroabsorption measurements (3.2– 3.4 eV) (Wemple, 1970). For transition metals with non-empty  $d$  bands, this error can be expected to be even larger, so that a Hubbard-U correction was employed for Fe and Ni, as described in the *methods* section. The electronic ground state configuration of each Fe containing composition was found to be high spin with antiferromagnetic ordering, resulting in symmetric DOS plots, as seen in Figure 5.7(a). Since the  $d^4$  electronic configuration of  $\text{Fe}^{4+}$  might potentially favor Jahn-Teller distorted geometries, we accommodated for such distortions by breaking the symmetry of the initial structures. Substituting Fe for Ti results in narrowing of the band gap and in the creation of defect states, so that the material becomes metallic, which is in line with our expectations, as outlined in the introduction.

For the Ni containing compositions low spin configurations were found to be stable, which is not surprising for  $d^6 \text{Ni}^{4+}$ . However, structural distortions, possibly due to the difference in  $\text{Ti}^{4+}$  and  $\text{Ni}^{4+}$  ionic radii, resulted in a small net magnetic moment, breaking the symmetry of the DOS (Figure 5.7(b)). As in the case of the Fe compositions, mixed Ti/Ni compositions are predicted to be metallic. Hexagonal  $\text{BaNiO}_3$  whose DOS is shown at the very right is, on the other hand, a semiconductor.

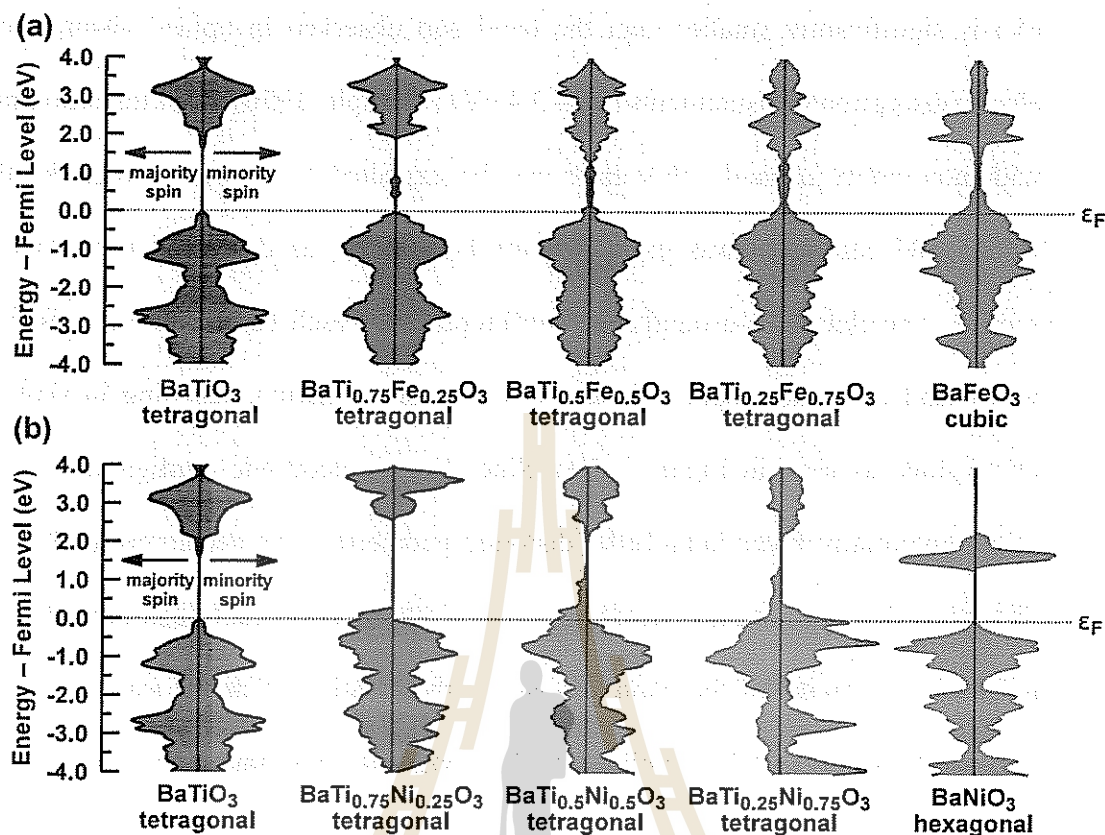


**Figure 5.7** Electronic density of states for pristine and (a) Fe-modified and (b) Ni-modified  $\text{BaTiO}_3$  compositions. The most stable structures of Figure 5.6 were used. For each structure, the majority spin density is shown to the left and the minority spin density to the right. All plots have been aligned at the Fermi level  $\epsilon_F$ . The cubic structure refers to space group  $\text{Pm}\bar{3}\text{m}$  ( $=O_h$ ) and the hexagonal structure belongs to the space group  $\text{P}6_3/\text{mmc}$ .

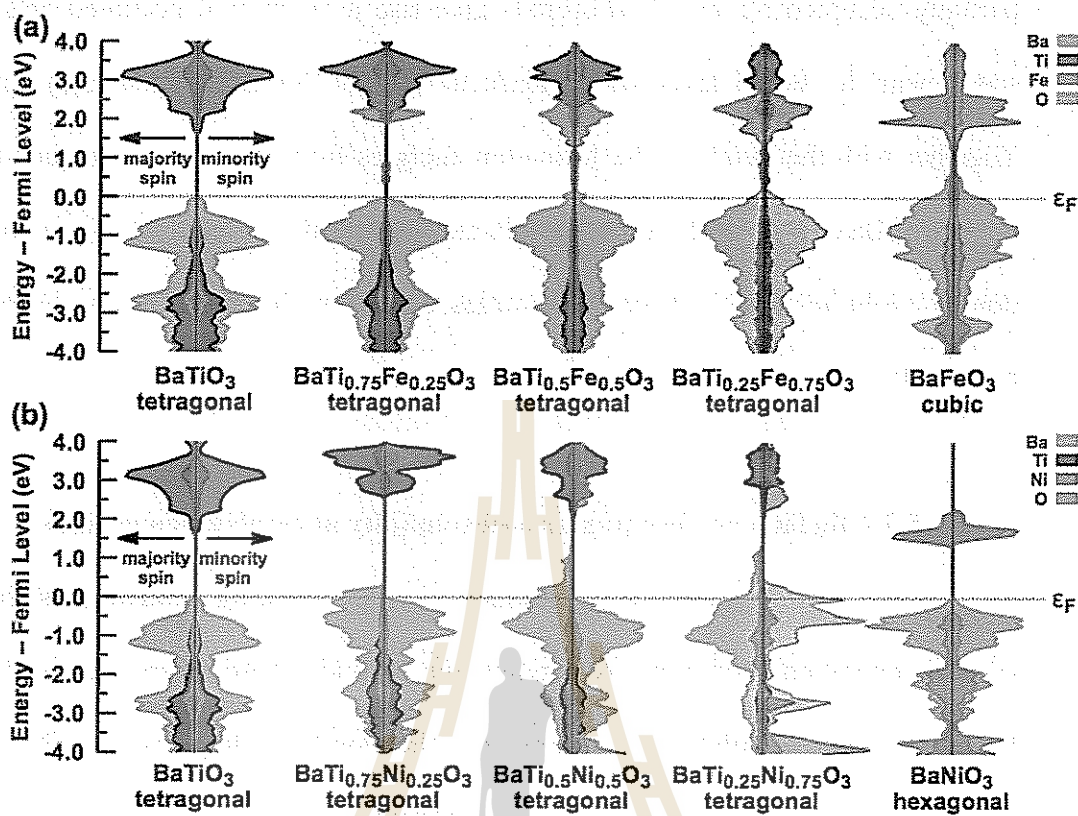


**Figure 5.8** Species-resolved electronic density of states (DOS) for pristine and (a) Fe-modified and (b) Ni-modified  $\text{BaTiO}_3$  compositions. This data was obtained as the sum of the orbital-projected partial DOS (PDOS) for all atoms of each atomic species. Note that the intensities depend on the chosen atomic radii (we employed VASP defaults). The structures are the same as in Figure 5.7.

By summation over the orbital-projected DOS for all atoms of each chemical species the species-resolved (partial) DOS was obtained (Figure 5.8). As seen in the figure, the valence band edge of  $\text{BaTiO}_3$  is dominated by oxygen states, and the occupied  $s$  and  $p$  Ti states contribute mostly to density that is more than 1 eV below the Fermi level. The conduction band is mostly given by the empty Ti  $d$  states. The

partially occupied Ni and Fe *d* orbitals give rise to additional occupied and vacant states near the Fermi level which leads to metallic (or semiconductive) behavior. Together with the trends in the formation energies from above, we conclude that Fe doping of BaTiO<sub>3</sub> is likely to be feasible and will result in electrical conductivity. Ni doping might be possible in small quantities, and Ni-modified BaTiO<sub>3</sub> is also likely to be metallic.

#### 5.3.4 BaTiO<sub>3</sub> surface phases and solubility at catalytic conditions

The most fundamental requirement for any working catalyst is stability at catalytic operation conditions. To estimate the *pH* and potential dependent stability of BaTiO<sub>3</sub> against dissolution, we computed the Pourbaix diagrams for Ba and Ti, corresponding to the BaO- and TiO<sub>2</sub>-terminated BaTiO<sub>3</sub> surfaces. The Pourbaix diagrams are shown in Figure 5.9 and 5.10. The relevant potentials for water oxidation are above the top dashed line that intersects  $U = 1.23$  V at *pH* = 0 in Figure 5.9 and 5.10. Further, water electrolysis over perovskite oxides is typically more efficient at alkaline conditions (Bockris and Otagawa, 1984), so that stability at high *pH* is most important. As seen in Figure 5.9, Ba favors dissolution at a wide range of *pH* values and potentials either as Ba<sup>2+</sup> or as BaOH<sup>+</sup>. Barium oxide is only stable at high potentials that are not relevant for (efficient) water electrolysis. Hence, it is unlikely that the BaO-terminated BaTiO<sub>3</sub> surfaces are stable at operation conditions.

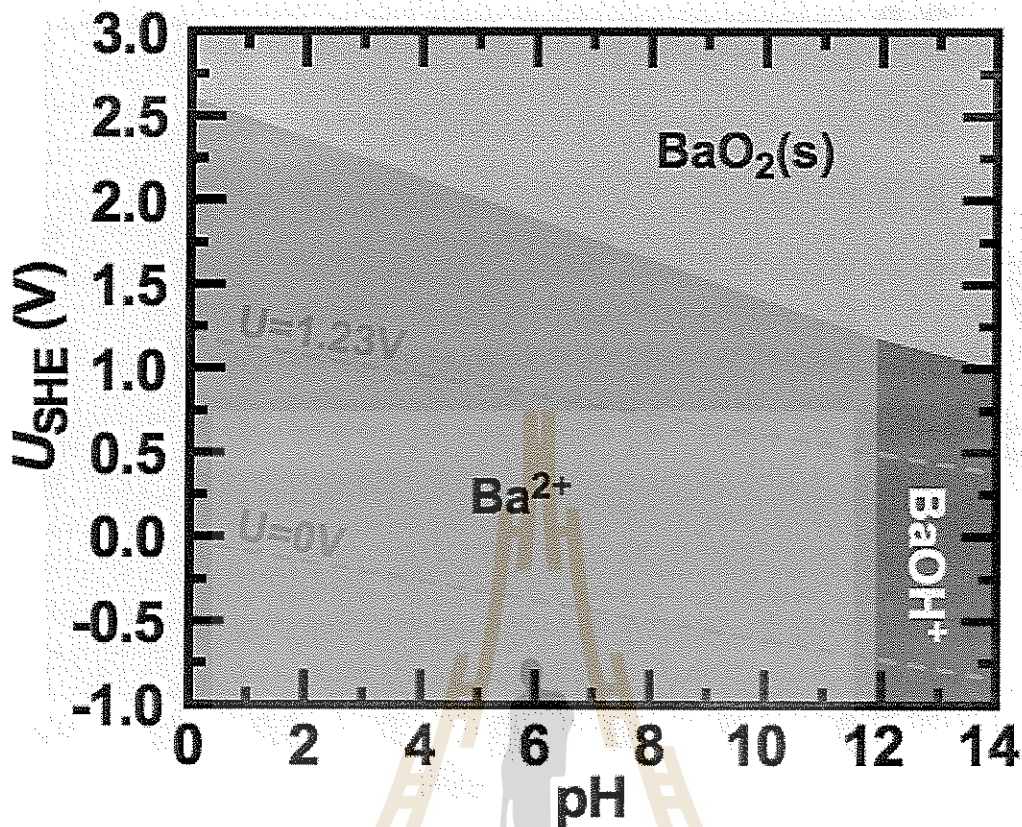


**Figure 5.9** Computed Ba Pourbaix diagram with an ionic concentration of  $10^{-8}$  M. The dashed orange lines indicate the potentials for water oxidation ( $2 H_2O \rightarrow O_2 + 4H^+ + 4e^-$ ,  $U = 1.23$  V at  $pH=0$ ) and reduction ( $4H^+ + 4e^- \rightarrow 2H_2$ ,  $U = 0$  V at  $pH=0$ ).

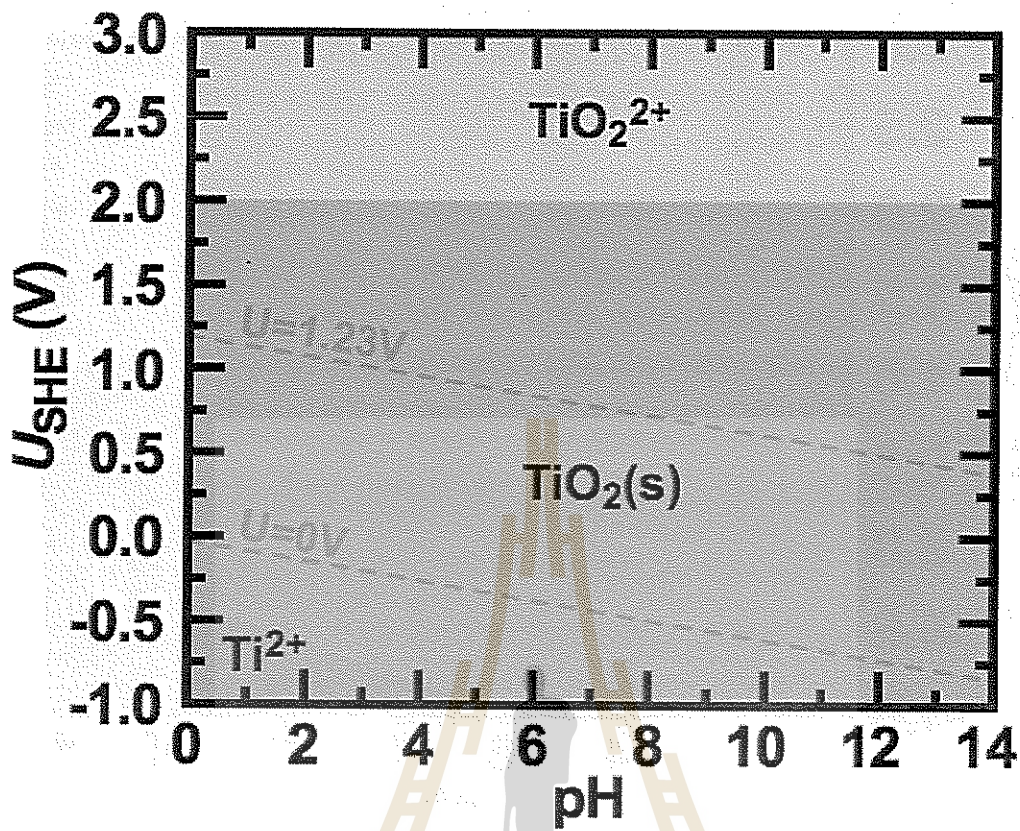


Figure 5.10 Computed Ti Pourbaix diagram with an ionic concentration of  $10^{-8}$  M. The dashed orange lines indicate the potentials for water oxidation ( $2 H_2O \rightarrow O_2 + 4H^+ + 4e^-$ ,  $U = 1.23V$  at  $pH=0$ ) and reduction ( $4H^+ + 4e^- \rightarrow 2H_2$ ,  $U = 0V$  at  $pH=0$ ).

TiO<sub>2</sub>-based catalysts for water splitting are known (Kudo and Miseki, 2009) so that it is not surprising that the situation is different for Ti. Indeed, TiO<sub>2</sub> is predicted by the computed Pourbaix diagram to be the stable Ti phase at the relevant potentials independent of the *pH* value, as seen in Figure 5.10. From the Ba and Ti Pourbaix diagrams, one can conclude that only the TiO<sub>2</sub>-terminated BaTiO<sub>3</sub> surfaces are relevant at the conditions required for water electrolysis. Not only dissolution, but also poisoning of the active surface sites may lead to catalytic deactivation. Further, water molecules may react with residual activated oxygen species on the catalyst surface (Song et al., 2016). We therefore computed the *pH* and potential dependent surface phase diagram of BaTiO<sub>3</sub>, examining small molecules that could potentially act as catalyst poisons. We only consider the (001) surface with both BaO and TiO<sub>2</sub> termination, as it is by far the most stable for BaTiO<sub>3</sub> (Padilla and Vanderbilt, 1997). In addition to the reaction intermediates of the OER, i.e., H<sub>2</sub>O, OH, O, OOH, and O<sub>2</sub>, we also looked at the adsorption of hydrogen molecules on the surface and at formation of oxygen vacancies. For each of the molecules/defects, surface coverages equivalent to 1,  $\frac{1}{4}$ ,  $\frac{1}{2}$ , and  $\frac{3}{4}$  monolayers were modeled and the results are shown in Table 5.3.

The resulting surface phase diagram is shown in Figure 5.11. Despite the various considered adsorbants and coverages, we find that only three different phases are predicted to occur: (i) The hydrogen-covered TiO<sub>2</sub>-terminated surface is stable at very negative potentials (reducing conditions), (ii) the bare BaO-terminated surface has a small stability region at high *pH* and low potential, and (iii) the bare TiO<sub>2</sub>-terminated surface is stable over the remaining area of the phase diagram including the relevant regions for water electrolysis. Based on the computed Pourbaix diagrams



and the surface phase diagram, the  $\text{TiO}_2$ -terminated  $\text{BaTiO}_3(001)$  surface is stable at the  $p\text{H}$  and potential required for water electrolysis, and it is not sensitive to poisoning by the reaction intermediates and hydrogen.

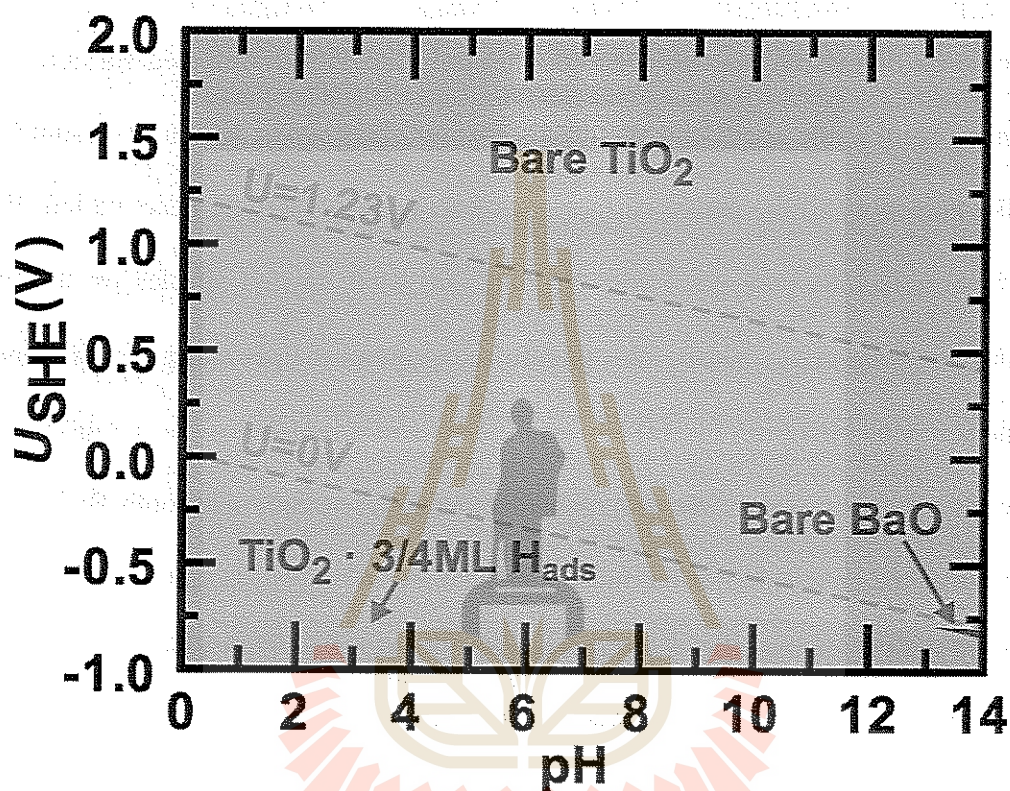


**Figure 5.11** Stable  $\text{BaTiO}_3(001)$  surface phase as function of the  $p\text{H}$  and the applied potential. The clean  $\text{BaO}$  and  $\text{TiO}_2$  terminated surfaces were considered, as well as these surfaces with hydrogen coverages between 1/4 and 1 monolayer (ML). As in Figure 5.9 and Figure 5.10, dashed orange lines indicate the water oxidation and reduction potentials.

**Table 5.4** Summary of adsorption energies of intermediate molecule ( $H^*$ ,  $O^*$ ,  $OH^*$  and  $OOH^*$ ) on BaO and  $TiO_2$  terminated. The coverage of  $1/4ML$ ,  $1/2ML$ ,  $3/4ML$  and  $1ML$  are considered.

Terminated	Coverage	$E_{H^*}/eV$	$E_{O^*}/eV$	$E_{OH^*}/eV$	$E_{OOH^*}/eV$
BaO	1/4ML	0.48	2.48	1.41	3.46
	2/4ML	0.56	2.54	1.75	3.62
	3/4ML	0.65	2.51	1.05	3.40
	1ML	0.65	2.62	1.22	4.03
$TiO_2$	1/4ML	2.45	3.96	1.14	4.36
	2/4ML	2.52	4.37	1.37	4.48
	3/4ML	0.03	3.45	1.38	4.13
	1ML	0.80	4.45	1.45	4.51

### 5.3.5 Oxygen evolution reaction over pristine and Fe-/Ni-modified $BaTiO_3$

Having established that electrically conducting Ni- and Fe-modified  $BaTiO_3$  can potentially be made and that the  $TiO_2$ -terminated  $BaTiO_3$  (001) surface is likely to be stable at operation conditions, we proceed to evaluate the reaction free energy profile for the OER as described in the methods section. The surfaces of the modified compositions were modeled by replacing a single surface Ti atom with either Fe or Ni, and the sites on top and next to this defect were considered for the adsorbed species.

Figure 5.12 shows the reaction free energies for water oxidation over pristine (black), Fe- modified (red), and Ni-modified (blue) BaTiO<sub>3</sub> at the ideal potential of  $U = 1.23$  V (solid lines) and at the predicted required overpotentials (dashed lines) following the elemental reactions of Eq. 5.1. The overpotential for the reaction on the ideal TiO<sub>2</sub>-terminated surface is  $\eta = 1.22$  V. Fe and Ni doping reduces the overpotential to 0.91 V and 0.89 V, respectively. On the unmodified surface, the potential-determining step is the second hydrogen dissociation from \*OH to \*O. Interestingly, Fe and Ni affect the reaction pathway in fundamentally different ways: Fe results in stronger binding of all three reaction intermediates, which reduces the overpotential but maintains the OH dissociation as potential-determining step. In contrast, Ni stabilizes the \*OOH binding, so that the reaction from \*OOH to +O<sub>2</sub> becomes the potential-determining step. Although, the reduced overpotentials for Fe- and Ni-modified BaTiO<sub>3</sub> are still too high to compete with Pt-group water electrolysis catalysts, or with La-based perovskite materials (Bockris and Otagawa, 1984) the large differences in the reaction profiles demonstrate that small compositional changes can have a strong positive impact on the catalytic activity.

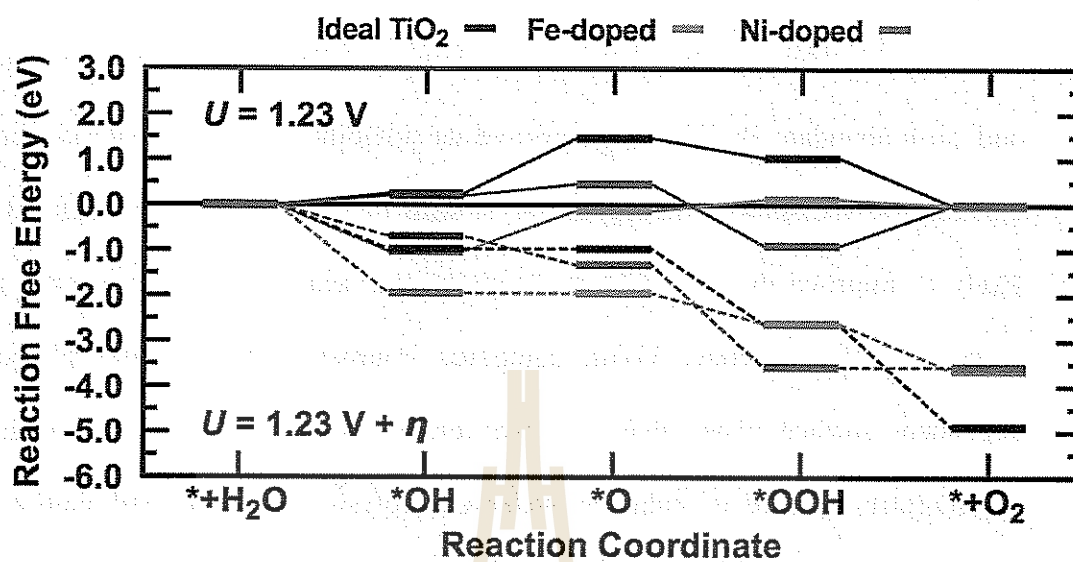


**Figure 5.12** Reaction free-energy diagram for the oxygen evolution reaction over ideal (black) and Fe (red) and Ni (blue) doped BaTiO<sub>3</sub> following the elementary reaction steps of Eq. 5.1. The solid lines indicate the reaction pathway without applied potential ( $U = 0 \text{ V}$ ) and the dashed lines are the reaction profiles at the required overpotentials for ideal Ti ( $\eta = 1.22 \text{ V}$ ), Fe dopants ( $\eta = 0.91 \text{ V}$ ), and Ni dopants ( $\eta = 0.89 \text{ V}$ ).

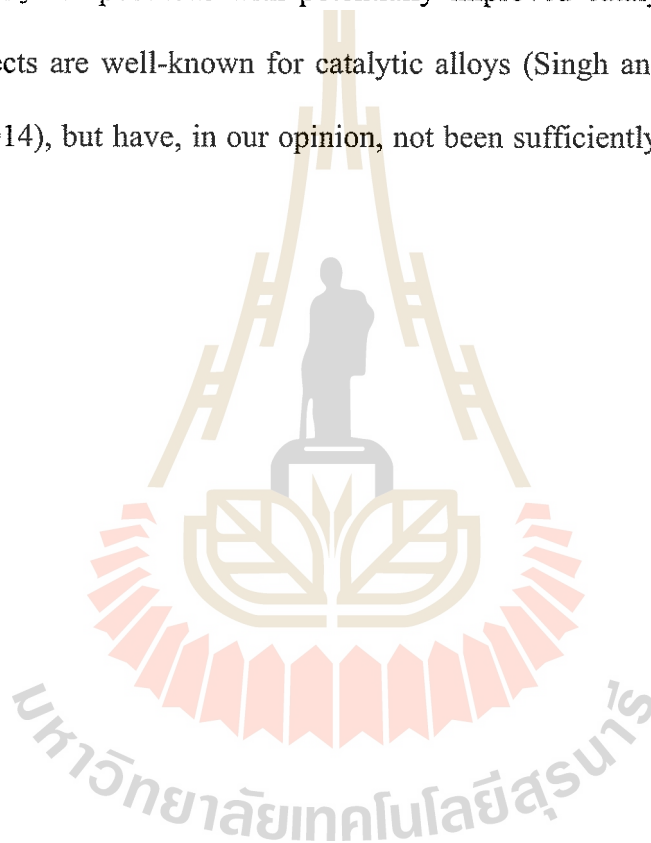
## 5.4 Discussion

In this work, we demonstrated that compositional modification of inexpensive and earth-abundant  $\text{BaTiO}_3$  may improve its suitability as anode material for water electrolysis. We showed that replacing Ti with Fe or Ni on the perovskite B site is likely to improve the electrical conductivity and reduces the overpotential for the water oxidation reaction. Using computed Pourbaix diagrams and pH-potential dependent surface phase diagrams we further showed that the  $\text{TiO}_2$ -terminated  $\text{BaTiO}_3(001)$  surface is stable at water electrolysis conditions and that it is not sensitive with respect to poisoning by reaction intermediates or hydrogen. We note that Fe and Ni can both assume oxidation states lower than 4+ and may give rise to oxygen deficiency when substituted on the B site in  $\text{BaTiO}_3$  (Hagemann and Hennings, 1981). Indeed, slightly oxygen deficient  $\text{BaFeO}_{3.5}$  is known to be stable, and strongly oxidizing conditions are required to synthesize stoichiometric Fe(IV)  $\text{BaFeO}_3$  (Hayashi et al., 2011). Since oxygen vacancies have previously been found to play an important role in CO oxidation (Elias et al., 2016), we can currently not rule out their involvement in water oxidation over modified  $\text{BaTiO}_3$ .

Another assumption made implicitly in the present study is that Fe and Ni dopants are stable against dissolution. Since the ideal  $\text{TiO}_2$ -terminated surface is stable, it seems reasonable that small dopant concentration can be stabilized in the  $\text{BaTiO}_3$  surface. However, if the dopant concentration is too small, the number of active sites on the catalyst surface may become rate limiting. As remarked in the previous section, Fe and Ni doping alters the reaction free energy profile in contrasting ways by stabilizing different reaction intermediates (Figure 5.7). If it were possible to simultaneously achieve the OH and O binding energies of Ni-modified

BaTiO<sub>3</sub> and the OOH binding energy of the Fe-modified system, a catalyst with close to ideal overpotential could be obtained. Therefore, it would be interesting to investigate the properties of Fe and Ni co-doped BaTiO<sub>3</sub>.

Finally, it is known that BaTiO<sub>3</sub> forms solid solutions with a large number of other perovskite oxides (Lemanov, 2007), opening up a large composition space for modified BaTiO<sub>3</sub> compositions with potentially improved catalytic activities. Such synergistic effects are well-known for catalytic alloys (Singh and Xu, 2013; Artrith and Kolpak, 2014), but have, in our opinion, not been sufficiently explored for oxide material.



## CHAPTER VI

### CONCLUSIONS AND FUTURE RESEARCH

$\text{LiAlO}_2$  in the natural and high-pressure phases,  $\gamma$ -LAO and  $\delta$ -LAO, was studied by first principles calculations based on the HSE and PBE functionals. By analyzing the equation of states of both phases it was found that the natural phase  $\gamma$ -LAO is in thermodynamic equilibrium with the high-pressure phase  $\delta$ -LAO at 2.3 GPa (HSE) and 3.1 GPa (PBE), respectively. The homogeneous phase transformation between the  $\gamma$ -LAO and  $\delta$ -LAO was also studied. By varying the lattice parameter  $c/a$ , the transformation path and the homogenous transformation barrier were determined. The electronic band structures and the partial density of states of both phases at ambient pressure were also calculated and reported. HSE calculations showed that  $\gamma$ -LAO has a direct band gap of 6.54 eV in good agreement with the experimental value of 6.2 eV. On the other hand, GGA calculations predict a significantly smaller band gap of 4.64 eV, due to the well-known DFT problems. HSE calculations predict the band gap of the high-pressure phase  $\delta$ -LAO to be indirect with a value of 8.11 eV, which is 24% larger than the band gap of the natural phase.

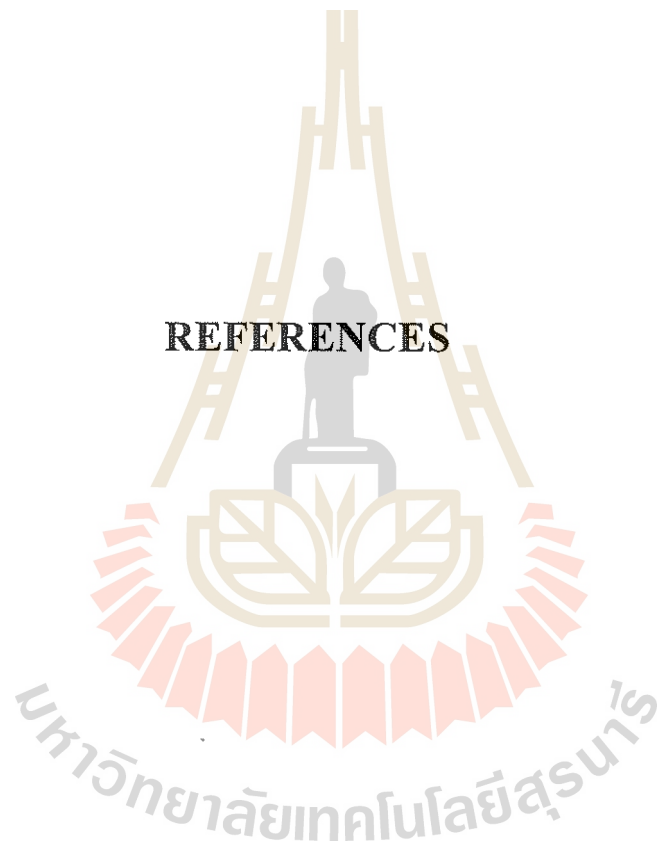
A detailed study of the phase transformations of  $\beta$ -LGO under different pressure conditions was carried out using first principles enthalpy calculations. In addition to the well-studied high pressure rocksalt-like  $R3m$  phase ( $RS''$ ), we identified 3 new

metastable LGO phases with symmetries  $oP16$ ,  $I41/amd$  and  $P4_12_12$ , which were named  $HX'$ ,  $RS'$ , and  $BCT'$ , respectively. By modeling stress loads along different crystal directions, it was found that different metastable phases can be stabilized. For high hydrostatic pressure, only the transformation to the well-studied rocksalt-like phase ( $RS''$ ) should take place because the  $RS'$  phase has a much higher transformation pressure. The  $[001]$  compressive stress loading can cause the transformation into an orthorhombic phase  $oP16$  ( $HX'$ ). On the other hand, the uniaxial  $[001]$  tensile stress can stabilize a tetragonal structure  $P4_12_12$  ( $BCT'$ ).

Based on first principles computations it was found that compositional modification of  $BaTiO_3$  can be an effective avenue for the design of inexpensive, earth-abundant anode materials for electrocatalytic water splitting. At the example of Fe and Ni doping, it was demonstrated that slightly modified  $BaTiO_3$  compositions can have greatly improved electrical conductivity and reduced overpotential for the oxygen evolution reaction by more than 25%. Since the present work explored only a small composition space as a proof of concept, it is likely that tuned  $BaTiO_3$  compositions with yet better performance exists, and our results suggest Fe and Ni co-doping as a promising approach.



## REFERENCES



## REFERENCES

- Anisimov, V. I., Aryasetiawan, F. and Lichtenstein, A. I. (1997). First-principles calculations of the electronic structure and spectra of strongly correlated systems: the LDA + U method. **Journal of Physics: Condensed Matter** 9: 767.
- Artrith, N. and Kolpak, A. M. (2014). Understanding the Composition and Activity of Electro-catalytic Nanoalloys in Aqueous Solvents: A Combination of DFT and Accurate Neural Network Potentials. **Nano letters** 14: 2670.
- Artrith, N., Sailum, W., Limpijumng, S. and Kolpak, A. M. (2016). Reduced overpotential for electrocatalytic water splitting over Fe- and Ni-modified BaTiO<sub>3</sub>. **Physical Chemistry Physics** 18: 19561.
- Assael, M., Trusler, J. P. M. and Tsolakis, T. F. (1996). **Thermophysical Properties of Fluids: An Introduction to their Prediction**. London, U.K.: Imperial College Press.
- Atkins, P. W. and Paula, J. D. (2006). **Atkins' Physical Chemistry**. Oxford University.
- Badwal, S. P. S., Giddey, S. and Ciacchi, F. T. (2006). Hydrogen and oxygen generation with polymer electrolyte membrane (PEM)-based electrolytic technology. **Ionics** 12: 7.
- Becke, A. D. (1988). Density-functional exchange-energy approximation with correct asymptotic behavior. **Physical Review A** 38: 3098.

- Beltran, N., Fuenzalida, V. and Grahmann, C. (1991). Thin Films of Barium Titanate for Sensor Devices. **Euro-Ceram. II** 3: 2475–2479.
- Blöchl, P. E. (1994). Projector augmented-wave method. **Physical Review B** 50: 17953.
- Blum, V., Gehrke, R., Hanke, F., Havu, P., Havu, V., Ren, X., Reuter, K. and Scheffler, M. (2009). *Ab initio* molecular simulations with numeric atom-centered orbitals. **Computer Physics Communications** 180: 2175.
- Bockris, J. O. and Otagawa, T. (1984). The Electrocatalysis of Oxygen Evolution on Perovskites. **Journal of The Electrochemical Society** 131: 290.
- Boonchun, A. and Lambrecht, W. R. L. (2010). First-principles study of the elasticity, piezoelectricity, and vibrational modes in LiGaO<sub>2</sub> compared with ZnO and GaN. **Physical Review B** 81: 235214 .
- Born, M. and Oppenheimer, R. (1927). Zur Quantentheorie der Molekeln. **Annalen der Physik** 389: 457.
- Carmo, M., Fritz, D. L., Mergel, J. and Stolten, D. (2013). A comprehensive review on PEM water electrolysis." **International Journal of Hydrogen Energy**. **International Journal of Hydrogen Energy** 38: 4901.
- Casimir, H. B. G. (1948). On the attraction between two perfectly conducting plates. **Gems from a century of science Centenary issue of the Proceedings of the Royal Netherlands Academy of Arts and Sciences** 51: 61.
- Castelli, I. E., Landis, D. D., Thygesen, K. S., Dahl, S., Chorkendorff, I., Jaramillo, T. F. and Jacobsen, K. W. (2012). New cubic perovskites for one- and two-photon water splitting using the computational materials repository. **Energy & Environmental Science** 5: 9034.

- Ceder, G., Chiang, Y. M., Sadoway, D. R., Aydinol, M. K., Jang, Y. I. and Huang, B. (1998). Identification of cathode materials for lithium batteries by first-principles calculations. **Nature** 392: 694.
- Chang, C., Pelissier, M. and Durand, P. (1986). Regular Two-Component Pauli-Like Effective Hamiltonians in Dirac Theory. **Physica Scripta** 34: 394.
- Chen, C., Li, C. A., Yu, S. H. and Chou, M. M. C. (2014). Growth and characterization of  $\beta$ -LiGaO<sub>2</sub> single crystal. **Journal of Crystal Growth** 402: 325.
- Coulomb, P. M. (1785) Histoire de l'Académie Royale des Sciences. Imprimerie Royale. pp. 569–577. In Histoire de l'Académie Royale des Sciences. Imprimerie Royale.
- Cui, C., Gan, L., Heggen, M., Rudi, S. and Strasser, P. (2013). Compositional segregation in shaped Pt alloy nanoparticles and their structural behaviour during electrocatalysis. **Nature Materials** 12: 765.
- Desgreniers, S. (1998). High-density phases of ZnO: structural and compressive parameters. **Physical Review B** 58: 14102.
- Dirac, P. A. M. (1930). Note on Exchange Phenomena in the Thomas Atom. **Mathematical Proceedings of the Cambridge Philosophical Society** 26: 376.
- Donald, D. W., William, H. E., Vivian, B. P., Richard, H. S., Iva, H., Sylvia, M. B., Kenneth, L. C. and Ralph, L. N. (1982). The NBS tables of chemical thermodynamic properties Selected values for inorganic and C1 and C2 organic substances in SI units. **Journal of Physical and Chemical Reference Data** 11: 215.

- Elias, J. S., Artrith, N., Bugnet, M., Giordano, L., Botton, G. A., Kolpak, A. M. and Shao-Horn, Y. (2016). Elucidating the Nature of the Active Phase in Copper/Ceria Catalysts for CO Oxidation. *ACS Catalysis* 6: 1675.
- Grades, Z. E. d. A. (2015) Graphene Engineering: An ab initio Study of the Thermodynamic Stability of Epitaxial Graphene and the Surface Reconstructions of Silicon Carbide. In PhysikDer Humboldt Universitat zu Berlin.
- Gupta, G., Slanac, D. A., Kumar, P., Wiggins-Camacho, J. D., Wang, X., Swinnea, S., More, K. L., Dai, S., Stevenson, K. J. and Johnston, K. P. (2009). Highly Stable and Active Pt-Cu Oxygen Reduction Electrocatalysts Based on Mesoporous Graphitic Carbon Supports. *Chemistry of Materials* 21: 4515.
- Hagemann, H.-J. and Hennings, D. (1981). Reversible Weight Change of Acceptor-Doped BaTiO<sub>3</sub>. *Journal of the American Ceramic Society* 64: 590.
- Hammer, B., Hansen, L. B. and Nørskov, J. K. (1999). Improved adsorption energetics within density-functional theory using revised Perdew-Burke-Ernzerhof functionals. *Physical Review B* 59: 7413.
- Harada, J., Pedersen, T. and Barnea, Z. (1970). X-ray and neutron diffraction study of tetragonal barium titanate. *Acta Crystallographica Section A* 26: 336.
- Hart, G. L., Nelson, L. J. and Forcade, R. W. (2012). Generating derivative structures at a fixed concentration. *Computational Materials Science* 59: 101.
- Hart, G. L. W. and Forcade, R. W. (2009). Generating derivative structures from multilattices: Algorithm and application to hcp alloys. *Physical Review B* 80: 014120.

- Havu, V., Blum, V., Havu, P. and Scheffler, M. (2009). Efficient integration for all-electron electronic structure calculation using numeric basis functions. **Journal of Computational Physics** 228: 8367.
- Hayakawa, T., Suzuki, S., Nakamura, J., Uchijima, T., Hamakawa, S., Suzuki, K., Shishido, T. and Takehira, K. (1999). CO<sub>2</sub> reforming of CH<sub>4</sub> over Ni/perovskite catalysts prepared by solid phase crystallization method. **Applied Catalysis A** 183: 273.
- Hayashi, N., Yamamoto, T., Kageyama, H., Nishi, M., Watanabe, Y., Kawakami, T., Matsushita, Y., Fujimori, A. and Takano, M. (2011). BaFeO<sub>3-x</sub> : A Ferromagnetic Iron Oxide. **Angewandte Chemie International Edition** 50: 12547.
- Heine, V. (1970). The Pseudopotential Concept. **Solid State Physics (Academic Press)** 1: 24.
- Hellman, E. S. and Harris, J. S. (1997). Epitaxial Growth and orientation of GaN on (100)  $\gamma$ -LiAlO<sub>2</sub>. **The MRS Internet Journal of Nitride Semiconductor Research** 4: 2.
- Heyd, J., Scuseria, G. E. and Ernzerhof, M. (2003). Hybrid functionals based on a screened Coulomb potential. **The Journal of Chemical Physics** 118: 8207.
- Hohenberg, P. and Kohn, W. (1964). Inhomogeneous Electron Gas. **Physical Review** 136: B864.
- Holladay, J. D., Hu, J., King, D. L. and Wang, Y. (2009). An overview of hydrogen production technologies. **Catalysis Today** 139: 244.
- Hwang, T. J. and Choi, G. M. (1993). Humidity Response Characteristics of Barium Titanate. **Journal of the American Chemical Society** 76: 766.

- Indris, S. and Heitjans, P. (2006). Local electronic structure in a  $\text{LiAlO}_2$  single crystal studied with  $^7\text{Li}$  NMR spectroscopy and comparison with quantum chemical calculations. . **Physical Review B** 74: 245120.
- Jain, A., Hautier, G., Moore, C. J., Ong, S. P., Fischer, C. C., Mueller, T. and Persson, K. A. (2011). A high-throughput infrastructure for density functional theory calculations. **Computational Materials Science** 50: 2295.
- Jain, A., Hautier, G., Moore, C. J., Ong, S. P., Fischer, C. C., Mueller, T., Persson, K. A. and Ceder, G. (2011). A high-throughput infrastructure for density functional theory calculations. **Computational Materials Science** 50: 2295.
- Jones, R. O. and Gunnarsson, O. (1989). The density functional formalism, its applications and prospects. **Reviews of Modern Physics** 61: 689.
- Junghwan, S. and Limpijumnong, S. (2004). First-principles study of the wurtzite-to-rocksalt homogeneous transformation in  $\text{ZnO:A}$  case of a low-transformation barrier. **Physical Review B** 70: 054104.
- Karasiev, V. V., Sjostrom, T., Dufty, J. and Trickey, S. B. (2014). Accurate Homogeneous Electron Gas Exchange-Correlation Free Energy for Local Spin-Density Calculations. **Physical Review Letters** 112: 076403.
- Ke, X., Jun, X., Peizhen, D., Yongzong, Z., Guoqing, Z., Rongsheng, Q. and Zujie, F. (1998).  $\gamma$ - $\text{LiAlO}_2$  single crystal: a novel substrate for GaN epitaxy. . **Journal of Crystal Growth Journal of Crystal Growth** 193: 127.
- Kennedy, J. H. and Frese, K. W. (1976). Photooxidation of Water At Barium titanate Electrodes. **Journal of the Electrochemical Society** 123: 1683-1686.
- Kittel, C. (1982) Introduction to Solid State Physics. In Jonh Wiley & Sons, IncCambridge University, United State of America.

- Kohn, W. and Sham, L. J. (1965) Self-Consistent Equations Including Exchange and Correlation Effects. In **Physical Review** 140: A1133.
- Kresse, G. and Furthmüller, J. (1996(a)) Efficiency of ab-initio total energy calculations for metals and semiconductors using a plane-wave basis set. In **Computational Materials Science** 6: 15.
- Kresse, G. and Furthmüller, J. (1996(b)). Efficient iterative schemes for {ab initio} total-energy calculations using a plane-wave basis set. **Physical Review B** 54: 11169.
- Kresse, G. and Hafner, J. (1994). Norm-conserving and ultrasoft pseudopotentials for first row and transition elements **Journal Physics Condence Matter** 6: 8245.
- Kudo, A. and Miseki, Y. (2009). Heterogeneous photocatalyst materials for water splitting. **Chemical Society Reviews** 38: 253-278.
- Kulkarni, A. J., Zhou, M., Sarasamak, K. and Limpijumnong, S. (2006). Nonvel phase transition in ZnO nanowires under tensile loading. **Physical review letters** 97: 105502.
- Lee, D., Lee, Y.-L., Grimaud, A., Hong, W. T., Biegalski, M. D., Morgan, D. and Shao-Horn, Y. (2014). Strontium influence on the oxygen electrocatalysis of  $\text{La}_{2-x}\text{Sr}_x\text{NiO}_4^\pm$ . **Journal of Materials Chemistry A** 2: 6480.
- Lee, J. G., Hwang, J., Hwang, H. J., Jeon, O. S., Jang, J., Kwon, O., Lee, Y., Han, B. and Shul, Y.-G. (2016). A New Family of Perovskite Catalysts for Oxygen-Evolution Reaction in Alkaline Media:  $\text{BaNiO}_3$  and  $\text{BaNi}_{0.83}\text{O}_{2.5}$ . **Journal of the American Chemical Society** 138: 3541.
- Lee, Y. L., Gadre, M. J., Horn, Y. S. and Morgan, D. (2015). Ab initio GGA+U Study of Oxygen Evolution and Oxygen Reduction Electrocatalysis on the (001)



- Surfaces of Lanthanum Transition Metal Perovskites  $\text{LaBO}_3$  ( $B=\text{Cr, Mn, Fe, Co and Ni}$ ). **Physical Chemistry Chemical Physics** 17: 21643.
- Lei, L., Ohfuji, H., Qin, J., Zhang, X., Wang, F. and Irifune, T. (2013). High-pressure Raman spectroscopy study of  $\text{LiGaO}_2$ . **Solid State Communications** 164: 6.
- Lemanov, V. V. (2007). Barium Titanate-Based Solid Solutions. **Ferroelectrics** 354: 69-76.
- Lenthe, E. v., Baerends, E. J. and Snijders, J. G. (1993). Relativistic regular two-component Hamiltonians. **The Journal of Chemical Physics** 99: 4597.
- Li, X., Kobayashi, T., Zhang, F., Kimoto, K. and Sekine, T. (2004). A new high-pressure phase of  $\text{LiAlO}_2$ . **Journal of Solid State Chemistry** 177: 1939-1943.
- Li, X., Wang, B., Zhang, T. Y. and Su, Y. (2014). Water Adsorption and Dissociation on  $\text{BaTiO}_3$  Single-Crystal Surfaces. **The Journal of Physical Chemistry C** 118: 15910.
- Liechtenstein, A. I., Anisimov, V. I. and Zaanen, J. (1995). Density-functional theory and strong interactions: Orbital ordering in Mott-Hubbard insulators. **Physical Review B** 52: R5467.
- Lim, B., Jiang, M., Camargo, P. H. C., Cho, E. C., Tao, J., Lu, X., Zhu, Y. and Xia, Y. (2009). Pd-Pt bimetallic nanodendrites with high activity for oxygen reduction. **Science** 324: 1302.
- Limpijumnong, S. and Jungthawan, S. (2004). First-principles study of the wurtzite-to-tocksalt homogeneous transformation in  $\text{ZnO}$ : A case of a low-transformation barrier. **Physical Review B** 70: 054104.

- Limpijumnong, S. and Lambrecht, W. R. L. (2001). Theoretical study of the relative stability of wurtzite and rocksalt phases in MgO and GaN. . **Physical Review B** 63: 104103.
- Limpijumnong, S. and Lambrecht, W. R. L. (2001). Theoretical study of the relative stability of wurtzite and rocksalt phases in MgO and GaN. . **Physical Review B** 63: 104103.
- Limpijumnong, S., Lambrecht, W. R. L., Segall, B. and Kim, K. (1996). Band Structure and Cation Ordering in LiGaO<sub>2</sub>. **MRS Online Proceedings Library** 449: 905.
- Luo, J., Im, J.-H., Mayer, M. T., Schreier, M., Nazeeruddin, M. K., Park, N.-G., Tilley, S. D., Fan, H. J. and Gratzel, M. (2014). Water photolysis at 12.3% efficiency via perovskite photovoltaics and Earth-abundant catalysts. . **Science** 345: 1593.
- Luspin, Y., Servoin, J. L. and Gervais, F. (1980). Soft Mode Spectroscopy in Barium Titanate. **Journal of Physics C** 13: 3761.
- Man, I. C., Su, H.-Y., Calle-Vallejo, F., Hansen, H. A., Martínez, J. I., Inoglu, N. G., Kitchin, J., Jaramillo, T. F., Nørskov, J. K. and Rossmeisl, J. (2011). Universality in oxygen evolution electrocatalysis on oxide surfaces. **ChemCatChem** 3: 1159.
- Marezio, M. (1965). The Crystal Structure and Anomalous Dispersion of  $\gamma$ -LiAlO<sub>2</sub>. **Acta Crystallographica**. 19: 396.
- Marezio, M. (1965). The crystal structure of LiGaO<sub>2</sub>. **Acta Crystallographica** 18: 481.

- Marezio, M. (1965). The crystal structure of  $\text{LiGaO}_2$ . **Acta Crystallographica**. 18: 481.
- Marezio, M. and Remeika, J. P. (1965). High pressure phase of  $\text{LiGaO}_2$ . **Journal of Physics and Chemistry of Solids** 26: 1277.
- Marezio, M. and Remeika, J. P. (1966). Polymorphism of  $\text{LiMO}_2$  Compounds and High-Pressure Single-Crystal Synthesis of  $\text{LiBO}_2$ . **The Journal of Chemical Physics** 44: 3348.
- Martin, R. M. (2004) *Electronic Structure: Basic Theory and Practical Methods*. Cambridge University Press, United Kingdom.
- McCrory, C. C. L., Jung, S., Peters, J. C. and Jaramillo, T. F. (2013). Benchmarking Heterogeneous Electrocatalysts for the Oxygen Evolution Reaction. **Journal of the American Chemical Society** 135: 16977.
- McNaught, A. D. and Wilkinson, A. (1997) *Compendium of Chemical Terminology*. In International Union of Pure and Applied Chemistry (IUPAC) Oxford Blackwell Scientific Publications,.
- Mefford, J. T., Rong, X., Abakumov, A. M., Hardin, W. G., Dai, S., Kolpak, A. M., Johnston, K. P. and Stevenson, K. J. (2016). Water electrolysis on  $\text{La}_2\text{O}_3$ . **Nature Communications** 7: 11053.
- Miao, M. S. and Lambrecht, W. R. L. (2003). Unified path for high-pressure transitions of  $\text{SiC}$  polytypes to the rocksalt structure. **Physical Review B** 68: 092103.
- Momma, K. and Izumi, F. (2011). VESTA 3 for three-dimensional visualization of crystal, volumetric and morphology data. **Journal of Applied Crystallography** 44: 1272.

- Monkhorst, H. J. and Pack, J. D. (1976). Special points for Brillouin-zone integrations. **Physical Review B** 13: 5188.
- Mujica, A., Rubio, A., Munoz, A. and Needs, R. J. (2003). High-pressure phases of group-IV, III-V, and II-VI compounds. **Reviews of Modern Physics** 75: 863.
- Muller, U. (2013). **Symmetry Relationships between Crystal Structure. Applications of Crystallographic Group Theory in Crystal Chemistry**. Oxford Science Publications: International Union of Crystallography.
- Murnaghan, F. D. (1944). The compressibility of media under extreme pressures. **Proceedings of the National Academy of Science** 30: 4.
- Nasby, R. D. and Quinn, R. K. (1976). Photoassisted Electrolysis of Water Using a BaTiO<sub>3</sub> Electrode. **Materials Research Bulletin** 11: 985-992.
- Norskov, J. K., Rossmeisl, J., Logadottir, A. and Lindqvist, L. (2004). Origin of the Overpotential for Oxygen Reduction at Fuel-Cell Cathode. **The Journal of Physical Chemistry B** 108: 17886.
- Omata, T., Nagatani, H., Suzuki, I. and Kita, M. (2015). Wurtzite-derived ternary I-III-O<sub>2</sub> semiconductors. **Science and Technology of Advanced Materials** 16: 024902.
- Omata, T., Tazuke, A., Nose, K. and Matsuo, S. O. Y. (2011). Synthesis of LiGaO<sub>2</sub> nanocrystals and their application toward bright UV emission from ZnO quantum dot. **Journal of Crystal Growth** 330: 9.
- Ong, S. P., Richards, W. D., Jain, A., Hautier, G., Kocher, M., Cholia, S., Gunter, D., Chevrier, V. L., Persson, K. A. and Ceder, G. (2013). Python Materials Genomics (pymatgen): A robust, open-source python library for materials analysis. **Computational Materials Science** 68: 314.

- Padilla, J. and Vanderbilt, D. (1997). Ab initio study of BaTiO<sub>3</sub> surfaces. **Physical Review B** 56: 1625.
- Paier, J., Marsman, M., Hummer, K., Kresse, G., Gerber, I. C. and Angyan, J. G. (2006). Screened hybrid density functionals applied to solids **The Journal of Chemical Physics** 124: 154709.
- Parr, G. R. and Yang, W. (1989) Density-Functional Theory of Atoms and Molecules. Oxford University Press, The united States of America.
- Pauli, W. (1925). On the Connexion between the Completion of Electron Groups in an Atom with the Complex Structure of Spectra. **Zeitschrift fur Physik** 31: 765.
- Perdew, J. P., Burke, K. and Ernzerhof, M. (1996). Generalized Gradient Approximation Made Simple. **Physical Review Letters** 77: 3865.
- Perdew, J. P., Chevary, J. A., Vosko, S. H., Jackson, K. A., Pederson, M. R., Singh, D. J. and Fiolhais, C. (1992). Atoms, molecules, solids, and surfaces: Applications of the generalized gradient approximation for exchange and correlation. **Physical Review B** 46: 6671.
- Perdew, J. P., Ernzerhof, M. and Burke, K. (1996). Rationale for mixing exact exchange with density functional approximations. **The Journal of Chemical Physics** 105: 9982.
- Perdew, J. P. and Zunger, A. (1981). Self-interaction correction to density-functional approximations for many-electron systems. **Physical Review B** 23: 5048.
- Persson, K. A., Waldwick, B., Lazic, P. and Ceder, G. (2012). Prediction of solid-aqueous equilibria: Scheme to combine first-principles calculations of solids with experimental aqueous states. **Physical Review B** 85: 235438.

- Popescu, I., Săndulescu, I., Rédey, A. and Marcu, I.-C. (2011). Study of the Catalytic Activity-Semiconductive Properties Relationship For BaTiO<sub>3</sub> and PbTiO<sub>3</sub> Perovskites, Catalysts for Methane Combustion. **Catalysis Letters** 141: 445.
- Pourbaix, M. (1974). **Atlas of Electrochemical Equilibria in Aqueous Solutions**. Cebelcor Houston, Brussels: National Association of Corrosion Engineers.
- Power, E. A. and Thirunamachandran, T. (1993). Casimir-Polder potential as an interaction between induced dipoles. **Physical Review A** 48: 4761.
- Recio, J. M., Blanco, M. A., Luaña, V., Pandey, R., Gerward, L. and Olsen, J. S. (1998). Compressibility of the high-pressure rocksalt phase of ZnO. **Physical Review B** 58: 8949.
- Rodríguez, G. M., Kelm, K. and Saruhan, B. (2010). H<sub>2</sub>-selective catalytic reduction of NO<sub>x</sub> activity and microstructural analysis of new BaTi<sub>0.95</sub>Pd<sub>0.05</sub>O<sub>3</sub> catalyst. **Applied Catalysis A:General** 387: 173.
- Rong, X. and Kolpak, A. M. (2015). *Ab Initio* Approach for Prediction of Oxide Surface Structure, Stoichiometry, and Electrocatalytic Activity in Aqueous Solution. **Journal of Physics Chemistry Letters** 6: 1785.
- Rossmeyl, J., Qi, Z. W., Zhu, H., Kroes, G. J. and Norskoc, J. K. (2007). Electrolysis of water on oxide surface. **Journal of Electroanalytical Chemistry** 607: 83.
- Royer, S., Duprez, D., Can, F., Courtois, X., Batiot-Dupeyrat, C., Laassiri, S. and Alam-dari, H. (2014). Perovskites as Substitutes of Noble Metals for Heterogeneous Catalysis: Dream or Reality. **Chemical Reviews** 114: 10292.
- Sakurai, J. J. (1994) *Modern Quantum Mechanics* (Revised ed.). Tuan, San Fu, Addison-Wesley.

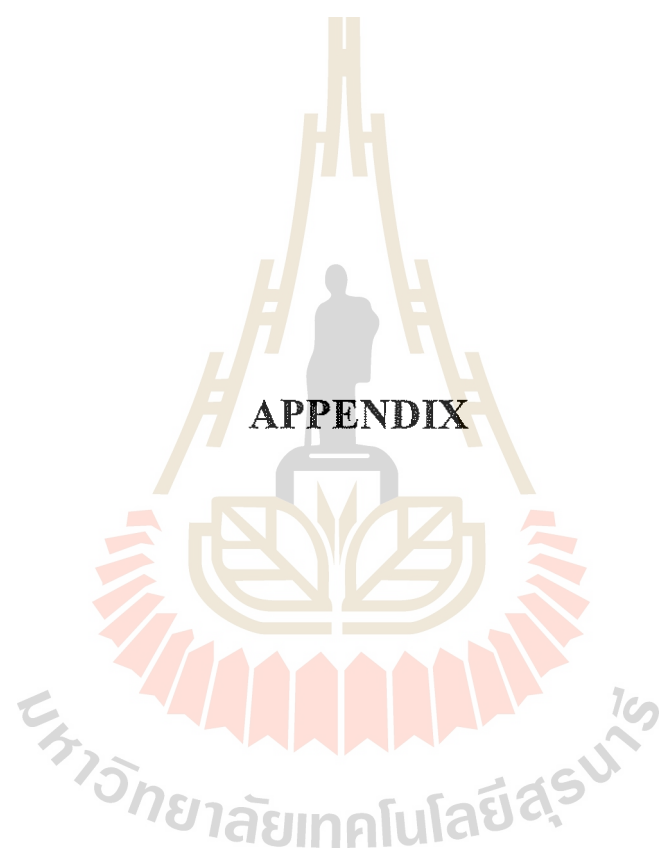
- Sarasamak, K., Kulkarni, A. J., Zhou, M. and Limpijumnong, S. (2008). Stability of wurtzite, unbuckled wurtzite, and rocksalt phases of SiC, GaN, InN, ZnO, and CdSe under loading of different triaxialities. **Physical Review B** 77: 024104.
- Sailuam, W., Sarasamak, K. and Limpijumnong, S. (2014). High Pressure Phase of LiAlO<sub>2</sub>: A First Principles Study. **Integrated Ferroelectrics** 156: 15-22.
- Sailuam, W., Sarasamak, K., Polanco, M. A.M., and Limpijumnong, S. (2017). Pressure-Induced Phase Transformation of LiGaO<sub>2</sub>: First Principles Study. **Ceramics International (manuscript)**.
- Schrödinger, E. (1926). An Undulatory Theory of the Mechanics of Atoms and Molecules. **Physical Review** 28: 1049.
- Shannon, R. D. (1976). Revised effective ionic radii and systematic studies of interatomic distances in halides and chalcogenides. **Acta Crystallographica Section A** 5: 751.
- Singh, A. K. and Xu, Q. (2013). Synergistic Catalysis over Bimetallic Alloy Nanoparticles. **ChemCatChem** 5: 652.
- Slater, J. C. (1951). A Simplification of the Hartree-Fock Method. **Physical Review** 81: 385.
- Song, Z., Fan, J., Shan, Y., Ng, A. M.-C. and Xu, H. (2016). **Physical Chemistry Chemical Physics** 18: 17341.
- Srilakshmi, C., Saraf, R., Prashanth, V., Rao, G. M. and Shivakumara, C. (2016). Structure and Catalytic Activity of Cr-Doped BaTiO<sub>3</sub> Nanocatalysts Synthesized by Conventional Oxalate and Microwave Assisted Hydrothermal Methods. **Inorganic Chemistry** 10: 4795.

- Stamenkovic, V. R., Fowler, B., Mun, B. S., Wang, G., Ross, P. N., Lucas, C. A. and Markovic, N. M. (2007). Improved oxygen reduction activity on Pt<sub>3</sub>Ni (111) via increased surface site availability. **Science** 315: 493.
- Suele, P., Kurth, V. E. and Doren, V. (1999). Orbital dependent exchange-only methods for periodic systems. **Physical Review B** 50: 5429.
- Suntivich, J., May, K. J., Gasteiger, H. A., Goodenough, J. B. and Shao-Horn, Y. A. (2011). Perovskite Oxide Optimized for Oxygen Evolution Catalysis from Molecular Orbital Principles. **Science** 334: 1383.
- Takeda, Y. K., F.; Shimada, M.; Koizumi, M. (1976). The crystal structure of BaNiO<sub>3</sub>. **Acta Crystallographica Section B** 32: 2464.
- Tang, K. T. and Toennies, J. P. (1977). A simple theoretical model for the van der Waals potential at intermediate distances. I. Spherically symmetric potential. **The Journal of Chemical Physics** 66: 1496.
- Teng, H. S. Z., Lin, H., T., J., Hou, X. and Wang, J. (2010). Growth and characterization of high-quality Mn-doped LiAlO<sub>2</sub> single crystal. **Chinese Optical L** 8: 4.
- Tkatchenko, A. and Scheffler, M. (2009). Accurate Molecular Van Der Waals Interactions from Ground-State Electron Density and Free-Atom Reference Data. **Physical Review Letters** 102: 073005.
- Urban, A., Seo, D.-H. and Ceder, G. (2016). Computational understanding of Li-ion batteries. **Computational Materials** 2: 16002.
- Valdeś, A., Qu, Z.-W., Kroes, G.-J., Rossmeisl, J. and Norskov, J. K. (2008). Oxidation and Photo-Oxidation of Water on TiO<sub>2</sub> Surface. **Journal of Physics Chemistry C** 2: 9872–9879.



- Van Lenthe, E., Baerends, E. J. and Snijders, J. G. (1994). Relativistic total energy using regular approximations. . **The Journal of Chemical Physics** 101: 9783.
- Vanfleet, R. R., Simmons, J. A., Hill, D. W., Chou, M. M. C. and Chai, B. H. (2008). Antiphase ordering and surface phases in lithium aluminate. **Journal of Applied Physics** 104: 093530.
- Wagman, D. D., Evans, W., Parker, V., Halow, I., Bailey, S. and Schumm, R. (2011). **Selected Values of Chemical Thermodynamic Properties, National Bureau of Standards: Washington, U.S.A.**, . National Bureau of Standards.
- Wang, J., Kulkarni, A. J., Sarasamak, K., Limpijumnong, S., Ke, F. L. and Zhou, M. (2007). Molecular dynamics and density functional studies of a body-centered-tetragonal polymorph of ZnO. **Physical Review B** 76: 172103.
- Wang, L., Maxisch, T. and Ceder, G. (2006). Oxidation energies of transition metal oxides within the GGA+U framework. **Physical Review B** 73: 195107.
- Wannakao, S., Artrith, N., Limtrakul, J. and Kolpak, A. M. (2015). Engineering Transition-Metal-Coated Tungsten Carbides for Efficient and Selective Electrochemical Reduction of CO<sub>2</sub> to Methane. **ChemSusChem** 8: 2745.
- Wemple, S. H. (1970). Polarization Fluctuations and the Optical-Absorption Edge in BaTiO<sub>3</sub>. **Physical Review B** 2: 2679.
- Wigner, E. (1934). On the Interaction of Electrons in Metals. **Physical Review** 46: 1002.
- Wolfram Quester Source [On-line] Available: <http://en.wikipedia.org/wiki/File:SketchPseudopotentials.png>.

- Wu, S. Q., Hou, Z. F. and Zhu, Z. Z. (2009). First-principles study on the structural, elastic, and electronic properties of  $\gamma$ -LiAlO<sub>2</sub>. **Computational Materials Science** 46: 221-224.
- Yeh, Y. and Tseng, T. (1988). Humidity-Sensitive Electrical Properties of Ba<sub>0.5</sub>Sr<sub>0.5</sub>TiO<sub>3</sub> Porous Ceramics. **Journal of Material Science Letters** 7: 766-768.
- Yu, Y. G., Wentzcovitch, R. M., Taku, T., Umemoto, K. and Weidner, D. J. (2007). First principles investigation of the postspinel transition in Mg<sub>2</sub>SiO<sub>4</sub>. **Geophysical Research Letters** 34: L16305.
- Zeng, K. and Zhang, D. (2010). Recent progress in alkaline water electrolysis for hydrogen production and applications. **Progress in Energy and Combustion Science** 36: 307.
- Zhang, J., Huang, R., Shi, L., Wang, L., Wei, F., Kong, T. and Cheng, G. (2013). Bi doping modulating structure and phase-change properties of GeTe nanowires. **Applied Physics Letters** 102: 063104.
- Zhang, J., Yang, H., Fang, J. and Zou, S. (2010). Synthesis and oxygen reduction activity of shape-controlled Pt<sub>3</sub>Ni nanopolyhedra **Nano letters** 10: 638.
- Zhang, Y. and Yang, W. (1998) Comment on Generalized Gradient Approximation Made Simple. In **Physical Review Letters** 80: 890.
- Zou, J., Dong, Y., Zhou, S., Sun, Y., Jun, W., Zhou, J., Huang, T., Yang, S. and Zhou, H. (2006). Study on the hydrolytic property and thermal stability of LiAlO<sub>2</sub> substrate. **Journal of Crystal Growth** 294: 339-342.



## APPENDIX

### PUBLICATIONS AND PRESENTATIONS

#### 1. List of publications

Sailuam, W., Sarasamak, K., and Limpijumnong, S. (2014). High pressure phase of  $\text{LiAlO}_2$ : A First principle study. *Integr. Ferroelectr.* Volume 156:1.

Artrith, N.\*, Sailuam, W.\*, Limpijumnong, S. and Kolpak, A. M. (2016). Reduced overpotentials for electrocatalytic water splitting over Fe- and Ni-modified  $\text{BaTiO}_3$ . *Phys. Chem. Chem. Phys.* 18:29561-29570. (\*These authors contributed equally to this work).

Sailuam, W., Sarasamak, K., Mendez Polanco, M.A. and Limpijumnong, S. (2016): Pressure-induced phase transformations of  $\text{LiGaO}_2$ . (Manuscript Accepted in *Ceram. Int.*).

#### 2. List of presentation.

Sailuam, W., Sarasamak, K., Mendez Polanco, M.A. and Limpijumnong, S. (2016): Stress-induced phase transformations of  $\text{LiGaO}_2$ . The 10<sup>th</sup> Asian Meeting on Electroceramics, (December 4-7, 2016), Taipei, Taiwan.

Sailuam, W., Artrith, N., Limpijumnong, S. and Kolpak, A. M. Structural and Dynamical Properties of Water on Defected  $\text{BaTiO}_3$  Surfaces: DFT and *Ab initio* Molecular Dynamic Simulations, 250<sup>th</sup> ACS National Meeting & Exposition, (August 16-20, 2015), Boston, MA, USA.

Sailuam, W., Sarasamak, K., and Limpijumnong, S. Structural Phase Transformation in  $\text{BaTiO}_3$  : Frist Principles Calculations, The 9<sup>th</sup> Asian Meeting on Ferroelectrics with The 9<sup>th</sup> Asian Meeting on Electroceramics (AMF-AMEC-2014), (October 26-30, 2014), Shanghai International Convention Center, Shanghai, CHAINA.

Sailuam, W., Sarasamak, K., and Limpijumnong, S. High pressure phase of  $\text{LiAlO}_2$ : A first principles study, The 7<sup>th</sup> Conference of the Asian Consortium on Computational Materials Science (July 23 – 28, 2013), Suranaree University of Technology, Nakhon Ratchasima, THAILAND (poster presentation).

Sailuam, W., Sarasamak, K., and Limpijumnong, S. High pressure phase of  $\text{LiGaO}_2$ : A first principles study, The 3<sup>rd</sup> Academic conference on natural science for master and PhD students from ASEAN countries in Cambodia, ( November 11-15, 2013), Royal University of Phnom Penh, Phnom Penh, CAMBODIA (poster presentation).

Sailuam, W., Sarasamak, K., and Limpijumnong, S. High pressure phase of  $\text{LiAlO}_2$  : Hybrid Functional Calculations, The Annual conference of the Thai Physics Society: Siam Physics Congress 2012 (March 21 – 23, 2013), Chiangmai Grandview Hotel, Chaing Mai, THAILAND (poster presentation).

Sailuam, W., Sarasamak, K., and Limpijumnong, S. First principles study of high-pressure phase transformation of  $\text{LiAlO}_2$  , The 8<sup>th</sup> Asia meeting on Ferroelectrics (December 9-14, 2012), Amari Orchid Hotel, Pattaya, THAILAND (poster presentation).

Sailuam, W., Sarasamak, K., and Limpijumnong, S. High pressure phase of  $\text{LiAlO}_2$ , The 7<sup>th</sup> Annual Conference of the Thai Physics Society : Siam Physics

Congress 2012 (May 9-12, 2012), Krungsri River Hotel, Phra Nakhon Si Ayutthaya, THAILAND (Oral presentation).

### 3. List of award.

Poster award presentation, Sailuam, W., Sarasamak, K., Mendez Polanco, M.A. and Limpijumnong, S. (2016): Stress-induced phase transformations of  $\text{LiGaO}_2$ . The 10<sup>th</sup> Asian Meeting on Electroceramics, (December 4-7, 2016), Taipei, Taiwan.

### 4. Professional activities.

TOMBO workshop (July 23 – 24, 2013), Suranaree university of technology, Nakhon Ratchasima, THAILAND.

Workshop staff, Computing and modeling in material science (November 24-26, 2013), Universiti Sains Malaysia (USM), MALAYSIA.

## High Pressure Phase of $\text{LiAlO}_2$ : A First Principles Study

WUTTHIGRAI SAILUAM,<sup>1,2</sup> KANOKNAN SARASAMAK,<sup>3</sup>  
 AND SUKIT LIMPIJUMNONG<sup>1,2,\*</sup>

<sup>1</sup>School of Physics and NANOTEC-SUT Center of Excellence on Advanced Functional Nanomaterials, Suranaree University of Technology, Nakhon Ratchasima 30000, Thailand

<sup>2</sup>Thailand Center of Excellence in Physics (ThEP Center), Commission on Higher Education, Bangkok 10400, Thailand

<sup>3</sup>College of Nanotechnology, King Mongkut's Institute of Technology Ladkrabang, Bangkok 10520, Thailand

*The homogeneous structural phase transition between the natural and high-pressure forms of  $\text{LiAlO}_2$ , i.e.,  $\gamma$ -LAO and  $\delta$ -LAO, were investigated by using first principles calculations. For the exchange-correlation functional, the generalized-gradient approximation (GGA) was used in comparison with the Heyd-Scuseria-Ernzerhof (HSE) hybrid functional. The projector augmented wave (PAW) method was used to allow a relatively low-energy cutoff plane wave expansion outside the core region while maintaining the complicated description of the wave function near the core region. Our calculations showed that both HSE and GGA calculations provided comparable energetic properties. For the electronic properties, the HSE calculations do not suffer from band gaps underestimations but require much more computation demand. The HSE calculations showed that, under hydrostatic pressure, the natural phase  $\gamma$ -LAO is in energetic equilibrium with the high-pressure phase  $\delta$ -LAO at 2.3 GPa. The calculated equilibrium phase pressures are in a reasonable agreement with the experimental transformation pressure (2 GPa) obtained by an anvil cell technique [J. Solid State Chem. 188, 6 (2008)]. However, the transformation pressure obtained by a shock recovery technique [J. Solid State Chem. 177, 5 (2004)] is much higher (9 GPa). The large difference in the transformation pressure obtained by different experimental techniques could be attributed to the energetic transformation barrier between the two phases. Based on HSE calculations, the enthalpy barrier for the homogeneous transformation between the two phases at the phase equilibrium pressures is 1.8 eV. The band structures and the partial density of states of both  $\gamma$ -LAO and  $\delta$ -LAO at the ambient pressure are also presented.*

**Keywords**  $\text{LiAlO}_2$ ; first-principles calculations; high pressure

### Introduction

Lithium aluminate,  $\text{LiAlO}_2$ , henceforth LAO, has potential applications in the energy industry as lithium battery cathodes and electrolyte tiles for molten carbonate fuel cells

Received July 23, 2013; in final form January 12, 2014.

\*Corresponding author. E-mail: sukit@sut.ac.th

Color versions of one or more of the figures in the article can be found online at [www.tandfonline.com/ginf](http://www.tandfonline.com/ginf).

(MCFE) [1]. It has been reported that LAO has at least four different phases, the hexagonal  $\alpha$ -phase [2] the monoclinic  $\beta$ -phase [2, 3], the tetragonal  $\gamma$ -phase [4], and the tetragonal  $\delta$ -phase [5]. The  $\gamma$ -LAO has attracted much attention as a promising substrate for GaN-based laser diodes. This is because the lattice mismatch between  $\gamma$ -LAO and GaN is only  $-1.4\%$  along [001] LAO and [11 $\bar{2}$ 0] GaN and  $-0.1\%$  along [010] LAO and [0001] GaN [6, 7]. The  $\gamma$ - to  $\delta$ -phase transformation of LAO has been experimentally studied using several techniques and a wide range of the phase transformation pressure has been reported, i.e. from 2 GPa based on an anvil cell technique [8] to 9 GPa based on a shock recovery technique [5]. However, to our knowledge, there is no computational study on the transformation published. Here, the  $\gamma$ - to  $\delta$ -phase transformation under hydrostatic pressure of LAO was investigated using first principles calculations within both Heyd-Scuseria-Ernzerhof (HSE) hybrid functional and generalized-gradient approximation (GGA). In addition, the electronic properties of both phases were also studied.

### Computational Methods

First principles calculations were carried out to study LAO in the  $\gamma$ - phase and the high-pressure phase,  $\delta$ -phase. The calculations were based on the density functional theory (DFT) and the projector-augmented wave method (PAW) [9] as implemented in the VASP code [10]. All calculations were carried out using a high performance computer system at the Synchrotron Light Research Institute (SLRI), Thailand. For an exchange-correlation functional, both generalized gradient approximation (GGA) and Heyd-Scuseria-Ernzerhof (HSE) hybrid functional calculation [11] were used. A cutoff energy for the plane wave basis set was set at 500 eV and 520 eV for GGA and HSE calculations, respectively. A  $k$ -point sampling mesh of  $10 \times 10 \times 8$  according to the Monkhorst-Pack scheme [12] was used for the GGA calculations. For the HSE calculations, which required a higher computational demand, a reduced  $k$ -point sampling mesh of  $2 \times 2 \times 2$  was used. In the HSE calculations, a consistent screening parameter of  $\mu = 0.2 \text{ \AA}^{-1}$  was used for the screened nonlocal exchange as suggested for the HSE06 functional [11]. The  $\gamma$ -LAO and  $\delta$ -LAO structures are described by the lattice parameters  $a$ ,  $b$ , and  $c$  as shown in Fig 1(a). To study a homogeneous phase transformation between the two phases, a common unit cell size containing 16 atoms (4 Li atoms, 4 Al atoms, and 8 O atoms) was used (see Fig. 1(b)). The stability of each phase can be determined by analyzing the enthalpy as a function of cell shape defined using  $c/a$  and  $b/a$ , as described in detail in Ref. [13]. The enthalpy ( $H$ ) under hydrostatic pressure is defined as

$$H = E + pV,$$

where  $E$  is the energy per unit cell,  $p$  is the pressure, and  $V$  is the unit cell volume. For each  $c/a$  and  $b/a$  pair, the unit cell volume,  $V$ , is allowed to relax to minimize  $H$ . In principle, for a given pressure,  $p$ , the  $c/a$  and  $b/a$  that give the lowest enthalpy define the most stable cell shape. In practice, because  $b/a$  is the same for both  $\gamma$ -LAO and  $\delta$ -LAO phases, the  $b/a$  value is fixed at 1 and only the  $c/a$  ratio is varied in the range from 1.20–2.15.

### Results and Discussion

The  $\gamma$ - LAO to  $\delta$ -LAO phase transformation occurs through the formations of addition O-Li bonds and O-Al bonds labeled by the dashed squares A and B in Fig. 1(b) and 1(c).



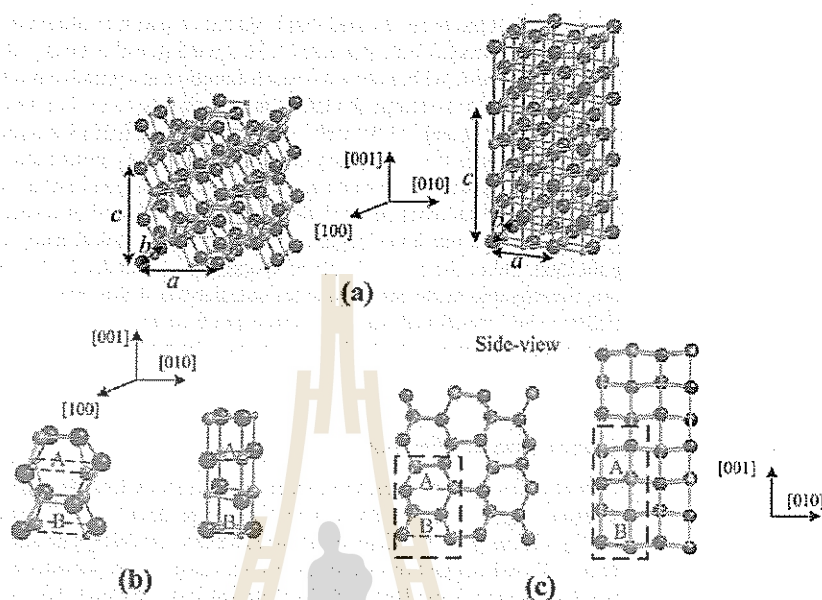


**Figure 1.** (a) Schematic illustration of the natural and high-pressure phases of  $\text{LiAlO}_2$ , i.e.,  $\gamma$ -LAO (left) and  $\delta$ -LAO (right) phases. Large spheres represent oxygen atoms, medium spheres: Al, and small spheres: Li. (b) The common unit cells of the two phases ( $\gamma$ -LAO and  $\delta$ -LAO), containing 16 atoms, used in the calculations. Red dashed squares A and B highlight the bond formation during the phase transformation (see text, for detail). (c) The side view of the crystal with the dashed black rectangles showing a unit cell.

The Li, Al and O atoms at the corner of A and B squares move toward the square center to form new bonds; making each of them 6-fold coordinated (see Fig 1(b) and 1(c)). While we only selectively labeled the dashed squares to highlight the bond formations, actual bond formations on the planes between A and B squares are also taken place. These bond formations lead to the elongation of the cell shape along the  $c$ -axis. The calculated lattice parameters of the  $\gamma$ -LAO and  $\delta$ -LAO for both HSE and GGA calculations in comparison with the literatures are tabulated in Table. 1. Similar to the trend generally observed in other materials, the GGA calculations give larger lattice parameters and cell volumes in comparison with the corresponding HSE calculations. Nevertheless, the two sets of calculations give the lattice parameters in agreement to within 1% and the cell volumes to within 3%. Our calculated results are also in good agreement with other computational results. The agreement is even better when we compare the results from the calculations that used the same exchange-correlation functional.

The calculated total energies, as a function of volume for both  $\gamma$ -LAO and  $\delta$ -LAO, are shown in Fig. 2(a). The minimum energy point of  $\gamma$ -LAO is lower than  $\delta$ -LAO, indicating that  $\gamma$ -LAO is the stable phase at ambient pressure. These energy curves are called the energy of states (EOS). The phase equilibrium pressure is defined by the slope of the common tangent between the EOS curves of the two phases shown using the dashed line in Fig. 2(a). From the slopes, we obtained the phase equilibrium pressures

18/[174]

W. Sailuam *et al.*

**Table 1**  
Calculated lattice parameters ( $a$ ,  $b$  and  $c$ ), equilibrium volume ( $V$ ) and energy gap ( $E_g$ ) for  $\gamma$ -LAO and  $\delta$ -LAO from HSE and GGA calculations

Parameters	$\gamma$ -LAO			$\delta$ -LAO		
	Present			Present		
	HSE	GGA	Others	HSE	GGA	Others
$a$ (Å)	5.172	5.221	5.223 <sup>a</sup> 5.168 <sup>b</sup> 5.18 <sup>c</sup>	3.866	3.923	3.886 <sup>d</sup>
$b$ (Å)	Same as $a$ , due to symmetry			Same as $a$ , due to symmetry		
$c$ (Å)	6.250	6.308	6.309 <sup>a</sup> 6.268 <sup>b</sup> 6.29 <sup>c</sup>	8.328	8.397	8.300 <sup>d</sup>
$V$ (Å <sup>3</sup> )	41.79	43.04	43.03 <sup>a</sup> 42.19 <sup>b</sup> 41.86 <sup>c</sup>	31.34	32.19	
(eV)	6.56( $E_d$ )	4.64( $E_d$ )	6.2 <sup>f</sup>	8.11( $E_i$ )	5.74( $E_i$ )	

<sup>a</sup> DFT-GGA calculations by Wu *et al.* [17].

<sup>b</sup> XRD measurement by Marzio [4].

<sup>c</sup> Li nuclear magnetic resonance measurements by Heitjans *et al.* [18].

<sup>d</sup> shock recovery technique by Li *et al.* [5].

<sup>f</sup> measured from a single crystal growth by Czochralski method by Hao Teng *et al.* [15].

*Note:* The  $E_d$  and  $E_i$  in parentheses indicate that the band gaps are direct and indirect, respectively.

of 2.3 GPa and 3.1 GPa for the HSE and GGA calculations, respectively. The calculated equilibrium pressure is in a reasonable agreement with the transformation pressure of 2 GPa obtained by an anvil cell technique [8]. Note, however, that the value obtained by a shock recovery technique is much higher at 9 GPa [5]. The strong dependency on the measuring technique of the transformation pressure could be attributed to a transformation barrier between the two phases. To overcome the barrier, a higher pressure than the equilibrium value is needed. Different techniques might have different difficulty in overcoming this barrier.

While the actual transformation process is too complicated to simulate with the DFT calculations, the calculations of homogeneous phase transformation were proven to be useful and possible to be performed with DFT level [14]. Here, we studied the homogeneous transformation between  $\gamma$ -LAO and  $\delta$ -LAO. This was done by calculating the enthalpy,  $\Delta H = \Delta E + p\Delta V$ , along the path  $b/a = 1.00$  at different pressures, where,  $E$  and  $V$  were taken at the volume for which the enthalpy was minimized. The  $\Delta$  sign means the difference from  $\delta$ -LAO. The enthalpy curves for different pressures are shown in Fig. 2(b). At an ambient pressure,  $\gamma$ -LAO has lower enthalpy than  $\delta$ -LAO by  $\sim 0.6$  eV and  $\sim 0.8$  eV for the HSE and GGA calculations, respectively. At higher pressures, the enthalpy differences between the two phases decrease. The enthalpies of both phases ( $\gamma$ -LAO and  $\delta$ -LAO) are equal at  $p = 2.3$  GPa and 3.1 GPa for the HSE and GGA calculations, respectively. At this pressure, the two phases are in equilibrium. This is equivalent to the phase equilibrium pressure calculated from the common tangent between the EOS curves of the two phases. Above the phase equilibrium pressure,  $\delta$ -LAO turn to be more stable (has lower enthalpy). At the equilibrium pressure, it can be seen that the transformation barriers between the two phases are  $\sim 1.7$  eV and  $\sim 1.5$  eV for the HSE and GGA calculations, respectively. These

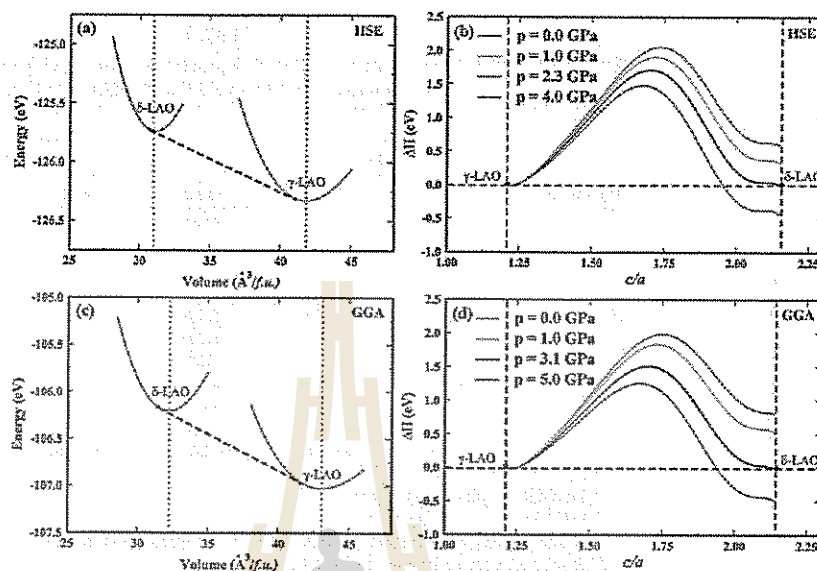


**Figure 2.** (a) The calculated HSE total energy as a function of volume for  $\gamma$ -LAO and  $\delta$ -LAO and the common tangent construction. (b) The enthalpy as a function of  $c/a$  ratio at various pressures. (The  $c/a$  ratio can be considered as the transformation coordinate of the homogeneous transformation from  $\gamma$ -LAO to  $\delta$ -LAO.) The black curve shows the enthalpy at the phase equilibrium pressure where both phases have the same enthalpy. The highest enthalpy point between the two phases defines the transformation barrier. (c) and (d) are the same as (a) and (b) but calculated using GGA functional.

transformation barriers are quite high and would certainly raise the transition pressure in real experiment beyond the phase equilibrium pressure. In order for the transition to take place, not only the enthalpy of the targeted phase has to be equal or lower than the initial phase, but the enthalpy barrier between the two phases also has to be sufficiently low [13]. To lower the barrier, often the pressure has to be increased passed the equilibrium pressure. Therefore, it is not surprising that the transition pressure can go up as high as 9 GPa in the shock recovery technique [5].

Next, we look at the electronic properties of  $\gamma$ -LAO and  $\delta$ -LAO. The band structures of both phases at the ambient pressure calculated using HSE and GGA are shown in Fig. 3 and Fig. 4, respectively. From the band structures we can see that  $\gamma$ -LAO has a direct band gap with the band gap values of 6.56 eV and 4.64 eV for HSE and GGA calculations, respectively. Unlike  $\gamma$ -LAO,  $\delta$ -LAO has an indirect band gap with the band gap values of 8.11 eV and 5.74 eV for HSE and GGA calculations, respectively. These large band gaps indicate that both phases of LAO are insulators. The band gap values are shown in Table 1 in comparison with the known experimental value for  $\gamma$ -LAO. For  $\delta$ -LAO, to our knowledge, no experimental band gap value has been reported. We can see that the band gap value of  $\gamma$ -LAO obtained by GGA calculation is underestimated compared to the experimental value due to well-known DFT problems, as expected. On the other hand, HSE calculations [15] give the band gap in a good agreement with the

20/[176]

W. Sailuam et al.

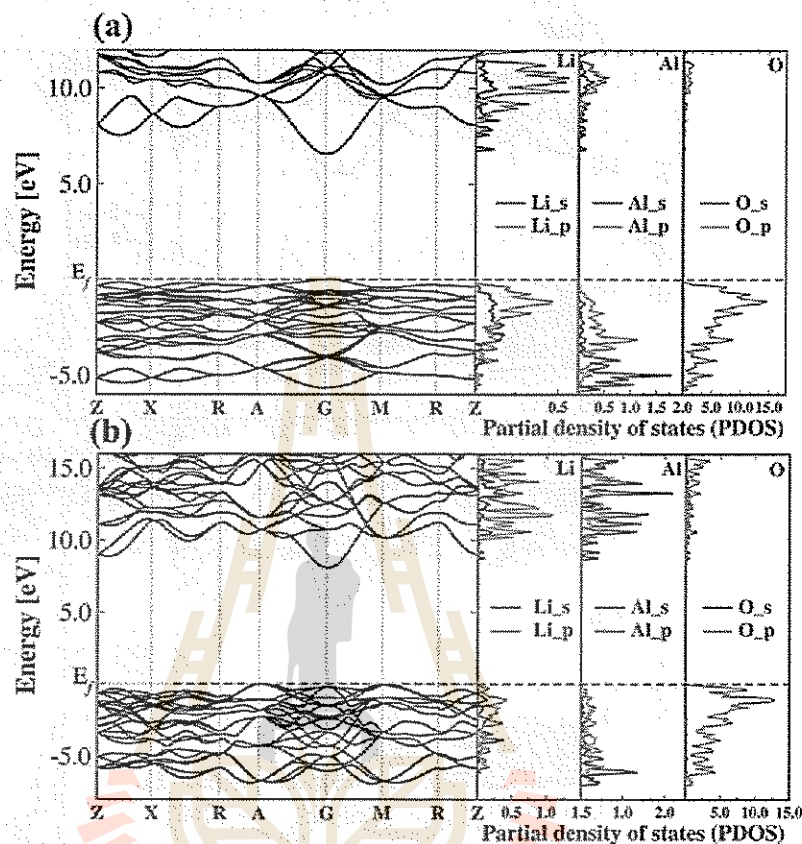


Figure 3. Electronic band structures and partial density of states (PDOS) of (a)  $\gamma$ -LAO and (b)  $\delta$ -LAO obtained from HSE calculations. The special  $k$ -points used for the band structures plot are according to the cubic Brillouin zone defined in Ref. [16].

experiment with the error of only  $\sim 5\%$ . Similar accuracy of the calculated band gap can be expected for the high-pressure phase where there is no experimental value to compare. To investigate the source of the electron states near the band edges, the partial density of states (PDOS) were calculated (Fig. 3 and Fig. 4). Both HSE and GGA calculations gave similar PDOS. Note that, because of a limited  $k$ -point sampling used, the PDOS of HSE calculations appears to be discontinuous especially near the conduction band minimum. If more  $k$ -points were used, the PDOS would be continuous similar to what obtained by GGA calculations. For  $\gamma$ -LAO, the valence band maximum is dominated by O  $2p$  states with some contributions from Li  $p$ . The conduction band minimum is dominated by Li  $s$ . For  $\delta$ -LAO, the valence band maximum is dominated by O  $2p$  states with some contributions from of Al  $p$  and Li  $p$  states. The conduction band minimum is dominated by Al  $s$ .

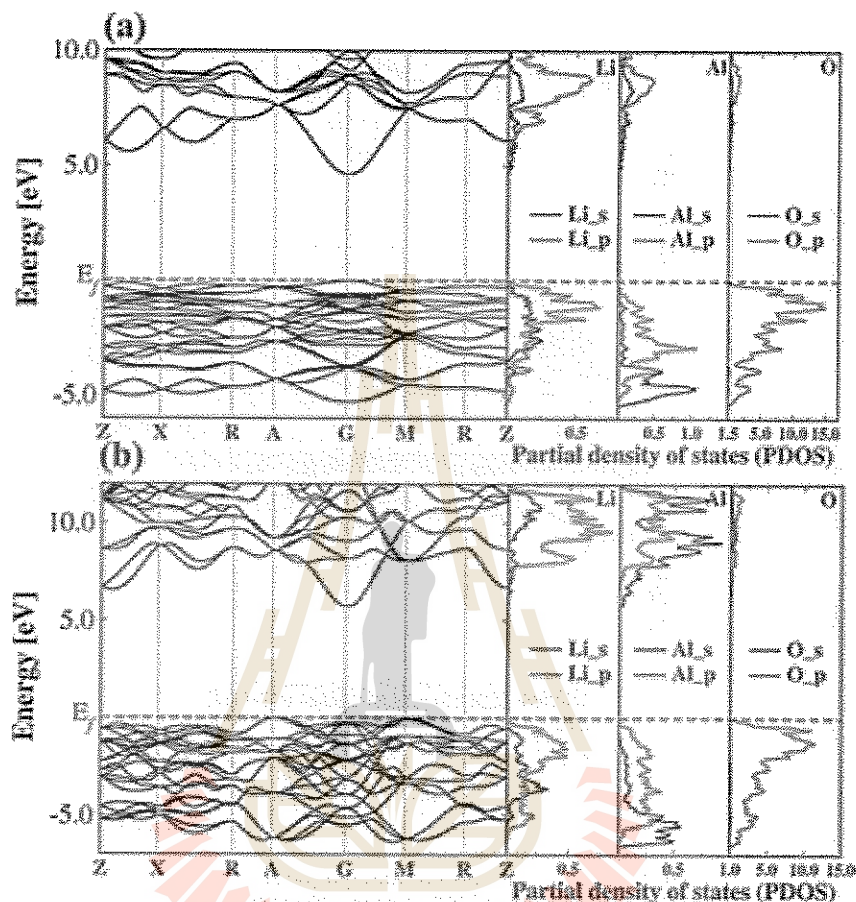


Figure 4. Electronic band structures and partial density of states (PDOS) of (a)  $\gamma$ -LAO and (b)  $\delta$ -LAO obtained from GGA calculations.

### Conclusions

$\text{LiAlO}_2$  in the natural and high-pressure phases, namely  $\gamma$ -LAO and  $\delta$ -LAO were studied by first principles calculations with HSE and GGA functional. By analyzing the equation of states of both phases, the natural phase  $\gamma$ -LAO is in thermodynamic equilibrium with the high-pressure phase  $\delta$ -LAO at 2.3 GPa and 3.1 GPa based on the HSE and GGA calculations, respectively. The homogeneous phase transformation between the  $\gamma$ -LAO and  $\delta$ -LAO was also studied. By varying the lattice parameter  $c/a$ , the transformation path and the homogenous transformation barrier was determined. The electronic band structures and the partial density of states of both phases at the ambient pressure were also calculated and reported. HSE calculations showed that  $\gamma$ -LAO has a direct band gap with the band gap value of 6.54 eV in a good agreement with the experimental values of 6.2 eV. On the other hand, GGA calculations gave the band gap value significantly lower, i.e., 4.64 eV, due to the well-known DFT problems. With HSE calculations, the band gap

22/[178]

W. Sailuam et al.

of the high-pressure phase  $\delta$ -LAO was predicted to be indirect with the value of 3.11 eV, which is 24% larger than the band gap of the natural phase.

### Funding

This work was partially supported by NANOTEC, NSTDA (Thailand) through its Center of Excellence Network program. One of the authors (WS) is supported by the Development and Promotion of Science and Technology Talents Project.

### References

1. G. Ceder, Y. M. Chiang, D. R. Sadoway, M. K. Aydinol, Y. I. Jang, and B. Huang, Identification of cathode materials for lithium batteries guided by first-principles calculations. *Nature*. **392**, 694–696 (1998).
2. M. Marzino, and J. P. Remick, Polymorphism of  $\text{LiMO}_2$  Compounds and High-Pressure Single-Crystal Synthesis of  $\text{LiBO}_2$ . *The Journal of Chemical Physics*. **44**, 3348–3353 (1966).
3. J. Zou, Y. Dong, S. Zhou, Y. Sun, W. Jun, J. Zhou, T. Huang, S. Yang, and H. Zhou, Study on the hydrolytic property and thermal stability of  $\text{LiAlO}_2$  substrate. *Journal of Crystal Growth*. **294**, 4 (2006).
4. M. Marzino, The Crystal Structure and Anomalous Dispersion of  $\gamma$ - $\text{LiAlO}_2$ . *Acta Crystallographica*. **19**, 396 (1965).
5. X. Li, T. Kobayashi, F. Zhang, K. Kimoto, and T. Sekine, A new high-pressure phase of  $\text{LiAlO}_2$ . *Journal of Solid State Chemistry*. **177**, 5 (2004).
6. X. Ke, X. Jun, D. Peizhen, Z. Yongzong, Z. Guoqing, Q. Rongsheng, and F. Zujie,  $\gamma$ - $\text{LiAlO}_2$  single crystal: a novel substrate for GaN epitaxy. *Journal of Crystal Growth*. **193**, 127 (1998).
7. E. S. Hellman, Z. L.-W., and D. N. E. Buchanan, MRS. *Internet J. Nitride Semicond. Res.* **2**, 30 (1997).
8. L. Lei, D. He, Y. Zou, W. Zhang, Z. Wang, M. Jiang, and M. Du, Phase transitions of  $\text{LiAlO}_2$  at high pressure and high temperature. *Journal of Solid State Chemistry*. **181**, 6 (2008).
9. P. E. Blöchl, Projector augmented-wave method. *Physical Review B*. **50**, 17953 (1994).
10. G. Kresse and J. Furthmüller, Efficiency of ab-initio total energy calculations for metals and semiconductors using a plane-wave basis set. *Computational Materials Science*. **6**, 15–50 (1996).
11. J. Heyd, G. E. Scuseria, and M. Ernzerhof, Hybrid functionals based on a screened Coulomb potential. *The Journal of Chemical Physics* **118**, 8207 (2003).
12. J. D. Pack and H. J. Monkhorst, Special points for Brillouin-zone integrations. *Physical Review B*. **13**, 5188 (1976).
13. S. Jungthawan and S. Limpjumnong, First-principles study of the wurtzite-to-rocksalt homogeneous transformation in ZnO: A case of a low-transformation barrier. *Physical Review B*. **70**, 054104 (2004).
14. K. Sarasamak, A. J. Kulkarni, M. Zhou, and S. Limpjumnong, Stability of wurtzite, unbuckled wurtzite, and rocksalt phases of SiC, GaN, InN, ZnO, and CdSe under loading of different triaxialities. *Physical Review B*. **77**, 024104 (2008).
15. H. S. Z. Teng, H. Lin, T. Jia, X. Hou, and J. Wang, Growth and characterization of high-quality Mn-doped  $\text{LiAlO}_2$  single crystal. *Chinese Optical L*. **8**, 4 (2010).
16. S. Limpjumnong, and W. R. L. Lambrecht, Theoretical study of the relative stability of wurtzite and rocksalt phases in MgO and GaN. *Physical Review B*. **63**, 104103 (2001).
17. S. Q. Wu, Z. F. Hou, and Z. Z. Zhu, First-principles study on the structural, elastic, and electronic properties of  $\gamma$ - $\text{LiAlO}_2$ . *Computational Materials Science*. **46**, 221–224 (2009).
18. S. Indris, and P. Heitjans, Local electronic structure in a  $\text{LiAlO}_2$  single crystal studied with  $^7\text{Li}$  NMR spectroscopy and comparison with quantum chemical calculations. *Physical Review B*. **74**, 245120 (2006).

Manuscript published in Physical Chemistry Chemical Physics

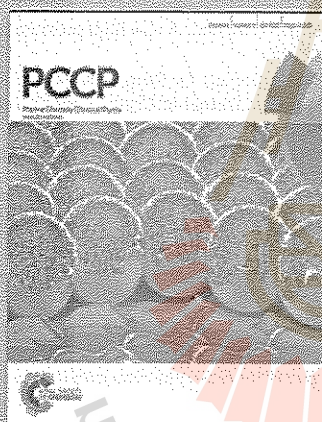


View Article Online  
View Journal

# PCCP

Accepted Manuscript

This article can be cited before page numbers have been issued, to do this please use: N. Arin, W. Sattum, S. Limprumrong and A. Koldak, *Phys. Chem. Chem. Phys.*, 2016, DOI: 10.1039/C6CP00031E



This is an Accepted Manuscript, which has been through the Royal Society of Chemistry peer review process and has been accepted for publication.

Accepted Manuscripts are published online shortly after acceptance, before technical editing, formatting and proof reading. Using this free service, authors can make their results available to the community, in citable form, before we publish the edited article. We will replace this Accepted Manuscript with the edited and formatted Advance Article as soon as it is available.

You can find more information about Accepted Manuscripts in the Information for Authors.

Please note that technical editing may introduce minor changes to the text and/or graphics, which may alter content. The journal's standard Terms & Conditions and the Ethical guidelines still apply. In no event shall the Royal Society of Chemistry be held responsible for any errors or omissions in this Accepted Manuscript or any consequences arising from the use of any information it contains.



[www.rsc.org/pccp](http://www.rsc.org/pccp)



PCCP

PAPER



Cite this: *Phys. Chem. Chem. Phys.*,  
2016, 18, 29561

## Reduced overpotentials for electrocatalytic water splitting over Fe- and Ni-modified BaTiO<sub>3</sub>

Nongnuch Artrith,<sup>†‡\*a</sup> Wutthigrai Sailuam,<sup>‡\*a,b</sup> Sukit Limpijumnong<sup>b</sup> and Alexie M. Kolpak<sup>a</sup>

Water electrolysis is a key technology for the replacement of fossil fuels by environmentally friendly alternatives, but state-of-the-art water oxidation catalysts rely on rare elements such as Pt groups and other noble metals. In this article, we employ first-principles calculations to explore the potential of modified barium titanate (BaTiO<sub>3</sub>), an inexpensive perovskite oxide that can be synthesized from earth-abundant precursors, for the design of efficient water oxidation electrocatalysts. Our calculations identify Fe and Ni doping as a means to improve the electrical conductivity and to reduce the overpotential required for water oxidation over BaTiO<sub>3</sub>. Based on computed Pourbaix diagrams and pH/potential-dependent surface phase diagrams, we further show that BaTiO<sub>3</sub> is stable under reaction conditions and is not sensitive with respect to poisoning by reaction intermediates and hydrogen adsorption. This proof of concept demonstrates that even minor compositional modifications of existing materials may greatly improve their catalytic activity, a fact that is often neglected when larger composition spaces are screened.

Received 1st September 2016,  
Accepted 30th September 2016

DOI: 10.1039/c6cp06031e

www.rsc.org/pccp

### Introduction

Water splitting into oxygen and hydrogen gas is an attractive technology for the production of renewable alternative fuels,<sup>1</sup> especially in combination with fuel cells.<sup>2</sup> Under standard conditions, the ideal voltage for the net water splitting reaction is 1.23 V, which is the potential difference between the anodic oxygen evolution reaction (OER; water oxidation) and the cathodic hydrogen evolution reaction (HER; water reduction). The OER half reaction that involves four elementary charge-transfer steps is, however, typically associated with large overpotentials and thus catalysts are required to increase the energy efficiency.<sup>3</sup> While photocatalytic water splitting (*i.e.* driving the reaction by light-induced currents) is appealing, it requires catalysts with simultaneous activity for both OER and HER that at the same time also absorb light in the visible spectrum.<sup>3</sup> Electrocatalytic water splitting (water electrolysis), on the other hand, allows the individual tuning of cathode and anode materials so that generally greater energy efficiency can be achieved. Unfortunately, the most efficient and stable known OER catalysts rely on rare and expensive Pt and noble metal

based alloys<sup>4,5</sup> rendering a global fuel economy based on water electrolysis nonviable.

On the search for inexpensive, earth-abundant, and environmentally benign alternatives for Pt group catalysts, perovskite oxides have emerged as a promising class of materials.<sup>6,7</sup> Owing to their tunable electronic properties, perovskite-based materials are among the most efficient known photocatalysts for water splitting.<sup>1,3,8,9</sup> Recently, an improved understanding of the electronic-structure/reactivity relationship has further spurred the interest in perovskites as inexpensive catalysts for water electrolysis.<sup>10,11</sup> Motivated by these new insights, we explore in the present article to which extent the catalytic reactivity of barium titanate (BaTiO<sub>3</sub>) can be controlled by slightly altering its chemical composition.

BaTiO<sub>3</sub> is one of the most thoroughly investigated ferroelectric oxides and is used in diverse technical applications as a piezoelectric material, a dielectric ceramic, and as a crystal in non-linear optics. As a catalyst, Ni-supported BaTiO<sub>3</sub> is active for CO<sub>2</sub> reforming,<sup>12</sup> and also water electrolysis over BaTiO<sub>3</sub> electrodes has been reported.<sup>13,14</sup> Interestingly, in some cases small compositional modifications by introducing transition-metal dopants on the Ti site (the B site in the general ABO<sub>3</sub> perovskite formula) have been found to increase the catalytic activity of BaTiO<sub>3</sub> significantly. For example, Pd-modified BaTiO<sub>3</sub> efficiently catalyzes NO<sub>x</sub> reduction,<sup>15</sup> and Cr-modified BaTiO<sub>3</sub> catalyzes the reduction of nitrobenzene and aniline.<sup>16</sup> A strong impact of compositional modification on the catalytic activity has also been reported for other oxides<sup>17,18</sup> and carbides,<sup>19,20</sup> which opens up exciting opportunities for the

<sup>a</sup> Department of Mechanical Engineering, Massachusetts Institute of Technology, Cambridge, MA, USA. E-mail: nartrith@alum.mit.edu

<sup>b</sup> School of Physics and NANOTEC-SUT Center of Excellence on Advanced Functional Nanomaterials, Suranaree University of Technology, Nakhon Ratchasima 30000, Thailand

<sup>†</sup> Present address: Department of Materials Science and Engineering, University of California, Berkeley, CA, USA

<sup>‡</sup> These authors contributed equally to this work.





For optimal computational efficiency, geometry optimizations with FHI-aims employed the predefined light basis set (4th order expansion of the Hartree potential, radial integration grids with 302 points in the outer shell, and a tier 1 basis set). Structural energies were subsequently refined with the tight basis set (6th order expansion, 434 grid points, and a tier 2 basis set). All these calculations employed  $k$ -point meshes corresponding to  $8 \times 8 \times 8$  for the BaTiO<sub>3</sub> bulk structure.

#### Structure models

At room temperature BaTiO<sub>3</sub> crystallizes in a tetragonal structure (space group  $P4mm$ ) in which the atoms are slightly displaced from their sites in the ideal symmetric cubic ( $Pm\bar{3}m$ ) perovskite structure.<sup>26,46,47</sup> This atomic displacement results in ferroelectric polarization parallel to the (001) plane. In this work we consider the non-polar (001) surface.<sup>48,49</sup>

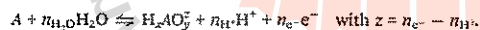
Symmetric surface slab models with a surface area of  $2 \times 2$  surface unit cells, a thickness of 5 atomic layers, and 15 Å of vacuum were used to model adsorption of OER intermediates and hydrogen on BaTiO<sub>3</sub> surfaces. The lower 3 layers of the slabs were kept fixed at the bulk atomic positions, and the topmost 2 layers were fully relaxed. An example of a surface slab model is shown in Fig. 1d.

At 120 °C, BaTiO<sub>3</sub> undergoes a phase transition to the cubic ( $Pm\bar{3}m$ ) perovskite structure, which is thus the relevant structure under synthesis conditions. To estimate the feasibility of Ni and Fe incorporation, we therefore considered the formation energy of mixed compositions in the cubic structure.

#### Pourbaix and surface-phase diagrams

Pourbaix diagrams map the preferred states of an electrochemical system in equilibrium as a function of the electrochemical potential and the pH value and, thus, allow in the context of this work to predict whether an oxide is stable or if dissolution is thermodynamically favorable. To estimate the stability of the catalyst under operation conditions, we computed Pourbaix and pH/potential-dependent surface phase diagrams.

The Pourbaix diagram for a chemical species  $A$  is constructed by considering all relevant electrochemical equilibria of  $A$  in aqueous solution



Following the Nernst equation, the free energy of the aqueous species,  $\text{H}_z\text{AO}_y^z$ , relative to a free atom of species  $A$  can then be estimated as

$$\Delta G = \Delta G_{\text{SHE}}^{\circ} - n_{\text{e}^-}eU_{\text{SHE}} - n_{\text{H}^+}k_{\text{B}}T2.3\text{pH} + k_{\text{B}}T \ln a_{\text{H}_z\text{AO}_y^z},$$

where  $\Delta G_{\text{SHE}}^{\circ}$  is the free energy relative to the standard hydrogen electrode (SHE) under standard ambient conditions,  $eU_{\text{SHE}}$  is the energy due to the electrochemical potential  $U_{\text{SHE}}$  relative to the SHE,  $a_{\text{H}_z\text{AO}_y^z}$  is the activity,  $k_{\text{B}}$  is Boltzmann's constant, and  $T$  is the temperature (for a derivation see ref. 50). Note that the factor of 2.3 in front of the pH increases from the approximate conversion of the natural to the common logarithm.

The relevant electrochemical equilibria for Ba and Ti are shown in Table 1. Since uncorrected DFT energies are not sufficiently accurate to predict reliable Pourbaix diagrams,<sup>51</sup> measured values of the relative free energies under standard conditions,  $\Delta G^{\circ}$ , were obtained from thermochemical tables.<sup>41</sup> However, DFT surface-slab calculations were employed to evaluate the adsorption energy of reaction intermediates on the BaTiO<sub>3</sub> surface and the defect formation energies for the creation of surface Ba, Ti, or O vacancies

$$\Delta G_{\text{surface}} \approx E_{\text{recon}}^{\text{DFT}} - E_{\text{ideal}}^{\text{DFT}} + \Delta G_{\text{ads}},$$

where  $E_{\text{ideal}}^{\text{DFT}}$  and  $E_{\text{recon}}^{\text{DFT}}$  are the energies of the ideal and the reconstructed surfaces, and  $\Delta G_{\text{ads}}$  is the free energy change of the adsorbants. Combining these DFT energies with the solvation free energies from Table 1, the stable surface phases at different pH values and electrochemical potentials were determined.<sup>50</sup> A detailed description of the approach can be found in ref. 50.

As is commonly done,<sup>52</sup> the binding energy of O<sub>2</sub> was referenced to the energy of a water molecule in the gas phase,  $\frac{1}{2}E^{\text{O}_2} = E^{\text{H}_2\text{O}} - E^{\text{H}_2}$  because of the large DFT error for molecular oxygen.

#### Reaction free energy profiles

We consider the catalytic oxygen evolution reaction (OER) by water oxidation in four elementary reaction steps each involving

Table 1 Relative free energies of species occurring in the Ba and Ti Pourbaix diagrams under standard ambient conditions (25 °C and 1 bar). The free energies relative to the standard hydrogen electrode (SHE),  $\Delta G_{\text{SHE}}^{\circ}$ , were taken from ref. 41. All activities  $a_A$  were taken to be equal to  $10^{-8}$  M

Electrochemical equilibria	$\Delta G_{\text{SHE}}^{\circ}$ (eV)	$\Delta G(U, \text{pH})$ (eV)
$\text{Ba} \rightleftharpoons \text{Ba}^{2+} + 2\text{e}^-$	-5.81	$-2eU_{\text{SHE}} + 0.026 \ln a_{\text{Ba}^{2+}} - 5.81$
$\text{Ba} + \text{H}_2\text{O} \rightleftharpoons \text{Ba}(\text{OH})^+ + \text{H}^+ + 2\text{e}^-$	-5.11	$-2eU_{\text{SHE}} - 0.056\text{pH} + 0.026 \ln a_{\text{Ba}(\text{OH})^+} - 5.11$
$\text{Ba} + 2\text{H}_2\text{O} \rightleftharpoons \text{BaO}_2(\text{s}) + 4\text{H}^+ + 4\text{e}^-$	-1.08	$-4eU_{\text{SHE}} - 0.236\text{pH} - 1.08$
$\text{Ti} \rightleftharpoons \text{Ti}^{2+} + 2\text{e}^-$	-3.63	$-2eU_{\text{SHE}} + 0.026 \ln a_{\text{Ti}^{2+}} - 3.63$
$\text{Ti} + 2\text{H}_2\text{O} \rightleftharpoons \text{TiO}_2^{2+} + 4\text{H}^+ + 6\text{e}^-$	0.59	$-6eU_{\text{SHE}} - 0.236\text{pH} + 0.026 \ln a_{\text{TiO}_2^{2+}} + 0.59$
$\text{Ti} + 2\text{H}_2\text{O} \rightleftharpoons \text{TiO}_2(\text{s}) + 4\text{H}^+ + 4\text{e}^-$	-3.91	$-4eU_{\text{SHE}} - 0.236\text{pH} - 3.91$
$2\text{H}_2\text{O} + 2\text{e}^- \rightleftharpoons 2\text{OH}^- + \text{H}_2(\text{g})$	0.00	$2eU_{\text{SHE}} + 0.118\text{pH}$
$\frac{1}{2}\text{O}_2(\text{g}) + 2\text{H}^+ + 2\text{e}^- \rightleftharpoons \text{H}_2\text{O}$	-2.46	$2eU_{\text{SHE}} + 0.118\text{pH} - 2.46$

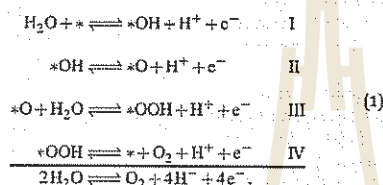
Paper

PCCP

Table 2 Zero-point energy corrections ( $\Delta ZPE$ ) and entropic contributions ( $T\Delta S$ ) to the free energy for adsorbed and gas-phase molecules under standard conditions taken from ref. 55

Species	$T\Delta S$ (eV)	$\Delta ZPE$ (eV)
$H_2O(g)$	0.67	0.56
$H_2(g)$	0.41	0.27
$^*O$	0.00	0.05
$^*OH$	0.00	0.35
$^*OH$	0.00	0.41
$^*H$	0.00	0.24

the transfer of a single electron-proton pair ( $*$  represents the catalyst adsorption site):



The reaction free energies of these charge transfer steps at the ideal equilibrium potential ( $U = 1.23$  V) determine the overpotential  $\eta$  that is required to drive the overall reaction.<sup>52–54</sup>

Using the computational standard hydrogen electrode (CSHE) approach, the reaction free energy  $\Delta G$  of the charge transfer reaction  $AH \rightleftharpoons A + H^+ + e^-$  under standard ambient conditions ( $U = 0$  V,  $pH = 0$ ,  $p = 1$  bar,  $T = 25$  °C) can be related to the reaction  $AH \rightleftharpoons A + \frac{1}{2}H_2$ .<sup>52–54</sup> The reaction free energies of the individual charge transfer steps,  $\Delta G_I$ ,  $\Delta G_{II}$ ,  $\Delta G_{III}$ , and  $\Delta G_{IV}$ , were approximated as

$$\Delta G_i = \Delta E_i + \Delta ZPE_i - T\Delta S_i - eU, \tag{2}$$

where  $\Delta E_i$  was obtained as a difference of DFT energies, and the zero-point energy (ZPE) difference,  $\Delta ZPE_i$ , and the vibrational entropy contributions,  $T\Delta S_i$ , were taken from ref. 55 (see Table 2). The final term in eqn (2) accounts for the electrode potential  $U$  ( $e$  is the elementary charge). For a given catalyst, the overpotential is thus given by the smallest potential  $\eta$  such that for  $U = 1.23$  V +  $\eta$  all reaction steps are exothermic, i.e.  $\Delta G_i \leq 0$ .

As in the case of surface Pourbaix diagrams, the binding energy of molecular  $O_2$  was referenced to the energy of water.

## Results

### Energetics and electronic structure of Fe/Ni-modified BaTiO<sub>3</sub>

As a first sanity check whether the modification of BaTiO<sub>3</sub> by Fe and Ni doping on the perovskite  $B$  site can be feasible, we consider the formation energy of structures with mixed compositions in the cubic and the tetragonal perovskite structures. The formation energy  $E_f^{BaTi_{1-x}B_xO_3}$  of a structure with composition BaTi<sub>1-x</sub>B<sub>x</sub>O<sub>3</sub> ( $B = Fe, Ni$ ) relative to the end members BaTiO<sub>3</sub> and BaBO<sub>3</sub> is given by

$$E_f^{BaTi_{1-x}B_xO_3} = E^{BaTi_{1-x}B_xO_3} - (1-x)E^{BaTiO_3} - xE^{BaBO_3} \tag{3}$$

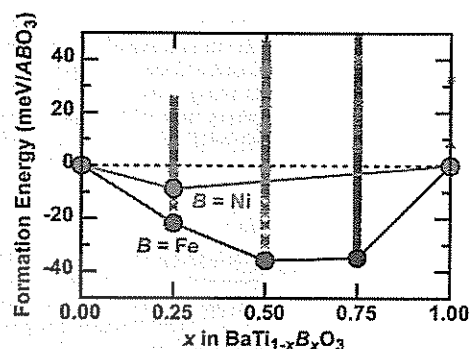


Fig. 2 Formation energies for BaTi<sub>1-x</sub>B<sub>x</sub>O<sub>3</sub> with  $B = Fe$  (red) and  $B = Ni$  (blue) in the cubic and tetragonal perovskite structures obtained from enumeration of 626 distinct atomic configurations and spin orderings. The (high-temperature) cubic BaTiO<sub>3</sub> structure was used as a reference for the formation energy, so that negative formation energies mean that doping of cubic BaTiO<sub>3</sub> with species  $B$  is facile. The stable compositions are indicated by filled circles and connected by solid lines. 820 unstable and metastable structures are shown as red stars (Fe) and blue triangles (Ni).

where  $E^{BaTi_{1-x}B_xO_3}$ ,  $E^{BaTiO_3}$ , and  $E^{BaBO_3}$  are total energies obtained from (VASP) DFT calculations. With this definition, negative formation energies mean that doping with species  $B$  is facile. The thermodynamically stable compositions lie on the lower convex hull of all negative formation energies.<sup>56</sup>

Fig. 2 shows the formation energies of compositions with 25%, 50%, and 75% Ti replaced by species  $B$ . These compositions were chosen as a proxy for the general mixing energetics, as they can be realized with relatively small numbers of atoms. To ensure convergence to the correct configurational and electronic ground state, we enumerated all symmetrically distinct Ti/ $B$  arrangements in structures with unit cells containing up to 8 ABO<sub>3</sub> formula units (i.e. 40 atoms) using a technique developed by Hart and coworkers.<sup>36–38</sup> Since the electronic convergence can be problematic (especially for compositions containing  $d^4$  Fe<sup>4+</sup>), every calculation was additionally repeated with different initial spin states (low spin/high spin) and spin orderings (ferromagnetic and antiferromagnetic) for all Fe and Ni atoms, so that a total of 626 configurations was evaluated. The energies of all of these structures are visualized in Fig. 2.

As seen in Fig. 2, the negative formation energies indicate that Ni and Fe doping of cubic BaTiO<sub>3</sub>, i.e. the stable BaTiO<sub>3</sub> structure under solid-state synthesis conditions, is energetically favorable in the bulk. Note, however, that the reference for Ni doping in the figure is the (hypothetical) cubic BaNiO<sub>3</sub> structure, whereas the thermodynamic ground state structure is actually hexagonal. The cubic reference was chosen as it allows us to estimate the tendency for phase separation in the same structural framework, which is the relevant quantity when only small amounts of Ni are doped into BaTiO<sub>3</sub>. The formation energies relative to the hexagonal BaNiO<sub>3</sub> structure (not shown in the figure) are generally greater than 0.2 eV/ABO<sub>3</sub>, which means that

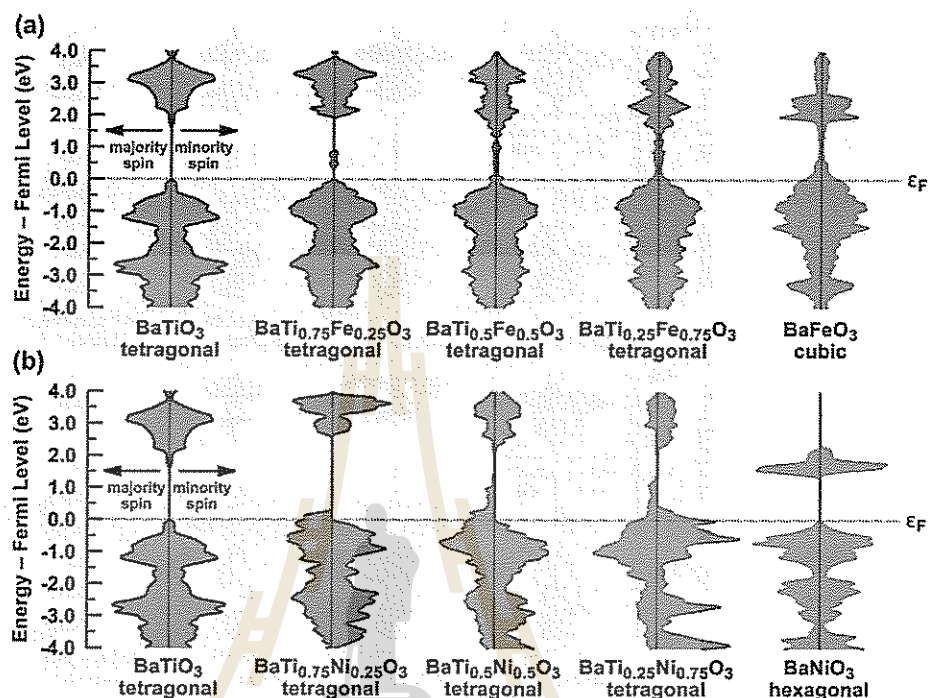


Fig. 3 Electronic density of states for pristine and (a) Fe-modified and (b) Ni-modified  $\text{BaTiO}_3$  compositions. For each structure, the majority spin density is shown to the left and the minority spin density to the right. All plots have been aligned at the Fermi level  $\epsilon_F$ . The tetragonal structure refers to space group  $P4mm$  and the hexagonal structure belongs to the space group  $P6_3/mmc$ .

compositions with comparable Ti and Ni concentrations are thermodynamically unstable against phase separation into the parent perovskites. For Fe there is no such ambiguity regarding the reference structure, as  $\text{BaFeO}_3$  forms in the cubic perovskite structure. Hence, our calculations predict with reasonable certainty that mixed compositions containing Fe and Ti on the B site can be synthesized.

The electronic density of states (DOS) was computed for the most stable structure at each composition to gain insight into the effect of compositional modification on the electronic structure and conductivity. The results are visualized in Fig. 3. Note that the band gap of  $\text{BaTiO}_3$ , predicted by our GGA calculations (1.7 eV) is significantly smaller than the band gap observed in optical absorption and electroabsorption measurements (3.2–3.4 eV).<sup>21</sup> For transition metals with non-empty d bands, this error can be expected to be even larger, so that a Hubbard-U correction was employed for Fe and Ni, as described in the Methods section.

The electronic ground state configuration of each Fe containing composition was found to be high spin with antiferromagnetic ordering, resulting in symmetric DOS plots, as seen

in Fig. 3a. Since the  $d^4$  electronic configuration of  $\text{Fe}^{4+}$  might potentially favor Jahn-Teller distorted geometries, we accommodated for such distortions by breaking the symmetry of the initial structures. Substituting Fe for Ti results in narrowing of the band gap and in the creation of defect states, so that the material becomes metallic, which is in line with our expectations, as outlined in the Introduction.

For the Ni containing compositions low spin configurations were found to be stable, which is not surprising for  $d^6 \text{Ni}^{4+}$ . However, structural distortions, possibly due to the difference in  $\text{Ti}^{4+}$  and  $\text{Ni}^{4+}$  ionic radii, resulted in a small net magnetic moment, breaking the symmetry of the DOS (Fig. 3b). As in the case of the Fe compositions, mixed Ti/Ni compositions are predicted to be metallic. Hexagonal  $\text{BaNiO}_3$ , the DOS of which is shown at the very right is, on the other hand, a semiconductor.

By summation over the orbital-projected DOS for all atoms of each chemical species the species-resolved (partial) DOS was obtained (Fig. 4). As seen in the figure, the valence band edge of  $\text{BaTiO}_3$  is dominated by oxygen states, and the occupied s and p Ti states contribute mostly to density that is more than 1 eV below the Fermi level. The conduction band is mostly given by

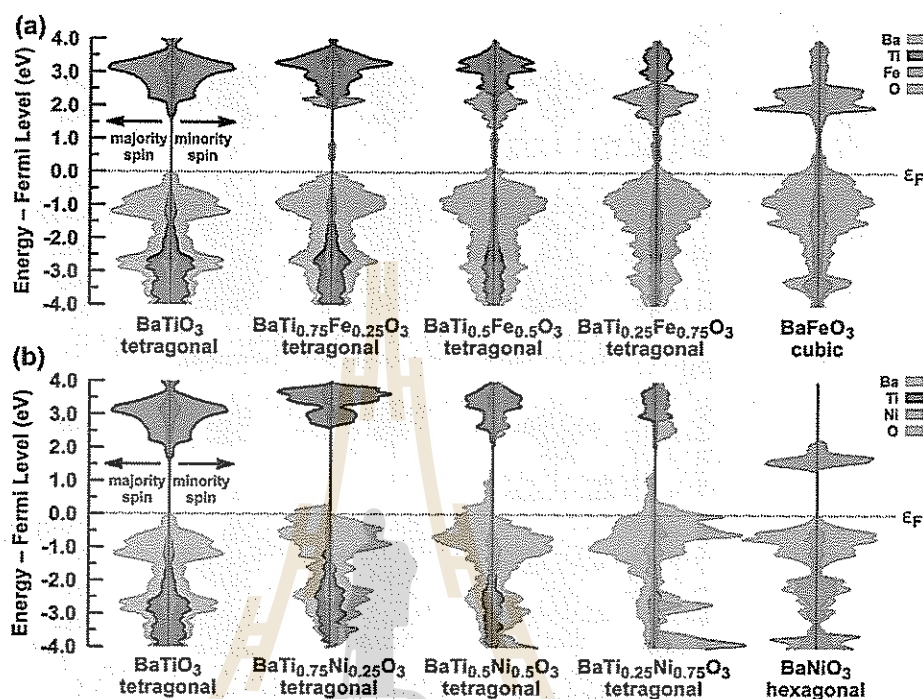


Fig. 4 Species-resolved electronic density of states (DOS) for pristine and (a) Fe-modified and (b) Ni-modified  $\text{BaTiO}_3$  compositions. These data were obtained as the sum of the orbital-projected partial DOS (PDOS) for all atoms of each atomic species. Note that the intensities depend on the chosen atomic radii (we employed VASP defaults). The structures are the same as in Fig. 3.

the empty Ti d states. The partially occupied Ni and Fe d orbitals give rise to additional occupied and vacant states near the Fermi level which leads to metallic (or semiconductive) behavior.

Together with the trends in the formation energies from above, we conclude that Fe doping of  $\text{BaTiO}_3$  is likely to be feasible and will result in electrical conductivity. Ni doping might be possible in small quantities, and Ni-modified  $\text{BaTiO}_3$  is also likely to be metallic.

#### $\text{BaTiO}_3$ surface phases and solubility under catalytic conditions

The most fundamental requirement for any working catalyst is stability under catalytic operation conditions. To estimate the pH and potential dependent stability of  $\text{BaTiO}_3$  against dissolution, we therefore computed the Pourbaix diagrams for Ba and Ti, corresponding to the  $\text{BaO}$ - and  $\text{TiO}_2$ -terminated  $\text{BaTiO}_3$  surfaces. The Pourbaix diagrams are shown in Fig. 5.

The relevant potentials for water oxidation are above the top dashed line that intersects  $U = 1.23$  V at pH = 0 in Fig. 5. Furthermore, water electrolysis over perovskite oxides is typically more efficient under alkaline conditions,<sup>57</sup> so that stability at high pH is most important.

As seen in Fig. 5a, Ba favors dissolution in a wide range of pH values and potentials either as  $\text{Ba}^{2+}$  or as  $\text{BaOH}^+$ . Barium oxide is only stable at high potentials that are not relevant for (efficient) water electrolysis. Hence, it is unlikely that the  $\text{BaO}$ -terminated  $\text{BaTiO}_3$  surfaces are stable under operation conditions.

$\text{TiO}_2$ -based catalysts for water splitting are known,<sup>1</sup> so that it is not surprising that the situation is different for Ti: indeed,  $\text{TiO}_2$  is predicted by the computed Pourbaix diagram to be the stable Ti phase at the relevant potentials independent of the pH value, as seen in Fig. 5b. From the Ba and Ti Pourbaix diagrams, one can conclude that only the  $\text{TiO}_2$ -terminated  $\text{BaTiO}_3$  surfaces are relevant under the conditions required for water electrolysis.

Not only dissolution, but also poisoning of the active surface sites may lead to catalytic deactivation. Furthermore, water molecules may react with residual activated oxygen species on the catalyst surface.<sup>58</sup> We therefore computed the pH and potential dependent surface phase diagram of  $\text{BaTiO}_3$ , examining small molecules that could potentially act as catalyst poisons. We only consider the non-polar (001) surface with both BaO and  $\text{TiO}_2$  termination.<sup>48</sup> In addition to the reaction intermediates of the

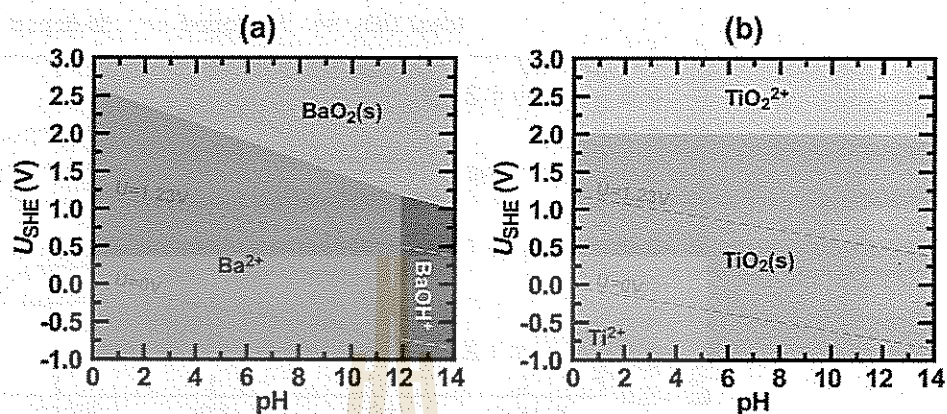


Fig. 5 Computed (a) Ba and (b) Ti Pourbaix diagrams with an ionic concentration of  $10^{-5}$  M. The dashed orange lines indicate the potentials for water oxidation ( $2\text{H}_2\text{O} \rightarrow \text{O}_2 + 4\text{H}^+ + 4\text{e}^-$ ,  $U = 1.23$  V at pH = 0) and reduction ( $2\text{H}_2\text{O} + 2\text{e}^- \rightarrow 2\text{OH}^- + \text{H}_2$ ,  $U = 0$  V at pH = 0).

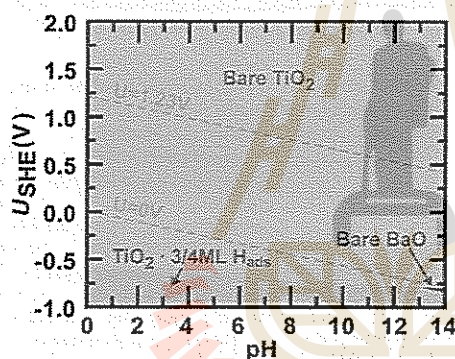


Fig. 6 Stable  $\text{BaTiO}_3(001)$  surface phase as a function of the pH and the applied potential. The clean BaO and  $\text{TiO}_2$  terminated surfaces were considered, as well as these surfaces with hydrogen coverages between  $1/4$  and 1 monolayer (ML). As shown in Fig. 5, the water oxidation and reduction potentials are indicated by dashed orange lines.

OER, *i.e.*  $\text{H}_2\text{O}$ ,  $\text{OH}$ ,  $\text{O}$ ,  $\text{OOH}$ , and  $\text{O}_2$ , we also looked at the adsorption of hydrogen molecules on the surface and at the formation of oxygen vacancies. For each of the molecules/defects, surface coverages equivalent to 1,  $\frac{1}{2}$ ,  $\frac{1}{3}$ , and  $\frac{1}{4}$  monolayers were modeled.

The resulting surface phase diagram is shown in Fig. 6. Despite the various considered adsorbants and coverages, we find that only three different phases are predicted to occur: (i) the hydrogen-covered  $\text{TiO}_2$ -terminated surface is stable at very negative potentials (reducing conditions), (ii) the bare BaO-terminated surface has a small stability region at high pH and low potential, and (iii) the bare  $\text{TiO}_2$ -terminated surface is stable over the remaining area of the phase diagram including the relevant regions for water electrolysis.

Based on the computed Pourbaix diagrams and the surface phase diagram, the  $\text{TiO}_2$ -terminated  $\text{BaTiO}_3(001)$  surface is stable at the pH and potential required for water electrolysis, and it is not sensitive to poisoning by the reaction intermediates and hydrogen.

#### OER over pristine and Fe-/Ni-modified $\text{BaTiO}_3$

Having established that electrically conducting Ni- and Fe-modified  $\text{BaTiO}_3$  can potentially be made and that the  $\text{TiO}_2$ -terminated  $\text{BaTiO}_3(001)$  surface is likely to be stable under operation conditions, we proceed to evaluate the reaction free energy profile for the OER as described in the Methods section. The surfaces of the modified compositions were modeled by replacing a single surface Ti atom with either Fe or Ni, and the sites on top and next to this defect were considered for the adsorbed species.

Fig. 7 shows the reaction free energies for water oxidation over pristine (black), Fe-modified (red), and Ni-modified (blue)  $\text{BaTiO}_3$  at the ideal potential of  $U = 1.23$  V (solid lines) and at the predicted required overpotentials (dashed lines) following the elemental reactions of eqn (1). The overpotential for the reaction on the ideal  $\text{TiO}_2$ -terminated surface is  $\eta = 1.22$  V. Fe and Ni doping reduces the overpotential to 0.91 V and 0.89 V, respectively.

On the unmodified surface, the potential-determining step is the second hydrogen dissociation from  $^*\text{OH}$  to  $^*\text{O}$ . Interestingly, Fe and Ni affect the reaction pathway in fundamentally different ways: Fe results in stronger binding of all three reaction intermediates, which reduces the overpotential but maintains the OH dissociation as a potential-determining step. In contrast, Ni stabilizes the  $^*\text{OOH}$  binding, so that the reaction from  $^*\text{OOH}$  to  $^* + \text{O}_2$  becomes the potential-determining step.

Although, the reduced overpotentials for Fe- and Ni-modified  $\text{BaTiO}_3$  are still too high to compete with Pt-group water

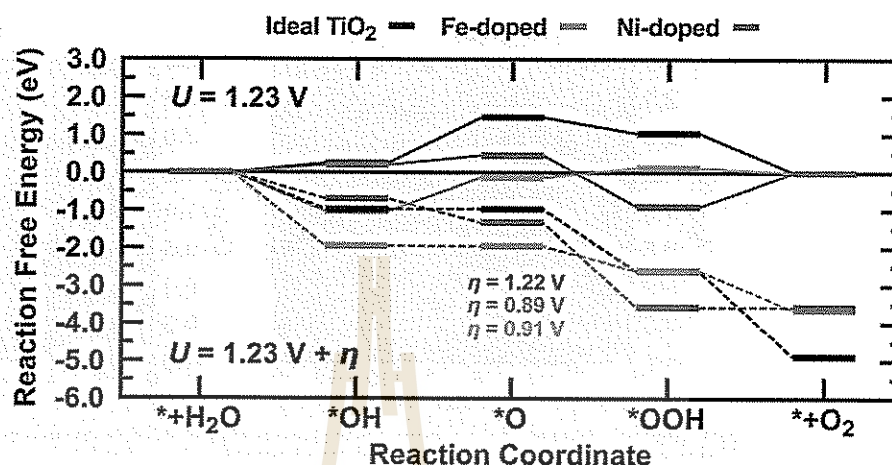


Fig. 7 Reaction free-energy diagram for the oxygen evolution reaction over ideal (black) and Fe (red) and Ni (blue) doped  $\text{BaTiO}_3$  following the elementary reaction steps of eqn (1). The solid lines indicate the reaction pathway without applied potential ( $U = 0$  V) and the dashed lines are the reaction profiles at the required overpotentials for ideal Ti ( $\eta = 1.22$  V), Fe dopants ( $\eta = 0.91$  V), and Ni dopants ( $\eta = 0.69$  V).

electrolysis catalysts, or with La-based perovskite materials<sup>57</sup> the large differences in the reaction profiles demonstrate that small compositional changes can have a strong positive impact on the catalytic activity.

## Discussion

In this work, we demonstrated that compositional modification of inexpensive and earth-abundant  $\text{BaTiO}_3$  may improve its suitability as an anode material for water electrolysis. We showed that replacing Ti with Fe or Ni on the perovskite B site is likely to improve the electrical conductivity and reduces the overpotential for the water oxidation reaction. Using computed Pourbaix diagrams and pH-potential dependent surface phase diagrams we further showed that the  $\text{TiO}_2$ -terminated  $\text{BaTiO}_3(001)$  surface is stable under water electrolysis conditions and that it is not sensitive with respect to poisoning by reaction intermediates or hydrogen.

We note that Fe and Ni can both assume oxidation states lower than 4+ and may give rise to oxygen deficiency when substituted on the B site in  $\text{BaTiO}_3$ .<sup>59</sup> Indeed, slightly oxygen deficient  $\text{BaFeO}_3$  is known to be stable, and strongly oxidizing conditions are required to synthesize stoichiometric  $\text{Fe}^{(n)}$   $\text{BaFeO}_3$ .<sup>25</sup> Since oxygen vacancies have previously been found to play an important role in CO oxidation,<sup>60</sup> we currently cannot rule out their involvement in water oxidation over modified  $\text{BaTiO}_3$ .

Another assumption made implicitly in the present study is that Fe and Ni dopants are stable against dissolution. Since the ideal  $\text{TiO}_2$ -terminated surface is stable, it seems reasonable that small dopant concentration can be stabilized on the

$\text{BaTiO}_3$  surface. However, if the dopant concentration is too small, the number of active sites on the catalyst surface may become rate limiting.

As remarked in the previous section, Fe and Ni doping alters the reaction free energy profile in contrasting ways by stabilizing different reaction intermediates (Fig. 7). If it were possible to simultaneously achieve the OH and O binding energies of Ni-modified  $\text{BaTiO}_3$  and the OOH binding energy of the Fe-modified system, a catalyst with close to ideal overpotential could be obtained. Therefore, it would be interesting to investigate the properties of Fe and Ni co-doped  $\text{BaTiO}_3$ .

Finally, it is known that  $\text{BaTiO}_3$  forms solid solutions with a large number of other perovskite oxides,<sup>61</sup> opening up a large composition space for modified  $\text{BaTiO}_3$  compositions with potentially improved catalytic activities. Such synergistic effects are well-known for catalytic alloys,<sup>62–65</sup> but have, in our opinion, not been sufficiently explored for oxide materials.

## Conclusions

Using first-principles calculations, we determined the formation energies, electronic structures, pH-potential-dependent surface phase diagrams, and free energy profiles for water oxidation of Fe- and Ni-modified  $\text{BaTiO}_3$ . The results of our analysis show that Fe/Ni doping is thermodynamically feasible and that even slightly modified  $\text{BaTiO}_3$  compositions can have greatly improved electrical conductivity and reduced overpotentials for the oxygen evolution reaction by more than 25%. This finding demonstrates that compositional modification of  $\text{BaTiO}_3$  can be an effective avenue for the design of inexpensive, earth-abundant anode materials for electrocatalytic water splitting. Our results further

suggest that tuned BaTiO<sub>3</sub> compositions with yet better performance may exist and identify Fe and Ni co-doping as a promising direction.

### Acknowledgements

The authors thank Xi(Jerry) Rong for discussions about the Pourbaix and surface-phase diagrams. NA and AK acknowledge financial support from the Skoltech-MIT Center for Electrochemical Energy. WS and SL thank the NANOTEC-SUT Center of Excellence on Advanced Functional Nanomaterials and Development and Promotion of Science and Technology Talents Project (DPST, Thailand) for partial support. This work used the Extreme Science and Engineering Discovery Environment (XSEDE), which is supported by National Science Foundation grant number ACL-1053575. In addition, resources of the National Energy Research Scientific Computing Center, a DOE Office of Science User Facility supported by the Office of Science of the U.S. Department of Energy under Contract No. DE-AC02-05CH11231, are gratefully acknowledged.

### References

- 1 A. Kudo and Y. Miseki, *Chem. Soc. Rev.*, 2009, **38**, 253–278.
- 2 J. Suntivich, K. J. May, H. A. Gasteiger, J. B. Goodenough and Y. Shao-Horn, *Science*, 2011, **334**, 1383–1385.
- 3 C. C. L. McCrory, S. Jung, J. C. Peters and T. F. Jaramillo, *J. Am. Chem. Soc.*, 2013, **135**, 16977–16987.
- 4 C. Cui, L. Gan, M. Heggen, S. Rudi and P. Strasser, *Nat. Mater.*, 2013, **12**, 765–771.
- 5 G. Gupta, D. A. Slanac, P. Kumar, J. D. Wiggins-Camacho, X. Wang, S. Swinnea, K. L. More, S. Dai, K. J. Stevenson and K. P. Johnston, *Chem. Mater.*, 2009, **21**, 4515–4526.
- 6 S. Royer, D. Duprez, F. Can, X. Courtois, C. Batiot-Dupeyrat, S. Laassiri and H. Alamdari, *Chem. Rev.*, 2014, **114**, 10292–10368.
- 7 Z. Fan, K. Sun and J. Wang, *J. Mater. Chem. A*, 2015, **3**, 18809–18828.
- 8 I. E. Castelli, D. D. Landis, K. S. Thygesen, S. Dahl, I. Chorkendorff, T. F. Jaramillo and K. W. Jacobsen, *Energy Environ. Sci.*, 2012, **5**, 9034.
- 9 J. Luo, J.-H. Im, M. T. Mayer, M. Schreier, M. K. Nazeeruddin, N.-G. Park, S. D. Tilley, H. J. Fan and M. Gratzel, *Science*, 2014, **345**, 1593–1596.
- 10 J. T. Mefford, X. Rong, A. M. Abakumov, W. G. Hardin, S. Dai, A. M. Kolpak, K. P. Johnston and K. J. Stevenson, *Nat. Commun.*, 2016, **7**, 11053.
- 11 X. Rong, J. Parolin and A. M. Kolpak, *ACS Catal.*, 2016, **6**, 1153–1158.
- 12 T. Hayakawa, S. Suzuki, J. Nakamura, T. Uchijima, S. Hamakawa, K. Suzuki, T. Shishido and K. Takehira, *Appl. Catal., A*, 1999, **183**, 273–285.
- 13 J. H. Kennedy and K. W. Frese, *J. Electrochem. Soc.*, 1976, **123**, 1683–1686.
- 14 R. D. Nasby and R. K. Quinn, *Mater. Res. Bull.*, 1976, **11**, 985–992.
- 15 G. M. Rodriguez, K. Kelm and B. Saruhan, *Appl. Catal., A*, 2010, **387**, 173–184.
- 16 C. Srilakshmi, R. Saraf, V. Prashanth, G. M. Rao and C. Shivakumara, *Inorg. Chem.*, 2016, **55**, 4795–4805.
- 17 N. B. Halek, V. Petykin, P. Krtil and J. Rossmeisl, *Phys. Chem. Chem. Phys.*, 2014, **16**, 13682.
- 18 D. Lee, Y.-L. Lee, A. Grimaud, W. T. Hong, M. D. Biegalski, D. Morgan and Y. Shao-Horn, *J. Mater. Chem. A*, 2014, **2**, 6480.
- 19 T. Sheng, X. Lin, Z.-Y. Chen, P. Hu, S.-G. Sun, Y.-Q. Chu, C.-A. Ma and W.-F. Lin, *Phys. Chem. Chem. Phys.*, 2015, **17**, 25235–25243.
- 20 S. Wannakao, N. Artrith, J. Limtrakul and A. M. Kolpak, *ChemSusChem*, 2015, **8**, 2745–2751.
- 21 S. H. Wemple, *Phys. Rev. B: Solid State*, 1970, **2**, 2679–2689.
- 22 I. Popescu, I. Săndulescu, Á. Rédey and I.-C. Marcu, *Catal. Lett.*, 2011, **141**, 445–451.
- 23 J. G. Lee, J. Hwang, H. J. Hwang, O. S. Jeon, J. Jang, O. Kwon, Y. Lee, B. Han and Y.-G. Shul, *J. Am. Chem. Soc.*, 2016, **138**, 3541–3547.
- 24 Y. Takeda, F. Kanamura, M. Shimada and M. Koizumi, *Acta Crystallogr., Sect. B: Struct. Crystallogr. Cryst. Chem.*, 1976, **32**, 2464–2466.
- 25 N. Hayashi, T. Yamamoto, H. Kageyama, M. Nishi, Y. Watanabe, T. Kawakami, Y. Matsushita, A. Fujimori and M. Takano, *Angew. Chem., Int. Ed.*, 2011, **50**, 12547–12550.
- 26 Y. Luspini, J. L. Servoin and F. Gervais, *J. Phys. C: Solid State Phys.*, 1980, **13**, 3761–3773.
- 27 R. D. Shannon, *Acta Crystallogr., Sect. A: Cryst. Phys., Diffr., Theor. Gen. Crystallogr.*, 1976, **32**, 751–767.
- 28 Y.-L. Lee, M. J. Gadre, Y. Shao-Horn and D. Morgan, *Phys. Chem. Chem. Phys.*, 2015, **17**, 21643–21663.
- 29 A. I. Liechtenstein, V. I. Anisimov and J. Zaanen, *Phys. Rev. B: Condens. Matter Mater. Phys.*, 1995, **52**, R5467–R5470.
- 30 V. I. Anisimov, F. Aryasetiawan and A. I. Liechtenstein, *J. Phys.: Condens. Matter*, 1997, **9**, 767.
- 31 A. Jain, G. Hautier, C. J. Moore, S. P. Ong, C. C. Fischer, T. Mueller, K. A. Persson and G. Ceder, *Comput. Mater. Sci.*, 2011, **50**, 2295–2310.
- 32 J. Perdew, K. Burke and M. Ernzerhof, *Phys. Rev. Lett.*, 1996, **77**, 3865–3868.
- 33 P. E. Blöchl, *Phys. Rev. B: Condens. Matter Mater. Phys.*, 1994, **50**, 17953–17979.
- 34 G. Kresse and J. Furthmüller, *Phys. Rev. B: Condens. Matter Mater. Phys.*, 1996, **54**, 11169–11186.
- 35 G. Kresse and J. Furthmüller, *Comput. Mater. Sci.*, 1996, **6**, 15–50.
- 36 G. L. W. Hart and R. W. Forcade, *Phys. Rev. B: Condens. Matter Mater. Phys.*, 2008, **77**, 224115.
- 37 G. L. W. Hart and R. W. Forcade, *Phys. Rev. B: Condens. Matter Mater. Phys.*, 2009, **80**, 014120.
- 38 G. L. Hart, L. J. Nelson and R. W. Forcade, *Comput. Mater. Sci.*, 2012, **59**, 101–107.
- 39 S. P. Ong, W. D. Richards, A. Jain, G. Hautier, M. Kocher, S. Cholia, D. Gunter, V. L. Chevrier, K. A. Persson and G. Ceder, *Comput. Mater. Sci.*, 2013, **68**, 314–319.



- 40 K. Momma and F. Izumi, *J. Appl. Crystallogr.*, 2011, **44**, 1272–1276.
- 41 D. D. Wagman, W. Evans, V. Parker, I. Halow, S. Bailey and R. Schumm, *Selected Values of Chemical Thermodynamic Properties*, National Bureau of Standards, Washington, USA, 1968–1971.
- 42 V. Blum, R. Gehrke, F. Hanke, P. Havu, V. Havu, X. Ren, K. Reuter and M. Scheffler, *Comput. Phys. Commun.*, 2009, **180**, 2175–2196.
- 43 B. Hammer, L. B. Hansen and J. K. Nørskov, *Phys. Rev. B: Condens. Matter Mater. Phys.*, 1999, **59**, 7413–7421.
- 44 A. Tkatchenko and M. Scheffler, *Phys. Rev. Lett.*, 2009, **102**, 073005.
- 45 E. van Lenthe, E. J. Baerends and J. G. Snijders, *J. Chem. Phys.*, 1994, **101**, 9783.
- 46 J. Harada, T. Pedersen and Z. Barnea, *Acta Crystallogr., Sect. A: Cryst. Phys., Diffr., Theor. Gen. Crystallogr.*, 1970, **26**, 336–344.
- 47 B. Ravel, E. A. Stern, R. I. Vedrinskii and V. Kraizman, *Ferroelectrics*, 1998, **206**, 407–430.
- 48 J. Padilla and D. Vanderbilt, *Phys. Rev. B: Condens. Matter Mater. Phys.*, 1997, **56**, 1625–1631.
- 49 A. M. Kolpak, D. Li, R. Shao, A. M. Rappe and D. A. Bonnell, *Phys. Rev. Lett.*, 2008, 036102.
- 50 X. Rong and A. M. Kolpak, *J. Phys. Chem. Lett.*, 2015, **6**, 1785–1789.
- 51 K. A. Persson, B. Waldwick, P. Lazic and G. Ceder, *Phys. Rev. B: Condens. Matter Mater. Phys.*, 2012, **85**, 235438.
- 52 J. K. Nørskov, J. Rossmeisl, A. Logadottir, L. Lindqvist, J. R. Kitchin, T. Bligaard and H. Jónsson, *J. Phys. Chem. B*, 2004, **108**, 17886–17892.
- 53 J. Rossmeisl, Z.-W. Qu, H. Zhu, G.-J. Kroes and J. Nørskov, *J. Electroanal. Chem.*, 2007, **607**, 83–89.
- 54 I. C. Man, H.-Y. Su, F. Calle-Vallejo, H. A. Hansen, J. I. Martínez, N. G. Inoglu, J. Kitchin, T. F. Jaramillo, J. K. Nørskov and J. Rossmeisl, *ChemCatChem*, 2011, **3**, 1159–1165.
- 55 Á. Valdés, Z.-W. Qu, G.-J. Kroes, J. Rossmeisl and J. K. Nørskov, *J. Phys. Chem. C*, 2008, **112**, 9872–9879.
- 56 A. Urban, D.-H. Seo and G. Ceder, *npj Comput. Mater.*, 2016, **2**, 16002.
- 57 J. O. Bockris, *J. Electrochem. Soc.*, 1984, **131**, 290.
- 58 Z. Song, J. Fan, Y. Shan, A. M.-C. Ng and H. Xu, *Phys. Chem. Chem. Phys.*, 2016, **18**, 25373–25379.
- 59 H.-J. Hagemann and D. Hennings, *J. Am. Ceram. Soc.*, 1981, **64**, 590–594.
- 60 J. S. Elias, N. Artrith, M. Bugnet, L. Giordano, G. A. Botton, A. M. Kolpak and Y. Shao-Horn, *ACS Catal.*, 2016, **6**, 1675–1679.
- 61 V. V. Lemanov, *Ferroelectrics*, 2007, **354**, 69–76.
- 62 A. K. Singh and Q. Xu, *ChemCatChem*, 2013, **5**, 652–676.
- 63 N. Artrith and A. M. Kolpak, *Nano Lett.*, 2014, **14**, 2670–2676.
- 64 C. Liu, H. He, P. Zapol and L. A. Curtiss, *Phys. Chem. Chem. Phys.*, 2014, **16**, 26584–26599.
- 65 N. Artrith and A. M. Kolpak, *Comput. Mater. Sci.*, 2015, **110**, 20–28.

Manuscript submitted in Ceramics International

**PRESSURE-INDUCED PHASE TRANSFORMATIONS OF  $\text{LiGaO}_2$ :  
FIRST PRINCIPLES STUDY**

Wuthigrai Sailuam<sup>1,2,3\*</sup>, Kanoknan Sarasamak<sup>4</sup>, Miguel Angel Mendez Polanco<sup>5</sup> and  
Sukit Limpijumong<sup>1,2,3</sup>

<sup>1</sup> School of Physics and NANOTEC-SUT Center of Excellence on Advanced Functional  
Nanomaterials, Suranaree University of Technology, Nakhon Ratchasima 30000,  
Thailand

<sup>2</sup> Synchrotron Light Resesearch Institute, Nakhon Ratchasima 30000, Thailand

<sup>3</sup> Thailand Center of Excellence in Physics (ThEP Center), Commission on Higher  
Education, Bangkok 10400, Thailand

<sup>4</sup> College of Nanotechnology, King Mongkut's Institute of Technology Ladkrabang,  
Bangkok 10520, Thailand

<sup>5</sup> Department of Mechanical Engineering, Massachusetts Institute of Technology,  
Cambridge, Massachusetts 02139, United States

**Abstract**

Phase transformations of  $\beta\text{-LiGaO}_2$  ( $\text{Pna}2_1$ ) under different pressure conditions are studied using first principles calculations. Under specific conditions, LGO can exist in various structures some of which have not been previously reported ( $\text{oP}16$  and

## Manuscript submitted in Ceramics International

P4<sub>1</sub>2<sub>1</sub>2). Under sufficiently strong hydrostatic pressure, LGO can transform into a rocksalt-like structure. Under strong uniaxial stress LGO can transform into a tetragonal structure or an orthorhombic structure depending on the orientation of the applied stress. The stability of different crystal structures under different applied stresses and the phase transformation processes are studied by calculating the enthalpy surfaces and transformation barriers under different stresses.

*Keywords:* Phase transformations, LiGaO<sub>2</sub>, High pressure



\* Corresponding author, *E-mail:* wutthigraiphys33@gmail.com

## 1. Introduction

$\beta$ -LiGaO<sub>2</sub> (Pna2<sub>1</sub>) is the ambient-pressure structure of LiGaO<sub>2</sub> (LGO) that can be obtained in a large single crystal form by a conventional Czochralski melt-pulling method [1,2]. This material has a wurtzite derived structure with a good lattice match to epitaxially grown GaN and ZnO thin-films. Both GaN and ZnO are technologically important materials for blue and purple optoelectronic devices [1,3]. The crystal structure of  $\beta$ -LiGaO<sub>2</sub> (Pna2<sub>1</sub>) is an analogous of the wurtzite ZnO in which the group-II Zn is alternately substituted by group-III Ga and group-I Li. Due to the relaxation of the oxygen sub-lattice and symmetry-breaking cations, the structure of this ternary oxide slightly differs from the perfect wurtzite-type structure (P6<sub>3</sub>mc) [4]. This relaxation is mainly a result of the difference between LiO<sub>4</sub> and GaO<sub>4</sub> tetrahedra with LiO<sub>4</sub> being bigger than GaO<sub>4</sub>. The average bond lengths are 1.985 Å and 1.848 Å for Li-O and Ga-O, respectively. The difference between the average Li-O and Ga-O bond distances is less than 4%, allowing the formation of an orthorhombic structure (Pna2<sub>1</sub>) with the lattice parameters  $a = 5.402$  Å,  $b = 6.372$  Å,  $c = 5.007$  Å, and density = 4.187 g.cm<sup>-3</sup> [5].  $\beta$ -LiGaO<sub>2</sub> is known to have a band gap of 5.6 eV; making it a good candidate for applications in bright UV optoelectronic applications [6,7].

Pressure induced phase transformations of wurtzite ZnO have been previously studied experimentally and theoretically [8,19]. It has been predicted that a 10 GPa tensile stress along the [0110] direction or 6 GPa compressive stress along [0001] direction [8] could transform a wurtzite ZnO into an un-buckled phase (HX) [9]. A 7 GPa tensile stress along [0001] induces a formation of a body-centered-tetragonal phase (BCT-4) [10]. A hydrostatic pressure of about 8.5 GPa leads to the well-known and

experimentally-observed rocksalt cubic phase [19]. First principles study on the stable phases and phase transformations of LGO is scarce. Due to the similar in the structural of  $\beta$ -LGO ( $Pna2_1$ ) to that of wurtzite ZnO, we propose to employ the theoretical investigations in a similar manner as those have been employed successfully for the case of ZnO [8]. These studies are very important to identify transition mechanisms and to predict the undiscovered phases of LGO that can be reached by proper experimental conditions.

In this work, we used density functional theory (DFT) calculations to study phase transformations of LGO under hydrostatic and uniaxial pressures. We explored the LGO phase-space through the modeling of stress loads along different crystal directions. Three metastable phases of LGO, namely,  $oP16$ ,  $I41/amd$ , and  $P4_12_12$  are predicted based on the enthalpy surface diagrams for the transformations from ambient-pressure  $\beta$ -LGO ( $Pna2_1$ ). The compressive stress loading along the  $[001]$  direction produces the five-fold orthorhombic phase ( $oP16$ ). The uniaxial tensile strain along  $[001]$  direction stabilizes a tetragonal structure ( $P4_12_12$ ). The hydrostatic pressure leads to two structures that are energetically close to each other. One phase is the body center tetragonal (BCT,  $I41/amd$ ) and another phase is trigonal ( $R3m$ ) structure, previously found in experiments [17]. All structures are shown in Fig. 1 and the comparison with the analogous ones in the binary compound ZnO is shown in Fig. 2. For simplicity, henceforth the LGO phases are named after the analogous ones in ZnO, i.e., the orthorhombic ( $Pna2_1$ ) is named WZ', the body-center tetragonal ( $I41/amd$ ) is named RS', the rhombohedral ( $R3m$ ) is named RS'', the orthorhombic ( $oP16$ ) is named HX', and the tetragonal ( $P4_12_12$ ) is named BCT'.

## 2. Material and methods

First principles density functional theory (DFT) calculations with the generalized gradient approximations (GGA) as the exchange correlation (XC) functional [11] was employed. The ultrasoft pseudopotentials with the projector augmented wave method (PAW) as implemented in the VASP package [12] were used. GGA gives the lattice constant of  $\beta$ -LiGaO<sub>2</sub> in better agreement with the known experimental value than local density approximation (LDA) XC functional [13] which has been used to study ZnO [4,14]. A typical LGO unit cell for the study of a homogeneous phase transformation consists of 16 atoms (4 Li atoms, 4 Ga atoms, and 8 O atoms). For the basis set we used the plane wave expansions set up to 520 eV and for the k-point sampling of the Brillouin zone for the energy integrations, we used at least 7×7×7 Monkhorst-Pack scheme [15]. For the structural relaxations, the calculations are considered converged when the acting forces on each atom is less than 0.1 meV/Å; corresponding to the total energies convergence of ~ 0.1 meV/atom. The stability of each phase can be determined by analyzing the enthalpy as a function of cell shape defined using the ratios  $c/a$  and  $b/a$ , as described in detail by Jungthawan and Limpijumnong [2]. For different loading conditions, we used distinct equations of state from which we obtain the minimum enthalpy for each combination of  $c/a$ - $b/a$  pairs and loading conditions. When two phases share the same minimum enthalpy, those two phases are equally favored.

The enthalpy ( $H$ ) under hydrostatic pressure is defined as

$$H = E + pV, \quad (1)$$

Manuscript submitted in Ceramics International

where  $E$  is the energy per unit cell,  $p = -(\partial E / \partial V)$  is the pressure, and  $V$  is the unit cell volume. For each  $c/a$  and  $b/a$  pairs,  $V$  is allowed to relax to minimize  $H$ . In principle, for a given  $p$ , the  $c/a$  and  $b/a$  ratios that give the lowest enthalpy define the most stable cell shape. In practice, we calculated the enthalpy surface as a function of two independent strain parameters, i.e.,  $c/a$  and  $b/a$  in the range from 0.787 to 0.468 and 0.848 to 0.468, respectively. A total of 36 strained configurations, corresponding to the increments of 0.05 in  $c/a$  and 0.05 in  $b/a$  in the  $c/a$ - $b/a$  space (Fig. 3), were investigated.

For uniaxial loadings, the stability of each crystal and compound can be determined from the enthalpy.

$$H\left(\frac{c}{a}, \frac{b}{a}\right) = E(c, b, a) \mp A_{jk} \times \sigma_i q_i, \quad (2)$$

where  $E$  is the energy per unit cell,  $\sigma_i$  is the stress along the  $i$  direction,  $q_i$  is the lattice parameter in the  $i$  direction,  $A_{jk}$  is the cross section area of the unit cell perpendicular to the stress direction, and  $A_{jk} \times \sigma_i q_i$  is the external work. For the stress along the  $c$  axis,  $i = c$ ,  $A_{ab} = ab$  and  $q_c = c$ , with  $-\sigma_c$  representing the compressive stress and  $+\sigma_c$  representing the tensile stress. For each strained configuration (each  $c/a$ - $b/a$  pair), the energies associated with at least five different unit cells are calculated. An equation of state (energy-volume relation) is obtained by a third-degree polynomial fit.

### 3. Results and Discussion

In addition to the natural phase of LGO (WZ'), there are other phases that are metastable and have rather low energies (within 25 meV/atom). They are orthorhombic oP16 (HX'), and tetragonal P4<sub>1</sub>2<sub>1</sub>2 (BCT'). Fig. 3 shows the total energies of five

Manuscript submitted in Ceramics International

different phases of LGO as a function of the unit-cell volume. They are orthorhombic Pna2<sub>1</sub> (WZ'), orthorhombic oP16 (HX'), body center tetragonal I41/amd (RS'), rhombohedral R3m (RS'') and tetragonal P4<sub>1</sub>2<sub>1</sub>2 (BCT'). The minimum point of each curve gives the equilibrium cohesive energy of the corresponding phase of LGO and the stable volume. As expected, the WZ' structure which is the natural phase [5] of LGO is the computationally most stable one.

Interestingly, we also found other metastable phases close in energy to the ground state WZ'. The HX' and BCT' have energies only 0.021 eV/atom and 0.017 eV/atom, respectively, higher than that of WZ'. The RS' has the highest relative energy among structures studied at 0.037 eV/atom above WZ'. The relative energies of the five phases follow the order of RS' > HX' > RS'' > BCT' > WZ'. By using the common tangent approach [18], two WZ-RS phase transitions under hydrostatic pressure: WZ' → RS'' and WZ' → RS' are predicted to take place at the equilibrium hydrostatic pressures of 1.4 GPa and 3.7 GPa, respectively. Table 1 shows the calculated equilibrium lattice parameters, bulk modulus ( $B_0$ ), transformation pressures ( $P_t$ ), stresses, and volumes for all the different phases studied under pressure conditions. The lattice parameters of these structures are in good agreement with previous theoretical and experimental data. Because the calculated transition pressure under hydrostatic pressure of WZ' → RS'' is much lower than that of WZ' → RS', in principle, the former will be more likely to take place and RS' is unlikely to form. Based on this formation energy plot, other phases of LGO cannot be achieved by applying hydrostatic compression. We will show next that the WZ' → HX' can be achieved by applying uniaxial pressure and WZ' → BCT' can take place if one can apply sufficient negative



hydrostatic pressure (i.e., expand the volume). We calculated the enthalpy as a function of two crystal parameters ( $c/a$  and  $b/a$ ), forming the enthalpy surfaces under different pressure conditions. Compression along the [001] direction transforms WZ'  $\rightarrow$  HX' by means of the reduction in the  $c$  lattice parameter, and consequently decreasing the unit cell volume ( $c$ -axis of HX' is 16.87% shorter than that of WZ' with a smaller volume of 17.45%). Fig. 4(a) and Table 1 show the lattice parameters change during this phase transformation. The stability of the HX' phase can be better analyzed through the enthalpy difference  $\Delta H = H^{HX'} - H^{WZ'}$  as a function of the compressive stress along the  $c$  direction. For this, we obtained the enthalpy surface and energy cross-section corresponding to an applied compressive stress along the  $c$ -axis,  $-\sigma_c$  (negative sign indicates compression) as shown in Fig. 4(a) and 4(b) for compressive stress at 0 GPa and 3.5 GPa, respectively. We found the equilibrium stress for the WZ'  $\rightarrow$  HX' transformation is  $\sigma_c = 3.5$  GPa. At this stress, the enthalpy of WZ' phase (four-fold) and HX' (five-fold) phase are equal and both phases can co-existed. The calculated homogeneous transformation enthalpy barrier is only 12.5 meV/atom for this WZ'  $\rightarrow$  HX' transformation. The BCT' can be stabilized by applying uniaxial tensile stress along [001] on the WZ'. This transformation occurs through a combination of: 1) The breaking of every other Li-O bond along the [001] direction (bonds labeled B in Fig. 5(a)), and 2) The formation of an equal number of Li-O bonds (labeled A in Fig. 5(a)). This bond breaking and bond formation is repeated between Ga-O bond and Li-O on alternate planes along the [010] direction. Table 2 shows the calculated lattice parameters for the tetragonal phase at different values of tensile stress. For WZ',  $c/a$  and  $b/a$  ratios are 0.787 and 0.848, respectively. Through the transformation,  $b/a$  remains

constant (0.848), while  $c/a$  increases with stress as shown in Fig. 5. Increasing tensile stress the relative stability of BCT' with respect to that of the WZ', while the unit cell volume increases by 5.3%, 5.7%, 6.8%, and 7.9% for  $\alpha_c = 0, 2, 4.1, 6$  GPa, respectively. Because both WZ' and HX' share the same  $b/a$  ratio at 0.848, it is not necessary to vary this parameter when studying the relative phase stability. Fig. 5 shows cross-sections of enthalpy surfaces at  $b/a = 0.848$  at different values of tensile strain. At 0 GPa, WZ' is the most stable crystal structure and its enthalpy is lower than that of BCT' by 0.26 eV/atom, see Fig. 5(b). As the stress is increased to 2 GPa (Fig. 5(c)), the enthalpy difference decreases, and at the stress of 4.1 GPa (Fig. 5(d)) the two minima,  $H^{WZ}$  and  $H^{BCT}$  become equal. This means the two phases are equally favored and 4.1 GPa is the equilibrium tensile stress. Above this equilibrium stress BCT' becomes more stable. At 6 GPa (Fig. 5(e)), BCT' is more stable than WZ' by 0.13 eV/atom. The enthalpy barrier at the equilibrium pressure 4.1 GPa is estimated by measuring the  $\Delta H$  between the minima of the plots and their intersection point ( $c/a = 0.85$ ). This gives the barrier of only 3.36 meV/atom.

#### 4. Conclusions

A detailed study of phase transformations of  $\beta$ -LGO under different pressure conditions is carried out using first principles enthalpy calculations. In addition to the well-studied high pressure rocksalt-like  $R3m$  phase (RS'), we identified 3 new metastable phases of LGO with symmetries  $oP16$ ,  $I41/amd$  and  $P4_12_12$ , which we named them HX', RS', and BCT', respectively. By modeling stress loads along different

## Manuscript submitted in Ceramics International

crystal directions, we found that different metastable phases can be stabilized. For high hydrostatic pressure, only the transformation to the well-studied rocksalt-like phase (RS'') should take place because the RS' phase has a much higher transformation pressure. The [001] compressive stress loading can cause the transformation into an orthorhombic phase oP16 (HX'). On the other hand, the uniaxial [001] tensile stress can stabilize a tetragonal structure P4<sub>1</sub>2<sub>1</sub>2 (BCT').

**Acknowledgements**

The work was supported by NANOTEC-SUT Center of Excellence on Advanced Functional Nanomaterials and Thailand Center of Excellence in Physics. W. Sailuam was supported by the scholarship from the Development and Promotion of Science and Technology Talents Project (DPST, Thailand). Computations were carried out at the Synchrotron Light Research Institute (Public Organization), Thailand.

**References**

- [1] C. Chen, C.-A. Li, S.-H. Yu, and M. M. C. Chou, *Journal of Crystal Growth* **402**, 325 (2014).
- [2] S. Limpijumngong and S. Jungthawan, *Physical Review B* **70**, 054104 (2004).
- [3] C. Chen, H. Huang, C. Lu, and M. M. C. Chou, *Materials Letters* **120**, 101 (2014).
- [4] S. Limpijumngong, W. R. L. Lambrecht, B. Segall, and K. Kim, *MRS Online Proceedings Library* **449**, null (1996).

Manuscript submitted in *Ceramics International*

- [5] M. Marezio, *Acta Crystallographica* 0365-110X **18**, 481 (1965).
- [6] T. Omata, A. Tazuke, K. Nose, and S. Otsuka-Yao-Matsuo, *Journal of Crystal Growth* **330**, 9 (2011).
- [7] O. Takahisa, N. Hiraku, S. Issei, and K. Masao, *Science and Technology of Advanced Materials* **16**, 024902 (2015).
- [8] K. Sarasamak, A. J. Kulkarni, M. Zhou, and S. Limpijumnong, *Physical Review B* **77**, 024104 (2008).
- [9] A. J. Kulkarni, M. Zhou, K. Sarasamak, and S. Limpijumnong, *Physical Review Letters* **97**, 105502 (2006).
- [10] J. Wang, A. J. Kulkarni, K. Sarasamak, S. Limpijumnong, F. J. Ke, and M. Zhou, *Physical Review B* **76**, 172103 (2007).
- [11] J. P. Perdew, K. Burke, and M. Ernzerhof, *Physical Review Letters* **77**, 3865 (1996).
- [12] G. Kresse and J. Furthmüller, *Computational Materials Science* **6**, 15 (1996).
- [13] J. P. Perdew and A. Zunger, *Physical Review B* **23**, 5048 (1981).
- [14] A. Boonchun and W. R. L. Lambrecht, *Physical Review B* **81** (2010).
- [15] H. J. Monkhorst and J. D. Pack, *Physical Review B* **13**, 5188 (1976).
- [16] L. Lei, H. Ohfuji, J. Qin, X. Zhang, F. Wang, and T. Irifune, *Solid State Communications* **164**, 6 (2013).
- [17] M. Marezio and J. P. Remeka, *Journal of Physics and Chemistry of Solids* **26**, 1277 (1965).

- [18] Y. G. Yu, R. M. Wentzcovitch, T. Tsuchiya, K. Umemoto, and D. J. Weidner, *Geophysical Research Letters* **34**, (2007).
- [19] J. M. Recio, M. A. Blanco, V. Luaña, Ravindra Pandey, L. Gerward, and J. Staun Olsen, *Physical. Review. B* **58**, 8949 (1998).

#### List of Table

Table 1. Schematic illustrations of lattice parameters, percentage changes, Bulk modulus  $B_0$ , average bond length and average bond angles for Pna2<sub>1</sub> (WZ'), oP16 (HX'), R3m (RS'') and I41/amd (RS') structures under their equilibrium and loading conditions.

Table 2. Lattice parameters for the tetragonal P4<sub>1</sub>2<sub>1</sub>2 (BCT') LGO under tensile loading along [001] direction for  $\sigma_c = 0, 2, 4, 1$  and 6 GPa.

#### List of Figures

Fig. 1. Schematic illustrations of the ambient and the high-pressure crystal structures of LGO: (a) Orthorhombic (Pna2<sub>1</sub>) - ambient condition structure, (b) Body-centered tetragonal (I41/amd) - hydrostatic compression ( $P_1$ ) structure, (c) the Rhombohedral (R3m) - another hydrostatic compression ( $P_1$ ) structure, (d) Orthorhombic (oP16) - [001] compressive stress ( $-\sigma_c$ ) structure, and (e) tetragonal (P4<sub>1</sub>2<sub>1</sub>2) - [001] tensile stress ( $\sigma_c$ ) structure. In the structures, the green spheres represent Ga cations, blue spheres represent Li cations and red spheres represent O anions.

Fig. 2. Relationship between the crystal phases of the binary compound ZnO and the analogous ones of the ternary compound LGO.

Fig. 3. Total energy versus volume for five LGO structures: Green (RS''), Red (WZ'), black circles (HX'), black squares (RS') and blue squares (BCT').

Fig. 4. (a) the enthalpy surface for the compression stress  $\sigma_c = -3.5$  GPa and (b) 2-D sections of the enthalpy surface maps with the compression stress  $\sigma_c = -3.5$  GPa for  $b/a = 0.468$  (red line) and  $b/a = 0.848$  (blue line).

Fig. 5 (a) Schematic comparison of WZ' and BCT' LGO structures. Enthalpy (eV) as a function of  $c/a$  for  $b/a = 0.848$  at different tensile stresses: (b)  $\sigma_t = 0$  GPa, (c)  $\sigma_t = 2$  GPa, (d)  $\sigma_t = 4.1$  GPa and (e)  $\sigma_t = 6$  GPa.

มหาวิทยาลัยเทคโนโลยีสุรนารี

Table 1. Schematic illustrations of lattice parameters, percentage changes, Bulk modulus  $B_0$ , average bond length and average bond angles for Pna2<sub>1</sub> (WZ'), oP16 (HX'), R3m (RS'') and I41/amd (RS') structures under their equilibrium and loading conditions.

Parameters	WZ' ( $p=0$ GPa)			HX' $\alpha_c=-3.5$ GPa	RS'' ( $p_f=1.5$ GPa)			RS' $p_f=3.7$ GPa
	Present	LDA <sup>a,b</sup>	Exp <sup>d</sup>		Present	Exp <sup>c</sup>	LDA <sup>b</sup>	
$a$ (Å)	6.457	6.255 <sup>a</sup>	6.372	6.891	2.997	2.911	2.903	8.728
$b$ (Å)	5.479	5.361 <sup>a</sup>	5.402	5.781	2.997	2.911	2.903	4.082
$c$ (Å)	5.080	4.953 <sup>a</sup>	5.007	4.223	14.693	14.47	14.401	4.082
$b/a$	0.848			0.839	1.000			0.468
$c/a$	0.787			0.613	4.903			0.468
$V$ (Å <sup>3</sup> /f.u.)	44.93	41.53 <sup>a</sup>	43.09	33.65	22.55			29.09
$\Delta V$ (%)	-			-7.45	-49.36			-19.99
$\Delta b$ (%)	-			5.51	-45.31			-25.50
$\Delta c$ (%)	-			-16.87	65.42			-19.65
$B_0$ (GPa)	80.93	95.69 <sup>b</sup>		102.58	189.2		142.29	164.79
Average bond lengths (Å)								
Ga-O	1.896	1.858 <sup>b</sup>	1.848	1.984	2.021	2.00		2.029
Li-O	1.988	1.923 <sup>b</sup>	1.985	2.061	2.208	2.14		2.161
Average bond angles (Å <sup>2</sup> )								
O-Ga-O	110.21	112.3 <sup>b</sup>	109.2	90.54	92.87	93.4		92.21
O-Li-O	108.68	107.5 <sup>b</sup>	103.3	89.60	85.39	85.9		90.36

<sup>a</sup> VASP code DFT- LDA calculation by A. Boonchun et al.[14]

<sup>b</sup> CASTEP code DFT-LDA calculation by Li Lei et al.[16]

<sup>c</sup> Piston and cylinder device by M.Mareziro [17]

<sup>d</sup> General Electric XRD by M.Mareziro [5]

Table 2. Lattice parameters for the tetragonal P4<sub>1</sub>2<sub>1</sub>2 (BCT') LGO under tensile loading along [001] direction for  $\sigma_c = 0, 2, 4.1$  and 6 GPa.

Parameters	BCT'			
	$\sigma_c=0$	$\sigma_c=2$	$\sigma_c=4.1$	$\sigma_c=6$
	GPa	GPa	GPa	GPa
$a$ (Å)	6.476	6.442	6.382	6.364
$b$ (Å)	5.406	5.377	5.327	5.313
$c$ (Å)	5.406	5.485	5.647	5.738
$V$ (Å <sup>3</sup> /f.u.)	47.32	47.50	47.97	48.50
$c/a$	0.835	0.852	0.885	0.902



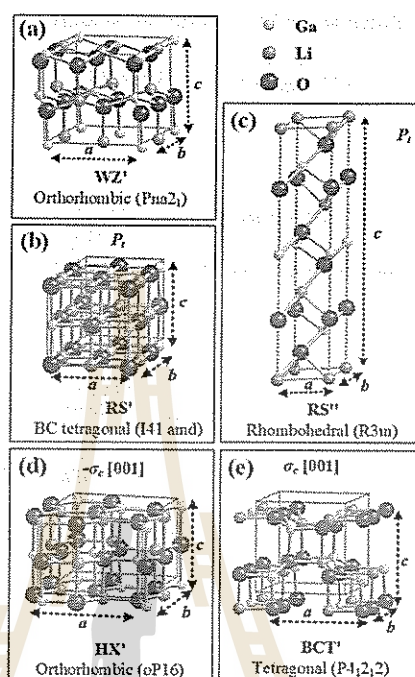


Fig. 1. Schematic illustrations of the ambient and the high-pressure crystal structures of LGO: (a) Orthorhombic ( $Pna2_1$ ) - ambient condition structure, (b) Body-centered tetragonal ( $I4_1/amd$ ) - hydrostatic compression ( $P_c$ ) structure, (c) the Rhombohedral ( $R3m$ ) - another hydrostatic compression ( $P_c$ ) structure, (d) Orthorhombic ( $oP16$ ) -  $[001]$  compressive stress ( $-\sigma_c$ ) structure, and (e) tetragonal ( $P4_12_12$ ) -  $[001]$  tensile stress ( $\sigma_c$ ) structure. In the structures, the green spheres represent Ga cations, blue spheres represent Li cations and red spheres represent O anions.

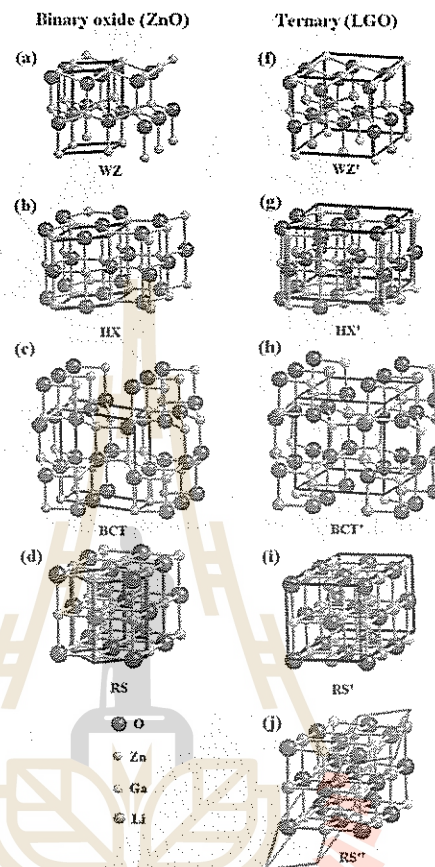


Fig. 2. Relationship between the crystal phases of the binary compound ZnO and the analogous ones of the ternary compound LGO.

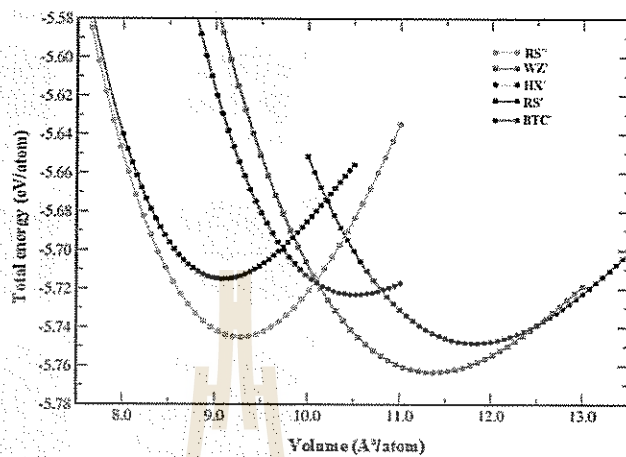


Fig. 3. Total energy versus volume for five LGO structures: Green (RS''), Red (WZ'), black circles (HX'), black squares (RS') and blue squares (BCT').

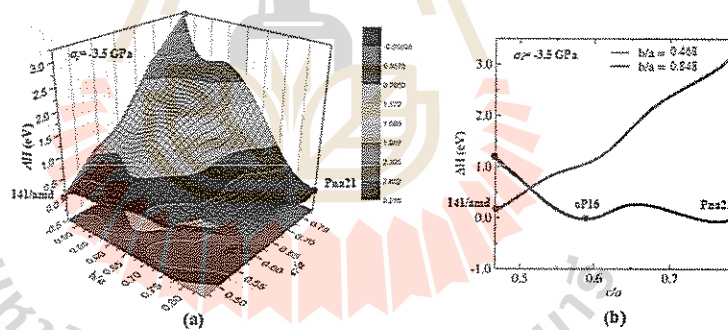


Fig. 4. (a) The enthalpy surface for the compression stress  $\sigma_c = -3.5$  GPa and (b) 2-D sections of the enthalpy surface maps with the compression stress  $\sigma_c = -3.5$  GPa for  $b/a = 0.468$  (red line) and  $b/a = 0.848$  (blue line).

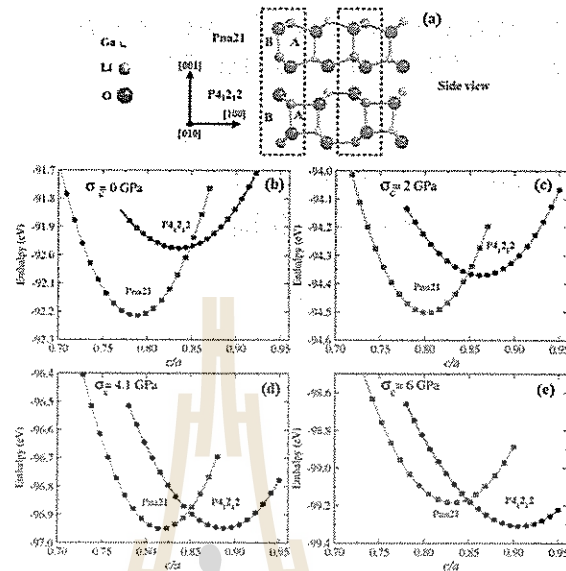


Fig. 5 (a) Schematic comparison of WZ' and BCT' LGO structures. Enthalpy (eV) as a function of  $c/a$  for  $b/a = 0.848$  at different tensile stresses: (b)  $\sigma_c = 0$  GPa, (c)  $\sigma_c = 2$  GPa, (d)  $\sigma_c = 4.1$  GPa and (e)  $\sigma_c = 6$  GPa.



Abstract for the ACS National Meeting & Exposition, (August 16-20, 2015), Boston, MA, USA.

**Structural and Dynamical Properties of Water on Defected BaTiO<sub>3</sub> Surfaces: DFT and *Ab initio* Molecular Dynamic Simulations**

Wutthigrai Sailuam,<sup>1,2</sup> Nongnuch Artrith<sup>1</sup>, Sukit Limpijumnong<sup>2</sup> and Alexie M. Kolpak<sup>1</sup>

(1) Department of Mechanical Engineering, Massachusetts Institute of Technology, Cambridge, Massachusetts 02139, United States.

(2) School of Physics, Institute of Science, Suranaree University of Technology, Nakhon Ratchasima 30000, Thailand

E-mail: wsailuam@mit.edu

**Abstract:**

Catalytic water splitting is a promising clean-energy technology for the production of emission free fuels. Highly active catalysts based on perovskite (ABO<sub>3</sub>) materials are of particular interest because of their low cost and earth abundance. Here we report a computational study of the water structure and dynamics on non-ideal ferroelectric BaTiO<sub>3</sub> surfaces as a prototypical example. Using *ab initio* molecular dynamics simulations, realistic equilibrium structures of the solid/liquid interface at operation temperatures are obtained. The effects of surface defects and transition metal dopants (on A and B site) on the hydration shell are assessed. Additionally, we discuss the influence of the ferroelectric polarization direction in the (001) and (011) surfaces and changes in the electronic structure. This computational understanding of the water/surface interface is an important foundation for the investigation of the water splitting reaction over modified BaTiO<sub>3</sub> and related perovskites.

Abstract for The 10<sup>th</sup> Asian Meeting on Electroceramics, (December 4-7, 2016),

Suranaree University of Technology, Nakhon Ratchasima, Thailand, Taipei, Taiwan.

AMEC-2016

The 10th Asian Meeting on Electroceramics

Dec. 04-07, 2016, Taipei, Taiwan

## Stress-Induced Phase Transformations in LiGaO<sub>2</sub>: First Principle Study

Wutthigrai Sailuam<sup>1,2,\*</sup>, Kanoknan Sarasamak<sup>3</sup>, Miguel Angel  
Mendez Polenco<sup>4</sup> and Sukit Limpijumnong<sup>1,2</sup>

<sup>1</sup>*School of Physics and NANOTEC-SUT Center of Excellence on Advanced Functional  
Nanomaterials, Suranaree University of Technology, Nakhon Ratchasima 30000, Thailand*

<sup>2</sup>*Synchrotron Light Resesearch Institute, Nakhon Ratchasima 30000, Thailand*

<sup>3</sup>*College of Nanotechnology, King Mongkut's Institute of Technology Ladkrabang, Bangkok  
10520, Thailand*

<sup>4</sup>*Department of Mechanical Engineering, Massachusetts Institute of Technology, Cambridge,  
Massachusetts 02139, United States.*

Phase transformations of  $\beta$ -LiGaO<sub>2</sub> (Pna2<sub>1</sub>) under different pressure conditions were studied using first principles calculations. We found that under specific stress conditions, LiGaO<sub>2</sub> can be stable in different structures, some of which have not been previously reported, i.e., oP16, I41/amd, and P4<sub>2</sub>12. Under sufficiently high hydrostatic pressure, a rocksalt-like structure can be stabilized. The uniaxial stresses can stabilize the tetragonal or orthorhombic structures; depending on the direction of the applied stress. We characterized the phase transformation processes by calculating the enthalpy surfaces on the crystal parameters' space and identified the barriers between each local minimum. The equilibrium pressures between the phases are calculated by using the common tangent method. The details of stresses and directions that lead to the new phases of LiGaO<sub>2</sub> will be presented and discussed.

**Keywords:** Phase transformations, LiGaO<sub>2</sub>, High pressure

\* Corresponding author's email: wutthigraiphys33@gmail.com

Abstract for The 9<sup>th</sup> Asian Meeting on Ferroelectrics with The 9<sup>th</sup> Asian Meeting  
on Electroceramics (AMF-AMEC-2014), (October 26-30, 2014), Shanghai

International Convention Center, Shanghai, CHINA.

**AMF-AMEC-2014**

*The Joint Conference of  
9<sup>th</sup> Asian Meeting on Ferroelectrics &  
9<sup>th</sup> Asian Meeting on Electroceramics  
Oct. 26-30, 2014, Shanghai, China*

---

**Structural Phase Transition in BaTiO<sub>3</sub>: First Principles Calculations**

Wuthigrai Sailuam<sup>1,2,\*</sup>, Jiraroj T-Thienprasert<sup>3</sup>, Kanoknan Sarasamak<sup>4</sup>, Sukit  
Limpijumnong<sup>1</sup>

<sup>1</sup>School of Physics and NANOTEC-SUT Center of Excellence on Advanced Functional  
Nanomaterials, Suranaree University of Technology, Nakhon Ratchasima 30000, Thailand

<sup>2</sup>Thailand Center of Excellence in Physics (ThEP Center), Commission on Higher Education,  
Bangkok 10400, Thailand

<sup>3</sup>Department of Physics, Kasetsart University, Bangkok 10900, Thailand

<sup>4</sup>College of Nanotechnology, King Mongkut's Institute of Technology Ladkrabang, Bangkok  
10520, Thailand

\*email: [wuthigraiphys33@gmail.com](mailto:wuthigraiphys33@gmail.com)

**Abstract**

BaTiO<sub>3</sub> in the cubic (Pm-3m) and tetragonal (P4mm) phases were studied by density functional first principles calculations. Their energetic phase stabilities and charge densities were studied. To study the phase stability with respect to temperature, the crystal phonons were calculated using the so-called frozen phonon approximation. The temperature-dependent thermodynamic quantities, such as entropy, Helmholtz free energy, and zero-pressure heat capacity were calculated based on the phonon band structures. When compare the free energies of the two phases with respect to the temperature, structural phase transformation can be calculated. The comparison with available experimental results will be shown and discussed.

**Keywords:** BaTiO<sub>3</sub>, perovskite oxides, first principles calculations, phase transformation

Poster award presentation in the 10<sup>th</sup> Asian Meeting on Electroceramics,  
(December 4-7, 2016), Taipei, Taiwan.

# AMEC-2016

*The 10<sup>th</sup> Asian Meeting on Electroceramics*

## POSTER AWARD

Presented to

Wuthigrai Sailuam<sup>1,2,\*</sup>

Kanoknan Sarasamak<sup>3</sup>

Miguel Angel Mendez Polanco<sup>4</sup>

Sukit Limpijumnong<sup>1,2</sup>

<sup>1</sup>School of Physics and NANOTEC-SUT Center of Excellence on Advanced  
Functional Nanomaterials

<sup>2</sup>Synchrotron Light Resesearch Institute

<sup>3</sup>College of Nanotechnology, King Mongkut's Institute of Technology  
Ladkrabang

<sup>4</sup>Department of Mechanical Engineering, Massachusetts Institute of  
Technology

for the paper titled

Stress-Induced Phase Transformations in LiGaO<sub>2</sub>: First Principle Study

GIS TAIPEI TECH Convention Center, TAIPEI, TAIWAN  
December 04-07, 2016



Prof. Sea-Fue Wang  
General Chair of AMEC-2016





## **CURRICULUM VITAE**

Mr. Wutthigrai Sailuam was born on May 4, 1987 in Khonkaen, Thailand. He finished his high school from Kaennakhon Witthayalai. After that he received full scholarship for one who has talents in science and technology (DPST) to study physics at Faculty of Science, KhonKaen University. He received his B.Sc. in physics (second-class honors) in 2009. In the same year, he joined the Ph.D. program in the School of Physics, Suranaree University of Technology under the supervision of Prof. Dr. Sukit Limpijumnong. He has contributed to several national/international conferences (listed in APPENDIX). He has got award for outstanding poster presentation from the 10<sup>th</sup> Asian Meeting on Electroceramics, (December 4-7, 2016), Taipei, Taiwan. His publications are also listed in APPENDIX.

มหาวิทยาลัยเทคโนโลยีสุรนารี